Structure Formation during Organic Molecular Beam Deposition

Dissertation
der Mathematisch-Naturwissenschaftlichen Fakultät
der Eberhard Karls Univesität Tübingen
zur Erlangung des Grades eines
Doktors der Naturwissenschaften
(Dr. rer. nat.)

vorgelegt von
Berthold Reisz
aus Temeschburg, Rumänien

Tübingen
2021

Abstract

Organic thin films often exhibit semiconducting properties and are used in electronic devices such as organic light emitting diodes (OLEDs), organic field effect transistors (OFETs) and organic photovoltaic cells (OPVs). Their device performance crucially depends on the thin film structures. Suitable materials are small organic molecules and polymers. Small organic molecules can be deposited in vacuum by means of organic molecular beam deposition (OMBD), which ensures both a clean environment and a precise thickness control. The emerging thin films typically exhibit crystalline islands. Surface morphologies range from smooth films, which completely wet the substrate, to the growth of rough surfaces with pronounced clustering. In general, organic thin films are characterized by the sizes and orientations of crystallites, by their crystal structures and by their morphologies, i.e. surface roughness, island shapes, sizes and densities. Binary blends consisting of two molecular species are additionally characterized by their mixing behavior. Binary blends of donor and acceptor material are for instance applied in OPVs in order to separate optically excited charge carriers. Phase separation, large contact areas between donor and acceptor domains, as well as percolation paths to the respective electrodes are favorable for efficient charge carrier separation. Desirable structures can be obtained either by sequential deposition, which means that one compound is deposited first and then the second compound is deposited on top, or by co-deposition, i.e. both molecular species are deposited simultaneously from two different effusion cells. Depending on the growth conditions such as deposition rate, substrate temperature and mixing ratio, different thin film structures and morphologies can be realized.

The present work investigates the influence of deposition rate and substrate temperature during OMBD on the formation of crystallites and islands and discusses the role of molecular diffusion during the growth process. Three simple and small organic molecules were chosen: Copper phthalocyanine (CuPc), coronene and the Buckminster fullerene (C_{60}). Silicon wafers covered by an amorphous, native oxide layer were chosen as weakly interacting substrates. First, crystal structures and morphologies of the pure films are discussed and compared to each other. Subsequently, the morphologies and the mixing behavior of co-deposited 1:1 blends of CuPc and C_{60}, which are known to yield high photovoltaic efficiencies, are analyzed. A combination of real-space imaging comprising atomic force, scanning electron and light microscopy and various X-ray diffraction experiments served for the present studies. Additionally, advanced data evaluation and analysis methods provided quantitative results. The data demonstrates that elevated substrate temperatures, as well as reduced deposition rates lead to the formation of larger islands and lower island densities. Furthermore, the data demonstrates that the temperature driven downward diffusion of CuPc counteracts the roughening effect of C_{60} such that the overall roughness behavior strongly depends on the substrate temperature during growth of blended CuPc-C_{60} thin films.

Contents

Contents

1. Introduction and Theory

This section provides a brief introduction into the growth processes during organic molecular beam deposition. First, the present work is motivated by examples for possible applications. The importance of structure formation for the resulting device performance is pointed out.

1.1. Motivation: Applications for Organic Thin Films

Small organic molecules, consisting of a few hundred atoms or even less, have been applied as dyes and remedies since ages although their chemical structures were unknown for a long time. The development of diffraction techniques in the early 20th century enabled precise structure analyzes of crystallized organic molecules. The discovery of their semiconducting properties during the last decades finally gave rise to numerous studies on the technical applications such as organic photovoltaic (OPV), organic light emitting diodes (OLEDs) and organic field effect transistors (OFETs) [1]. Due to partially lower efficiencies and life-times, it is expected that organic semiconductors will not fully replace inorganic devices, but rather complement them by new features. Especially the possibility of depositing organic thin films on flexible substrates, makes organic electronics thin, light and pliable [2]. Semitransparent photovoltaic cells, integrated in windows, give shade while harvesting solar energy. The required layer thicknesses for sufficient absorption is in the range of a few hundred nanometers, whereas inorganic solar cell require an active layer of several micrometers [3]. The efficiency of organic solar cells can be increased by combining materials with complementary absorption spectra. Furthermore, the huge variety of organic semiconductors extends the color range of LED displays. OLEDs combined with flexible and semitransparent thin film transistors (TFTs) make curved screens possible. While curved screens are already on the market, pliable screens are not yet ready for commercial applications, but preliminary prototypes already exist [4–6]. Once that the degradation of organic layers by bending, shear and torsion forces is reduced, also mass productions of pliable screens are conceivable [4–6]. The choice of molecules is also important. Long polymer chains, on the one hand, are better suited for a cheap mass production. Shorter molecules (mono-, di- and oligomers) consisting of only 1-10 segments, on the other hand, exhibit better molecular ordering although their handling needs more effort [7]. The frequently mentioned low-cost production of organic devices by spin coating, ink-jet or roll-to-roll printing of diluted molecules [1, 2] entails on molecular disorder and impurities. Organic molecular beam deposition (OMBD) in vacuum is a more expensive way to produce organic thin films, but results in pure and well ordered structures owing to the clean environment and the better thickness control [8]. Controlling the growth parameters during OMBD is also important for basic research on growth processes. In the best case, only one parameter such as the substrate temperature T_{Sub} or the deposition rate R_{Dep} is altered while all other parameters are kept constant. This procedure allows to determine the impact of a single growth parameter on observables such as the molecular ordering and the evolving thin film morphology.

1.1.1. Organic Photovoltaic (OPV)

The working principle of organic solar cells is similar to their inorganic analogues. Nevertheless, there are also significant differences concerning their material properties, which has to be considered for the solar cell layout. The p- and n-doped regions of inorganic solar cells are replaced by organic donor and acceptor molecules. Although organic materials do not exhibit valence and conduction bands, optical excitation and charge transport is possible. Photons impinging at sufficiently high energies excite electrons from the highest occupied to the lowest unoccupied molecular orbitals (HOMO $\rightarrow$ LUMO), see Fig. 1 and Refs. [2, 3].

Figure 1:

Optical excitation of an electron from the highest occupied molecular orbital (HOMO) to the lowest unoccupied molecular orbital (LUMO) and subsequent separation from its hole by jumping into the energetically lower LUMO of the acceptor molecule. LUMO' indicates the energy level of the triplet state, which is energetically lower than the LUMO of the acceptor and impedes the charge carrier separation.
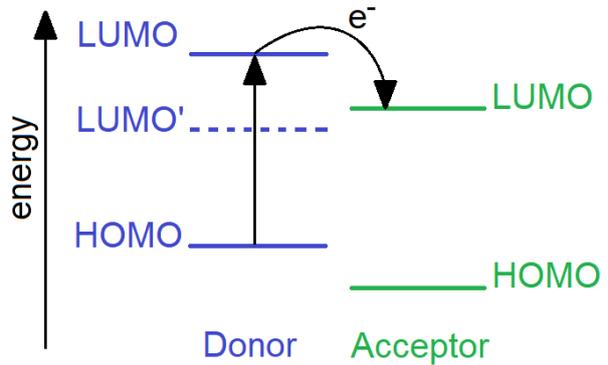
The comparatively low power conversion efficiency of the first organic solar cells can be explained by various loss mechanisms. One of them is the formation of so called excitons after absorption of light. Excitons are bound electron-hole pairs, whose radius r_0 and binding energy E_B can be calculated for a given dielectric constant ϵ_r according to the hydrogen atom:

$$E_B = E_R \cdot \frac{\mu}{m_e} \cdot \frac{1}{{\epsilon_r}^2} \tag{1}$$

$$r_0 = a_0 \cdot \frac{m_e}{\mu} \cdot \epsilon_r \tag{2}$$

E_R is the Rydberg energy, a_0 is the Bohr radius and μ is the reduced mass of electron and hole. The binding energy of excitons in conventional inorganic semiconductors is usually lower than the thermal energy of $k_B T \approx 25\,\text{meV}$ such that electrons and holes immediately dissociate at room temperature.

The lower dielectric constant ϵ_r of organic materials leads to excitons that are much more strongly bound [9]. Without external influences, electrons and holes recombine after a few nanoseconds and no electric current is generated. Hence, a separation of electron and hole at the donor-acceptor interface is vital for the power conversion. The photon is usually absorbed in the donor material by exciting an electron from the HOMO to the LUMO, which is then separated from its hole by

jumping into the energetically lower LUMO of the acceptor, see Fig. 1. This process occurs within less than 100 fs and is faster than any loss mechanism [3]. The first organic solar cell employing a planar donor-acceptor interface was presented in 1986 and achieved a power conversion efficiency of 1% [10].

In the following decades, the efficiency of organic solar cells was further increased by the application of bulk hetero-junctions. Generated excitons have to diffuse to the donor-acceptor interface within their life time, i.e. before they decay. Depending on the material, they can cover distances of 3-88 nm [11] and up to 100 nm in single crystals [12]. Hence, any point in the active layer should be less than 100 nm away from the interface. Furthermore, the separated charge carriers have to diffuse to the respective electrodes without passing further interfaces. Percolating networks with rough and interlocked interfaces fulfill the required conditions and lead to efficient devices.

Figure 2 shows different types of organic hetero-junctions [13]. Some of which require advanced preparation techniques such as co-deposition, which means that donor and acceptor molecules are evaporated simultaneously inside of a vacuum chamber. A hybrid planar-mixed hetero-junction, see Fig. 2 (g), with copper phthalocyanine (CuPc) as donor and the Buckminster fullerene (C60) as acceptor yielded a power conversion efficiency of (5.0±0.3)% in 2005, see Ref. [14].

Figure 2:

Different solar cell architectures:

(a) planar HJ

(b) HJ with rough interface

(c) HJ with interlocked interface

(d) gradient HJ

(e) molecular mixed bulk HJ

(f) phase-separated bulk HJ

(g) hybrid planar-mixed HJ

modified from Ref. [13].
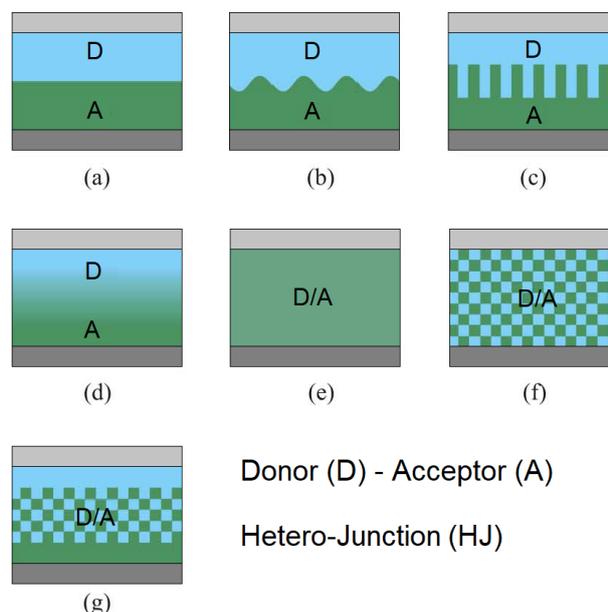
Note that the bottom electrode (indicated in dark gray) represents the substrate on which the organic materials are deposited. The top electrode (indicated in light gray) has to be semitransparent, such that light can enter the donor material from the top. Moreover, electrodes with suitable work functions have to be found [3]. Unfavorable work functions inhibit an efficient charge carrier extraction and lead to an accumulation of electrons or holes at the interface between the organic layer and the respective electrode. Possible electrode materials are thin metallic stripes, glass substrates

coated with transparent indium tin oxide (ITO) [15], or conducting polymer films such as the flexible and transparent poly(3,4-ethylenedioxythiophene), abbreviation PEDOT [16]. Additional passivation layers can counteract the charge carrier accumulation and improve the solar cell efficiency [17].

Further improvements were obtained during the last few years by combining several organic layers with complementary absorption spectra. A power conversion efficiency of 10.6% was achieved in a polymer-based tandem cell in 2013, see Ref. [18] and a power conversion efficiency of 17.3% was achieved in an even more sophisticated multilayer solar cell in 2018, see Ref. [19]. Also the molecular orientation with respect to the incoming light plays a role; the anisotropic transition dipole moment of organic molecules leads to orientation dependent absorption spectra of different absorption strengths [20, 21].

Before concluding this section, it should be mentioned that there are further loss mechanisms such as the generation of triplet excitons [3]. Triplet excitons exhibit significantly longer life times, which are in the range of milliseconds [3]. Nevertheless, they do not contribute to the electric power. The lower binding energy of triplet excitons impedes a charge transfer to the acceptor material, see Fig. 1 and Ref. [3]. Also charge carries that are trapped at impurities or crystal defects do not contribute to the electric power [22]. The various loss mechanisms are research fields on their own and would exceed the scope of this work. To summarize, this section demonstrated the importance of the thin film structure for efficient OPV devices.

1.1.2. Organic Light Emitting Diodes (OLEDs)

Not only the first organic bilayer solar cell, but also a prototype for organic light emitting diodes (OLEDs) was presented in the mid 1980ies [23]. An OLED is in principle a solar cell operated in reverse direction. Applying a voltage to the device leads to emission of light. Advantages of OLEDs compared to inorganic LEDs are the large variety of organic molecules providing a broad color range and the pronounced flexibility of organic materials, which makes curved and pliable screens possible [4–6]. Contrary to OPVs, the formation of triplet excitons is desired for good OLED efficiencies [24], since charge carrier recombination, which entails on the radiation of light, is more likely during the longer life time of triplet excitons. The pixels of conventional OLED displays are controlled by a passive matrix of cross-linked wires, which is cheap in production but looses voltage along the rows and columns. In order to reduce the power consumption of large OLED displays, an active matrix controlling each pixel separately is added to the background layer [25]. Each pixel of a so called AMOLED display has a separate power supply and can be switched on and off by a combination of thin film transistors (TFTs) and capacitors. So far, the TFTs are made up of inorganic materials such as amorphous silicon (A-Si) and low temperature polycrystalline silicon (LTPS) [26]. Also indium gallium zinc oxide (IGZO) turned out to be a suitable material [27]. However, organic field effect transistors are rarely mentioned in the context of OLED displays although they could be thin, flexible, light and transparent.

1.1.3. Organic Field Effect Transistors (OFETs)

Field effect transistors are tiny components on microchips for the regulation of electric currents through other chip components such as LED pixels. By applying a voltage at the gate contact, the current between source and drain can be switched on and off while an insulating layer inhibits electric currents through the gate, see Fig. 3. First, the channel between source and drain was replaced by organic materials in order to test their charge carrier mobilities, see Refs. [28, 29] for a comprehensive overview. The charge carrier mobility can be improved by either improving the preparation process or by synthesizing new organic materials [28, 29]. Evidences were given that molecular ordering [30] and larger grain sizes [31] improve the charge carrier mobility. The importance of the molecular orientation with respect to the channel direction was emphasized since the charge carrier mobility of organic molecules turned out to be highly anisotropic [30, 31]. Also structural defects and chemical impurities influence the charge carrier mobility [32, 33] and appear especially at grain boundaries [34]. An example for the successful application of OFETs in an AMOLED display is given in Ref. [35].

Figure 3:

Organic field effect transistors (**OFETs**) and possible device architectures (schematic sketch, modified from Ref. [29]):

Depending on the molecular orientation with respect to the channel direction, different charge carrier mobilities were measured [30, 31]:

a) standing up molecules

b) lying down molecules.

Note that the number of molecules, the size of molecules and the device dimensions are not to scale in this schematic sketch.
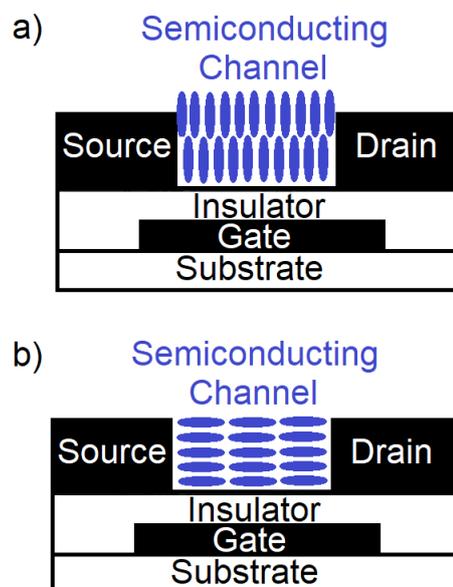
1.1.4. Summary

The importance of the thin film morphology in binary blends of donor and acceptor molecules was pointed out in this section for the solar cell efficiency. Large, pure and percolating networks with interlocked interfaces are suited best and can be prepared by co-deposition in vacuum. Furthermore, the grain sizes, and the molecular orientation play an important role, in particular for OFETs.

1.2. Intermolecular Interactions

1.2.1. Different Types of Interaction Forces

Crystal structure and thin film morphology are both governed by intermolecular interactions. There are various forces involved in intermolecular interactions. A combination of Van der Waals attractions and the Pauli-repulsion leads to a potential minimum defining the intermolecular distance [36].

The Pauli repulsion is based on the electrostatic repulsion of electrons in atomic orbitals of neighboring molecules and can be described quantum mechanically. It decreases with the power of 12. The attractive forces can be divided into polar and non-polar Van der Waals forces and decrease with the power of 6. Together with the Pauli repulsion, they form the Lennard-Jones potential, see Fig. 4. Due to the short range of the Pauli repulsion, the minimum of the Lennard-Jones potential and hence also the minimum distance between two atoms is in the order of a few Ångstrom.

Figure 4: Lennard-Jones potential:

This potential describes the interaction between atoms or particles in an ideal gas. It is repulsive at small distances, attractive around its global minimum and zero at long distances.

Lennard-Jones Potential

$$V_{\text{LJ}} \propto \left[\frac{1}{r^{12}} - \frac{1}{r^6} \right]$$
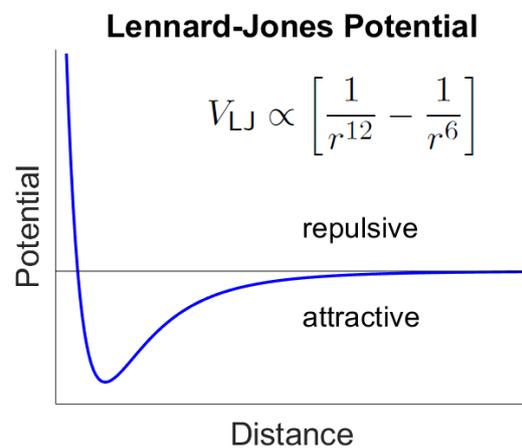
The non-polar attraction due to London is based on temporarily induced dipole moments. The effective interaction range amounts to a few nanometers, which is not much larger than the size of a single molecule. Long range attraction is lacking in this case, but when two molecules touch each other, a mutual dipole induction occurs and both molecules stick together. Nevertheless, larger nano-particles such as colloids do have a long range attraction. Their attractive forces sum up and the interaction range increases depending on the size an shape of the nanoparticles.

Polar molecules exhibit permanent electric dipoles stemming from polar covalent or ionic bonds that separate positive and negative charges permanently. Polar molecules arrange such that their dipole moments compensate each other due to Keesom. A polar molecule can also induce a dipole moment inside of a non-polar molecule due to Debye.

Furthermore, there are multipole interactions [37]. A prototypical example for a molecule with multipole interactions is the benzene ring (C_6H_6) [38]. This aromatic molecule has no permanent dipole moment. The first non-zero multipole moment is a quadrupol represented by the delocalized π-electrons of carbon (negative charges) and the hydrogen cores (positive charges). The negative charges are located above and below the molecular plane and the positive charges are located at the edges. Two kinds of configurations result from the quadrupole moment, the face-to-face and the face-to edge stacking [39]. The face-to-face stacking is mediated by interactions between π- and σ-orbitals of adjacent molecules [40]. The face-to-edge configuration, also known as herringbone stacking, is mediated by hydrogen bonds between hydrogen atoms and π-orbitals [38].

1.2.2. Interaction Energies in Binary Blends

This section refers to the book of Kitaigorodsky [41] and can be found in Ref. [42]. A binary blend is a material that consists of two different types, say A and B, of molecules. Whether these molecules prefer intermixing or separation into pure domains of either type A or type B, can be answered by regarding the free energy $F = U - T \cdot S$. The internal energy U represents the energy difference between mixed and unmixed state. The entropy $S \equiv k_B \cdot ln(P)$ is defined as the Boltzmann factor k_B times the natural logarithm of the number P of possible configurations. After some algebraic transformations, the total free energy of a binary mixture with fraction Φ_A of particles of type A and fraction Φ_B of particles of type B results in:

$$F = k_B T \cdot (\chi \cdot \Phi_A \cdot \Phi_B + \Phi_A \cdot ln(\Phi_A) + \Phi_B \cdot ln(\Phi_B)) \tag{3}$$

The interaction parameter χ, also known as Flory-Huggins parameter, depends on the temperature, the number Z of nearest neighbors and on the interaction energies W_{AA}, W_{BB} and W_{AB} between particles of type A and B:

$$\chi = \frac{Z}{2k_B T}(W_{AA} + W_{BB} - 2 \cdot W_{AB}) \tag{4}$$

Three cases appear, depending on the value of χ, see Fig. 5:

(1) Phase separation ($\chi >> 2$):
  The free energy $F(\Phi_A)$ exhibits a global maximum at $\Phi_A = \Phi_B = 0.5$

(2) Transition regime ($\chi > 2$ but close to 2):
  A maximum combined with two local minima on either sides appears.

(2) Intermixing ($\chi < 2$):
  The free energy $F(\Phi_A)$ exhibits a global minimum at $\Phi_A = \Phi_B = 0.5$

Note: $\Phi_A + \Phi_B \equiv 1$ per definition.

Phase-separation: For $\chi \gg 2$, the free energy has a maximum at $\Phi_A = \Phi_B = 0.5$, which means that the molecules prefer phase-separation into pure domains of either type A or type B in order to minimize the free energy.

Transition regime: While reducing χ, two local minima appear on either side of the maximum, which means that the phase-separated domains are not completely pure. In each domain, one type of molecules is abundant, but a little fraction of the respective other type is also present, see Fig. 5. So, the magnitude of χ is a measure for the purity. Lowering the value of χ, shifts the minima closer to each other and the purity decreases until complete intermixing is reached at $\chi \leq 2$.

Intermixing: For $X < 2$, the free energy has only one global minimum at $\Phi_A = \Phi_B = 0.5$. This means that the molecules intermix. On average, there is the same amount of molecules of type A as of type B around an arbitrarily chosen molecule.

Mixing scenarios: Two mixing scenarios are possible. One scenario is similar to intermetallic compounds. Two types of molecules form a new lattice with new lattice parameters and a fixed molecular ratio per unit cell. The other scenario is similar to alloys. The molecules are statistically mixed, which means that molecules of different types randomly occupy lattice sites. [43]

Similar interaction energies: For interaction energies of similar strength $W_{AA} = W_{BB} = W_{AB}$, the interaction parameter χ is close to 0 and leads to intermixing, which validates the Latin statement 'similia similibus solvuntur' (similar things are dissolved by similar things).

Figure 5:

Free energy $F(\Phi_A)$ of a binary blend in the case of $\chi = 3$.

The ratio Φ_A:Φ_B develops such that the F is minimized in each domain.

Two kinds of domains form:

Left minimum: $\Phi_A = 0.1$ and $\Phi_B = 0.9$

Right minimum: $\Phi_A = 0.9$ and $\Phi_B = 0.1$
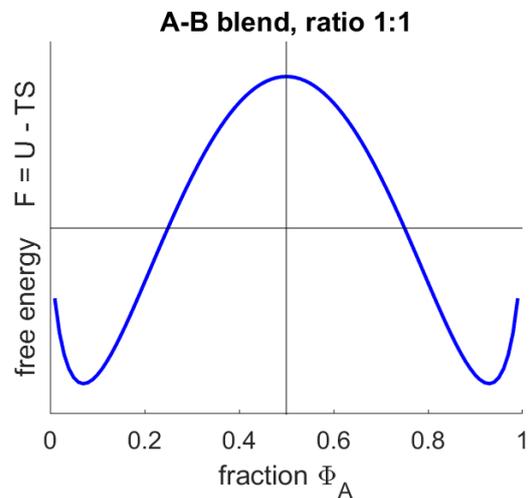
1.3. Diffusion Processes and Growth Models

The thin films of the present work are prepared by organic molecular beam deposition (OMBD, see Sec. 3). Briefly explained, molecules are heated up and evaporate from effusion cells inside a vacuum chamber. Their acceleration towards the substrate is solely caused by thermal energy and the molecular flux can be adjusted by changing the evaporation temperature. The resulting crystal structures and thin film morphologies strongly depend on the flux of molecules, the substrate temperature and on the above mentioned intermolecular interactions. This section focuses on the diffusion, which is influenced by the substrate temperature and the distinct interaction forces. The direct experimental observation of diffusion processes is quite challenging. Nevertheless, a large number of experimental, theoretical and numerical studies exist. The following considerations were derived for atomic growth but can be applied to molecules as well. The lateral diffusion on the substrate and the nucleation of islands will be discussed first. The second part addresses the vertical diffusion from one layer of deposited particles to another and explains the resulting evolution of roughness. Comprehensive compilations of the distinct growth models are given in Refs. [44–49].

1.3.1. Lateral Diffusion

As soon as a molecule approaches the substrate, interactions between molecule and substrate occur. Depending on the interaction strength, impinging molecules can stick on the substrate, diffuse on the substrate surface, or re-evaporate from the substrate. Particle diffusion on substrates can be described by a random walk model. Although the covered distance increases with time t, the particle cannot diffuse infinitely far away from the starting point, see Fig. 6 and Ref. [50]. For constant step sizes l, the direct distance from the starting point after N random steps is $|\vec{R}| = \sqrt{N} \cdot l$, see Ref. [51]. The diffusion length is defined by the covered distance $|\vec{R}|$ until a certain event happens. This event could be desorption from the substrate or attachment to a cluster of particles. Different energy barriers for diffusion and desorption have to be assumed depending on the kind of substrate.

Figure 6:

Random walk simulated in *Matlab*:

Blue arrow: Distance $\vec{R}$ from starting point after $N = 1000$ steps of constant step size l.
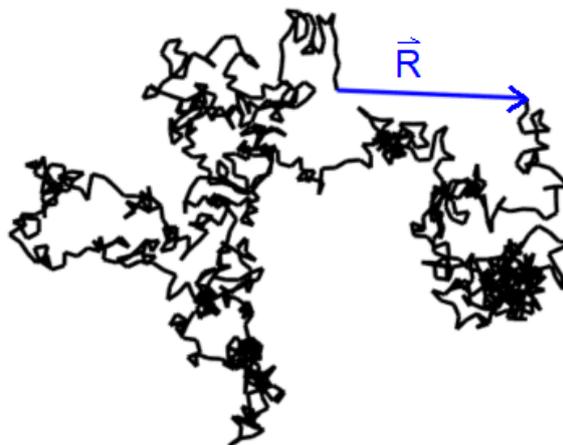
Generally, substrates can be divided into two subgroups: Inert substrates are amorphous inorganic materials and allow a continuous diffusion, though the diffusion is decelerated by electrostatic interactions between adsorbed particle and substrate, which can be regarded as a kind of friction. The second type of substrates is patterned and supports epitactic growth, which means that the growing film takes over the pattern of the substrate. Diffusion on patterned substrates is only possible in discrete steps from potential well to potential well and the corrugations of the substrate form the diffusion barriers.

Nucleation of Islands:

As the number of particles on the substrate increases, nucleation takes place. Nucleation means that two or more particles stick together and form a cluster. In the particular case of growth on substrates, those clusters are called islands. Islands may diffuse as a whole on the substrate surface or split up into smaller parts again. Whether diffusion or dissociation takes place or not, depends on the island size and the interaction energies. The maximum number i^* of particles at which an island can still dissociate is called the critical island size. Islands consisting of i^*+1 or more particles are more likely to grow than to decay, but they can still dissociate [52].

1.3.2. Lateral Growth Models

In the following, several growth models and their implications are presented. The history of growth models begins with simple numerical simulations on the microscopic scale and gradually turns into statistical studies which explain the overall behavior on larger length scales.

Eden Model (1961): [53]

One of the first and simplest simulations of horizontal growth processes is the Eden Model, which describes the fractal growth of bacteria colonies or cell clusters on a 2D lattice, see Fig. 7: One lattice site is occupied as nucleation center. Lattice sites next to an already occupied site are called growth sites. One randomly chosen growth site is occupied per time step. However, this model neither takes desorption into account nor diffusion.

Figure 7:

Simulated Eden Cluster of 1500 particles on a square lattice taken from Ref. [54]. A lattice site was occupied in the beginning as nucleation seed. Lattice sites next to an occupied site are called growth sites. The Eden Cluster finally forms by a random occupation of growth sites.
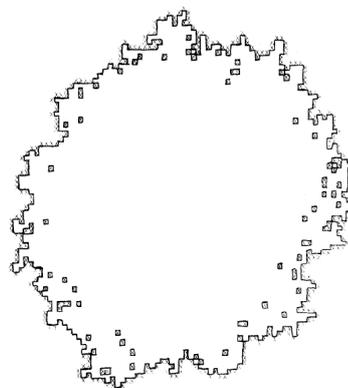
Williams and Bjerknes Model (1972): [55]

This model is an expansion of the Eden model and adds occupation and depletion rates to the growth sites, which simulates the contamination and recovery of neighboring biological cells during cancer growth. Obviously, the occupation rate has to be higher than the depletion rate for an effective growth of clusters. The depletion entails on the separation of an initial cluster into distinct smaller clusters and the discussion of percolation becomes relevant. All paths crossing solely occupied lattice sites are called percolation paths, which helps to assign lattice sites to distinct clusters. Two lattice sites of the same cluster can be connected to each other by a percolating path, which is not possible for lattice sites of different clusters. Although this model was developed for biological systems, it can also describe the formation of clusters during particle deposition on hot surfaces. Occupation and depletion correspond to deposition and desorption rates. Diffusion processes are completely neglected in this model and the particles are immediately attached to an existing cluster by definition.

Diffusion Limited Aggregation (DLA) Model (1981): [56, 57]

Witten and Sander extended the Eden model in 1981 by introducing diffusion moves. First, a lattice site is occupied as nucleation center. Then another particle is deposited at a random place and performs a random walk from lattice site to lattice site simulating a Brownian motion. As soon as the particle reaches the vicinity of an already occupied site, it sticks there permanently and another particle is deposited at a random place. Repeating this process over and over leads to dendritic structures, which resemble the ramified branches of a tree. Since the formation of dendritic islands is a diffusion limited process and occurs at rather low substrate temperatures, the dendrites are not infinitely stable in real experiments. Experimental evidence for the transition from fractal dendrites towards more compact islands by particle diffusion along the rim of islands was given by Bartelt and Evans in 1994, both for submonolayer [58] and multilayer growth [59] of platinum (Pt) on a planar Pt(111) substrate, as well as later on for gold on Ir(111) [60], see the inset in Fig. 8.

Figure 8:

Diffusion limited aggregation of 3600 particles on a square lattice, taken from Ref. [56].

Right side: Shape relaxation into more compact islands by thermally activated edge diffusion, taken from Ref. [60].

Inset: The diffusion along the edges stops as soon as the particle reaches a site at which the number of nearest neighbors is maximized, modified from Ref. [58]
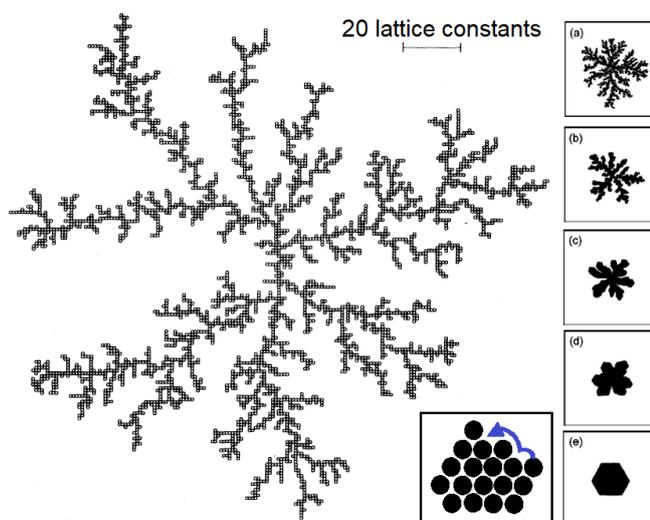
Cluster-Cluster Aggregation (1983): [61, 62]

Meakin, Kolb, Botet and Jullien developed a growth model, which considers not only the diffusion of single particles, but also diffusion and aggregation of entire particle clusters. It is reasonable that the diffusion constant depends on the cluster size. The question to be answered by experiments is how the diffusion constant scales with cluster size. Intuitively, larger clusters should diffuse slower than small ones and may get immobile at a certain size. Furthermore, the probability that two colliding clusters stick together and form a new and larger cluster may depend on the number of sticking sites.

Voronoi Tessellation:

With increasing amounts of deposited material, the number of islands increases and the probability that two or more particles meet and form a new cluster decreases such that the nucleation process stops at a certain stage of growth. Instead, existing islands grow laterally by capturing all particles that impinge within their vicinity. Those capture zones, also known as Voronoi cells, define all points which are closer to a given nucleation center than to any other island, see Refs. [63–65] and Fig. 9 for explanation. Of course, this Voronoi tessellation assumes that the layer coverage is still low enough such that all islands can be treated as point-like nucleation centers. Finally as the islands grow in diameter, the empty space on the substrate is consumed and the islands start to coalesce until the substrate coverage approaches 100%.

Figure 9:

Simulated Voronoi tessellation at a substrate coverage of 20%, taken from Ref. [64]:

Black circles indicate grown islands of different diameters. Bisection lines between the islands define the borders of the Voronoi cells and indicate all points whose distance from two neighboring islands is the same. Furthermore, the distance from three or more islands is equal at the corners where several bisection lines meet.
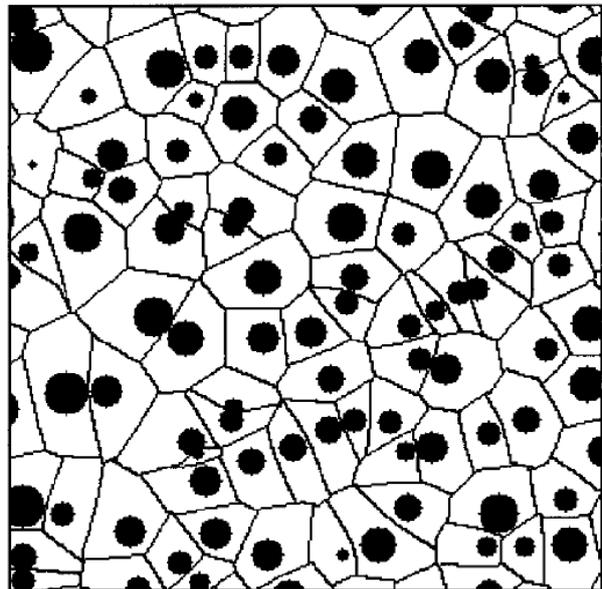
Droplet Model (1989): [66]

If the substrate temperature is close to the melting point of the deposited material the islands relax into the shape of truncated spheres by fast diffusion processes, which is in contrast to the highly diffusion limited aggregation of dendritic islands at low substrate temperatures. For this reason, coarse grained models simulate the nucleation and growth of droplets on surfaces instead of simulating the motion of each single particle. The size distribution of tin droplets on sapphire was well reproduced by nucleation simulations, see Fig. 10 (a) and Ref. [66]. This simulation distinguishes homogeneous and heterogeneous nucleation. Heterogeneous nucleation occurs at given impurities on the substrate in the beginning of growth and afterwards no new islands nucleate. The present islands simply grow in size according to the Voronoi construction. Homogeneous nucleation means that new islands can nucleate spontaneously at any time during growth. The droplets are not allowed to diffuse in this model, but once the radii of two neighboring islands have grown such that they touch or overlap each other, they merge into a new and larger droplet by shape relaxation. Of course, volume and mass are conserved during this kind of coalescence. Another study showed that smaller droplets are indeed incorporated by larger droplets in order to reduce the surface tension, which is known as Ostwald ripening [67]. A relation between the contact angle θ_e of droplets on a surface and the distinct surface tensions γ was found and is given by $\gamma_{\mathsf{LV}} \cdot \cos(\theta_e) = \gamma_{\mathsf{SV}} - \gamma_{\mathsf{SL}}$, see Fig. 10 (b) and Ref. [68]. The degree of wetting depends on the contact angle. Perfect wetting is obtained for $\theta_e \to 0$ and with increasing contact angle the particles tend more and more to de-wetting, i.e. forming tall islands of small base diameter and the substrate is not fully covered. The formation of such tall islands as well as the wetting of the substrate requires interlayer diffusion, which will be discussed in more detail in Sec. 1.3.3.
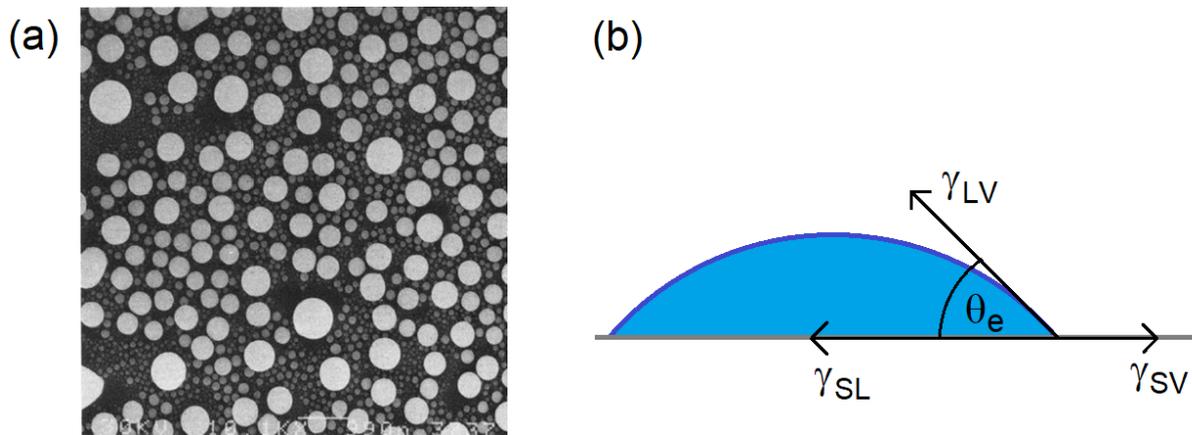
Figure 10: (a) Scanning electron micrograph of tin droplets on sapphire taken from Ref. [66] and (b) Contact angle θ_e of a droplet on a surface in equilibrium and surface tensions (γ_{SV} between solid and vapor, γ_{SL} between solid and liquid and γ_{LV} between liquid and vapor.

Island Size Distributions:

Before concluding this section about lateral growth and island formation, it should be mentioned that some effort was made for a statistical description of the overall behavior. Main observables are the fractal dimension of island shapes and the distribution of island sizes. One would expect a simple Poisson distribution resulting from random growth processes. Sophisticated distribution functions similar to the Poisson distribution were derived from numerical simulations and model the impact of various growth parameters such as diffusion and nucleation processes. In particular, the strong dependency on the minimum size i^*+1 for stable clusters was demonstrated by both simulations and experiments [69]. The assumption of immobile islands gathering impinging particles from their capture zone turned out to be well suited for the reproduction of realistic island size distributions [63]. Not only the size distribution of droplets, but also the size distribution of small fullerene clusters comprising only a few molecules was studied by scanning tunneling microscopy [70, 71]. Also the temporal evolution of island sizes was studied and dynamic scaling laws, describing how the island sizes scale with time, were derived [72]. The congruence between simulations, experiments and theory is excellent throughout numerous studies on island size distributions. To conclude, the theory of island size distributions is applicable on many growth phenomena ranging from microscopic to macroscopic length scales.

1.3.3. Vertical Diffusion

Interlayer Diffusion and Step Edge Barriers:

In addition to the diffusion on the substrate surface, particles can also diffuse from the substrate level to the top of an already grown layer. Of course, a downward diffusion is also possible. This kind of diffusion from one layer to another is called interlayer diffusion. The energy barrier for interlayer diffusion is usually enhanced, which was first observed and described in 1966 as step edge barrier for atomic growth by Ehrlich and Schwoebel, see Fig. 11 and Ref. [73]. Some computational studies assume that organic molecules are distorted or change their orientation during step edge diffusion, which requires, compared to atomic growth, additional energy [74].

Figure 11:

Step edge barrier (blue line) modified from Ref. [75]: The larger number of nearest neighbors in the recessed corner beneath the step edge entails on a deeper potential well, whereas the lower number of nearest neighbors during diffusion across the step edge enhances the energy barrier.
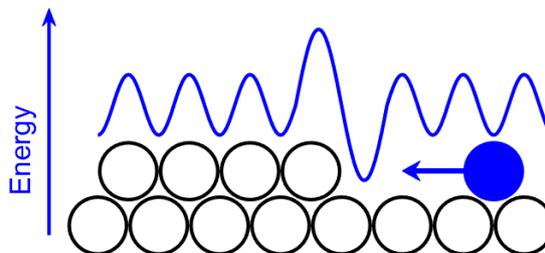
Figure 12:

Possible bending of a pentacene molecule at a step edge, taken from Ref. [74].
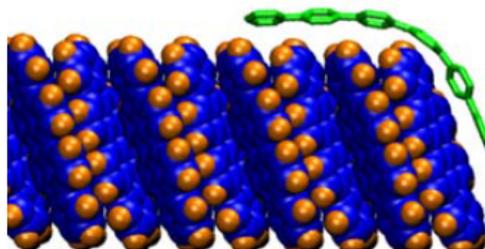
Particles can also impinge directly on top of an already grown layer, see Fig. 14. The probability that an incoming particle impinges on a given layer increases with increasing layer area. Nevertheless, this does not necessarily mean that a second layer grows. Only if the particles remain on top of the island until the critical number i^*+1 is reached, the growth mode changes from monolayer to multilayer growth, provided that the particles meet and form stable islands. Generally, downward diffusion is easier than upward diffusion since the energetically most favorable place is the deep potential well in the recessed corner beneath step edges, see Fig. 11. Nevertheless, the diffusion can also go upwards, which is favored, when the interparticle interactions are stronger than the interaction between particles and substrate. Small distances between the single step edges or in other words steeper slopes (see Fig. 13) facilitate upward diffusion further during the multilayer growth, which will be discussed in the following section. Which diffusion direction (up or down) is preferred depends on many parameters such as interaction strengths between particles and substrate, distances between step edges, molecular shapes (spherical, disc-, or rod-like) and geometric path ways along certain crystallographic directions [74].
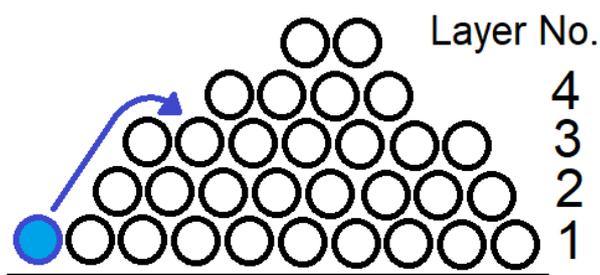
Figure 13: Upward diffusion of spherical particles along steep slopes: There is no step edge barrier across the first three layers and diffusion up to the third layer is not distinguishable from a horizontal diffusion on top of a grown layer. Actually, the implementation into the fourth layer is energetically favorable according to the larger number of nearest neighbors compared to the substrate level - provided that the interaction with the substrate is weak.

Multilayer Growth: [76, 77]

The occurrence of multilayer growth is a complex phenomenon and depends on many parameters. Impinging particles can diffuse on the substrate, attach to an island, diffuse upwards to the top of an already grown layer, or form a new layer by nucleation, see Fig. 14. Particles impinging on top of an already grown layer can diffuse downwards to the substrate level or form a second layer. Favorable conditions for the nucleation of a second layer are:

(1) **Flux and diffusion:** A larger deposition rate F and a slower diffusion D, also known as flux-to-diffusion ratio F/D, enhances both the number of impinging particles and their residence time on top of an island such that the critical island size i^*+1 for nucleation can be obtained before downward diffusion occurs.

(2) **Critical island radius:** Once an island has reached a critical diameter of size $2 \cdot R_c$, an impinging particle is on average further away from the rim of the island than the diffusion length, which makes the nucleation of a second layer more likely.

(3) **Critical island size:** Of course, also the critical island size i^*+1 for nucleation plays an important role. Simulations have shown that transition from monolayer to multilayer growth occurs suddenly at the critical island radius R_c when $i^*=1$. This sharp transition becomes statistically smeared out when the critical island size i^* is larger, which means that the fraction of islands with second layer nucleation increases slowly with time.

(4) **Island shape:** The influence of the shape of islands on second layer nucleation is inferred from item (2). Compact islands reduce the probability for downward diffusion and facilitate multilayer growth, whereas fractal islands, such as for instance ramified dendrites (see Sec. 1.3.4), provide too many opportunities for downward diffusion and hence allow no nucleation of a second layer. No place on top of such an island is further away from the rim than the diffusion length, although fractal islands can spread out to quite large radii.

(5) **Step edge barrier:** Finally, tall step edge barriers hamper the downward diffusion and favor the growth of a second layer, even though the above mentioned items are not fulfilled. The attempt frequency indicates how often a particle attempts to surmount a diffusion barrier per second. Attempt frequencies are estimated to be in the range of 10^{11} to 10^{12} per second for atomic growth.

Figure 14:

Diffusion processes during organic molecular beam deposition (OMBD) and formation of islands, taken from Ref.[78]
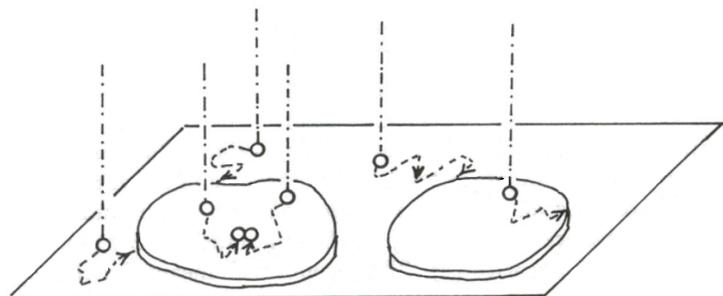
Distinct Growth Modes:

Vertical growth is generally divided into three growth modes, the layer-by-layer growth, the island growth and the island-plus-layer growth see Fig. 15 and Refs. [45, 79]:

Layer-by-layer growth (Frank-Van der Merwe): In LbL-growth scenarious, particles prefer downward diffusion until the currently growing layer is completely filled. Then, and only then, the next layer starts to grow on top. This growth mode requires low step edge barriers and an attractive molecule-substrate interaction leading to a preferential wetting of the substrate.

Island growth (Volmer-Weber): In this island growth scenario, the film does not wet the substrate. Instead distinct islands grow, which may cover the substrate by coalescence of neighboring islands after a certain amount of particles is deposited. Thin films resulting from island growth are rougher than films that grew layer by layer.

The **island-plus-layer growth mode** (Stranski-Krastanow) is a combination of both. Initially, smooth layers grow one after another. After a certain film thickness is reached, island growth starts to occur.
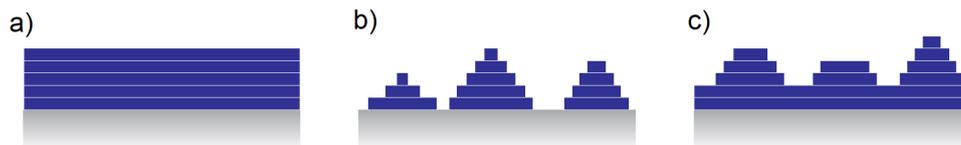
Figure 15: Three different growth modes during: (a) Frank-Van der Merwe growth, (b) Volmer-Weber growth, (c) Stranski-Krastanow, taken from Ref. [80]

Layer by layer growth is expected when the critical island radius R_c for multilayer growth is larger than half of the average interisland distance L_n, whereas island growth is expected in the opposite case ($R_c < L_n/2$) [76]. Island-plus-layer growth occurs in atomic heteroepitactic growth if the lattice constants of substrate and film are slightly different, which creates mechanic strain in the top layer. [81]. As the film grows, the strain increases and becomes larger than the chemical bonds at a critical height h_c. As a result, chemical bonds break and the growth mode changes from layer-by-layer to island growth. This growth mode should not be confused with non-epitactic layer-plus-island growth of molecules on inert substrates. There, other explanations such as the screening of the substrate potential might be suitable. Once the substrate potential is screened after a certain number of layers has grown, downward diffusion is no longer favorable and islands start to grow. Finally, the coalescence of neighboring islands during growth leads to similar film structures of completely filled layers and islands on top. Nevertheless, this is pure island growth. Although macroscopically the surface profile looks similar to island-plus-layer growth, the microscopic structure may differ. Differently oriented crystallites in the distinct islands lead to misfits at the grain boundaries and impede the charge carrier diffusion. So, avoiding those grain boundaries is of paramount importance for the device efficiency.

1.3.4. Vertical Growth Models

Although the development of vertical growth models was was not as straight forward as for lateral growth, the subsections of this section are ordered accordingly starting with microscopic growth and finishing with statistical consideration on larger length scales. In particular, dynamic scaling laws were derived from different numeric growth models in order to describe how the roughness σ scales with time t. Some vertical growth models are simplified by regarding 2D-growth on a 1D-substrate in side view instead of simulating 3D-growth on a 2D-substrate. Without diffusion, there is no difference between 2D- and 3D-growth, but as soon as diffusion enters the picture, the dimension becomes crucial for the resulting morphology.

Eden Model for Vertical Growth: [82]

The Eden Model model was further modified by Kertesz and Wolf for the simulation of porous 2D and 3D growth on a substrate: The bottom line (2D-growth) or bottom area (3D-growth) is occupied in advance and represents the substrate. The definition of growth sites and the rules for occupation remain unchanged. Although the structure grows predominately in vertical direction, overhangs can occur, which are defined by holes of unoccupied lattice sites underneath and lead to the typical porous structure, see Fig. 16. Since there is no diffusion or ballistic deposition in this model, it is more suitable for simulating the agglomeration of diluted particles such as blood cells, fat or lime at the inner walls of a vessel rather than simulating OMBD.

Figure 16:

2D growth in vertical direction according to the Eden model, taken from Ref. [82].

The bottom line was occupied in the beginning such that growth can start from the substrate level. In order to reduce the porosity, randomly selected growth sites were only occupied after **m** attempts. This kind of noise reduction makes sure that growth sites which were unoccupied for a long time are occupied first.
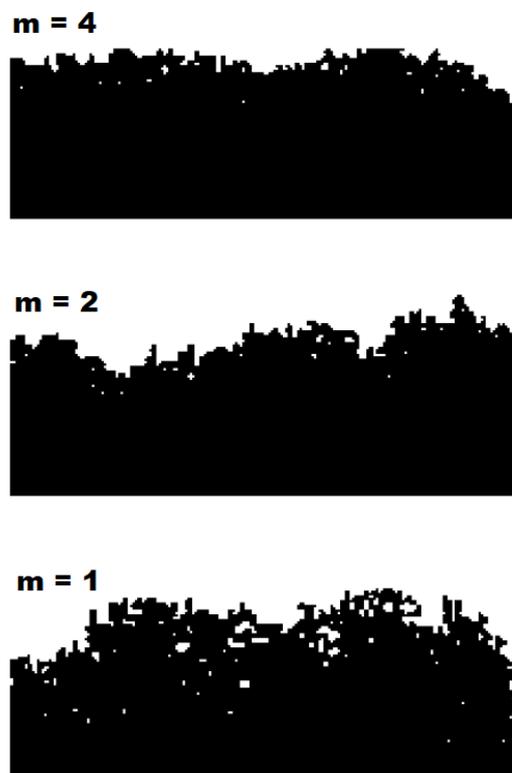
Ballistic Deposition:

Ballistic deposition describes the vertical growth processes of layers by dropping particles. The particles impinge on the substrate or on an already deposited particle, which stops their motion. As more and more particles arrive on the substrate, layer thickness and surface roughness increase. One of the first ballistic growth models might be the sedimentation of diluted rod-like particles, simulated on an IBM 709 computer by M. J. Vold in 1959 [83]. The influence of particle length on the formation of holes was investigated. Although this was one of the first simulations, there are even simpler ballistic deposition models such as the random growth.

Random Deposition:

Particles are randomly deposited on a 1D or a 2D square lattice without any kind of diffusion. Each particle occupies only one lattice site. Overhangs are not allowed. The particles "fall down" until they hit the substrate or impinge on another particle. The heights of such a random growth are Poisson distributed and the root mean square roughness σ_{RMS} is proportional to $\sqrt{N}$ for an average height of N layers [44, 84, 85]. If the number of deposited layers is $N \propto t$, the roughness scales with $t^{1/2}$. Since there is no lateral diffusion nor interlayer diffusion, it does not matter whether it is 2D or 3D growth. Also the size of the substrate is of minor importance.

Random Deposition plus Lateral Diffusion:

When the particles are allowed to diffuse laterally within their current layer but interlayer diffusion is still forbidden, terraced islands resembling the shape of wedding cakes arise [86]. In an experimental study, the step edge barrier was increased during homoepitactic growth of platinum on Pt(111) by decorating the step edges with carbon oxide such that no interlayer diffusion was possible [87] and the typical terraced islands were obtained. The tall step edge barriers prevent downward diffusion by reflecting diffusing particles at the rim of their current layer. Once those particles reach the rim of the next layer they are trapped in the deeper potential well instead of diffusing upward (see Fig. 11 in Sec. 1.3.3), which is responsible for the formation of terraces.

Random Deposition plus Erosion:

Family and Meakin extended the random deposition by additional erosion processes [88]. In order to ensure the erosion, particles were only allowed to diffuse horizontally of downwards, but not upwards. A complete smoothing was avoided by introducing a finite diffusion length before the next particle was deposited. A roughness evolution according to $\sigma_{\mathrm{RMS}} \propto L^{\beta} \cdot f(t/L^{z})$ was obtained from this simulation. $f(t/L^{z})$ is a function of time t and sample length L. The dependency on the substrate size L is clearly a finite size effect and has to be removed by regarding the limit $L \to \infty$ for realistic systems, in which diffusion lengths are significantly smaller than the substrate size L. The scaling exponents are $\alpha = (3-d)/4$, $\beta = (3-d)/2$ and $z = \alpha/\beta$ and depend on the dimension d of the interface. As final remark, it should be mentioned that the denomination of scaling exponents is not consistent and varies from publication to publication.

KPZ Equation (1986): [89]

A generalized model for the evolution of surface profiles during film growth was proposed in 1986 by Kardar, Parisi and Zhang. It is a non-linear differential equation ascribing the temporal evolution of height $h(x,t)$ at a given place x and a given time t:

$$\frac{\partial h(x,t)}{\partial t} \quad = \quad \nu \cdot \frac{\partial^2 h(x,t)}{\partial x^2} \quad + \frac{\lambda}{2} \cdot \left(\frac{\partial h(x,t)}{\partial x} \right)^2 \quad + \eta(x,t)$$

Simplified, this equation reads $\dot{h} = \nu \cdot \Delta h + (\lambda/2) \cdot (\vec{\nabla} h)^2 + \eta$. The first part is derived from Fick's law for diffusion ($\vec{j} = -D \cdot \vec{\nabla} h$) and the continuity equation ($\dot{c} = -\vec{\nabla}\vec{j}$), which combines to the heat equation $\dot{c} = D \cdot \Delta c$. Replacing the concentration $c(x,t)$ by the height $h(x,t)$ and the diffusion constant D by the surface tension ν results in $\dot{h} = \nu \cdot \Delta h$. This equation describes smoothing by surface tension. Together with a noise term $\eta(x,t)$, which simulates the random deposition of particles, we receive the Edwards and Wilkinson equation [90]. However, this equation underestimates the gain in height at tilted surfaces. Kardar, Parisi and Zhang added a further non-linear, slope-dependent term $(\vec{\nabla} h)^2$ for correction. This term was derived from trigonometric considerations and simplified by approximation for small tilt angles, which is reasonable for thin films whose islands are several hundred nanometers wide but only a few nanometer tall. Although this term is not exact, it works quite well for shallow slopes. Importantly, the square of $\vec{\nabla} h$ ensures a symmetric behavior such that both slopes on either side of a mound are treated equally. By adjusting the parameter λ and ν, the dynamic scaling of different numeric growth models can be reproduced, which is regarded as proof for the validity of the KPZ-equation.

2. Materials under Investigation

2.1. Copper Phthalocyanine

Copper phthalocyanine ($Cu\,C_{32}\,H_{16}\,N_8$), abbreviation CuPc, see Fig. 17 (a), is known since the early 20th century and is commercially used as blue dye until today. Its name goes back to the Greek words *cyano* for blue and *naphtha* for the rock oil from which the molecule was obtained as a by-product. [91]. During the development of functional organic thin films, CuPc became an important compound for technical applications such as organic solar cells [10], light emitting diodes [92, 93], transistors [94] and gas sensors [95]. Functionality and efficiency of such devices crucially depend on the crystal structure, the molecular orientation with respect to the substrate and the surface profile of the thin film, which was studied many times during the last decades [96, 97].

At least two polymorphic crystal structures of CuPc were reported, see Fig. 17 (b-c): The α-polymorph, whose crystal structure was unclear for a long time [98, 99], and the well known and more stable β-polymorph [100, 101]. Already in 1935, Robertson et al. prepared needle like single crystals of CuPc by low pressure sublimation and determined the unit cell parameters and the molecular orientation by X-ray diffraction as well as the space group $P2_1/a$ of this β-polymorph from the absence of pyroelectricity [100]. Although many derivatives such as for instance zinc-, iron-, platinum-, cobalt-, as well as metal-free phthalocyanine molecules exist, Robertson et al. showed that their crystal structures resemble each other and exhibit only small deviations [100]. Hence, CuPc can be taken as a model system for the entire family of phthalocyanines.


(a) Chemical structure of CuPc

(b) CuPc α-form [99]

(c) CuPc β-form [101]
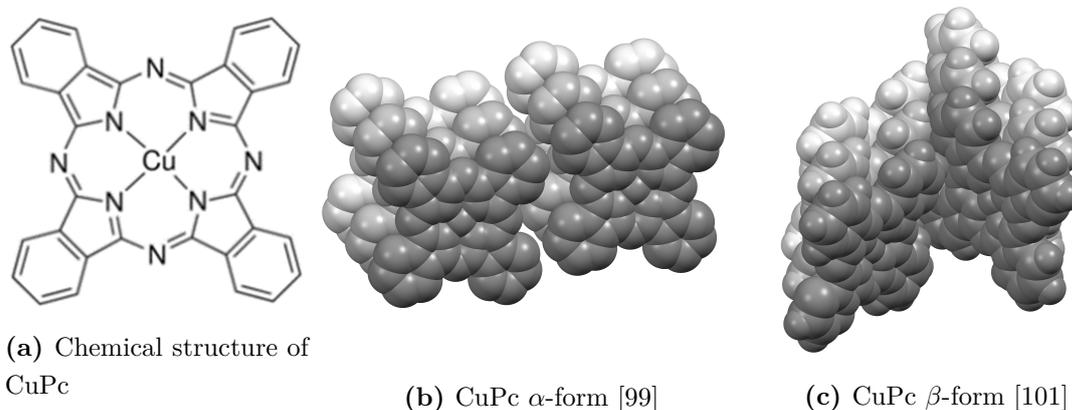
Figure 17: (a) Chemical structure and (b-c) crystal structures of copper phthalocyanine.

Initially, CuPc was mainly used as commercial dyestuff either as powder or as pastes although different color shades appeared. Hamm and van-Norman suggested in 1948 that the color variations stem from the transition between different CuPc crystal structures, rather than from the particle size as it was assumed till then [102]. Within the collection of X-ray diffraction rings for the recognition of standard dyes, three polymorphic structures of CuPc were reported in 1950, namely the α-, the β-, and the γ-form [103]. Two of them, the α- and the β-form, were identified as different polymorphs due to clearly different X-ray diffraction patterns and different infrared absorption spectra. The stable β-polymorph was assigned to the crystal structure determined by Robertson, but the crystal structure of the less stable α-polymorph remained unknown [104]. Although the preparation of a γ-polymorph of CuPc was reported [105], it turned out to be the α-polymorph, which was proven by their infrared spectra being the same [106]. The first attempt to determine the crystal structure of the α-polymorph was made in 1952 by Robinson and Klein, who suggested a tetragonal unit cell (probable space group P4/m) [107]. At that time, the α-polymorph was obtained in the conventional way by diluting CuPc molecules in a sulfuric acid and subsequent drying. In the following years, direct deposition onto a substrate under low pressure was found as an alternative way to produce small α-CuPc crystals [108]. It was shown that the crystals were highly oriented with respect to the substrate [109]. Finally, Honigmann and Ashida et al. reported a crystal structure for the α-form, which has a monoclinic space group $C2/c$ containing four molecules per unit cell and it was found by electron diffraction of CuPc deposited on mica and potassium chloride (KCl) at substrate temperatures around 150°C [98, 110]. Similar crystal structures were found for metal-free and further phthalocyanine derivatives [98]. The crystal structures of the α- and β-forms were redetermined for the Cambridge Crystallographic Data Centre (CCDC) [111]. The initially found β-structure of CuPc was confirmed [101], whereas the reported α-structure (space group $C2/c$) was ruled out and a primitive triclinic unit cell (space group $P\bar{1}$) was suggested instead [99].

Table 1 provides an overview of the reported α- and β-structures. Two examples, one for the α-form and one for the β-form, are shown in Fig. 17. The α-form exhibits parallel rows of stacked molecules, whereas the β-from shows a herringbone structure of interlocking molecules. Due to different preparation techniques and environmental conditions such as solvents, substrates, temperatures and pressure ranges, a large amount of polymorphic CuPc-structures were reported during the last three decades, both in scientific publications and in U.S. patents. Also the influence of microgravity on the growth of CuPc crystals was investigated in a space shuttle mission and resulted in a new polymorph called M-CuPc [112–117]. A continuous transition from the less stable α- to more stable β-structure with several intermediate states was observed during post-growth annealing after deposition in vacuum [95, 118], which could account for the large number of reported polymorphs.

Author(s)	Robertson	Ashida et al.	Brown	Hoshino et al.
Year	1935	1966	1968	2003
Polymorph	β	α	β	α
Space Group	$P2_1/a$	$C2/c$	$P2_1/a$	$P\bar{1}$
a [Å]	19.6	25.29	19.407	12.886(2)
b [Å]	4.79	3.79	4.790	3.769(3)
c [Å]	14.6	23.29	14.628	12.061(3)
α	90°	90°	90°	96.22(7)°
β	120.6°	90.4°	120.93°	90.62(4)°
γ	90°	90°	90°	90.32(8)°
V [Å^3]	1179.82	2292.65	1166.44	582.3(5)
Z	2	4	2	1

Table 1: Reported crystal structures of CuPc from its first synthesis until 2003. Unit cell lengths are indicated as a, b and c and unit cell angles as α, β and γ. V indicates the unit cell volume and Z the number of molecules per unit cell.

2.2. Buckminster Fullerene

The Buckminster fullerene C_{60} was discovered in the mid-1980ies. It is a spherical molecule consisting of 60 carbon atoms. A combination of hexagons and pentagons makes the spherical arrangement of carbon atoms possible, see Fig. 18 (a). The name goes back to the architect Buckminster Fuller, whose geodesic domes exhibit a similar structure. The molecule itself was discovered during the investigation of soot. Graphite was vaporized into a stream of helium by means of laser pulses in order to create small carbon clusters for understanding both the soot formation in combustion engines and the infrared spectra from interstellar space [119–121]. Time-of-flight mass spectroscopy gave evidence that particles comprising between 2 and 200 carbon atoms have formed [119]. For a sufficiently high helium vapor pressure, the signal of particles comprising 60 carbon atoms was predominant and with sufficient time and space for cooling down, only the C_{60}-signal remained together with a small fraction of C_{70} [120]. A spherical structure of a truncated icosahedron was suggested in order to avoid unsatisfied valence bonds. Calculations of strain energies finally demonstrated that the spherical C_{60} is the most stable compound among those carbon clusters and the molecule was named after the architect Buckminster Fuller [121].
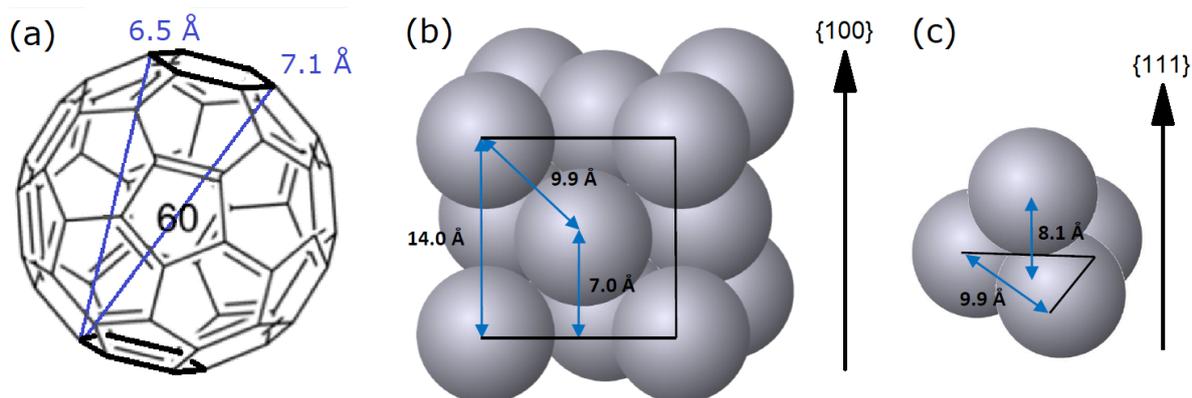
Figure 18: Chemical structure of the Buckminster fullerene C_{60} (a) and its face centered cubic (fcc) crystal structure of C_{60} in {100}-direction (b) and in {111}-direction (c). Each molecule is represented by a sphere in (b) and (c) for simplification.

Soon after the discovery, the crystal structure of condensed C_{60} powder was examined during the 1990ies and a face centered cubic (fcc) structure with freely rotating molecules was found [122]. Two further polymorphic structures were found, a simple cubic (sc) lattice with a fixed molecular orientation at temperatures below 249 K [122] and a small fraction of hexagonal closed packed (hcp) crystals at room temperature [123, 124]. Figure 18 (b) and (c) show the fcc-structure of C_{60}. The lattice spacings d_{LS} refer to repeating patterns along different crystallographic directions, see Tab. 2. Those patterns are indicated as AB- and ABC-stacking and depend on the number of monolayers until the pattern recurs. The height of a monolayer d_{ML} instead refers to a single layer (A,B, or C) of C_{60} molecules. d_{ML} is smaller than the diameter of a C_{60} molecule since the molecules fall into the sockets between adjacent molecules of the lower layer, see for instance Fig. 18 (c). Note that the frequently mentioned C_{60} diameter of 7.1 Å refers to the center-to-center distance between two opposing carbon atoms, see Fig. 18 (a). It can be misleading that the monolayer thickness in {100}-direction is coincidentally 7.0 Å. For calculating the outer radius of C_{60} one has to measure the distance between two opposing benzene rings, which is 6.5 Å, see Fig. 18 (a), and add further 1.7 Å on each side of the molecule for the Van der Waals radius of carbon, see Ref. [125]. The resulting 9.9 Å corresponds to the intermolecular distance in {110}-direction, which makes sense since the connection line between the centers of two neighboring C_{60} molecules is parallel to the {110}-direction and the point of contact is exactly in the middle of this connection line, see Fig 18 (b).

Table 2:

Lattice Spacings d_{LS} and monolayer thickness d_{ML} for different crystallographic direction in a face centered cubic C_{60} crystal.

direction	stacking	d_{LS}	d_{ML}
{100}	AB	14.0 Å	7.0 Å
{110}	AB	9.9 Å	4.9 Å
{111}	ABC	24.3 Å	8.1 Å

Some effort was made for the determination of the electrostatic potential of C_{60} in order to calculate intermolecular interactions as well as the interaction between C_{60} and the substrate.

C_{60}-C_{60} interaction: [126]

The interaction potential between two C_{60} molecules was calculated based on the integration of the Van der Waals forces over all carbon atoms and plotted in terms of sphere diameters (7.1 Å) and 10^{-14} ergs. The potential was recalculated according to the equation given in Ref. [126], transformed into terms of Ångström and meV and replotted in Fig. 19. It has a global minimum at an intermolecular distance of 10.05 Å, which is close to the outer diameter of C_{60}, albeit a bit larger. The attractive energy at the global minimum amounts to -277 meV. Note that the interaction range of C_{60} is smaller than the diameter of C_{60}. At 15 Å (1.5 times the outer diameter of C_{60}) the interaction energy is already (-12 meV) and at 10 Å (2.0 times the outer diameter of C_{60}) it is close to zero (-1.6 meV). It is therefore reasonable to consider only nearest neighbor interactions. Once two C_{60} atoms touch each other, they stick together and require a minimum energy of 277 meV for dissociation, which means that the critical number for stable islands is $i^* = 1$ at room temperature ($k_B T \approx 25$ meV). Even at 400 K ($k_B T \approx 35$ meV), the thermal energy would be still smaller than 277 meV.

Figure 19:

Girifalco potential between two C_{60} molecules recalculated in units of Ångström and meV and replotted from Ref. [126]. The minimum of the potential is located at (10.05 Å , -277 meV).
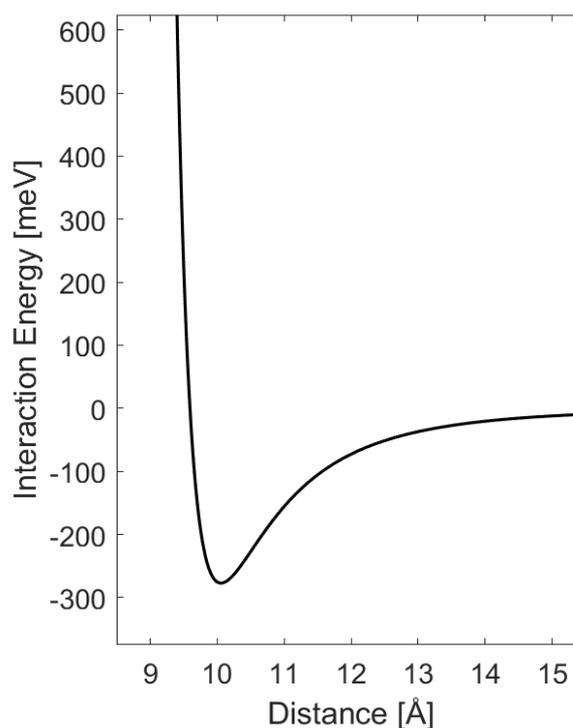
C_{60}-substrate interaction: [127]

In addition to the intermolecular interactions, the interaction of C_{60} with a graphene layer and a NaCl(001) layer was calculated and resulted in an adsorption energy of 955 meV–968 meV for graphene and 372 meV–416 meV for NaCl(001). The values differ depending on the molecular orientation and its location with respect to the substrate lattice. A diffusion barrier was estimated from the corrugation of the substrate surface plus an energy barrier for molecular rotation assuming that the diffusion comprises a rolling motion on the substrate. The potential corrugation amounts to 13 meV and the rotational energy barrier amounts to 28 eV for C_{60} on graphene and the corrugation of NaCl(001) amounts to 45 meV plus 20-30 meV for the rotational energy barrier. For comparison, the adsorption energy of C_{60} on a C_{60} layer was estimated to be around 813 eV exhibiting a diffusion barrier of 168 eV plus rotational energy barrier of 20 eV.

Motivated by the developement of technical applications such as solar cells [128, 129] and transistors [130, 131], a huge amount of studies on C_{60} thin films followed around the turn of the millennium. The growth parameters such as the deposition rate and the substrate temperature influence the formation of C_{60} clusters on given substrates significantly, as the present study shows in Sec.5.3.

The underlying diffusion processes were investigated several times during the last two decades. The diffusion of C_{60} on a metal surface was observed by *in-situ* scanning tunneling microscopy (STM) directly after deposition in ultra high vacuum (UHV) [132]. On insulating substrates however, the diffusion of C_{60} is too fast to be observed directly. Instead, island densities and island size distributions were measured by post-growth STM on epitactically and non-epitactically grown submonolayers of C_{60} [70, 71, 133–136]. All studies agree that larger islands at lower island densities grow at elevated substrate temperatures.

Also the multilayer growth of C_{60} was extensively investigated [137–141]. Evidences for a temperature driven growth of a second layer of C_{60} was interestingly found as unintended side result in a submonolayer AFM study [133]. An increasing fraction of C_{60} molecules was found on top of the first layer at elevated substrate temperatures [133]. This result was experimentally confirmed and explained by a molecular upward diffusion a few years later by another study comparing layer coverages, which were determined from both *in-situ* XRD and *ex-situ* AFM [142]. Thus far, mainly analytical models based on critical island sizes and capture zones (see Sec. 1) were employed in order to ascribe the growth of C_{60} thin films. As a result of improving computational power of today's computers, the multilayer growth was investigated further by various numeric growth simulations [142–144].

2.3. Coronene

Coronene ($C_{24}H_{12}$, abbreviation Cor) is, similar to CuPc, a planar molecule with disk-like shape. Its chemical structure is far simpler than the chemical structure of CuPc. Coronene solely consists of six hydrogen terminated benzene rings arranged in a closed ring, see Fig. 20. Note that the hydrogen atoms of both, CuPc and coronene are usually not drawn by convention, whereas C60 actually does not have any hydrogen atoms. Comparing the growth of two similar molecules such as CuPc and coronene allows us to study the influence of the chemical structure.

(a) Coronene ($C_{24}H_{12}$)

(b) γ-polymorph [145]
space group $P2_1/a$

(c) β-polymorph [146]
space group $P2_1/n$
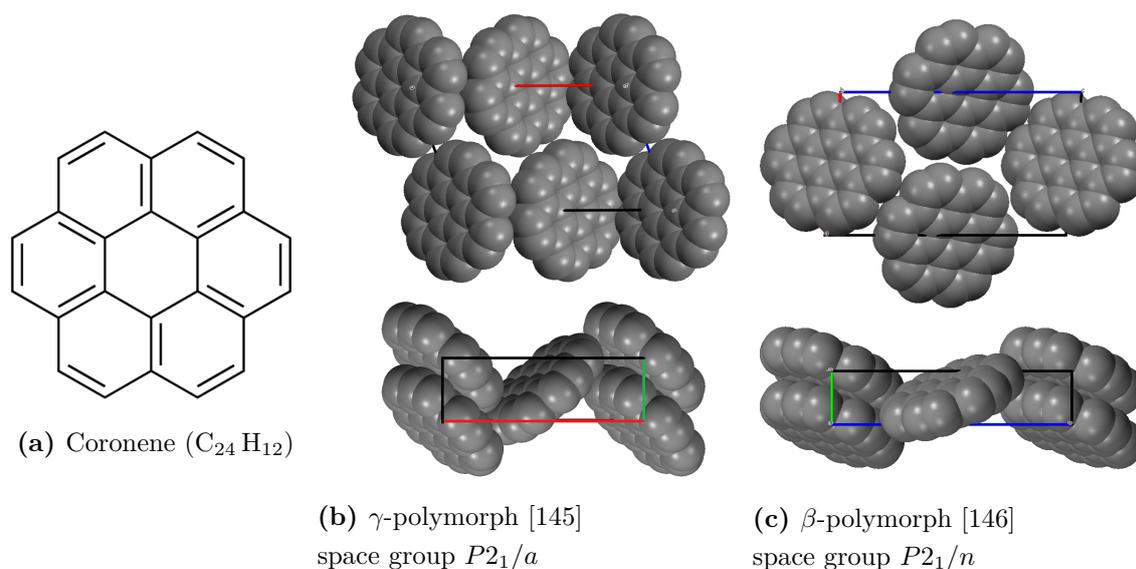
Figure 20: Chemical (left) and crystal structure (right) of Coronene

Two crystal structures of coronene were reported. The γ-polymorph (space group $P2_1/a$) is known since 1944 and was grown as single crystals from a solution by Robertson and White [145, 147]. It exhibits the same herring bone like structure as the CuPc-polymorph. The β-polymorph (space group $P2_1/n$) was reported in 1996 within the scope of a detailed study on benzenoid hydrocarbons, although mentioned without any details about the preparation [146]. 20 years later, a similar β-polymorph was discovered by applying a magnetic field to a supersaturated solution of coronene in toluene [148]. The reported space group was again $P2_1/n$, but the unit cell parameters differed. Particularly, the angle β of the monoclinic unit cell has changed from $106.02°$ to $96.235°$.

Figure 21 shows the needle-like single crystals of the β- and the γ-polymorph. A columnar growth along one crystallographic direction seems to be responsible for the formation of long needles, not only in coronene crystals but also in CuPc crystals (see Sec. 2.1. Furthermore, it was shown that β-polymorph grown in a magnetic field resulted in significantly longer single crystals compared to the γ-polymorph [148].

Fig. 21 shows that changing the space group also changes the optical properties of the crystal. The ubiquitous γ-polymorph exhibits green fluorescence, whereas the more recently discovered β-polymorph exhibits orange fluorescence under ultraviolet illumination [148].

Figure 21:

Two different coronene single crystals under ultraviolet light, taken from Ref. [148].

Left:

Recently found β-polymorph of coronene.

Right:

Ubiquitous γ-polymorph of coronene.
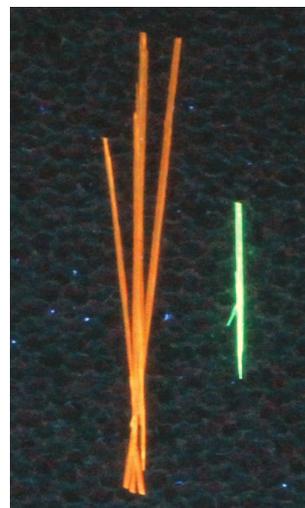
2.4. The Substrate

For the investigation on the thin film growth of the introduced compounds, a 6-inch p-type {100} silicon wafer was chosen as substrate and cut along the {110}-directions into 5 mm × 10 mm pieces see Fig. 22. An approximately 2 nm thin native silicon oxide layer has formed under ambient conditions (room temperature, ≈ 1.0 bar, $\approx 20\%$ oxygen). Pure silicon crystallizes in a cubic diamond structure (edge length = 5.43 Å), whereas the native silicon oxide is generally amorphous with a silicon to oxygen ratio of roughly 1:2. The electron density of pure silicon (0.70 el./Å^3) was calculated from its crystal structure. [149] The electron density of amorphous silicon oxide (0.66 el./Å^3) was calculated from its mass density [150]. A detailed explanation how the electron density was calculated is given in Appx. E.

Figure 22:

Silicon Wafer: p-type {100}

Diameter: 6 inch (15.24 cm)

$\rightarrow$ Wafer surface $\perp$ {100}-plane

$\rightarrow$ Primary Flat $\perp$ {110}-plane

$\rightarrow$ Secondary Flat: none (usage is obsolete)
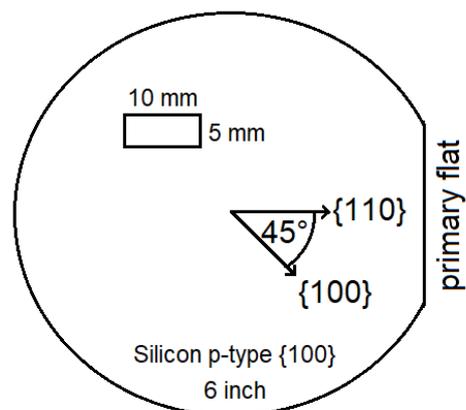
3. Experimental Techniques

3.1. Organic Molecular Beam Deposition (OMBD)

Organic thin films are mainly produced in two ways. Either droplets of diluted organic molecules wet a substrate and form a thin film by drying, i.e. the solvent evaporates, or organic molecules are evaporated in vacuum and precipitate as a thin film on the substrate surface. The first methods usually entails on varying film thicknesses. Covering a rotating substrate, which is know as spin coating, counteracts the inhomogeneities. Nevertheless, impurities stemming from the air are unavoidable during spin coating. The evaporation and deposition of organic molecules in vacuum is in contrast to spin coating a suitable technique for a controlled film growth ensuring both thickness control and a clean environment. This is, why organic molecular beam deposition (OMBD) in vacuum is so interesting for basic research. The following sections briefly introduce the vacuum pump system, the effusion cells and the vacuum chambers.

3.1.1. Vacuum Pumps

First of all, a rough pre-vacuum has to be created either by a scroll pump, by a membrane pump, or by a rotary vane pump. Those pumps can reach a pressure of approximately 10^{-2} mbar. When using a rotary vane pump, one has to take care, that the greasing oil does not evaporated into the chamber, whereas scroll and membrane pump work without grease. A turbo molecular pump (TMP) connected in series to the pre-vacuum pump reduces the pressure down to a high vacuum of approximately 10^{-8} mbar. Additionally, the chamber walls are baked with heating wires up to 373 K while pumping down such that condensed water evaporates from the walls. In order to reach ultra high vacuum (UHV), further pumps are attached to the vacuum chamber such as the ion getter pump (IGP) and the titanium sublimation pump (TSP). Those pumps are able to bind single molecules. The final presser goes down to 10^{-10} mbar.

3.1.2. Effusion Cells

Figure 23 shows the assembly of a typical Knudsen effusion cell. The core piece of an effusion cell is the crucible that contains the organic molecules. It is wrapped around by a heater foil. A coil of thin wires around this foil serve as electric heater. A thermocouple measures the temperature at the crucible. The crucible itself can be made up of glass or ceramic. Due to the higher heat capacity ceramic reacts slower to heating than glass, which important for the control circuit to keep a certain temperature. The temperature control can be a simple on-off circuitry, which turns off the heating as soon as the desired temperature is reached. Usually this leads to strong oscillations of the temperature especially for glass crucibles making a temperature control beyond 400 K impossible. A smarter solution is the use of *Eurotherm* controllers. Those devices are able to change the electric current accordingly to the heat capacity and the chosen target temperature, which damps the temperature oscillations down to a value of $\Delta T < 0.1$ K. By opening and closing the shutter in front of the effusion cell, the

deposition can be started, stopped and also interrupted. A standard flange with sealed power and thermocouple feedthroughs enables to attach the effusion cell to any standard vacuum chamber. A quartz crystal micro-balance (QCM) within the vacuum chamber monitors the deposition rate, which increases exponentially with the evaporation temperature. Every time material is deposited on this oscillating quartz crystal, the oscillation frequency changes and the change of frequency serves as measure for the deposition rate. The relation between deposition rate and evaporation temperature has to be determined experimentally before the actual experiment by growing films for a certain time at different evaporation temperatures and measuring their thickness afterward by other techniques such as X-ray diffraction (see next section). For growing blended thin films two effusion cells have to be attached to the chamber. Each effusion cell contains one species of molecules. The molecules can be deposited one after another, i.e. on top of each other, or they can be co-deposited, which means that both species are evaporated simultaneously. The deposition rate of the single species has to be accommodated according to the desired mixing ratio. A molar mixing ratio of 1:1 for instance is reached when the number of molecules of species A and species B is equal.

Figure 23:

Knudsen effusion cell due to Davies and Williams (1985) for thermal evaporation of organic molecules in vacuum, modified figure from Ref. [151]
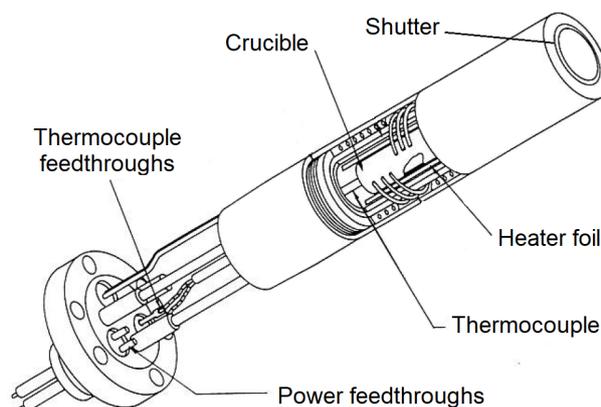
3.1.3. OMBD Chambers

Figure 24 shows a sketch of a portable vacuum chamber optimized for in-situ X-ray diffraction experiments during organic molecular beam deposition. [152] The chamber is equipped with a membrane pump, a turbo molecular pump at the top and an ion getter pump at the bottom. Two Knudsen effusion cells are attached to the chamber for evaporating the molecules and the quartz crystal micro-balances is attached to the backside of the chamber for monitoring the deposition rate. The substrate temperature can be controlled via a feed through for thermocouples and heating wires. A special part of the chamber is the 360° beryllium window, which represents a compromise between stability against pressure differences and transparency for X-rays, such that in-situ X-ray experiments can be performed in real time during the growth at a pressure below 10^{-8} mbar. Larger chambers are additionally equipped with a loadlock, which enables to exchange the specimens without breaking the vacuum inside the main chamber. Small substrate pieces are cut out from a native oxidized silicon waver and cleaned by aceton an isopropanol in an ultrasonic bath. During installation of the

specimens inside the vented loadlock, the main chamber is disconnected and sealed by a valve. The volume of the loadlock is so small, that is quickly pumped down to 10^{-8} mbar within 8–10 hours by a combination of roughening pump , turbo molecular pump and heating for evaporation of condensed water, whereas pumping down the main chamber would require several days. After high vacuum is reached, loadlock and main chamber are connected and the specimen is transferred. An already grown film can be taken out of the vacuum in the same way by transferring the specimen back to the loadlock and closing the valve.

Figure 24:

Portable OMBD chamber designed for *in-situ* X-ray diffraction during co-deposition of organic molecules. The chamber is equipped with two effusion cells, a quarz crystal microbalance (QCM), a 300° beryllium window, a turbo molecular pump (TMP) and an ion getter pump (IGP).
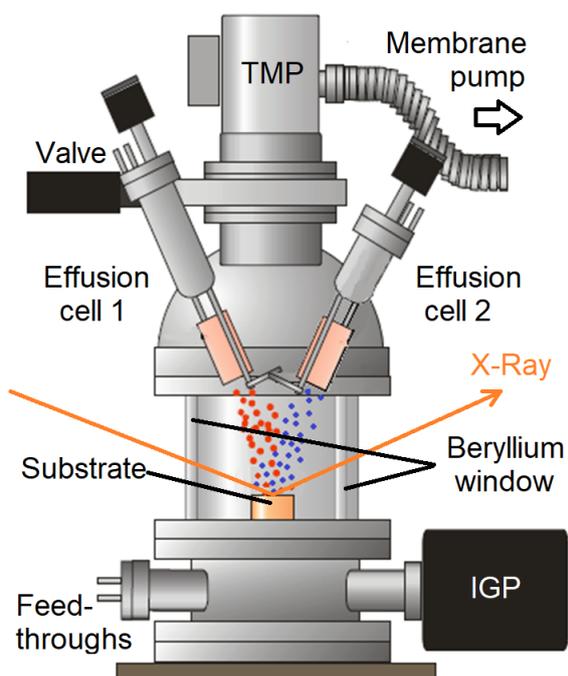
3.2. X-Ray Diffraction (XRD)

There is a large variety of X-ray diffraction (XRD) techniques. This section briefly introduces X-ray sources, detectors and some selected scattering geometries. A more detailed description of XRD can be found in the literature.

3.2.1. X-ray Sources

The simplest realization of an X-ray source is the acceleration of electrons by an electric field onto a metal block such as copper or molybdenum. A monochromator filters out all but one wavelength, for instance the Cu-Kα_1 radiation. Those sources can reach intensities up to one million photons per second. The signal to noise ratio can be increased by increasing the number of photons, either by extending the duration of acquisition or by increasing the beam intensity. Extending the duration of acquisition is no option for real-time experiments. So, higher intensities requiring a higher flux of electrons are wanted. Using rotating targets or a flux of liquid gallium instead of solid metal blocks helps to dissipate the heat, which would destroy the X-ray source after some time. A more expensive solution reaching intensities up to 10^{14} photons per second is the acceleration of electrons by a synchrotron ring. Bending magnets keep the electron beam on the ring. Undulators consisting of a series of magnets in alternating orientation make the electrons undulate perpendicular to the direction of their flux, which creates the desired X-rays. A set of monochromators, collimators and slits finally form a brilliant X-ray beam of finite width W.

3.2.2. Detectors

X-rays scattered from the sample can either be detected at a specific point using a Geiger-Müller tube, or full diffraction patterns can be acquired on a 2D-area detector using CCD-chips. There are several X-ray diffraction (XRD) geometries, which will be explained briefly in the following. A detailed description of the evaluation of XRD data will be given in the analysis section.

3.2.3. Small and Wide Angle X-ray Scattering (SAXS/WAXS)

Depending on the sample-detector distance (SDD), the diffraction patterns can be subdivided into small and wide angle X-ray scattering. While small angle X-ray scattering (SAXS) provides information about island distances and shapes, wide angle X-ray scattering (WAXS) provides information about the crystal structure. The X-ray beam can either go through the sample or it can be scattered from the sample surface. The samples of this study are relatively thin organic films ($\approx 20\,\mathrm{nm}$) on comparably thick silicon substrates ($\approx 0.5\,\mathrm{mm}$) such that only scattering from the sample surface is able to provide a measurable signal.

3.2.4. Grazing Incidence Small/Wide Angle X-ray Scattering (GISAXS/GIWAXS)

Many XRD setups operate in grazing incidence, which means that the X-ray beam hits the sample at a very small angle θ close to the critical angle θ_c of the substrate: $\theta_c = \arccos(n)$. Below the

critical angle, the beam is fully reflected from the substrate, which is due to the negative index of refraction n for X-rays, whose wavelengths are around $\lambda \approx 1\,\text{Å}$:

$$n = 1 - \delta = 1 - \frac{\rho \cdot r_e \cdot \lambda^2}{2\pi}$$

The electron density of silicon is $\rho = (14 \cdot 8)/(5.43\,\text{Å})^3 = 0.7\,\text{el.}/\text{Å}^3$ for 14 electrons in each of the 8 atoms within the cubic unit cell ($a = 5.43\,\text{Å}$) and $r_e \approx 2.81794 \cdot 10^{-5}\,\text{Å}$ as the classical electron radius. Nevertheless, the intensity drops at lower angles because of the footprint of the beam, whose length $l = w/\sin(\theta)$ is much larger than the specimen size s for a given beam width w, see Fig. 25 (a). The footprint is corrected by:

$$I_{\text{corr}} = I_{\text{meas}} \cdot \frac{l}{s} = I_{\text{meas}} \cdot \frac{w/\tan(\theta)}{s}$$

Above the critical angle, the beam intensity drops proportionally to q^4. To summarize, the intensity and associated with this the signal to noise ratio is highest close to the total reflection edge of the substrate. Three special scattering geometries will be presented in the following:

3.2.5. Reciprocal Space Maps (Q-Maps)

The beam comes in at a fixed angle in grazing incidence and the scattered X-rays are detected over a large angular range, which usually requires a motion of the detector around the specimen. After the data acquisition, the single images have to be matched into one large map and angles have to be assigned to the pixels. A flat-field correction has to be carried out for small sample detector distances (SDDs). For large SDDs, as it was the case for this study, the relation between angles and pixels can be approximated by a linear function and the flat-field correction can be neglected. Since the diffraction angle for a certain Bragg-peaks depends not only on the lattice spacing but also on the X-ray wavelength, the map has to be converted into reciprocal space, which makes it comparable to maps from other experimental setups operating at different wavelengths. More background about the conversion from angular to reciprocal space is given in the analysis section.

3.2.6. Grazing Incidence X-Ray Diffraction (GIXD)

According to the reciprocal space mapping, the beam comes in at a fixed angle in grazing incidence, but this time only a line scan along the total reflection edge of the substrate is measured, which is much faster and provides information about the in-plane structure of the sample, see Fig. 25 (b). The lateral size d_{coh} of coherently scattering domains was extracted from the peak widths Δq at the full width at half of maximum according to the Scherrer Formula $d_{\text{coh}} \approx K \cdot 2\pi/\Delta q$. The shape factor $K \approx 1$ was chosen in between the values $K = 0.93$ for N ideal (i.e. infinitely wide) lattice planes and $K = 1.11$ for perfectly spherical domains [153].

3.2.7. X-Ray Reflectivity (XRR)

The angle of incidence θ_i is continuously increased and the intensity of the reflected beam, which is emitted from the sample at the same angle $\theta_f = \theta_i$, is measured, see Fig. 25 (c). A typical example of a footprint corrected and normalized XRR-profile after conversion into reciprocal space is shown in Fig. 26. Constructive and destructive interferences of waves reflected from the film-substrate and the film-vacuum interfaces cause the Kiessig oscillations in the low q_z-range, whose frequency depends on the film thickness. The positions of Bragg-peaks depend on the lattice spacing in out-of-plane direction The frequency of the Laue oscillations at each side of the Bragg peaks depend on the number of coherently scattering lattice planes. All oscillations are damped when the film-vacuum interface becomes rough. A detailed explanation how film thickness, roughness and other parameters such as the layer coverages can be extracted from XRR data is given in Sec. 4.1.
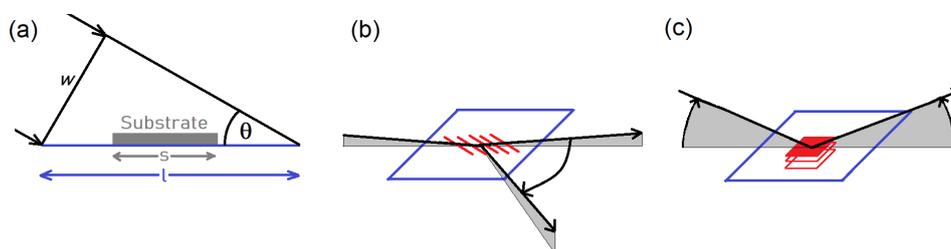
Figure 25: Schematic sketch of possible scattering geometries: **(a)** Footprint of size l for a beam width w and an angle of incidence θ. **(b)** Grazing Incidence X-Ray Diffraction (GIXD) geometry probing the in-plane lattice spacing. **(c)** X-Ray Reflectivity (XRR) geometry probing the lattice spacing in out-of-plane direction.
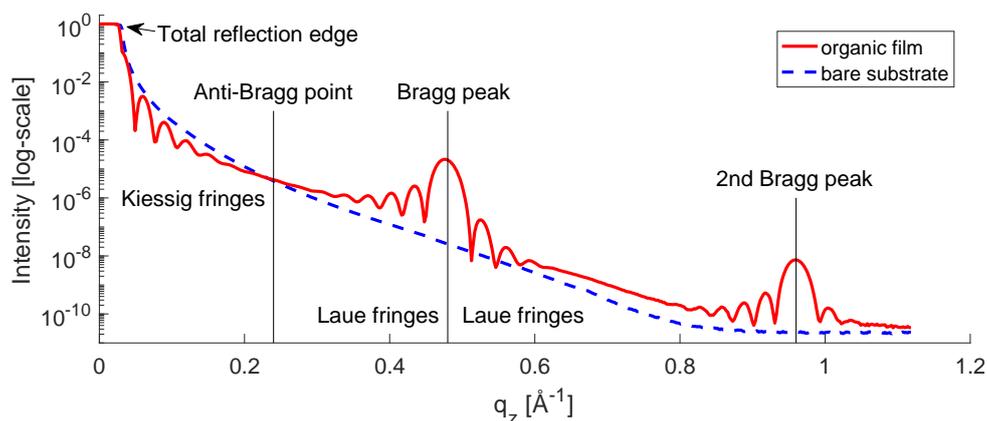
Figure 26: Example of a typical XRR profile. Dashed blue line: XRR profile of the bare silicon substrate covered with a thin and amorphous native silicon oxide layer. Solid red line: XRR profile of a 20 nm thin CuPc film grown at a deposition rate of 2 Å/min and a substrate temperature of 400 K.

3.3. Real Space Imaging

There are various techniques for the acquisition of real space images such as the atomic force and scanning electron microscopy. Additionally, the scanning electron microscopy can be complemented by an energy dispersive X-ray analysis.

3.3.1. Atomic Force Microscopy (AFM)

In order to obtain height profiles of the organic film surfaces, atomic force microscopy was applied. The working principle is as follows: A small tip, attached to a cantilever, is drawn across the sample surface while oscillating up and down in intermittent contact mode, see Fig. 27 (a). The up and down motion is obtained by applying an alternating voltage to a quartz crystal above the cantilever, i.e. using the piezoelectric features of quartz. When the tip approaches the sample surface repulsive forces lead to an upward bending of the cantilever. A laser beam is directed onto the top side of the cantilever, which reflects the beam towards a four-quadrant CCD detector, see Fig. 27 (b). Depending on the intensity ratio between the four quadrants up- and downward bending as well as torsion of the cantilever is detected. While and upward bending indicates that the tip is in contact with the sample, torsion indicates friction during continuous contact mode, which is an alternative way of measuring surface profiles. In both cases, the sample is probed line by line. During intermittent contact mode, the tip is moved up as soon as the upward bending of the cantilever exceeds a predetermined threshold value. During continuous contact mode, the tip height is adjusted such that the upward bending of the cantilever is kept at a constant value.

Figure 27:

(a) AFM tip in intermittent contact mode, modified from Ref. [154]

(b) Optical path of the laser beam, taken from Ref. [155].
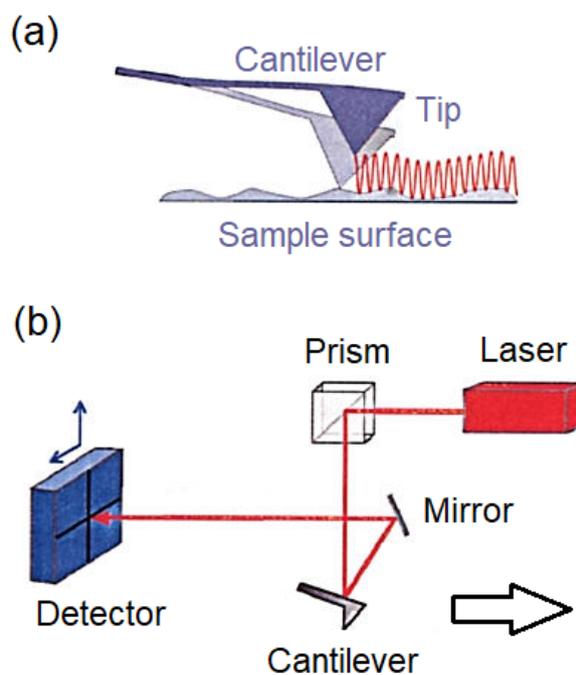
All AFM measurements were done in intermittent contact mode using a JPK Nanowizard II AFM-head and high resolution AFM tips from *AppNano*, probe model ACTA (material: silicon, shape: pyramidal, tip radius: 6 nm) and corresponding cantilevers (material: silicon, spring constant: $k = 13$ - 77 N/m, resonance frequency, $f = 200$ - 400 kHz, backside coated with aluminum for laser reflection). Sample areas of $3\,\mu m \times 3\,\mu m$ were scanned at a resolution of 512×512 pixels pixels resulting in 5.86 nm per pixel, which is in the order of the tip radius.

Afterwards, the AFM images were evaluated by several *Matlab* scripts. Line profile, which show a cross sectional view through the organic layers, were extracted. Histograms of the height distribution were prepared by dividing the vertical range from lowest to highest measured data point into 100 height classes. The fraction of pixels within each height class was determined and presented in percent. Furthermore, the islands seen from AFM were automatically detected, counted and their shape was fitted, which will be explained in more detail in Sec. 4.1. A possible convolution of tip and island shape was considered and is shown in Fig. 28.
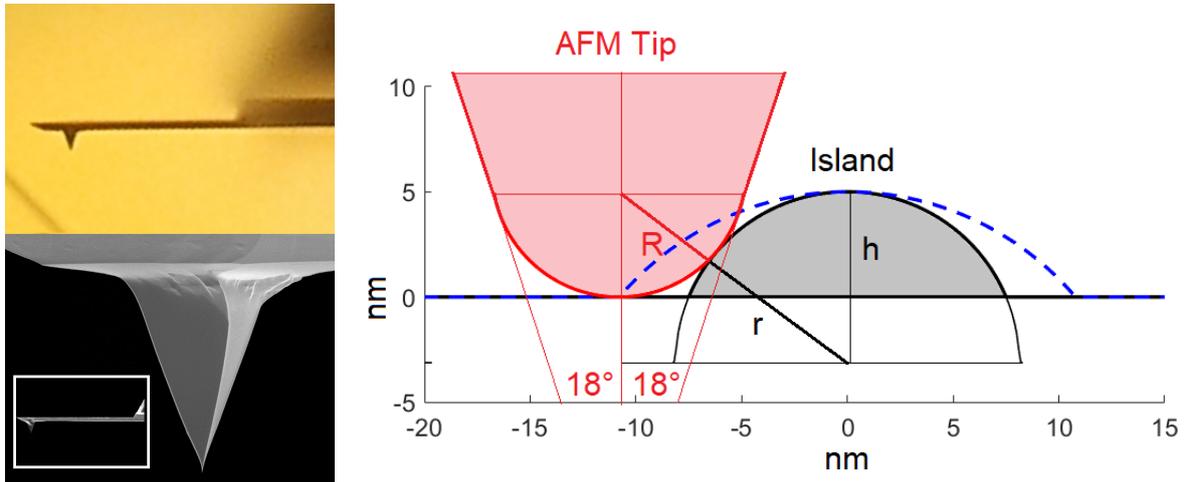

Figure 28: Upper left: Light microscopy image of one of the AFM tips. Lower left: Magnified SEM image provided by the company. Right: Convolution of island and tip shape indicated by the blue dashed line, see text. The aspect ratio of this side view is drawn true to scale.

A light microscopy image of one of the tips was acquired, see upper left part of Fig. 28 and compared to the SEM image, which was provided by the company, see lower left part of Fig. 28. A wedge angle of $2 \times 18°$ was measured from the images. The tip radius of R = 6 nm was given by the company. The right side of Fig. 28 shows the convolution of the tip and one of the smallest measurable islands covering only 2×2 pixels. Its shape is described by $h(x) = \sqrt{r^2 - x^2} - r + h$ and represents a truncated sphere of maximum height h = 5.0 nm above the substrate level and curvature radius r = 8.1 nm. The measured profile as result of tip-plus-island convolution is indicated in Fig. 28 as dashed blue line: $H(x) = \sqrt{(r+R)^2 - x^2} - (r+R) + h$.

The island becomes significantly broadened, but the spherical shape and the maximum height are preserved. A deviation from the spherical shape is only expected if the contact angle of the island exceeds 90° minus the wedge angle (18°) of the tip. Most of the measured islands were laterally much larger but not much taller such that the deviation between measured and true shape becomes sufficiently small and a deconvolution of surface profile and tip shape is not required.

3.3.2. Scanning Electron Microscopy (SEM)

Scanning electron microscopy (SEM) is complementary to AFM. Although the height information is lost in SEM, it offers some advantages such as faster and less invasive data acquisition. While AFM images usually show a small part of the sample in the range of 1-10 μm, SEM images can scan much larger areas ranging from 1 μm up to 1 mm. Due to the faster scanning, large areas can be viewed within a few seconds. This enables to check whether the thin film features are homogeneously distributed on the substrate. Additional features appear in the SEM image, which are not visible in the AFM images. Especially, long needles protruding from the organic thin film cannot be seen in AFM. Either the needles are bent down by the tip, or they just break off. The SEM is able to show these needles due to the less invasive scanning.

The scanning electron microscope *XL30 series* from *Philips* was used for this study. In the following, the working principle and the contrast effects of scanning electron microscopes will be explained (see Fig. 29). An electron beam is accelerated from a heated cathode-filament towards a pinhole anode by a high voltage between 5 and 30 kV. The Wehnelt-cylinder, which is part of the electron gun, focuses the electron beam in the so called first cross over spot. A set of two condenser lenses reduces the diameter of the cross over stepwise. Spray diaphragms avoid electrons passing the rim of these electromagnetic lenses and hence reduce spherical aberrations. The gun tilt- and shift-unit corrects the path of the beam in case the two condenser lenses are shifted or tilted with respect to each other. With the help of the scanning unit, the electron beam can move across the specimen line by line. The scanning unit consists of two deflector pairs (upper and lower) for each direction (x and y) and ensures that the beam always passes through the aperture diaphragm during the scan. The stigmator between the upper and lower scanning unit creates a magnetic quadrupole field in order to correct asymmetric beam shapes. Finally, the objective lens focuses the beam onto the sample. Of course, the specimen chamber, as well as the entire beam column is evacuated (specimen chamber 10^{-6} mbar and column $10^{-8} - 10^{-9}$ mbar). The electrons are scattered inside the specimen within a bulb-shaped volume, whose depth and lateral width depend on the beam energy of the incoming primary electrons (PE) and on the material under investigation. There is an Everhart Thronley detector at the side of the specimen chamber. A positively charged collector grid in front of the detector attracts mainly the slow secondary electrons (SE) stemming from inelastic scattering within a thin layer at the surface of the specimen. Partially back scattered electrons with higher energies stemming from deeper layers are also detected. All those electrons impinge on a plastic scintillator behind the collector grid and cause fluorescence there. The signal is amplified by a photomultiplier. The resulting signal is measured for each spot on the sample and the computer transfers the acquired

intensity pixel by pixel onto a screen. Although there is no absolute height information, the resulting image exhibits a 3D impression, which is due to different contrast effects, visualized in Fig. 29 (b). The inclination effect (I.) makes inclined planes appear brighter in the image than flat planes. The reason is the larger cross sectional area of the scattering bulb and the sample surface at steeper slopes. The edge effect (II.) leads to darker receding edges and brighter protruding edges for the same reason, i.e. smaller and larger cross sectional areas of scattering bulbs and sample surface, respectively. The shadowing effect is due to the fact that the detector is attached to the side of the specimen chamber. The collector potential is not sufficient to collect all high energy electrons, which are scattered quasi elastic without significant loss of energy. Especially, electrons of flanks, which are averted from the detector, are not collected and hence it follows that these areas appear darker in the image. A further contrast effect is the charging contrast, which means that positively charged areas, appear darker in the image as result of a reduced potential difference between collector grid and specimen. This effect can be observed due to electron depletion, when measuring for a long time on the same area. Also the opposite effect can appear due to electron accumulation in the sample during the measurement. For more information about SEM, the reader is referred to Ref. [156].

**(a)** SEM simplified setup
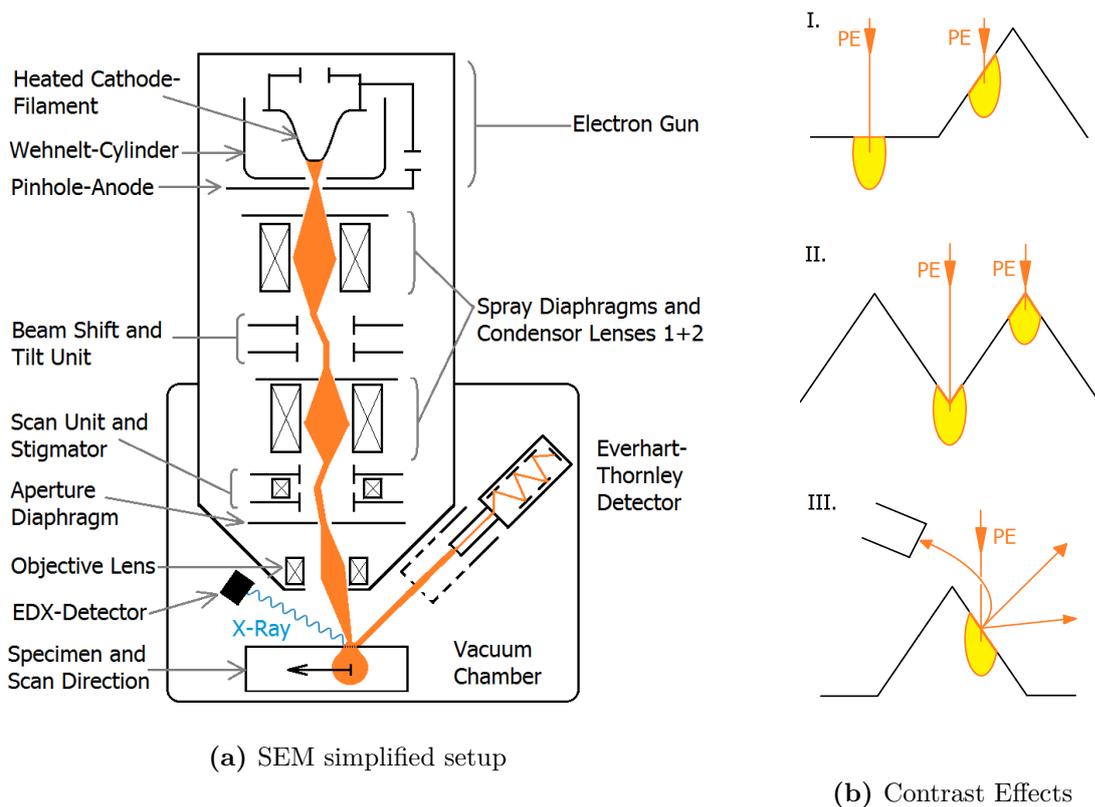
(b) Contrast Effects

Figure 29: (a) Simplified schematic sketch of a scanning electron microscope (Note that the geometries are not true to scale). (b) Contrast Effects: I. Inclination Contrast, II. Edge Contrast, III. Shadowing Contrast.

3.3.3. Energy Dispersive X-Ray Analysis (EDX)

Another benefit of SEM is the possibility of analyzing X-rays, which are emitted when electrons hit the sample. This technique is called energy dispersive X-ray analysis (EDX). Impinging electrons partially ionize the atoms in the sample. Missing electrons in inner shells of ionized atoms are replaced by electrons from the outer most shells. The corresponding energy differences are radiated as X-rays and they are characteristic for each chemical element. The X-ray energies are detected by a nitrogen cooled semiconducting detector and a chemical analysis can be carried out on specific spots on the sample. Electron bombardment on a single spot on the sample leads to a bulb of scattered electrons. The penetration depth and the lateral size of this bulb depend on the beam energy, the angle of incidence and on the material under investigation. Lowering the beam energy improves the lateral resolution and reduces the penetration depth, but it also lowers the amount of emitted X-rays. A suitable compromise between spacial resolution and signal strength has to be found.

4. Analysis Methods

4.1. X-ray Scattering and Reciprocal Space

4.1.1. Scattering Geometry and Reciprocal Space (Q-Space)

Several sets of XRD data were acquired at different experimental setups. The non-linear dependency between lattice spacings and scattering angles on the chosen wavelengths makes a direct comparison of these data sets difficult. For this reason, the data was converted into reciprocal space, which makes it independent from the wavelength. The reciprocal space refers to scattering vectors in terms of inverse lengths instead of angles. The x-y-plane is defined parallel to the sample surface and the z-axis parallel to the sample normal. The X-ray beam enters in the y-z-plane at an incidence angle θ towards the horizon, see Fig. 30 (a). The scattering intensity is measured at an arbitrary direction described by an angle δ towards the x-y plane and angle ω towards the y-z plane of the incoming beam. The reciprocal space vector is then defined in the following way:

$$\vec{q} = \vec{q}_{out} - \vec{q}_{in} = \frac{2\pi}{\lambda} \cdot \left[\begin{pmatrix} cos(\delta) \cdot sin(\omega) \\ cos(\delta) \cdot cos(\omega) \\ sin(\delta) \end{pmatrix} - \begin{pmatrix} 0 \\ cos(\theta) \\ -sin(\theta) \end{pmatrix} \right] = \begin{pmatrix} q_x \\ q_y \\ q_z \end{pmatrix}$$
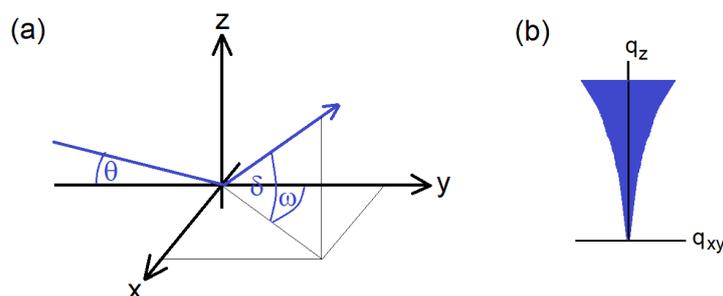

Figure 30: (a) General diffraction geometry and (b) wedge-shaped region of missing data points around $q_z = 0\,\text{Å}^{-1}$ in Q-maps.

Organic thin films on amorphous and inert substrates generally form 2D-powders meaning that the crystallites are well ordered in vertical direction, but randomly oriented along the substrate surface. As a result of this, the q_x- and the q_y-component cannot be distinguished and are combined to the q_{xy}-component in the experimental data:

$$|q_{xy}| = \sqrt{q_x{}^2 + q_y{}^2} = \frac{2\pi}{\lambda} \cdot \sqrt{cos(\delta)^2 + cos(\theta)^2 - 2 \cdot cos(\delta) \cdot cos(\omega) \cdot cos(\theta)}$$

Note that there is a region around the q_z-axis which is experimentally not accessible since there is always a q_{xy}-component larger than zero. This missing part of the Q-map has the shape of a wedge, see Fig. 30 (b), whose width depends on q_z, the angle of incidence θ, the chosen wavelength λ and the sample–detector distance (SDD). The q_z-component simplifies to $4\pi/\lambda \cdot sin(\theta)$ in the case of XRR, i.e. $\delta = \theta$.

4.1.2. The Unit Cell in Real Space

Unit cells describe the translational invariance of a crystal structure. They are defined by the length of their unit cell vectors $(\vec{a}, \vec{b}, \vec{c})$ and by the angles (α, β, γ) between these unit cell vectors. Any lattice in 3D-space can be assigned to one of the seven lattice systems listed in Tab. 3 below:

No.	Name	vectors	angles
1	triclinic	$a \neq b \neq c$	$\alpha \neq \beta \neq \gamma \neq 90°$
2	monoclinic	$a \neq b \neq c$	$\alpha = \beta = 90° \neq \gamma$
3	orthorhombic	$a \neq b \neq c$	$\alpha = \beta = \gamma = 90°$
4	tetragonal	$a = b \neq c$	$\alpha = \beta = \gamma = 90°$
5	rhombohedral	$a = b = c$	$\alpha = \beta = \gamma \neq 90°$
6	hexagonal	$a = b \neq c$	$\alpha = \beta = 90°, \gamma = 120°$
7	cubic	$a = b = c$	$\alpha = \beta = \gamma = 90°$

Table 3: Classification of lattice systems due to their unit cell parameters.

The most general case is the triclinic lattice, whose unit cell vectors are presented here in terms of Cartesian coordinates:

$$\vec{a} = \frac{a}{sin(\alpha)} \cdot \begin{pmatrix} cos(\gamma) - cos(\alpha) \cdot cos(\beta) \\ sin(\alpha) \cdot cos(\beta) \\ \sqrt{R} \end{pmatrix} \qquad \vec{b} = \begin{pmatrix} b \cdot sin(\alpha) \\ b \cdot cos(\alpha) \\ 0 \end{pmatrix} \qquad \vec{c} = \begin{pmatrix} 0 \\ c \\ 0 \end{pmatrix}$$

The c-axis was chosen parallel to the y-axis and the b-axis was set parallel to the x-y-plane. The derivation of the a-axis requires a few mathematical considerations, which are shown in Appx. A together with the derivation of R:

$$R = 1 - cos^2(\alpha) - cos^2(\beta) - cos^2(\gamma) + 2 \cdot cos(\alpha) \cdot cos(\beta) \cdot cos(\gamma)$$

The volume V of such a unit cell is given by:

$$V = \vec{a} \cdot \left(\vec{b} \times \vec{c} \right) = a \cdot b \cdot c \cdot \sqrt{R}$$

A separate derivation of equations for all other lattice systems is not necessary since their description is contained in these formulas with the special conditions listed in Tab. 3.

4.1.3. The Unit Cell in Reciprocal Space

The real-space unit cell vectors $(\vec{a}, \vec{b}, \vec{c})$ are converted into reciprocal lattice vectors by:

$$\vec{a}^* = \frac{2\pi}{V} \cdot \left(\vec{b} \times \vec{c}\right) \qquad \vec{b}^* = \frac{2\pi}{V} \cdot (\vec{c} \times \vec{a}) \qquad \vec{c}^* = \frac{2\pi}{V} \cdot \left(\vec{a} \times \vec{b}\right)$$

A general reciprocal lattice vector is given as linear combination of reciprocal unit cell vectors:

$$\vec{G}_{hkl} = h \cdot \vec{a}^* + k \cdot \vec{b}^* + l \cdot \vec{c}^*$$

The full expressions for the reciprocal unit cell vectors, the Cartesian components (G_x, G_y, G_z) of $\vec{G}_{hkl}$, as well as $G_{xy} = \sqrt{G_x^2 + G_y^2}$ are shifted to Appx.B. Also those expressions are valid for all lattice systems and can be reduced to simpler equations by inserting the conditions from Tab. 3 for lattices of higher symmetry.

4.1.4. Kinematic Scattering Theory

By comparing calculated G_{xy}- and G_z-values to the q_{xy}- and the q_z-values of measured diffraction peaks, the unit cell lengths (a, b, c) and angles (α, β, γ) can be determined. During this process, each peak has to be assigned to at least one triplet of Miller indices (h, k, l). The peak intensities I_{hkl} can be calculated using the kinematic scattering factor $f(\vec{G}_{hkl})$:

$$I_{hkl} = |f(\vec{G}_{hkl})|^2 = \left| \sum_{j=1}^{N} f_j(\vec{G}_{hkl}) \cdot \exp\left(i \cdot \vec{G}_{hkl} \cdot \vec{r}_j\right) \right|^2$$

$f_j(\vec{q})$ is the atomic form factor and r_j are the Cartesian coordinates of atom number j. For the sake of simplicity it is written $\vec{q}$ instead of $\vec{G}_{hkl}$. The atomic form factor $f_j(\vec{q})$ is described for X-rays by the following approximation

$$f_j(\vec{q}) = \int 4\pi |\vec{r}|^2 \cdot \rho_j(\vec{r}) \cdot \frac{sin(4\pi\vec{q} \cdot \vec{r})}{4\pi\vec{q} \cdot \vec{r}} d\vec{r} \quad \approx \quad \sum_{i=1}^{4} a_i \cdot \exp\left(-b_i \cdot |\vec{q}|^2\right) + c$$

The fitting parameters a_i and c are listed in the International Tables for Crystallography C for all stable chemical elements [157]. The atomic form factors $f_j(|\vec{q}|)$ of the most frequent elements in organic compounds are plotted in Fig. 31. Note that the phase factor $\exp\left(i \cdot \vec{q} \cdot \vec{r}_j\right)$ is used here in the crystallographic convention, but appears with a factor of 2π in the exponent if $\vec{a}^*$, $\vec{b}^*$ and $\vec{c}^*$ are defined without 2π, which is more common in solid-state physics. Contrary to dynamic scattering theory, which takes multiple scattering into account, the kinematic scattering theory assumes only one scattering event for each scattered wave. The kinematic scattering theory is sufficient for X-rays, but not valid for electron scattering, which requires the dynamic theory and is beyond the scope of this work.

Figure 31: Atomic form factors $f_j(q)$ of the most frequent elements in organic compounds. The intensity decreases with increasing q and for $q \to 0$, the form factors approach the atomic number Z of the respective element.
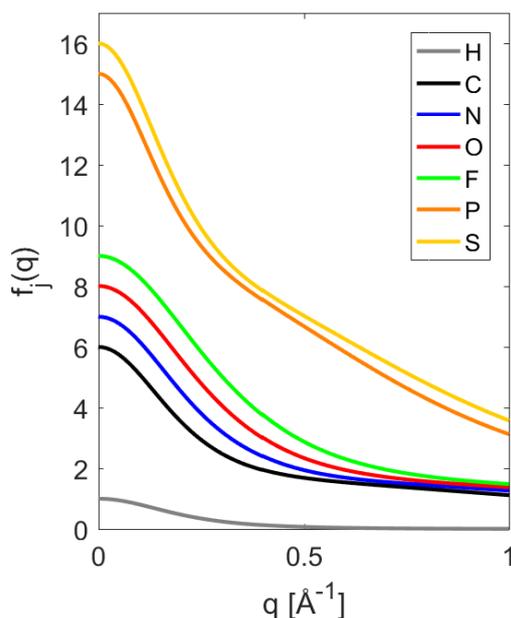
4.1.5. Space Group Symmetries

Special symmetries, which are described by the space group, lead to an extinction of specific waves during X-ray scattering. The space group can be determined from missing peaks in the measured diffraction patterns. For each space group, X-ray reflections corresponding to certain triplets (h, k, l) of Miller indices should be present due to the unit cell parameters, but are extinct due to the space group symmetries. The conditions for reflection and extinction are derived from kinematic scattering theory and listed in the International Tables for Crystallography A [158]. An example is shown and explained in Appx. C.

The symmetry of a crystal structure is described as follows: The corners of periodically repeating unit cells define a grid of lattice points and the translational invariance of the lattice. The classification of 3D-lattices can be extended to 14 Bravais lattices by adding further lattice points to the body or face centers of each unit cell. Each lattice point is occupied by one or more atoms or molecules and the crystal structure is defined as the lattice plus the atoms/molecules. A further subdivision of the 14 Bravais lattices into 32 point groups is possible by regarding the symmetries of the crystal structures. The point groups distinguish between the invariance to inversion at a point, which means x, y, z maps to $-x, -y, -z$, invariance to reflection at a mirror plane and invariance to rotation around an n-fold symmetry axis by $(360/n)°$. At least one point remains always the same during these symmetry operations. Some crystal structures exhibit further symmetries such as gliding mirror planes and screw axis. Those symmetry operations leave no point of the crystal unchanged and lead to the final subdivision into 230 space groups. Although there are many conventions for the denomination of space groups, the studies presented here refer to the most commonly used Hermann–Manguin convention. All symmetry operations are compiled in terms of equivalent Wyckoff positions for each space group on the Bilbao Crystallographic Server [159].

4.2. Modification of Crystal Structures

For the determination of crystal structures in this work, reported crystal structures were modified by changing the unit cell parameters and reorientation of the molecules within the unit cell until calculated and measured X-ray diffraction patters agreed.

4.2.1. File Formats Crystal Structures

As already mentioned, the crystal structure is ascribed by the lattice plus a certain arrangement of atoms/molecules located at each lattice point. The full crystal structure including atomic positions and molecular orientations is conventionally stored in crystallographic information frameworks (CIFs) for computational purposes. CIFs are formatted as ASCII files and obey a certain syntax, which is prescribed by the International Tables for Crystallography G [160]. Variables are declared an initialized by a variable name starting with an underscore followed by the corresponding numeric value. A table is initialized with the term "loop_" followed by a list of variable names, one for each column. Then the actual tabulated values follow. A CIF contains, amongst further parameters, the unit cell lengths (a, b, c), the unit cell angles (α, β, γ), the unit cell volume, a table of equivalent Wyckoff positions and a table for the atomic positions (x, y, z) in terms of unit cell vectors, which means the atoms are located at $\vec{r} = x \cdot \vec{a} + y \cdot \vec{b} + z \cdot \vec{c}$. This kind of description has the advantage that the equation for the kinematic scattering factor simplifies significantly as it is shown and explained in Appx. C. Note that sometimes not all atoms are listed. If the molecule is symmetric and its orientation within the unit cell agrees with the space group symmetries, only one half or one quarter of the molecule is listed as (x, y, z). The coordinates of remaining atoms and molecules are defined by the equivalent Wyckoff positions and can be calculated by applying the symmetry operations of the space group. Further information such as bond lengths and angles can be included in a CIF, but they are not essential for the studies of this work. A parsing *Matlab*-script was written during this work for the automated extraction of required information from CIF files.

4.2.2. Modification of Unit Cell Parameters

CIFs can be manually modified by editing their entries. Changing the unit cell parameters of inorganic crystals for instance by thermal expansion changes the inter-atomic distances. The situation is different for organic crystals and a few things have to be considered. While the intermolecular distances can vary, the bond lengths between atoms of the same molecule, have to remain constant. For this reason, the atomic coordinates have to be converted from terms of unit cell vectors (x, y, z) into Cartesian coordinates (X, Y, Z). Then the unit cell parameters can be modified without distorting the molecules. After the modification, the atomic coordinates have to be converted back such that they are expressed by the fractions (x, y, z) of the new unit cell vectors. We can rewrite the expression $\vec{r} = x \cdot \vec{a} + y \cdot \vec{b} + z \cdot \vec{c}$ as matrix–vector multiplication. The matrix M contains the Cartesian coordinates of the unit cell vectors $\vec{a}$, $\vec{b}$ and $\vec{c}$ in real space. The vector $\vec{v}$ expresses the atomic positions as fractions (x, y, z) of the unit cell vectors and the resulting vector $\vec{V}$ delivers the wanted Cartesian coordinates (X, Y, Z) of the atomic positions. For the back conversion into terms

of unit cell vectors, this linear equation system was solved in *Matlab*.

$$M \quad \cdot \quad \vec{v} \quad = \quad \vec{V}$$

$$x \cdot \vec{a} + y \cdot \vec{b} + z \cdot \vec{c} \quad = \quad \begin{pmatrix} a_x & b_x & c_x \\ a_y & b_y & c_y \\ a_z & b_z & c_z \end{pmatrix} \cdot \begin{pmatrix} x \\ y \\ z \end{pmatrix} = \begin{pmatrix} X \\ Y \\ Z \end{pmatrix}$$

### 4.2.3. Modification of Molecular Orientations

One encounters several obstacles when calculating the rotation of 3D-objects. The first challenge is to find a suitable and fast way to calculate the rotation of an atom placed at (X, Y, Z) around an arbitrarily chosen axis directing from the origin towards the point (u, v, w) by an angle φ. A common solution is the use of quaternions, i.e. complex 4D-numbers consisting of a real axis and three imaginary parts (i, j, k). The atomic coordinates are expressed by a fully imaginary vector representing the 3D-space: $\vec{r} = (Xi + Yj + Zk)$. The rotation axis is expressed by $\vec{s} = cos(\varphi/2) + sin(\varphi/2) \cdot (ui + vj + wk)$. By calculating $\vec{s} \cdot \vec{r} \cdot \vec{s}^*$, one obtains the rotated vector (X', Y', Z'). The absolute value of $\vec{s}$ has to be normalized to one in order to maintain the length of the rotated vector, which requires that $\sqrt{u^2 + v^2 + w^2} = 1$ is satisfied. Using the complex conjugated number $\vec{s}^* = cos(\varphi/2) - sin(\varphi/2) \cdot (ui + vj + wk)$ makes sure that the resulting vector goes back to the 3D-space. More background information on the calculation of rotations in 3D-space by quaternions is given in Appx. D.

4.2.4. Yaw-, Pitch- and Roll-Axes

The second challenge is to find an unequivocal definition for each configuration, since the final orientation depends on the order of rotations. An upright standing CuPc molecule aligned with the Cartesian axes was chosen as starting configuration, see Fig. 32. The central copper atom was placed at the origin and the 4-fold symmetry axis of CuPc was set parallel to the x-axis. The y- and z-axis pass through two of the nitrogen atoms, respectively and hence coincide with two of the 2-fold symmetry axis of CuPc. The configuration shown in Fig. 32 is called (x)-configuration and relates to the orientation of the benzene wings of CuPc, which are oriented like the letter "x" contrary to the (+)-configuration referring to benzene wings oriented like a plus sign. According to the aerospace industry, three axes fixed to the molecule were defined, the yaw-, pitch- and roll-axis, which indicate the orientation of the molecule relatively to the coordinate system like the orientations of satellites, aircraft and space vehicles are described relatively to the horizon. Yaw-, pitch- and roll-axes move with their object whenever the object changes its orientation. Furthermore, only rotations around those three axes are allowed. First, the molecule is rotated by an angle γ around its yaw-axis (z-axis) starting from the aforementioned configuration in order to define its horizontal orientation. Afterward, the molecule is rotated by an angle δ around its pitch-axis (y-axis) in order to define its inclination towards the x-y-plane (substrate surface). In a third step, the molecule is rotated by an angle φ around its roll-axis (x-axis), which finally defines the orientation of the molecule unequivocally.

Figure 32:

Chemical structure of copper phthalo-cyanine ($CuN_8C_{32}H_{16}$, abbreviation CuPc) and size of atoms due to their van der Waals radii: Copper ($1.40\,\text{Å}$), nitrogen ($1.55\,\text{Å}$), carbon ($1.70\,\text{Å}$) and hydrogen ($1.20\,\text{Å}$).
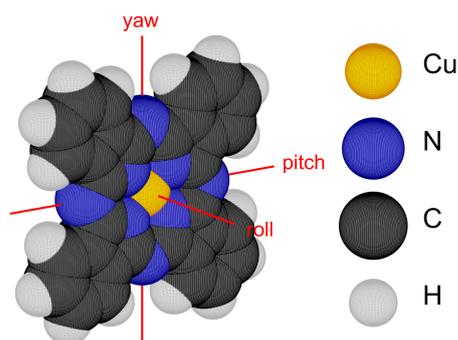
So far, we discussed the rotation of a single molecule. When rotating molecules within a unit cell, at least two things have to be considered, the excluded volumes and the space group symmetries, which will be discussed in the following.

4.2.5. Excluded Volume Considerations

First, the molecules should not overlap with their neighbors. There is a certain excluded volume that is already occupied by the atoms of other molecules and cannot be penetrated. The excluded volume was calculated by the van der Waals radius of each chemical element [125], see Fig 32. Although more complete sets of van der Waals radii were published [161, 162], the values of Ref. [125] are best suited and recommended for organic compounds. Not only overlaps inside the unit cell, but also overlaps between molecules from neighboring unit cells were taken into account by applying periodic boundary conditions. The degree of overlap was determined for each pair of atoms by calculating their distance and subtracting it from the sum of their van der Waals radii. Atomic pairs that were further away from each other than the sum of their van der Waals radii and atoms belonging to the same molecule were ignored. The sum of the remaining pairs of atoms finally delivers the total degree of overlap for each configuration.

4.2.6. Rotations According to the Space Group

Secondly, neighboring molecules should rotate accordingly to the space group symmetries of their crystal structure. Otherwise, the extinction conditions would change and peaks that should be extinct reappear. This part becomes important for base, face and body centered unit cells. Depending on the space group, molecules placed at one of these centers may rotate into the opposite direction compared to the molecules placed at the corners of each unit cell. This counter-rotating motion assures that the space group symmetry is maintained. The corresponding calculations start from the rotation of the first molecule, whose center is placed at the origin (lower left corner of a unit cell). Subsequently, the rotated coordinates of all other molecules are calculated from the coordinates of the first molecule using the equivalent Wyckoff positions of the respective space group from the Bilbao Crystallographic Server [159].

4.2.7. Exploration of Suitable Configurations by Monte-Carlo

The loss of phase information makes a direct calculation of molecular orientations from diffraction patterns impossible. So, orientations have to be found such that measured and calculated peak intensities agree. The first approach of the present work to find a suitable configuration that fulfills both, agreement of peak intensities and zero overlap between neighboring molecules, was a simple Monte-Carlo algorithm. The molecules were rotated randomly in small steps of $0.1°$–$1°$ around their yaw-, pitch- and roll-axis. The random rotations were repeated twenty times and the total degree of overlap was calculated for each configuration. The configuration with the lowest degree of overlap was chosen as starting point for the next iteration of random rotations. This procedure was repeated until a configuration without overlap was reached. Starting from this configuration the same procedure was applied for minimizing the deviation between measured and calculated peak intensities. Only configurations with zero overlap were accepted, which means that the molecules glide past each other into the configuration that fits best to the measured diffraction pattern. One disadvantage of this Monte-Carlo approach is that the algorithm may be trapped in a local minimum, which is not the actual solution. The step size and the number of iterations can be increased in order to escape from a local minimum, but still the resulting configuration may depend on the starting point and there is no guarantee that another, better minimum exists.

4.2.8. Exploration of the Entire Configuration Space

For this reason, the second approach of the present work was a full scan of the entire configuration space, which requires an unequivocal definition of the molecular orientation and a fast calculation as it was described above. The molecules were systematically rotated around their yaw-, pitch- and roll-axis from $-45°$ to $+45°$ in steps of $1°$. Larger angles than $45°$ are not reasonable in the case of CuPc for symmetry reasons and due to the limited space inside the unit cell. The total degree of overlap was calculated for each configuration resulting in a $91 \times 91 \times 91$- matrix. This matrix contains $91^3 \approx 0.75$ million data points. In order to accelerate the calculations, the algorithm stops when the total degree of overlap exceeds $10\,\text{Å}$ and jumps directly to the next configuration which is based on the assumption that the overlap does not drop from $10\,\text{Å}$ to $0\,\text{Å}$ within a rotation by less than $1°$. For the remaining configurations, X-ray peak intensities were calculated and compared to the measured diffraction pattern. The degree of deviation was measured by the mean square error $\chi^2 = \sum_n \left(I_{n,\text{exp}} - I_{n,\text{calc}}\right)^2$ and $I_{n,\text{exp}}$ is the intensity of the experimentally measured peak n and $I_{n,\text{calc}}$ the corresponding calculated intensity. The total scan of all 753,571 configurations including overlap check and intensity comparison was done with *Matlab* and took about 31 hours on a commercial computer (*Intel(R) Core(TM)* with $i5$ processor and $8\,\text{GB}$ rapid access memory).

4.3. Thin Film Morphology

4.3.1. Layer Coverages and Roughness from XRR

The XRR profiles were evaluated by using the software *GenX*, which is based on the Parratt formalism and able to simulate X-ray and neutron reflectivity curves for user-defined thin film models consisting of several layers. [163] The thin film model for CuPc (see Appx. F) was built up as follows: It starts with a $575\,\mu$m thick silicon substrate and a thin silicon oxide layer on top. The electron density of amorphous silicon oxide ($0.66\,\text{el.}/\text{Å}^3$) and the electron density of pure silicon ($0.70\,\text{el.}/\text{Å}^3$) were calculated from their mass densities (amorphous SiO$_2$: $\rho = 2.2$ g/cm^3 and pure Si: $\rho = 2.3$ g/cm^3) taken from the literature [150]. A void layer between the organic thin film and the substrate simulates the charge carrier density at the film-substrate interface. The organic thin film itself is made up of several bilayers. Each bilayer consists of a CuPc layer and a void layer simulating the periodically varying electron density in vertical direction from bottom to top, which is shown as scattering length density (SLD) in the upper right corner of Fig. 33. The bilayer thickness (≈ 13.1 Å) was determined from the position of the XRR Bragg peaks and assumed to be the same for all layers. Partially filled layers were simulated by lowering their electron density proportional to their layer coverages Θ_n. Missing values for thickness, roughness, and electron density of the individual layers were fitted by the software until experimental curve (black) and simulated curve (red) agreed, see Fig. 33. Agreement means in the context of *GenX* that the figure of merit (FOM), which is a measure for the deviation between experimental and simulated curve, approaches a constant value below 0.1 [163]. Detailed background information about the layer model and the fitting procedure is given in the Appx. E and F. Due to the missing Bragg peaks in XRR data sets of pure C60 thin films and blends with C60, the layer coverages cannot be determined from these data sets. Nevertheless, GenX is able to fit solely the damped Kiessig oscillations in the low q_z-range up to $0.2\,\text{Å}^{-1}$. The electron density, the film thickness and the root mean square roughness σ_{RMS} are the resulting parameters. This kind of fit is possible for all thin films with and without Bragg peaks as long as Kiessig oscillations appear. The Kiessig oscillations of thin films, whose roughness is larger than 15% of their current thickness, are completely damped and no fit is possible. The only way of determining their thickness and roughness is the evaluation of AFM images.

4.3.2. Layer Coverages and Roughness from AFM

All heights measured by atomic force microscopy (AFM) were divided into 100 classes from zero up to the maximum height and the occurrence of each height was calculated in percent. The distribution of heights will be shown as histograms on the left side of each AFM image. The root mean square roughness σ_{RMS} was directly extracted from the distribution of heights:

$$\sigma_{\text{RMS}} = \sqrt{\sum_{x,y}^{N_x,N_y} \left(h_{xy} - \bar{h}\right)^2} \qquad \text{and} \qquad \bar{h} = \frac{\sum_{x,y}^{N_x,N_y} h_{xy}}{N_x \cdot N_y}$$

This equation is generally valid for all AFM images of size $N_x \times N_y$ pixels. h_{xy} is the height measured

Figure 33: *In-situ* X-ray reflectivity (XRR) profiles of CuPc: Experimental data (black line), simulated data (red line) and corresponding scattering length density (SLD) of electrons. The differences between measured and simulated curves are so small that they are almost not discernible, which underlines that the extracted layer coverages are indeed trustworthy.
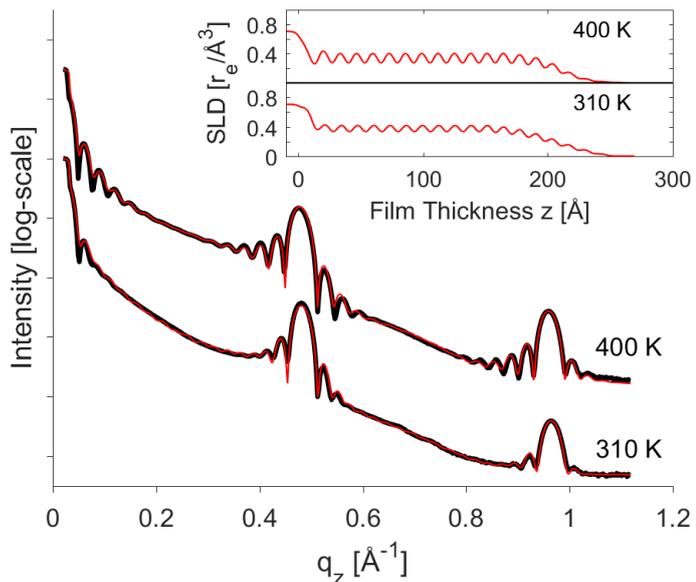
at the coordinate (x, y) and $\bar{h}$ is the average height. The coverage Θ_n of each layer was determined by a vertical scan through the AFM-profiles in steps of 13.1 Å for CuPc and in steps of 8.1 Å for C60 from bottom to top. Note that the lowest data points in the AFM images are not necessarily the substrate level, since there might be further completely filled layers below. The number of completely filled layers was chosen such that the average thickness equals the thickness determined from XRR.

4.3.3. Layer Coverages and Roughness from Simulation

For comparison to the layer coverage without diffusion or any kind of molecular interactions, a random deposition of 15×3000^2 particles on a 3000×3000 lattice was simulated by a *Matlab* script, see Fig. 45 in Sec. 5.1 and Fig. 55 in Sec. 5.3 for instance. The number $N = 15$ was chosen for CuPc such that the amount of deposited material per area is 15×13.1 Å $= 196.5$ Å in agreement with the experiment (2 Å/min $\times$ 100 min $= 200$ Å). Random deposition means in this context here that one of the 3000×3000 lattice sites is randomly chosen at each time step and a particle is deposited at this lattice site. The particles are not allowed to move to a different place at any time, which means that they stay at the lattice site where they were first deposited. After the deposition, the distribution of heights and the roughness σ_{RMS} are measured by the same procedure as for AFM images. It is well known that the heights resulting from a random deposition of non-diffusing particles are Poisson distributed and that σ_{RMS} is proportional to $\sqrt{N}$ for an average height of N layers. [84, 85] Several similar but more complex simulations were carried out in the past confirming this result [164–166]. The comparison to experimentally determined layer coverages will show that interlayer diffusion actually occurs and the experimentally determined layer coverages deviate from the simulated random deposition without diffusion. Furthermore, it can be distinguished from the layer coverages whether the molecules tend to upward or to downward diffusion.

4.3.4. Island Densities and Sizes

The automated detection and counting of islands in AFM images can be quite challenging and suitable counting algorithms have to be found. A simple method for detection islands is the usage of a threshold value. All pixels whose heights exceed the threshold value are marked in black, see the left side of Fig. 34. All other pixels remain white. The black area represents the layer coverage at this height level as it was discussed in the last sections. However, the islands are not yet discernible. The distinction between separate islands requires the following considerations: Two pixels which can be connected by a percolating path, i.e. without leaving the marked area, belong to the same island. In other words, all pixels on a coherent area belong to the same island. Each island was painted in a different color and counted, see the right part of Fig. 34. This method is explained in Appx. G.

The method of counting islands solely by applying a threshold, as it is usually done in common AFM evaluation software such as Gwyddion, holds various disadvantages. It only works reliably when all islands exhibit the same height, which is rarely the case for organic thin films. If the threshold level is too low, neighboring islands coalesce and are counted as one large island. The networks of coalescing islands in Fig. 35 demonstrate that this can be a serious issue. If the threshold level is too high on the other hand, low islands are not detected any more. In both cases, the real number of islands is underestimated. Figure. 36 illustrates that under certain circumstances there is no threshold level at which the number of islands is counted correctly. The figures in the Appx. H confirm this result by experimental evidences.
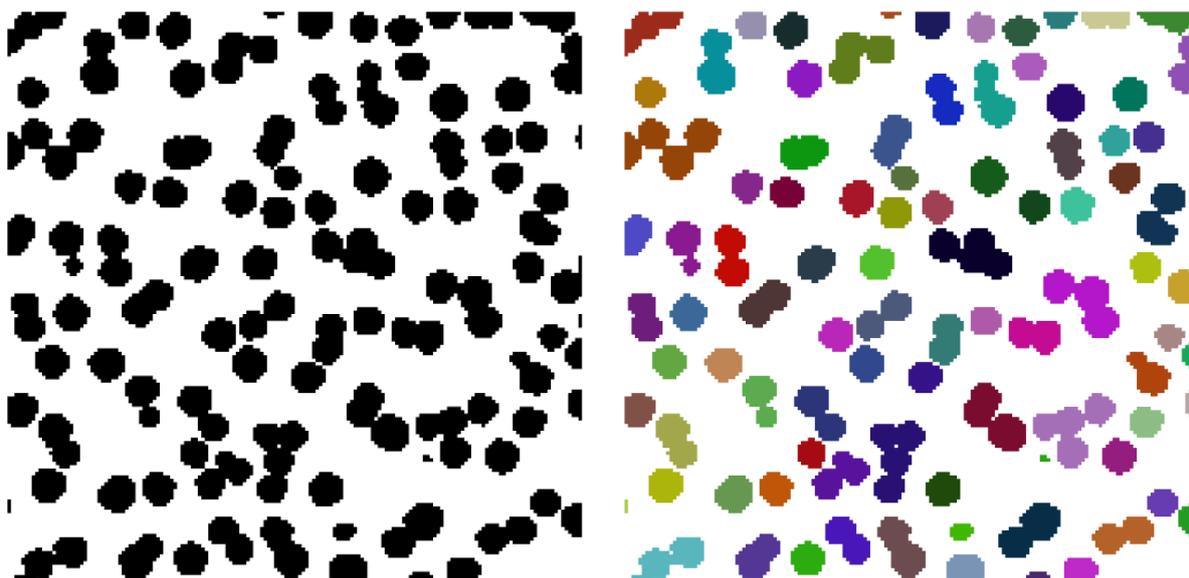

Figure 34: $1 \times 1\,\mu m^2$ AFM image of a pure C_{60} thin film grown at $400\,K$ and $2\,Å/min$ for $7\,minutes$. Left: Pixels exceeding a height of $2\,nm$ are marked in black. The black area represents the layer coverage at this height. Right: In a second step, each island is painted in a different color for counting. Coalescing islands are counted as one large island and receive the same color.

Figure 35: Networks of coalescing islands in a $3 \times 3\,\mu m^2$ AFM image of a pure C_{60} thin film grown at $340\,K$ and $2\,Å/min$ for $7\,minutes$. Pixels exceeding a threshold of $3.7\,nm$ are colored. Each network is marked in a different color.
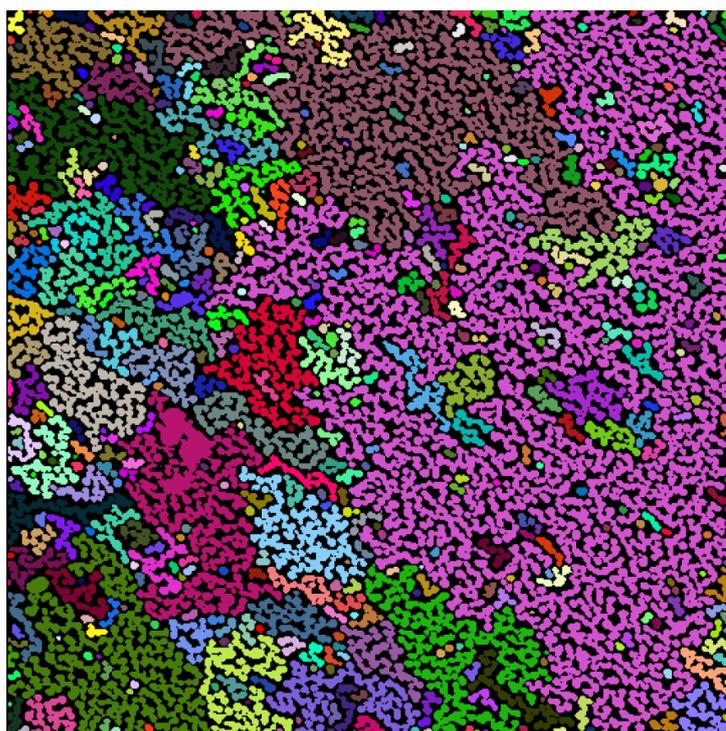

Figure 36:

Schematic sketch of a cross sectional side view through an organic thin film illustrating the challenges of counting islands of different heights.
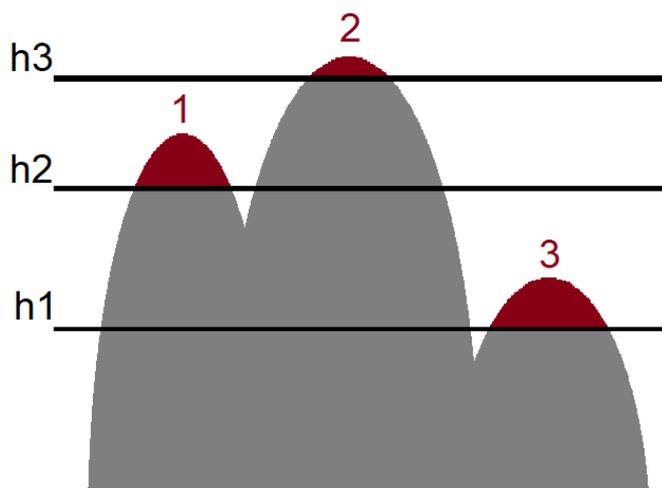

Explanation of Fig. 36:

(i) Island 1 and 2 coalesce at the height level h1 and will be counted as one single island.

(ii) At height h2, island 1 and 2 are separated, but island 3 is already too small to be detected.

(iii) The number of detected island during a vertical scan from bottom to top depends on the step size. Skipping step h2 would neglect island 1.

In order to count the number of islands correctly, the image was scanned layer by layer from bottom to top. An island was counted as soon as its top was reached, i.e. when there was no island detected at the same place in the layer above. It turned out that also the vertical step size of the bottom-to-top scanning affects the number of detected islands. Recalling Fig. 36 for illustration makes clear that skipping the height h2 neglects island number 1. For this reason, the total number of islands was determined at different vertical step sizes ranging from 1.0 nm down to 0.05 nm. Figure 37 shows a linear relationship between the vertical step size and the number of detected islands. An extrapolation of the fitted lines towards an infinitely small step size finally delivers the true number of islands, which can be extracted from the intersection points of the fitted lines with the ordinate axis. Note that the number of islands per image amounts to several thousands depending on the substrate temperature, which underlines the importance of automated counting algorithms for the evaluation of such AFM images. We see an increasing island density at lower substrate temperatures and due to the steeper slope of the fitted lines, the influence of the vertical step size becomes more and more important.

Figure 37: Number of detected islands after scanning $3\,\mu\text{m} \times 3\,\mu\text{m}$ AFM images of pure C60 thin films from bottom to top using different vertical steps sizes. Each line corresponds to a specific substrate temperature (310 K, 340 K, 370 K, and 400 K) and 7 minutes of deposition at a deposition rate of $2\,\text{Å/min}$ each. The intersection points of the fitted lines with the ordinate axis indicate the true number of islands for an infinitely small step size.
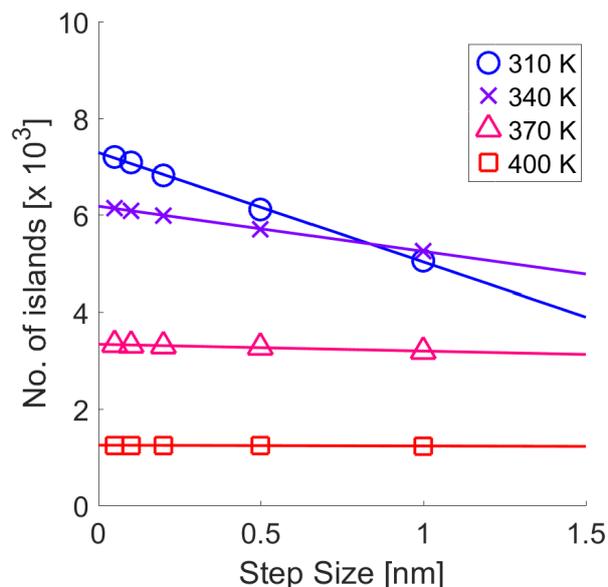
The automated detection of islands allows not only counting, but also an automated investigation of island shapes and sizes. Due to the isotropic silicon oxide substrate and the isotropic shape of C60 molecules, the islands exhibit a round shape in top view. In side view, the cross section through almost all C_{60} islands was best reproduced by a parabola curve $z(x) = z_0 - w \cdot (x - x_0)^2$, see the red solid line in Fig. 38. For fitting the cross sectional shapes, the AFM images were scanned layer by layer in steps of 0.05 nm and the cusp of each island was detected at the coordinates (x_0, y_0, z_0). A cross sectional line cut through each island was automatically extracted and fitted by using the position x_0 and the height z_0 as starting parameters. The boundaries for fitting were automatically detected by the changing slope at each side of an island, see the dashed vertical lines in Fig. 38. As soon as the slope between neighboring pixels changes significantly, a flank was detected as kink in

the line profile. The island diameter at the basement was calculated by $2 \cdot \sqrt{z_0/w}$. Islands whose diameters were smaller than $15\,\text{nm}$ could not be detected since their area at the basement covers less than $3 \times 3\,\text{pixels}$. Failures during the automated detection of flanks returned a few very large islands (diameters $> 150\,\text{nm}$ and heights $> 25\,\text{nm}$), which had to be ignored for the statistics. They mainly appeared at tightly clustered islands seeming like one big island and partially also at the rim of the AFM images, where only fractions of the islands were measured. These failures occurred rather rarely compared to the large number of well fitted islands.
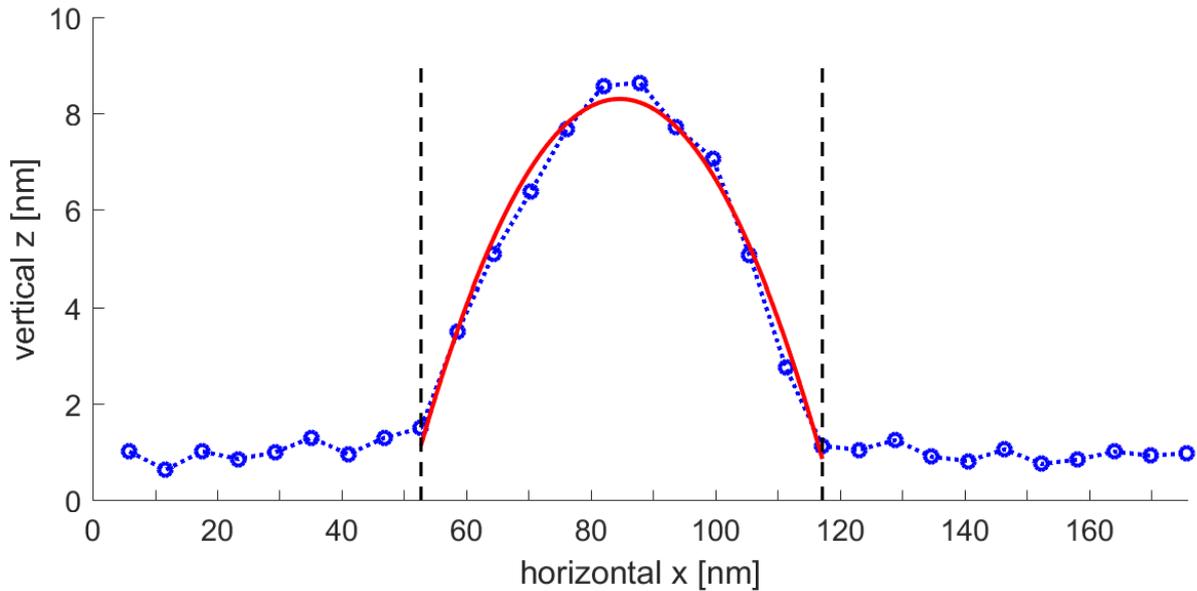
Figure 38: Cross section through a C_{60} island in side view. The blue circles indicate the measured data points. The red solid line indicates the automatically fitted parabola curve and the dashed vertical lines indicate the automatically detected flanks of the present island. Note that the vertical z-axis is stretched in order to make the island visible. In the actual 1:1 aspect ratio, the islands would be extremely flat.

5. Results and Discussion of Pure Thin Films

In order to understand the behavior of blended thin films, it is useful to analyze the behavior of pure films in advance. Crystal structures, molecular orientations and thin film morphologies of pure CuPc thin films, pure Cor thin films and pure C60 thin films will be discussed in this section. Special attention is payed to polymorphism, which means the occurence of different crystal structures, as well as to roughness and island densities, which are key parameters for characterizing thin film morphologies.

5.1. Pure CuPc Thin Films

5.1.1. Preparation and Measurements

Copper Phthalocyanine (CuPc) was bought from Sigma Aldrich (purity 99.9 % by gradient sublimation) and installed in a vacuum chamber for organic molecular beam deposition. $10 \times 5 \, mm^2$ pieces of an amorphous native silicon oxide substrate were cut. The thickness of the native oxide layer was measured in advance by XRR and amounts to approximately 1–2 nm. The substrates were cleaned by acetone and isopropanol in an ultrasonic bath for 5 minutes each and then installed inside the load lock. The load lock was pumped down to approximately 10^{-6} mbar and the substrates were heated for more than 10 hours above 500 K in order to remove condensed water until the pressure reached approximately 10^{-9} mbar. Subsequently, the substrate temperature was set to 310 K for the first sample and to 400 K for the second sample in order to investigate its influence on the thin film morphology. After cooling down to the desired temperature, the specimens were transferred to the main chamber. The molecules were evaporated from a Knudsen effusion cell and deposited onto the substrates at a deposition rate of 2.0 Å/min for 100 min resulting in an average film thickness of 200 Å, each. After 100 min of deposition, the shutter of the effusion cell was closed and the samples were kept in vacuum until they cooled down to room temperature. Finally, the samples were taken out of the vacuum and their surface profiles were measured *ex situ* under the AFM. Additionally, Q-maps of both samples were measured *ex situ* at the ID03 beamline of the European Synchrotron Radiation Facility (ESRF) using a 2D-Maxipix area detector (512×512 pixels of size $55 \times 55 \, \mu m^2$). The X-ray energy was set to 24.0 keV corresponding to a wavelength of 0.517 Å and the angle of incidence ($0.030°$, $0.013 \, Å^{-1}$) was set below half of the total reflection edge of silicon. This setup is very surface sensitive due to the low penetration depth of the beam at this grazing angle of incidence. The single images were merged and converted into reciprocal space as described in the analysis section 3.2.

Another two samples were prepared under the same conditions (deposition rate 2 Å/min for 100 min at a substrate temperature of 310 K and 400 K, respectively) in a portable vacuum chamber [152] at the material science beamline MS-X04 SA of the Swiss Light Source in order to measure XRR and GIXD *in situ* directly after the growth. The beam energy was set to 12.7 keV corresponding to a wavelength of 0.976 Å and the angle of incidence ($0.120°$, $0.027 \, Å^{-1}$) was chosen close to the total reflection edge of silicon, which probed the crystal structure throughout the entire film thickness.

5.1.2. Size and Orientation of Crystallites

Figure 39 shows the XRR and GIXD profiles of CuPc grown at 310 K and 400 K. The Bragg peaks and the pronounced Laue oscillations seen from the XRR profiles indicate a well ordered layer structure in vertical direction. The layer coverages were determined by fitting the XRR profiles with the help of *GenX* as it was described in Sec. 4.3. The layer coverages from XRR will be compared to layer coverages from AFM and from simulations and will discussed in more detail in Sec. 5.1.7. The Kiessig oscillations in the low q_z-range demonstrate that the film grown at 400 K is smoother than the one grown at 310 K. The $(0kl)$ GIXD peaks are in good agreement with the space group $P\bar{1}$ of the CuPc α-structure, which was reported in 2003 by Hoshino et al. [99]. In contrast to the vertical ordering, the crystallites can have any azimuthal orientation. This 2D powder-like structure leads to GIXD peaks of all $(0kl)$ directions. The GIXD peak widths reveal that the lateral size of coherently scattering domains in (001)-direction amounts on average to 21 nm at 310 K and 31 nm at 400 K. To summarize, the thin films exhibit a well ordered layer structure in vertical direction, but small crystallites of random orientation in horizontal direction. Furthermore, elevating the substrate temperature leads to smoother thin films and larger crystallites.
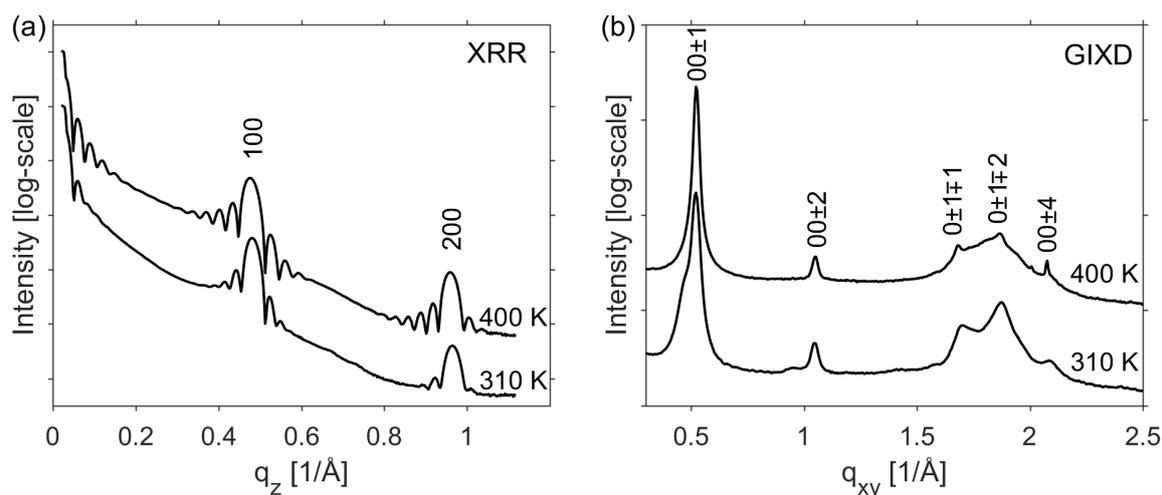

Figure 39: (a) *In-situ* XRR and (b) *in-situ* GIXD of CuPc grown at a deposition rate of 2 Å/min for 100 min at two different substrate temperatures (310 K and 400 K).

5.1.3. Crystal Structure

The Q-maps of CuPc grown at 310 K and at 400 K are shown in Fig. 40 and Fig. 41. The peak positions agree at both substrate temperatures although the peaks are markedly stronger at 400 K. At first, the unit cell parameters (a = 26.(1) Å, b = 3.8(2) Å, c = 24.(0) Å, α = 90.0°, β = 94.(0)°, γ = 90.0°) were determined from the peak positions. A precision of two significant figures was obtained for all unit cell lengths. The third significant figure is less accurate and therefore indicated in parentheses. Note that the short b-axis can be determined accurately with two decimal places. The unit cell lengths are closest to the α-structure ($C2/c$) reported in 1966 [98] and deviate less than

1 Å. The angle β had to be changed from $90.4°$ to approximately $94.0\pm0.8°$, which is responsible for the vertical splitting into $(h\,k\,{+}l)$ and $(h\,k\,{-}l)$ reflections. The variation of $\pm0.8°$ comes from the vertically elongated diffraction peaks. To which degree the reported unit cell dimensions deviate from each other depends most likely on the choice of the substrate, which was mica and potassium chloride in 1966 and is native silicon oxide for this study. Despite the deviations between unit cell lengths and angles, the characteristic peak extinctions proof that the space group must be $C2/c$. Only $(h\,0\,l)$ reflections with h and l being even and $(h\,{\pm}1\,l)$ reflections with h being odd remain visible and are indicated in Fig. 40 and 41 by white circles. All other peaks in between are extinct by the C-centering in the a-b-plane, by the 2-fold screw axis along the b-direction and by the gliding mirror plane along the c-direction. For a detailed explanation of extinctions by space group symmetries see the examples in Appx. C. Peaks with large Miller indices are also not visible, presumably due to the limited crystallite sizes. In order to avoid an overcrowded figure, only $(h\,{\pm}1\,l)$ peaks for $h=1$ are labeled and the peaks for $h=3$ are indicated without labeling. The peaks for $h=5$ are covered by the strong silicon $\{1\,1\,1\}$ reflection stemming from the silicon substrate. This peak is not visible in the Q-map of CuPc grown at 310 K and also not in the background measurement. The reason for this is the azimuthal orientation of the substrate during the measurements. In contrast to the polycrystalline CuPc films, the substrate consists of one single crystal and peaks appear only under certain circumstances. When the $\{110\}$ direction of the silicon substrate is parallel to the incoming X-ray beam, the condition for the Si-$\{1\,1\,1\}$-reflection is fulfilled and this peak appears in the Q-map. Small deviations from the parallel alignment lead to a vanishing of this peak, which is exceptionally wanted in this case since we want to probe the organic film and not the substrate. The broad expansion of the usually sharp and quite strong silicon $\{1\,1\,1\}$ reflection might stem from scattering of x-rays at the silicon oxide layer, the organic layer and the air.

Last but not least, two weak peaks appear between $q_{xy} = 1.5 - 2.0\,\text{Å}^{-1}$ slightly above the dotted red line at $q_z = 0\,\text{Å}^{-1}$ in Fig. 40 and Fig. 41. They cannot be explained by the space group $C2/c$, but agree with the primitive triclinic unit cell (space group $P\bar{1}$), whose a- and c-axis are halved [99]. Since this primitive structure cannot explain most of the other peaks in the Q-map, a co-existence of both α-structures ($C2/c$ and $P\bar{1}$) is inferred. In the lower part of Fig. 40 and Fig. 41, the corresponding *ex-situ* GIXD profiles are shown. Peaks of both α-structures appear in the GIXD patterns. The position of the $P\bar{1}$ $(0\,0\,{\pm}1)$ peak and the $C2/c$ $(0\,0\,{\pm}2)$ peaks coincide. The remaining GIXD peaks stem solely from the primitive structure $P\bar{1}$. Those peaks are substantially smaller in the *in-situ* GIXD data, see Fig. 39, indicating that only a little fraction of the crystallites exhibits the primitive structure $P\bar{1}$ directly after the growth, particularly when considering that the intensity scale is logarithmic. In contrast to this, the *ex-situ* GIXD profiles in the lower part of Fig. 40 and Fig. 41, which were measured at half of the total reflection angle of silicon some time after the growth, exhibit a lower difference between the $P\bar{1}$ and the $C2/c$ intensities. A post-growth transition from the $C2/c$ to the $P\bar{1}$ structure, which occurs most likely at the film-air interface, is inferred from the comparison of *in-situ* and *ex-situ* data. Since the grazing angle of incidence was changed at the same time, it cannot be exactly discerned whether the elapsed time after the growth, or the difference between bulk and surface plays the most important role.
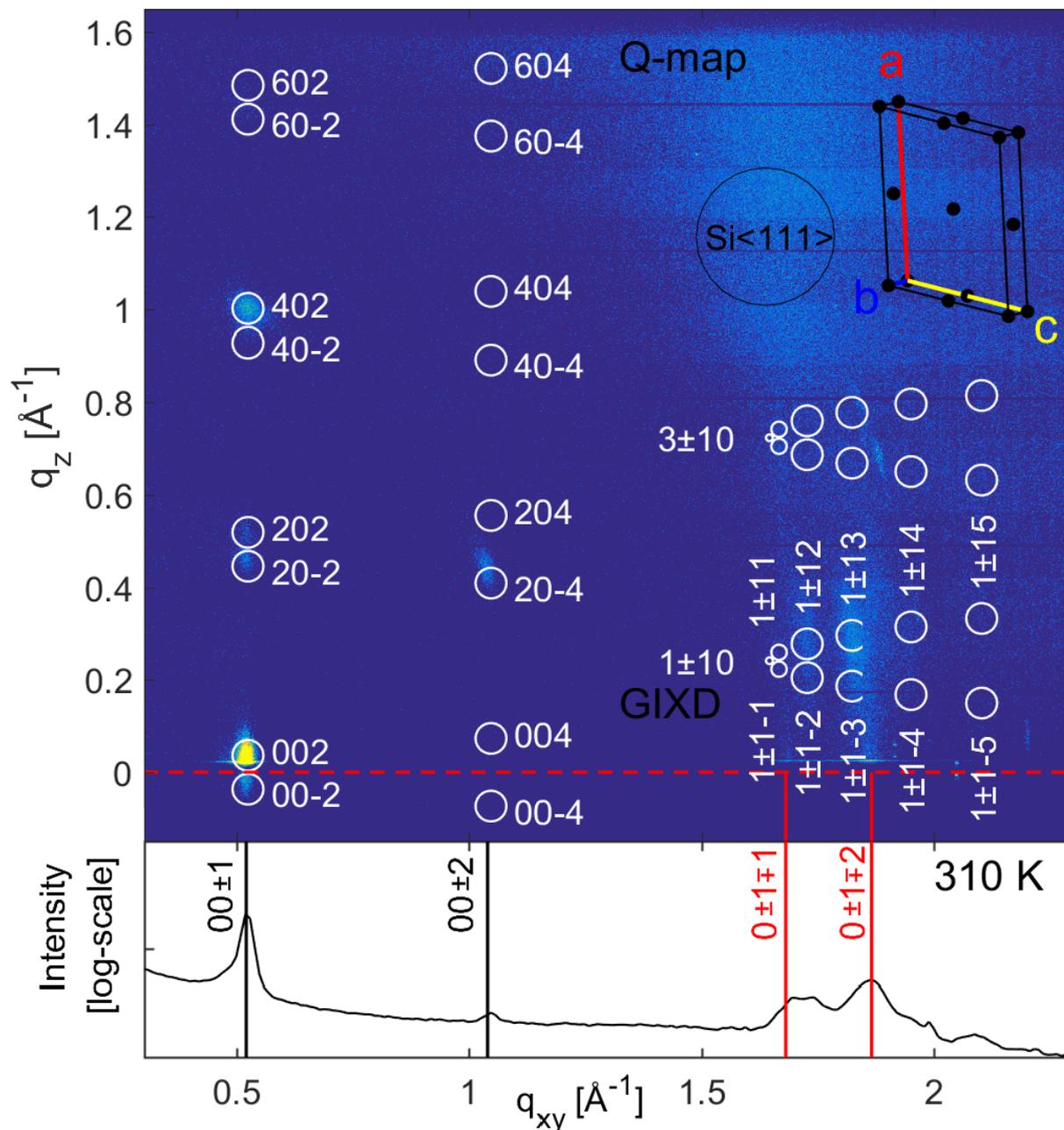
**Figure 40:** Q-map of 20 nm CuPc grown on native silicon oxide at 2 Å/min and 310 K. White circles indicate the calculated peak positions for the $C2/c$-structure (a = 26.1 Å, b = 3.82 Å, c = 24.0 Å, β = 94.0°) The corresponding unit cell is shown in the upper right corner. Black dots mark the positions at which the molecules have to be placed in consideration of the space group symmetries. The corresponding GIXD pattern is indexed below due to the primitive triclinic crystal structure ($P\bar{1}$), whose a- and c-axis are halved. [99]
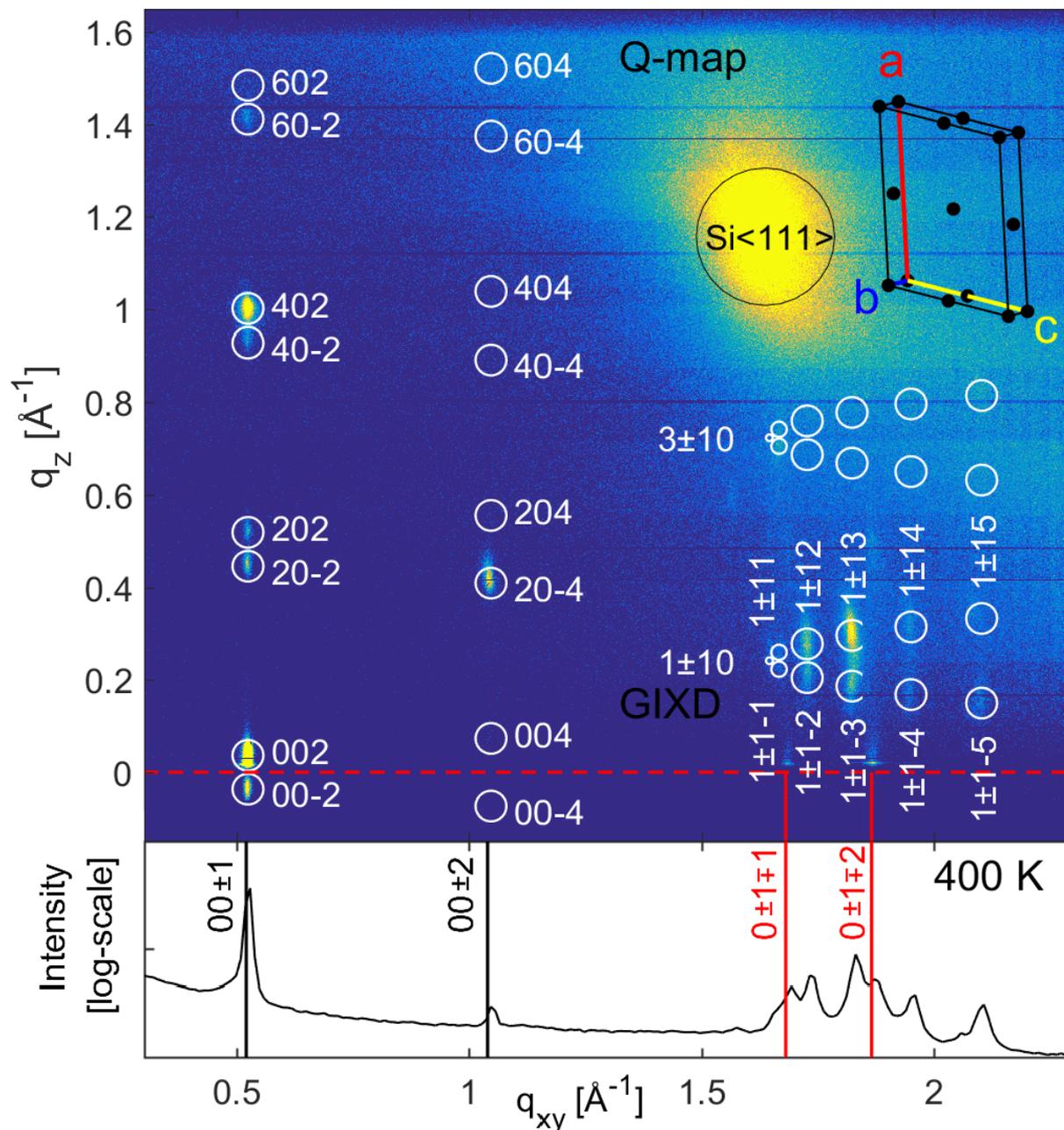
Figure 41: Q-map of 20 nm CuPc grown on native silicon oxide at 2 Å/min and 400 K. White circles indicate the calculated peak positions for the $C2/c$-structure (a = 26.1 Å, b = 3.82 Å, c = 24.0 Å, β = 94.0°) The corresponding unit cell is shown in the upper right corner. Black dots mark the positions at which the molecules have to be placed in consideration of the space group symmetries. The corresponding GIXD pattern is indexed below due to the primitive triclinic crystal structure ($P\bar{1}$), whose a- and c-axis are halved. [99]

5.1.4. Orientation of the Unit Cell

First we discuss the orientation of the unit cell with respect to the substrate surface and secondly the orientation of the molecules within the unit cell. A possible configuration of the $C2/c$-structure is shown in Fig. 42. Regarding the peak positions in the Q-maps, the b- and c-axes are parallel to the substrate surface. The a-axis (26.1 Å) has twice the length of the vertical lattice spacing determined from XRR such that two molecules can be stacked on top of each other within each unit cell. Also the c-axis (24.0 Å) provides enough space for two molecules. Four molecules per unit cell stacked in rows along the short b-axis and hence also along the substrate surface result in good agreement with previous studies [109, 167]. Note that further molecules were added to the plot in Fig. 42 in order to demonstrate the lattice periodicity. Recalling the GIXD profiles of Fig. 39, a shoulder at the left side of the first GIXD-peak (00 ± 1) appears at 310 K, but not at 400 K. It indicates that the unit cell of some crystallites is tilted around the b-axis by 86° such that the a-b-plane instead of the b-c-plane is parallel to the substrate surface. Based on the knowledge that the a-axis (26.1 Å) is longer than the c-axis (24.0 Å), it is clear that this shoulder has to appear on the left side in reciprocal space. The partial unit cell rotation at 310 K might be a kinetic effect induced by the growth process. At higher substrate temperatures such kinetically limited effects are less likely to occur since the molecular diffusion length is larger.

**Figure 42:**

Unit cell:

Space group: $C2/c$

a $= 26.1$ Å, $\alpha = 90.0°$

b $= 3.82$ Å, $\beta = 94.0°$

c $= 24.0$ Å, $\gamma = 90.0°$

Possible molecular orientation:

yaw: $+33°$, pitch: $-21°$, roll: $+3°$
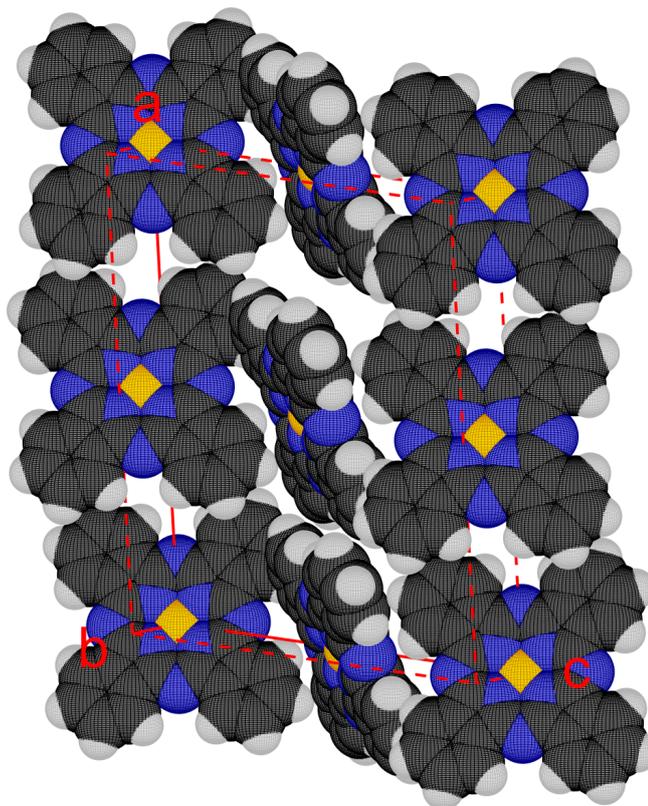
5.1.5. Molecular Orientations

In order to determine possible molecular orientations within the unit cell, the molecules were systematically rotated around their yaw-, pitch- and roll-axes from -45° to +45° in steps of 1° in consideration of the present space group symmetries as it was described in section 4.2. The overlap between neighboring molecules was calculated according to section 4.2 and visualized in a 91×91×91-matrix, see Fig. 43. It turned out that there are many $C2/c$ configurations without overlap. However, none of them exhibits a good agreement between calculated and measured peak intensities. On the other hand, the extinctions of specific peaks in the Q-map clearly evidence that the $C2/c$ structure is present. To resolve this contradiction, the coexistence of various molecular arrangements can be assumed. The molecular orientation may vary from crystallite to crystallite entailing on diffraction patterns whose peak intensities cannot be easily calculated. Since there is no 'best' configuration, a classification of possible configurations is provided here. There are $2^3 = 8$ main configurations, two for each of the symmetry axes (yaw, pitch and roll), see Fig. 43. Coherent regions without molecular overlap appear in Fig. 43. Configurations within a coherent region are close to each other in the configuration matrix, i.e. assigned to neighboring matrix elements. So, continuous transitions from one configuration to another are possible. Further calculations revealed that the molecules can glide past each other without penetrating the excluded volume, but also distinct areas appear in Fig. 43 meaning that not all configurations can be reached by a continuous transition. Such transitions would require an expansion followed by a contraction of the unit cell. One configuration is presented in Fig. 42 as an example for a possible molecular orientation. The hydrogen atoms of neighboring molecules are interlocked. Furthermore, the pitch angle cannot become 0° because of the limited space in the vertical direction. The same applies to the yaw angle due to the limited space in the horizontal direction. The roll angle stays well below 45° such that only the (×)-configuration is possible, which was denominated in this manner by Hoshino et al. in contrast to the (+)-configuration and refers to orientation of the four benzene rings of CuPc with respect to the substrate surface [99].

Figure 43:

Visualization of the configuration space $(91 \times 91 \times 91\text{-matrix})$ showing regions whose total degree of overlap is below $1.0\,\text{Å}$.

The calculations refer to the α-structure of CuPc:

Space group $C2/c$ (a = 26.1 Å, b = 3.82 Å, c = 24.0 Å, β = 94.0°).

61
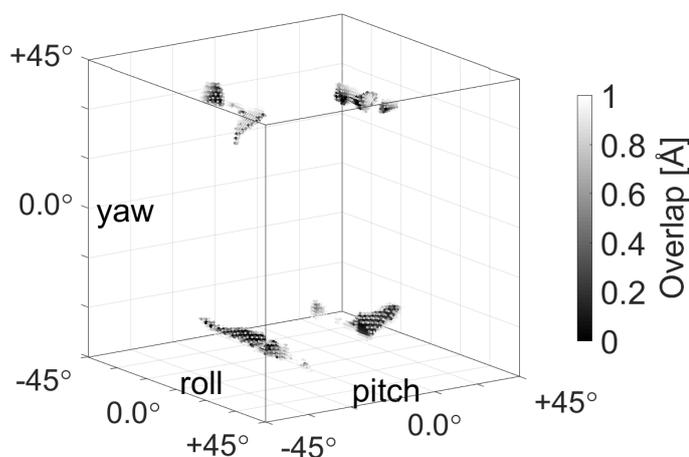
5.1.6. Morphology

Figure 44 shows AFM images of CuPc grown at 310 K and at 400 K. The islands were automatically counted as described in Sec. 4.3 and the root mean square roughness σ_{RMS} was determined from the distribution of heights, which is shown on the left side of each AFM image as histogram along with the color bar. The AFM images show that elevating the substrate temperature leads to two remarkable effects on the thin film morphology. Firstly, larger islands form, while the island density decreases by a factor of 10. Note that the lateral size of coherently scattering crystallites d_{coh}, which was determined from the width of the first (001) GIXD peak (see Sec. 4.3 and Sec. 5.1.2), increases as well from 21 nm at 310 K to 31 nm at 400 K. Nevertheless, the crystallites are much smaller than the island sizes, which grow from a length of approximately 50 nm at 310 K to a length of several hundred nanometers at 400 K. Hence, each island must consist of several crystallites. The second remarkable effect concerns the surface roughness. The film grown at 400 K is smoother than the one grown at 310 K. The difference between σ_{RMS} determined from AFM and XRR is only 1-2 Å and validates the applicability of both techniques to this study. The small deviations between *ex-situ* AFM and *in-situ* XRR also tells that no major morphological post-growth effects occurred. The results of X-ray diffraction and atomic force microscopy are summarized in Tab. 4. Despite all differences between 310 K and 400 K, the worm-like shape of islands is preserved at both substrate temperatures as the insets in Fig. 44 show.
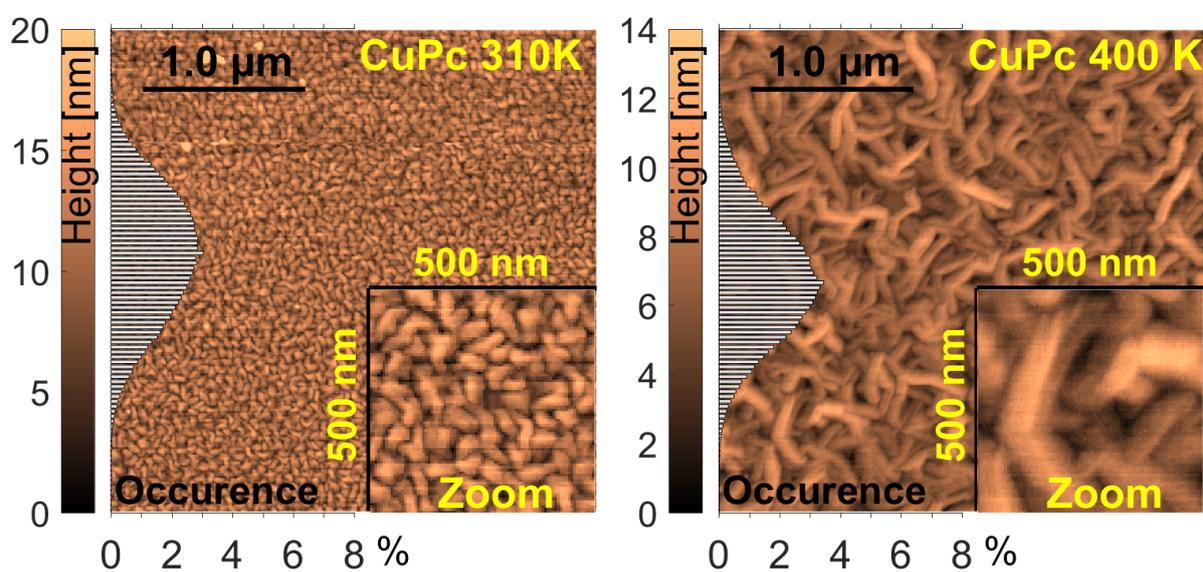

Figure 44: $3\,\mu m \times 3\,\mu m$ AFM images of 20 nm thin CuPc films grown at 2 Å/min for 100 min at two different substrate temperatures, 310 K and 400 K. The distributions of heights are shown as histograms on the left side of each image together with the color bar.

Table 4:

T_{sub}: Substrate temperature
d_{coh}: Size of coherently scattering crystallites
ρ: Island density
σ_{RMS}: Root mean square roughness.

T_{Sub}	310 K	400 K
d_{coh}	21 nm	31 nm
ρ	$400 \, \mu m^{-2}$	$40 \, \mu m^{-2}$
σ_{RMS}, XRR	2.9 nm	1.8 nm
σ_{RMS}, AFM	2.7 nm	1.7 nm

5.1.7. Layer Coverages

The XRR profiles indicate a layered thin film structure. The height of the CuPc layers was determined from the XRR Bragg peak positions and amounts to 13.1 Å. The following considerations assume that each layer has the same height of 13.1 Å. The deposition at 2 Å/min for 100 min resulted in an average film thickness of 200 Å. A perfectly smooth film would consist of approximately 15 completely filled layers. The simulation in the upper part of Fig. 45 shows how the layer coverages would look like if there was neither diffusion nor any kind of molecular interactions. Missing matter from the lower 15 layers appears in the layers above leading to a pronounced roughness. The heights are Poisson distributed and σ_{RMS} amounts to $\sqrt{15} \times 13.1 \, \text{Å} \approx 5.1 \, \text{nm}$, which is much larger than the experimentally determined roughness shown in Tab. 4. This comparison reveals that molecular downward diffusion occurred during the growth. Furthermore, the evaluation of the XRR-data resulted in 11–12 completely filled and 7 partially filled layers, both at 310 K and at 400 K, though the coverages of lower layers are larger at 400 K than at 310 K indicating that heat facilitates the downward diffusion. A similar trend is seen when regarding the layer coverages extracted from AFM. According to the little change between *in-situ* XRR and *ex-situ* AFM, the downward diffusion took place mainly during and not after the growth.

5.1.8. Summary of Results

The crystal structures and the morphologies of vacuum deposited CuPc thin films on native silicon oxide were studied in detail. Evidences for the co-existence of two α-structures were found by reciprocal space mapping. A base centered monoclinic crystal structure, space group $C2/c$, was found. As reported in 1966, the unit cell consists of four molecules, [98] but the unit cell parameters found in here deviate from the ones reported in 1966 and had to be redetermined. A little fraction of the crystallites exhibits the primitive triclinic structure, space group $P\bar{1}$, whose a- and c-axes are halved such that there is space for only one molecule per unit cell. The unit cell parameters agree with the reported crystal structure reported in 2003. [99] It is conceivable that the $P\bar{1}$ structure emerges from the $C2/c$ structure after the growth as result of a reorganization process at the surface of the thin film.

Figure 45:

Comparison of experimentally determined layer coverages from *in-situ* XRR and *ex-situ* AFM with a simulated layer coverage resulting from random deposition without diffusion or any kind of molecular interactions.
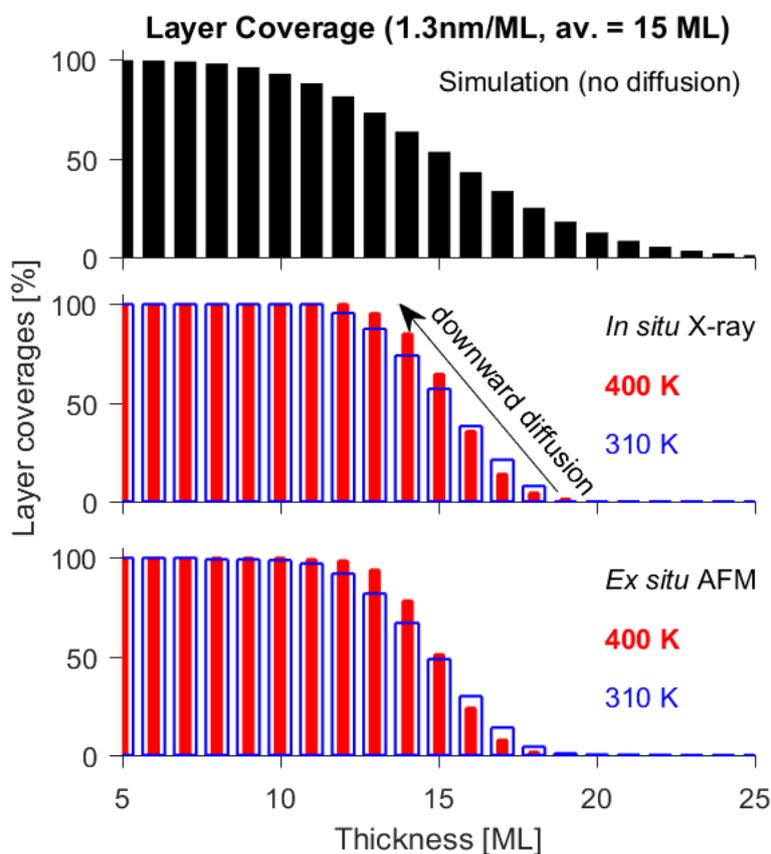
The so far missing molecular orientation of the $C2/c$-structure was determined by excluded volume considerations. None of the possible configurations was able to reproduce the relative peak intensities of the Q-maps and hence a co-existence of several $C2/c$-configurations was assumed. The calculations showed that continuous transitions from one configuration to another are possible. The molecules can glide past each other without changing the unit cell or the space group symmetry, whereas major changes require an expansion followed by a contraction of the unit cell.

AFM images, Q-maps, XRR and GIXD profiles show a thin film, whose crystallites are randomly oriented in horizontal direction, but exhibit a strict ordering in vertical direction. The molecules are stacked rows along the short b-axis parallel to the substrate surface and in well ordered layers perpendicular to the substrate surface. The comparison of experimental and simulated layer coverages clearly shows that molecular downward diffusion leads to a smoothing of the film surface, which is even more pronounced at an elevated substrate temperature of 400 K. Furthermore, the islands become larger at 400 K and the island density decreases by a factor of 10 compared to the island density at 310 K. The islands must be polycrystalline since the sizes of coherently scattering crystallites are considerably smaller than the islands sizes. Finally, the small differences between *in-situ* XRR and *ex-situ* AFM indicate that no morphological changes occurred after the growth.

5.2. Pure Coronene Thin Films

5.2.1. Preparation and Measurements

Coronene molecules were bought from Sigma Aldrich (purity 99.9% by gradient sublimation), filled into a ceramic crucible and installed into a vacuum chamber inside of a Knudsen effusion cell. The native silicon oxide substrates were prepared in the same way as for the growth of CuPc thin films. They were cut into $5\,mm \times 10\,mm$ pieces, cleaned in aceton and in isopropanol in an ultrasonic bath for 5 minutes each and installed inside the load lock, which was then evacuated and heated for 10 hours above 500 K until a pressure of 10^{-9} mbar was reached. After cooling down to 310 K and transferring the specimens to the main chamber, a deposition at $2\,Å/min$ was tested, but no molecules impinged upon the substrate. The rate calibration revealed that the first molecules appeared on the substrate at a deposition rate of at least $4\,Å/min$. Figure 46 explains why. At a deposition rate of $4\,Å/min$ only the lower left corner of the substrate was covered by molecules, whereas a deposition of 10–$25\,Å/min$ was able to cover the entire substrate. Obviously, the molecular beam did not directly point at the center of the sample. It seems that increasing the deposition rate increases the divergence of the beam. As a result of this, molecules from the rim of the cone-shaped beam impinge on the substrate surface as soon as the cone is wide enough to hit the specimen. Owing to this misalignment, the films had to be grown at larger deposition rates instead, which makes a direct comparison to the CuPc thin films difficult. Nevertheless, some conclusions can still be drawn and yet, studies on vacuum deposited coronene thin films are rare in the literature.
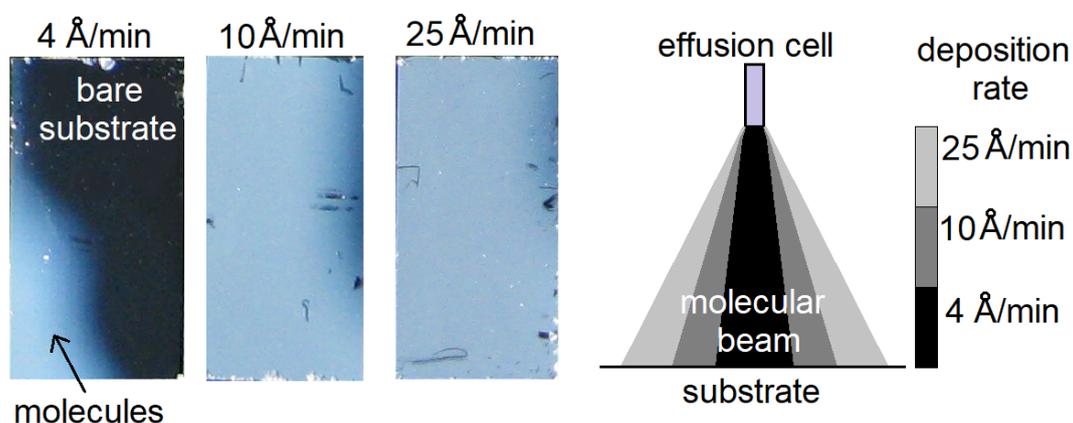

Figure 46: Coronene thin films on native silicon oxide at three different deposition rates (left) and divergence of the cone-shaped molecular beam depending on the deposition rate shown on the right.

Coronene thin films were grown at three different deposition rates, each on average around 100 nm thin: 250 min at 4 Å/min, 100 min at 10 Å/min and 40 min at 25 Å/min. The substrate temperature was 310 K for all three samples. XRR and GIXD profiles as well as Q-maps were acquired *ex situ* a few days after the growth at the I07 beamline of the Diamond Light Source (UK). The beam energy was set to 14.0 keV corresponding to a wavelength of 0.886 Å^{-1} and the angle of incidence was set to 0.11° close to the total reflection edge of silicon (0.027 Å^{-1}) for GIXD and for the Q-maps. The acquisition of AFM images was difficult due to the pronounced roughness. It quickly became clear that coronene molecules form several micrometer long needle-like crystals of random orientation on native silicon oxide. There was no alignment with the substrate and the needles towered 1 μm high. So, light microscopy and scanning electron microscopy were employed instead of AFM.

5.2.2. Crystal Structure

Due to the pronounced roughness, there are no Kiessig oscillations in the XRR-profiles in Fig. 47 (a). Peaks of all crystallographic directions are present in the GIXD profiles in Fig. 47 (b) indicating that there is no preferential alignment with the substrate. Also the ring-shaped diffraction patterns in the Q-maps, see Fig. 48, indicate that there is no alignment with the substrate independently from the deposition rate. The broad spot around $(q_{xy}, q_z) = (1.6 \text{ Å}^{-1}, 1.2 \text{ Å}^{-1})$ stems from the silicon $\{1\,1\,1\}$ reflection of the substrate as it was already observed in the Q-maps of CuPc. The occurrence of this peak in Q-maps of different organic thin films measured at different beamlines makes clear that this peak neither stems from the organic thin film, nor from any parts of the beamline. Similarly to CuPc, this peak is not visible in all coronene Q-maps. It is strongest at 4 Å/min, weaker at 10 Å/min and not visible at 25 Å/min depending on the azimuthal orientation of the substrate.

The XRR and GIXD peaks can be assigned to the ubiquitous γ-polymorph, which was already found in 1944 [145, 147]. A few peaks cannot be explained by the γ-polymorph and indicate the coexistence of a second coronene polymorph. The positions of those peaks agree with the β-polymorph, which was recently found in 2016 [148]. Only the (1-12) peak is slightly shifted with respect to the expected position. As the study on polymorphism in CuPc thin films has already shown, small deviations of unit cell lengths and angles can occur depending on the chosen substrate. Neither the GIXD profiles of the γ-polymorph nor the GIXD profiles of the β-polymorph change significantly at different deposition rates, but comparing the relative peak intensities of γ- and β-polymorph reveals that the fraction of the β-polymorph increases at lower deposition rates. The β-(002) peak is smaller than the γ-(001) peak at 25 Å/min and becomes taller at 4 Å/min. The same applies to the β-(10-3) peak compared to the γ-(201) peak as well as to the β-(1-12) peak compared to the γ-(3-10) peak. To summarize, the less known β-structure of coronene grows preferentially at lower deposition rates, whereas the ubiquitous γ-structure prevails at higher deposition rates.
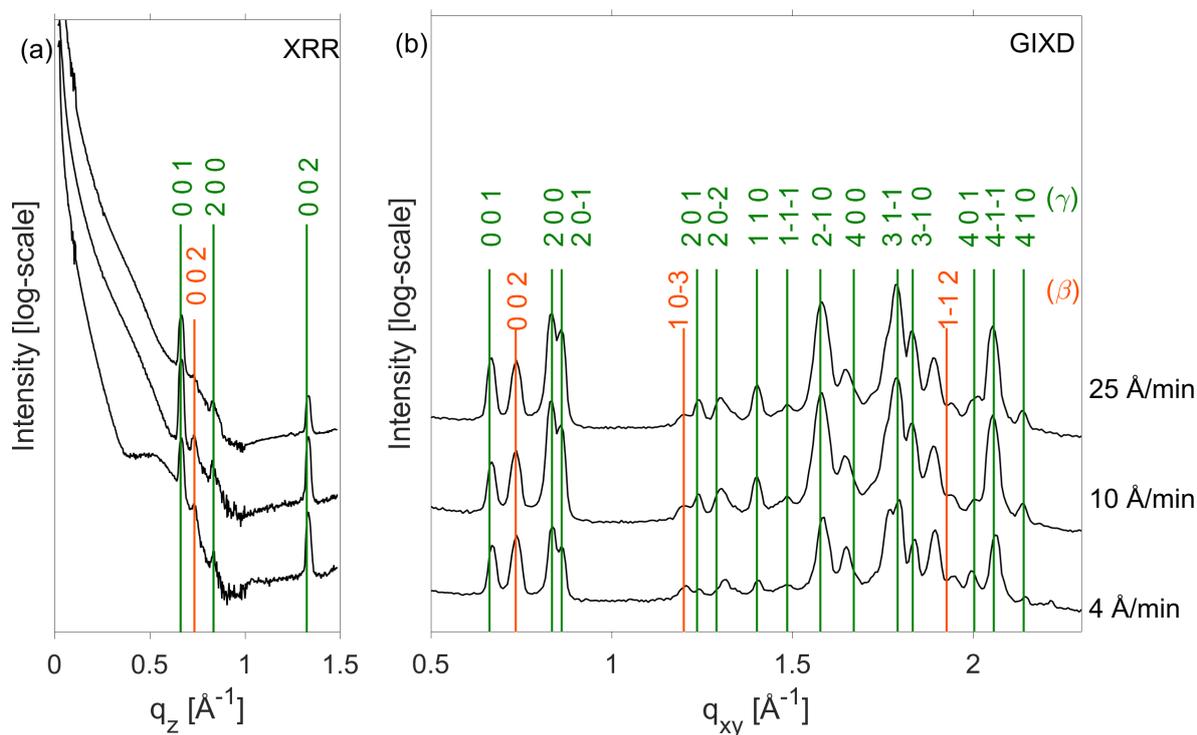
Figure 47: (a) XRR and (b) GIXD of coronene grown at 310 K and three different deposition rates: 4 Å/min, 10 Å/min and 25 Å/min.

The sizes of coherently scattering crystallites were estimated from the width of GIXD peaks, the width of the γ-(001) peak delivered 23–25 nm, the width of the β-(002) peak delivered to 21 nm and the width of the γ-(200) peak delivered 26–27 nm. The sizes are similar for all deposition rates. Regarding the several micrometer long needles in the real space images (see the next section) makes clear that each needle is polycrystalline, i.e. consists of many small crystallites of different orientations as it was also found for CuPc. Also stacking faults can reduce the size of coherently scattering domains. Note that the molecules are stacked along the short-b axis, but the crystallite sizes were measured along the a- and c-axis, i.e. along the (001) and (100) directions. The crystallites might be much larger along the b-axis, but a pure (0k0) peak did not appear in the X-ray diffraction patterns such that the determination of crystallite sizes along this direction is not possible from experimental data.
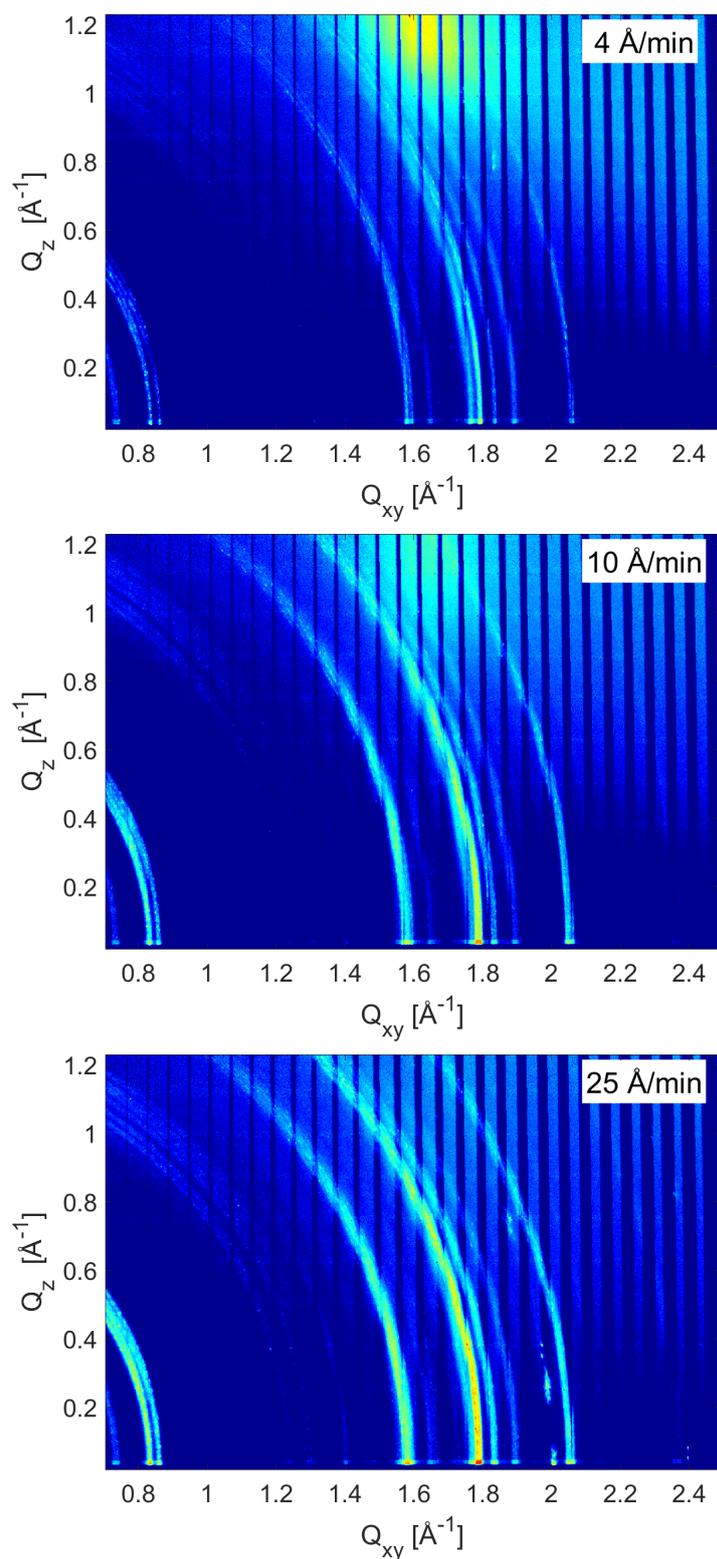
Figure 48: Reciprocal space maps of coronene thin films grown at 310 K and three different deposition rates: 4 Å/min, 10 Å/min and 25 Å/min.

5.2.3. Morphology

A $5\,\mu m \times 5\,\mu m$ AFM image of coronene grown at $25\,\text{Å/min}$ for $40\,\text{min}$ is shown in Fig. 49. Long needle-like crystals loom up and reach a length of 1–$2\,\mu m$ and a height of $1\,\mu m$. The 3D-profile on the right shows that these needles are randomly oriented in space. They point into all directions and have no alignment with the substrate, which was already concluded from the ring-shaped diffraction patterns in the Q-maps. Due to the notably large roughness, the acquisition of AFM images was quite challenging. Fortunately, the contrast in SEM images is excellent due to the high roughness and the islands are sufficiently large to be seen by light microscopy, see Fig. 50. Somehow, neither the size nor the density of the coronene needles changed at lower deposition rates. Dissimilar to the worm-like CuPc islands, coronene islands are rather rigid rods, not aligned with the substrate and by orders of magnitude larger than the CuPc islands. A strong π-π interaction between the benzene rings could account for this behavior. The influence of the longer duration of deposition at enhanced deposition rates cannot be completely excluded, but seems to be a rather minor effect regarding the SEM images of the $4\,\text{Å/min}$ coronene thin film, which is close to $2\,\text{Å/min}$ and exhibits still extremely large and randomly oriented needles.
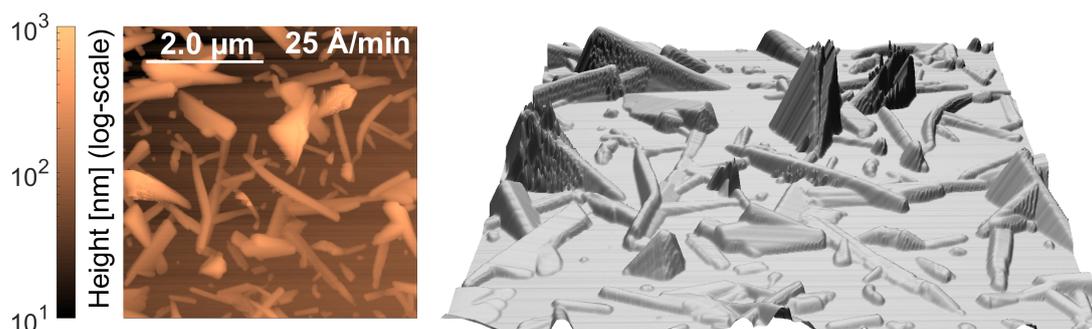

Figure 49: AFM image of the coronene thin film grown at $25\,\text{Å/min}$ left and the corresponding 3D-plot on the right.

5.2.4. Impact of Impurities

Finally, a peculiar finding suggests that there is a long range attraction between coronene molecules and the substrate. Figure 51 shows a little grain of $100\,\mu m$ length and $50\,\mu m$ width surrounded by coronene needles. This grain might be a piece of silicon that broke off from the edge of the silicon substrate, which can happen when picking up the specimen with a pair of tweezers. The SEM image on the right shows little needles on top of the grain indicating that it was already on the substrate before the growth has started. The light microscopic image on the left shows that the needles are visibly enlarged within a radius of approximately $50\,\mu m$ around this grain. Not only the size of the needles is enlarged but also their density is reduced.

**(a)** 4 Å/min   **(b)** 10 Å/min   **(c)** 25 Å/min
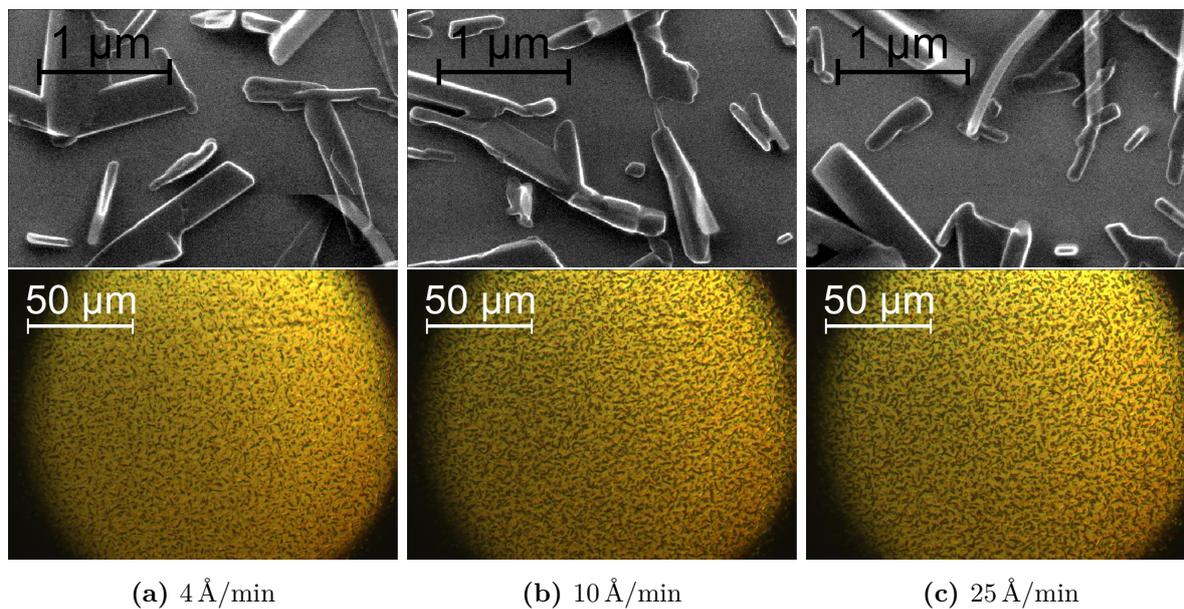
Figure 50: SEM images (top) and LM images (bottom) of coronene thin films grown at different deposition rate.
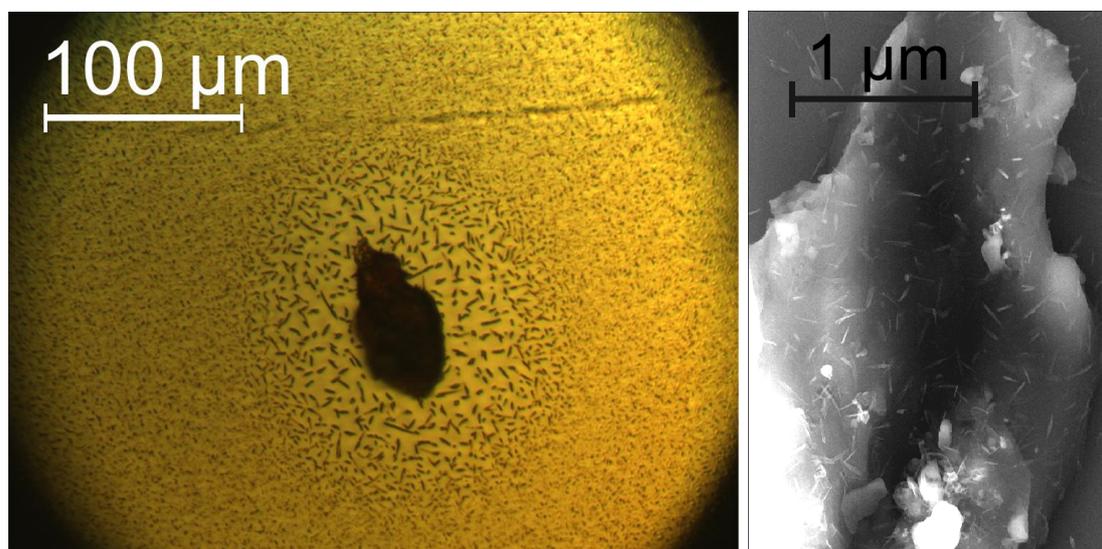

Figure 51: Left: LM image of the coronene thin film grown at 4 Å/min. Rigth: SEM image of the contamination.

5.2.5. Summary of Results

The similar shape of coronene and CuPc molecules lead to similar results as it was expected, but also differences emerged due to the different chemical structure. As it was already observed for CuPc, also coronene thin films exhibit polymorphism. Crystals of the γ- and the β-structure co-exist in vacuum deposited coronene thin films on native silicon oxide. The fraction of the recently found β-structure increases at lower deposition rates, whereas the well known γ-structure prevails at higher deposition rates. Regarding the morphology of coronene thin films, long needle-like crystals appear on native silicon oxide. The crystals are randomly oriented and exhibit no alignment with the substrate. Strong π-π-interactions between the benzene rings could be the reason for the formation of these straight and rigid needles. The size and density of coronene needles is independent from the deposition rate.

Finally, an interesting and unexpected effect was found in the surrounding of a grain, presumably silicon that broke off from the edge of the substrate. In the vicinity of this grain, the coronene crystals grew much larger at a lower density, which clearly indicates a long-range interaction between the grain and the molecules. The influence of the grain got lost after a certain distance. This finding opens up further possibilities for the investigation of intermolecular long-range interactions. As an outlook on possible future experiments, nano-particles of different sizes and chemical compositions could be deposited on a native silicon oxide substrate and their influence on the growth of small organic molecule clusters could be observed, in particular their radius of impact.

5.3. Pure C_{60} Thin Films

5.3.1. Preparation and Measurements

Buckminster fullerene molecules (C_{60}) were bought from Sigma Aldrich (purity 99.9 % by gradient sublimation). The molecules were filled into a ceramic crucible of a Knudsen effusion cell for thermal evaporation and the effusion cell was attached to a vacuum chamber for molecular beam deposition [152]. Silicon wafers of 575 μm thickness with a native oxide layer of 2 nm were cut into small pieces (5×10 mm^2) and cleaned with aceton and isoproponal in an ultrasonic bath for 5 min each. After installing the substrates inside the vacuum chamber, the chamber was pumped down and the substrates were heated up to 500 K and kept at this temperature for 10 hours in oder to evaporated condensed water. While the effusion cell was heated up to the evaporation temperature of C_{60}, the substrate was cooled down to the desired temperatures of 310 K, 340 K, 370 K, and 400 K, respectively. The base pressure of the vacuum chamber reached $3 \cdot 10^{-8}$ mbar, which was maintained during the entire deposition. A quartz crystal micro-balance was used in order to monitor the amount of deposited material and a rate calibration employing X-ray reflectivity for thickness determination was carried out in advance.

The influence of three different growth parameters (substrate temperature T_{sub}, deposition rate R_{dep} and amount of deposited material) on the roughness, island densities and islands sizes was investigated. One parameter was systematically varied while the other two parameters were kept constant. First, C_{60} molecules were deposited at four different substrate temperatures (310 K, 340 K, 370 K and 400 K) and a constant deposition rate of 2 Å/min for the duration of 7:00 min each. Additionally, two C_{60} thin films were grown at 400 K and two different deposition rates, 1 Å/min for 14:00 minutes and 4 Å/min for 3:30 minutes. The duration of deposition was adapted to the deposition rates such that the total amount of deposited material was always the same. Finally, another set of samples was prepared at 400 K and 2 Å/min for 3:45 min, 7:30 min and 11:15 min in order to investigate how the amount of deposited material influences the morphology.

After the growth, the substrate heating was stopped and the substrates were kept in vacuum until they reached room temperature, which took between 2 and 4 hours depending on the initial temperature. Finally, the vacuum pumps were stopped and the chamber was vented. The specimens were taken out and 3 $\mu m \times 3 \mu m$ AFM images were acquired in intermittent contact mode in air at a resolution of 512×512 pixels using a JPK Nanowizard II instrument. The resulting lateral resolution thus amounts to 5.86 nm per pixel, which is in the range of the average AFM tip radius of approximately 6 nm. Roughness, island densities and island sizes, both laterally and vertically, were determined from the AFM images as described in Sec. 4.

For the comparison to CuPc, two further C_{60} thin films were grown in a portable vacuum chamber [152] under the same conditions as the CuPc thin films, i.e. at 310 K and at 400 K at a deposition rate of 2 Å/min for 100 minutes each. *In-situ* XRR and GIXD data sets were acquired directly after the growth at the material science beamline MS-X04 SA of the Swiss Light Source and Q-maps were measured *ex situ* at the ID03 beamline of the ESRF. The experimental setup was the same as for CuPc, see Sec. 5.1, i.e. an X-ray energy of 12.7 keV corresponding to a wavelength of 0.976 Å and grazing angle of incidence of $0.120°$ $(0.027\,\text{Å}^{-1})$, which was close to the total reflection edge of silicon and probed the thin film throughout the entire film thickness.

5.3.2. Crystal Structure and Unit Cell Orientation

Figure 52 shows XRR and GIXD profiles of C60 grown at two different substrate temperatures (310 K and 400 K) at a deposition rate of 2 Å/min for 100 min. The profiles were measured *in situ* directly after the growth. The peak positions correspond to the reported fcc structure (face centerd cubic, see Ref. [122]). There is a shoulder at the left side of the {111} GIXD peak in the 400 K profile, which was assigned to the hcp structure of C_{60} (hexagonal close packed, see Ref. [124]), which is adopted by a small fraction of C_{60}-crystallites [168]. Regarding the XRR profiles of C_{60}, no Bragg peaks appear, which portends to the conclusion that there is no vertical layer ordering. Regarding the GIXD patterns, this presumption is corroborated. Peaks of all crystallographic directions appear and indicate that the C_{60} crystallites are randomly oriented into all directions in 3D-space. All peaks, whose Miller indices refer to an entire family of crystallographic directions, were labeled in curled brackets.
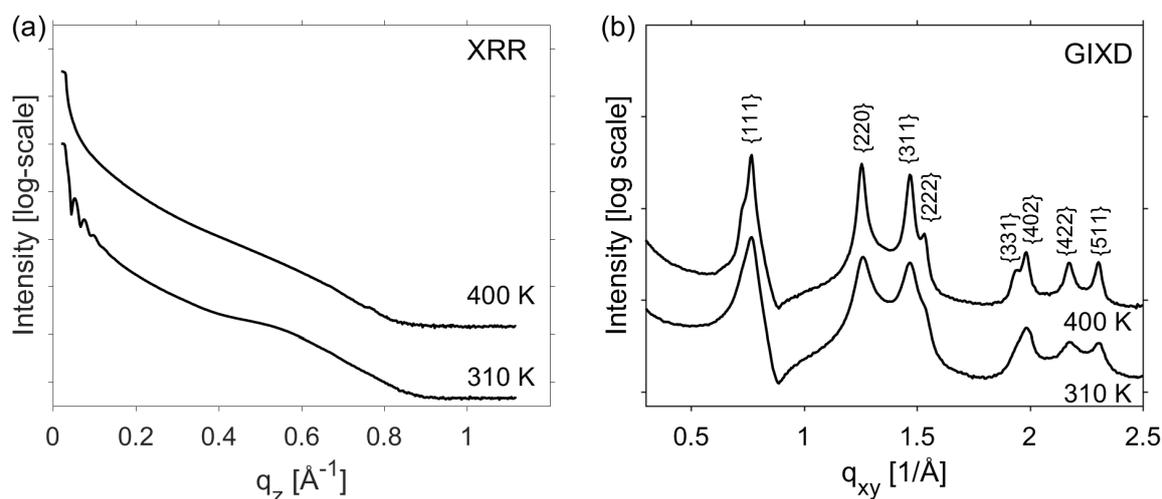

Figure 52: (a) *In-situ* XRR and (b) *in-situ* GIXD of C_{60} grown at a deposition rate of 2 Å/min for 100 min at two different substrate temperatures (310 K and 400 K).

Figure 53 shows the reciprocal space map of C_{60} grown at 400 K. The concentric rings confirm the random orientation of crystallites. The intensities are homogeneously distributed along the rings and indicate that there is no preferential orientation. The Q-map of C_{60} grown at 310 K was acquired as well but is not shown here since no features appeared. The signal-to-noise ratio was probably too low due to the smaller size of crystallites, which will be discussed in the next section. According to the Q-maps of CuPc and coronene, the silicon $\{111\}$ peak appeared as well in the Q-map of C_{60}.
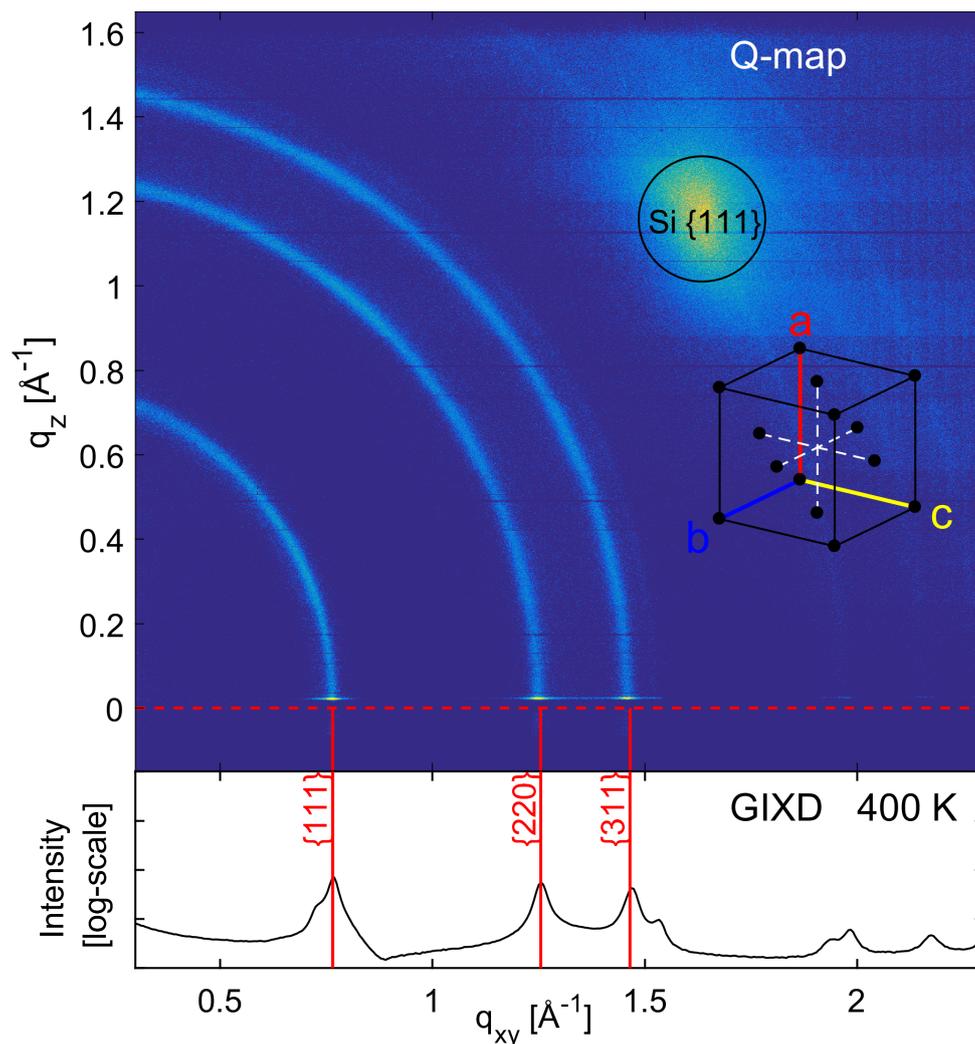
Figure 53: Q-map of 20 nm C_{60} grown on native silicon oxide at 2 Å/min and 400 K. The corresponding unit cell (fcc-structure, a = 14.0 Å, Ref. [122]) is shown on the right side. Black dots mark the positions at which the molecules have to be placed in consideration of the space group symmetries. The corresponding GIXD pattern is shown below.

5.3.3. Morphology

Figure 54 shows $3\,\mu m \times 3\,\mu m$ AFM images of C_{60} grown at two substrate temperatures (310 K and 400 K) at a deposition rate of $2\,\text{Å/min}$ for 100 min. The islands were counted as described in Sec. 4.3 and the island density ρ was calculated by dividing the number of islands by the area of the AFM image. The average size of coherently scattering domains d_{coh} was determined from the width of the $\{111\}$ GIXD peak and amounts to 13 nm at 310 K and 22 nm at 400 K. Furthermore, the root mean square roughness σ_{RMS} was determined from the Kiessig oscillations in XRR as well as from the distribution of heights in the AFM images. Table 5 compiles the sizes of coherently scattering domains d_{coh} determined from GIXD, the island densities ρ determined from AFM images and σ_{RMS} determined from both XRR and AFM. The data reveals that increasing the substrate temperature during growth has two effects: Similar to CuPc, the islands become larger and the island density decrease at 400 K, although the C_{60} domain sizes are generally smaller than the ones of CuPc at both substrate temperatures. The second reaction of C_{60} upon heating of the substrate during growth is that σ_{RMS} increases, which is in contrast to CuPc films, whose roughness decreases upon heating. It was reported that C_{60} molecules react to substrate heating by island formation resulting from a temperature driven upward diffusion of molecules [142], which explains the enhanced roughness at 400 K. Note that the XRR roughness at 400 K is not available due to the missing Kiessig oscillations. Instead a lower limit of 2.9 nm was estimated, which is the highest roughness of 20 nm thin films at which Kiessig oscillations are still visible.
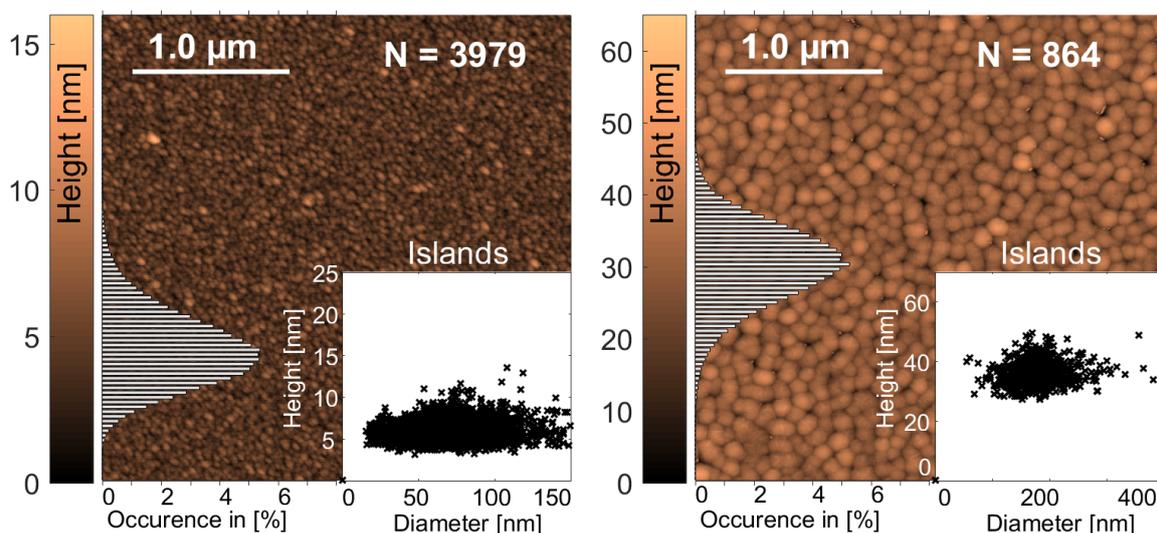

Figure 54: $3\,\mu m \times 3\,\mu m$ AFM images of 20 nm thin C_{60} films grown at $2\,\text{Å/min}$ for 100 min at two different substrate temperatures, 310 K (left) and 400 K (right). The distributions of heights are shown as histograms on the left side of each image together with the color bar. The total number N of counted islands is given in the upper right corner. Heights and diameters of all islands are plotted in the lower right inset. Each data point corresponds to one of the islands.

T_{Sub}	310 K	400 K
d_{coh}	13 nm	22 nm
ρ	442 μm^{-2}	96 μm^{-2}
σ_{RMS}, XRR	2.3 nm	> 2.9 nm
σ_{RMS}, AFM	1.3 nm	5.5 nm

Table 5: Resulting sizes of coherently scattering domains d_{coh} from GIXD, island densities ρ from AFM and root mean square roughness σ_{RMS} from both XRR and AFM of C_{60} thin films grown at two different substrate temperatures (T_{sub}) at a deposition rate of $R_{dep} = 2.0$ Å/min for 100 min

Last but not least, the shape of C_{60} islands should be discussed. From a top view, those islands look like truncated spheres as they are known from condensed liquid droplets on cold surfaces, see Sec. 1.3. It makes sense that the nearly isotropic particles exhibit no preferred growth direction and form round islands. In cross sectional side view, the shape of a parabola curve fits better to the C_{60} islands than truncated spheres, see Fig. 38 in Sec. 4.3. A convolution with the tip shape can be excluded as reason since the islands are sufficiently flat (contact angles $<< 45°$), see Sec. 3.3.1. Considering that C_{60} is rather crystalline than liquid at temperatures between 310 K and 400 K may explain the deviation from the spherical shape and the compact shape of islands is rather a result of shape relaxation by edge diffusion, see Sec. 1.3

5.3.4. Layer Coverages

Similar to CuPc, the layer coverages of C_{60} grown at 310 K and 400 K and a deposition rate of 2 Å/min for 100 min were determined from the AFM images and compared to a simulated random deposition without any kind of diffusion or molecular interactions. Layer coverages from XRR are not available due to the missing Kiessig oscillations. A layer thickness ≈ 0.8 nm corresponding to the monolayer spacing of C_{60} in {111} direction was assumed. 25 completely filled layers are required in order to reach the target film thickness of 20 nm (i.e. 2 Å/min × 100 min). As already discussed for CuPc, missing material in the layers below the average height of 25 layers adds up to the layers beyond 25 for mass conservation. The comparison of experimental and simulated data shows that a downward diffusion of molecules occurred at 310 K, but the molecules tend to diffuse upward at 400 K, though the upward diffusion at 400 K is less pronounced than the downward diffusion. The last finding is in great contrast to CuPc. While the downward diffusion of CuPc molecules is accelerated by elevating the substrate temperature, C_{60} molecules exhibit the opposite behavior. The different reactions of CuPc and C60 upon heated substrates during growth could be explained by the molecular shape and the crystal structure. The planar CuPc molecules tend to grow in rows along the substrate and enhanced substrate temperatures lead to a faster growth along the preferred crystallograpic direction, i.e. along the substrate surface, which makes the film smoother and requires a molecular downward diffusion. In contrast to this, the shape of C60 molecules is almost isotropic and no crystallographic growth direction is preferred.

Figure 55:

Experimentally determined layer coverages from *ex-situ* AFM images of C_{60} thin films grown at two different substrate temperatures at a deposition rate of 2 Å/min for 100 min and comparison to a simulated layer coverage resulting from random deposition without diffusion or any kind of molecular interactions.
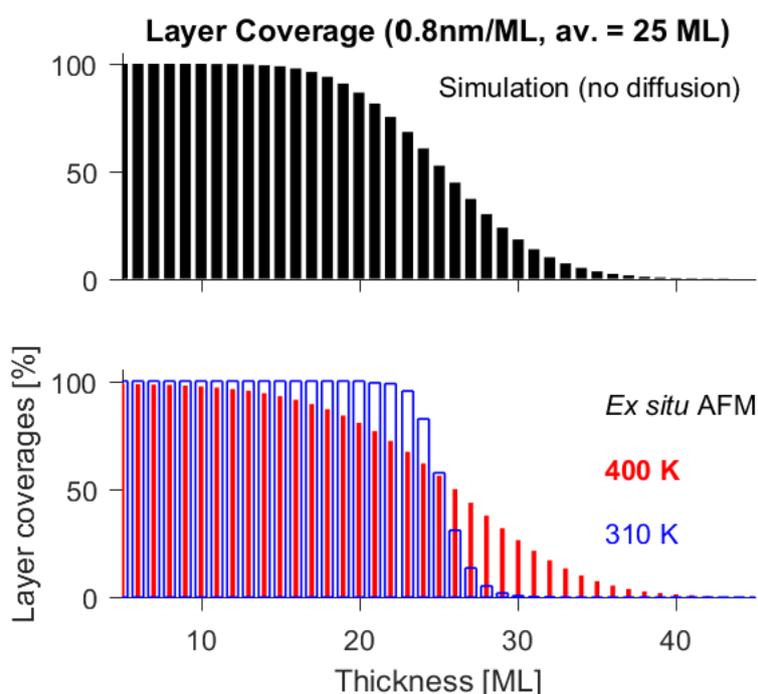
5.3.5. Island Sizes

A special part of this thesis is the automated evaluation of AFM images. The islands were automatically detected, counted and their cross sectional shape was fitted by a parabola curve as described in Sec. 4.3. Height and base diameter of each island were extracted and shown in the insets of Fig. 54. Note that islands whose diameter is smaller than 15 nm could not be detected since their area covers less than 3×3 pixels. At 310 K, the diameters range from 15 nm up to 150 nm and the heights from 5 nm to 10 nm. At 400 K, the diameters range between 50 nm and 400 nm and the heights are on average 35.7±3.8 nm. This shows that not only the size d_{coh} of coherently scattering domains but also the size of islands increase upon heating during growth. Nevertheless, the islands are much larger than d_{coh}, which means that each islands consists of several crystallites of various orientations. This could be a hint that entire clusters diffuse on the substrate and aggregate to larger islands, see Sec. 1.3, or stacking faults may lead to a lower d_{coh}. Furthermore, a transition from a complete coverage of the substrate to de-wetting can be observed. While the height of islands at 310 K is lower than the average film height of 20 nm and the lowest measured data point is certainly not the substrate level, the islands exceed the 20 nm at 400 K and the gaps between the islands in Fig. 54 go down to the substrate level. The high island density at 310 K entails on merging islands at a very early stage of growth and hence on a completely covered substrate, whereas the low island density at 400 K leaves some gaps between the islands.

Owing to the success of the automated AFM evaluations, more C_{60} thin films were systematically grown under various conditions. $3 \, \mu m \times 3 \, \mu m$ AFM images were acquired, evaluated and compared. First, the films grown at different substrate temperatures are compared. The deposition rate of $2 \, \text{Å/min}$ and the duration of deposition of 7 minutes was kept constant for all samples. Figure 56 shows island densities, average heights and diameters of the islands as a function of the substrate temperature. The error bars refer to the standard deviation and represent to which degree heights and diameters scatter around the average value. The error bars of the island densities were calculated by $\sqrt{N}$ and refer to the Poisson distribution of counted numbers. Due to the large number N of islands in each image, those error bars are so small that they cannot be seen in the plot, but their values are indicated as numbers below each data point. Bear in mind that the plots display island densities in terms of islands per square micrometer, but each image has $3 \times 3 = 9 \, \mu m^2$, which is the reason for the low error and demonstrates the high precision of the results. Also the horizontal error bars referring to a deviation of $\Delta T_{sub} = \pm 0.1°$ are so small that they cannot be seen in the plots. Below the visualization of statistical data, the underlying AFM images and the corresponding distributions of island heights and diameters are shown. Enlarged AFM images of all samples can be found in Appx. I.
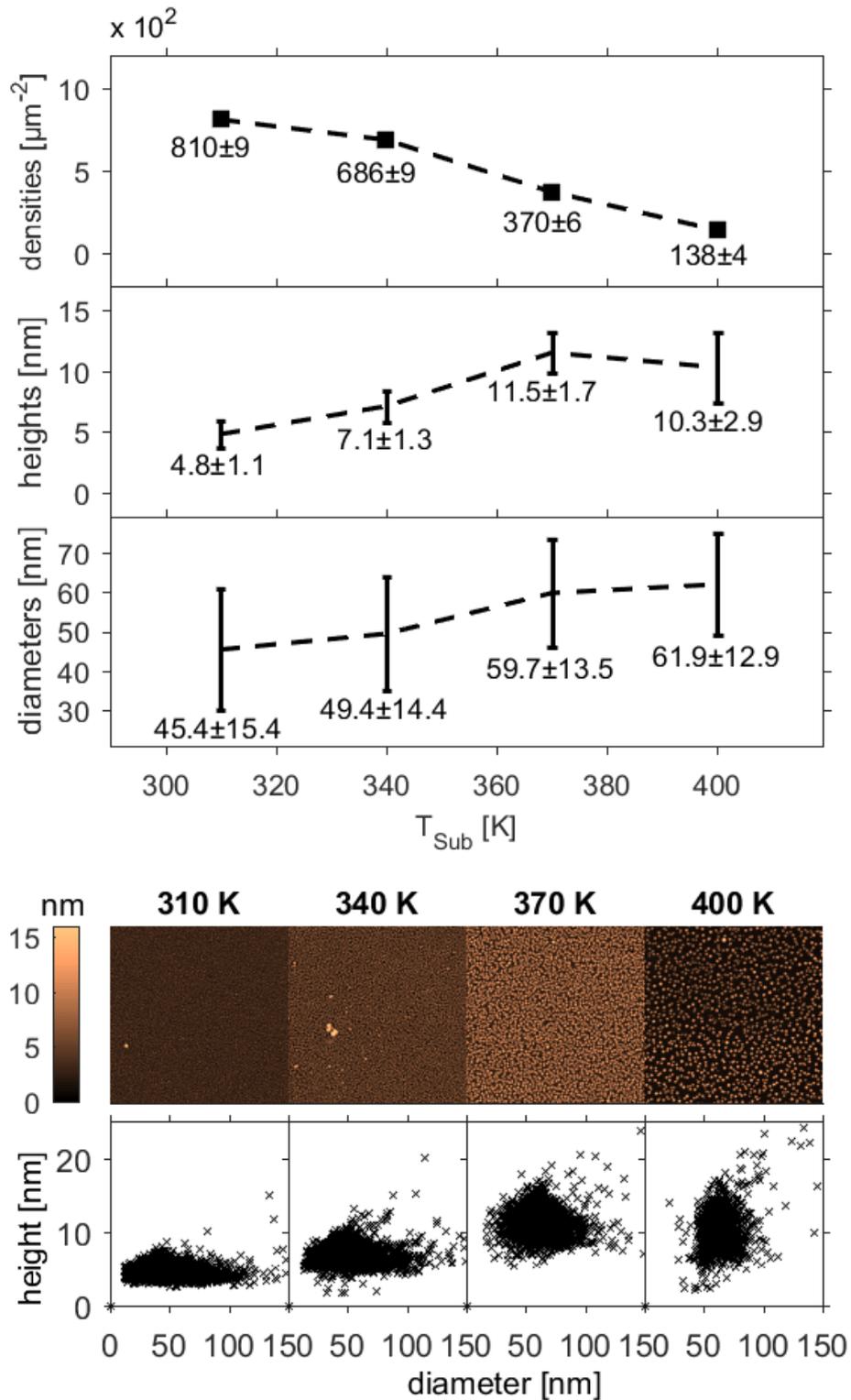
Figure 56: Influence of Substrate Temperatures:

C_{60} thin films grown at $2\,\text{Å/min}$ for $7\,\text{min}$ each at four different substrate temperatures ($310\,\text{K}$, $340\,\text{K}$, $370\,\text{K}$ and $400\,\text{K}$).

Concerning the results found from Fig. 56, we see a continuous decrease of island densities with increasing substrate temperature. At the same time, the islands are getting taller and laterally larger, which can be seen from the increasing heights and diameters. Interestingly, this effect saturates at 370 K. While the increase of diameters almost stops, the average height reaches its maximum at 370 K and starts to decrease at 400 K. Nevertheless, the standard deviation of heights increases continuously, whereas the standard deviation of diameters exhibits a continuous decrease. Note that the islands are generally flat since their diameters are much larger than their heights. The average diameter ranges from 45 nm to 62 nm, but the average height ranges solely from 4.8 nm to 11.5 nm. So, the diameter-to-height ratio is approximately 10 at 310 K and 5 at 400 K. From 310 K to 400 K, the diameters increase only by $1/3$ but the heights are more than doubled. This observation can be regarded as a result of the temperature driven upward diffusion of C60 molecules.

Figure 57 shows samples grown at different deposition rates. The duration of deposition was adapted to the deposition rate such that the same amount of material was deposited in each sample and the substrate temperature was kept constantly at 400 K. Reducing the deposition rate from 2 Å/min to 1 Å/min, has a quite strong influence on the thin film morphology. The island density drops by a factor of 10 and the average diameter increases by almost 40%. At the same time, the average height decreases by 39%. Certainly, the molecules do not diffuse faster at lower deposition rates, but they have more time for diffusion before the next particles impinge within their vicinity, which reduces the nucleation rate. In other words, the probability that a critical number $i^* + 1$ of particles meet and form a stable cluster decreases, see Sec. 1.3. Consequently, the nucleation of a second layer on top of a grown layer is less likely and the islands become flatter. The same applies to the diffusion on the substrate surface. The molecules cover a larger distance until they meet a cluster of critical size i^* and aggregate. Hence, the Voronoi cells of growing clusters (see Sec. 1.3) become larger and gather more particles from their environment such that the island diameters can grow up to considerable sizes.

The impact of an increased deposition rate of 4 Å/min turned out to be much smaller, which could come from an unknown saturation effect. One would expect a larger nucleation density at higher deposition rates. The diffusion and aggregation of entire clusters may counteract. Extremely small islands, very close to each other, could diffuse, merge and reduce the number of islands such that there is an upper limit for the island density. Although, those considerations seem to be plausible, this data set has to be interpreted carefully due to the large uncertainty of the actual deposition rates. A wrong assessment of the deposition rate and associated with this, a wrong choice for the duration of deposition would lead to a different amount of deposited material. For this reason, also the impact of the amount of deposited material on the morphology was investigated by changing the duration of deposition at constant rates and substrate temperatures.
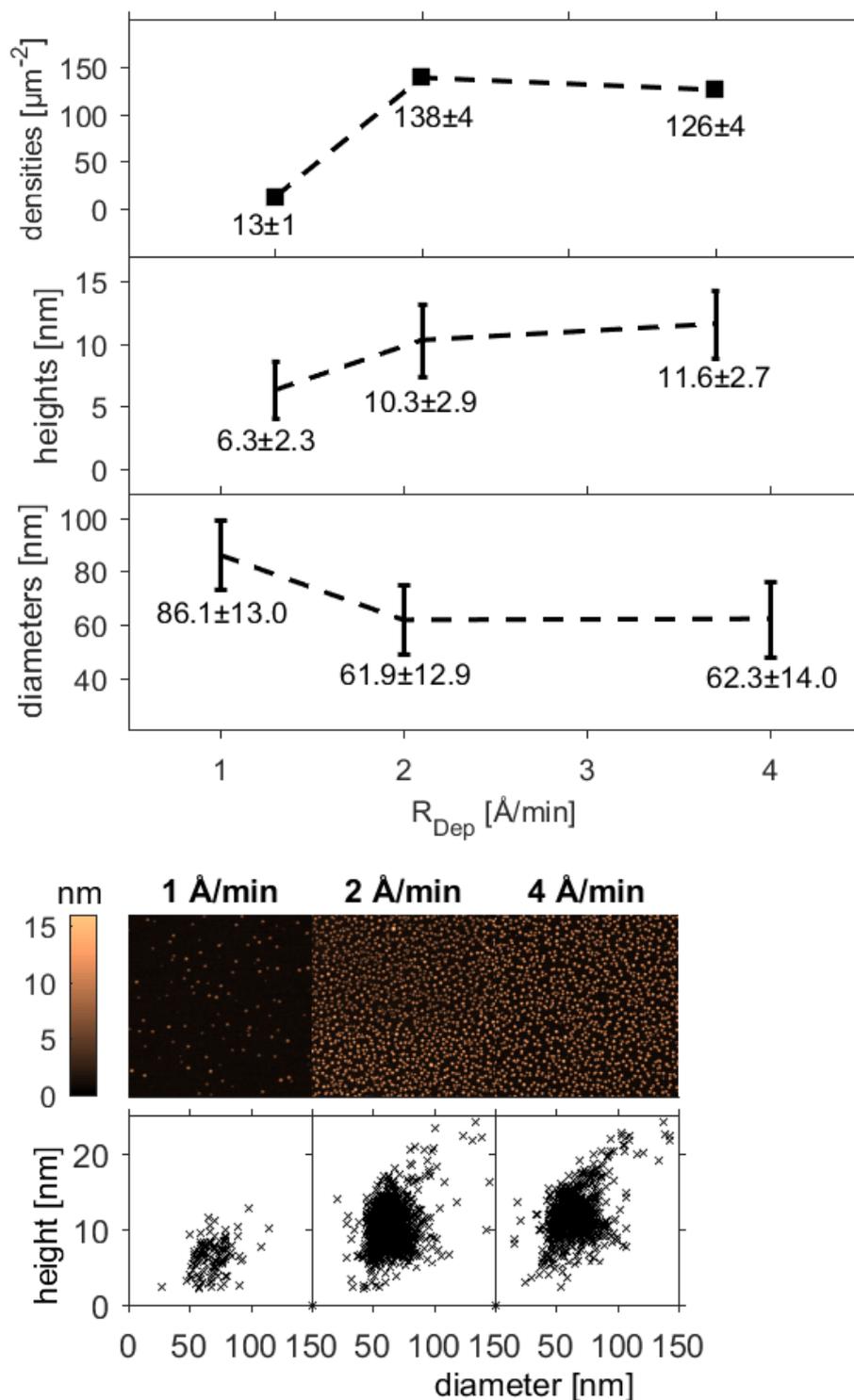
Figure 57: Influence of Deposition Rates:

C_{60} thin films grown at $T_{sub} = 400\,\mathrm{K}$ each and $1\,\text{Å/min}$ for $14{:}00\,\mathrm{min}$, $2\,\text{Å/min}$ for $7{:}00\,\mathrm{min}$ and $4\,\text{Å/min}$ for $3{:}00\,\mathrm{min}$.

Figure 58 compares the statistics of samples grown at the same deposition rate of 2 Å/min and the same substrate temperature of 400 K. The amount of deposited material was varied by changing the duration of deposition from 3:45 min up to 100 min. The data sets indicate a clear tendency towards lower island densities and larger heights and diameters. The decreasing island density is a result of merging islands, either by lateral growth until neighboring islands touch each other or by cluster diffusion and cluster-cluster aggregation, see Sec. 1.3. The larger heights and diameters are probably due to the increased amount of material. The right side of Fig. 58 shows that this effect is stronger at 400 K than at 310 K, but the island density does not change as much during the growth at 400 K as it does at 310 K since it is already low at the beginning of growth. Enlarged AFM images of the corresponding samples are shown in Appx. I.
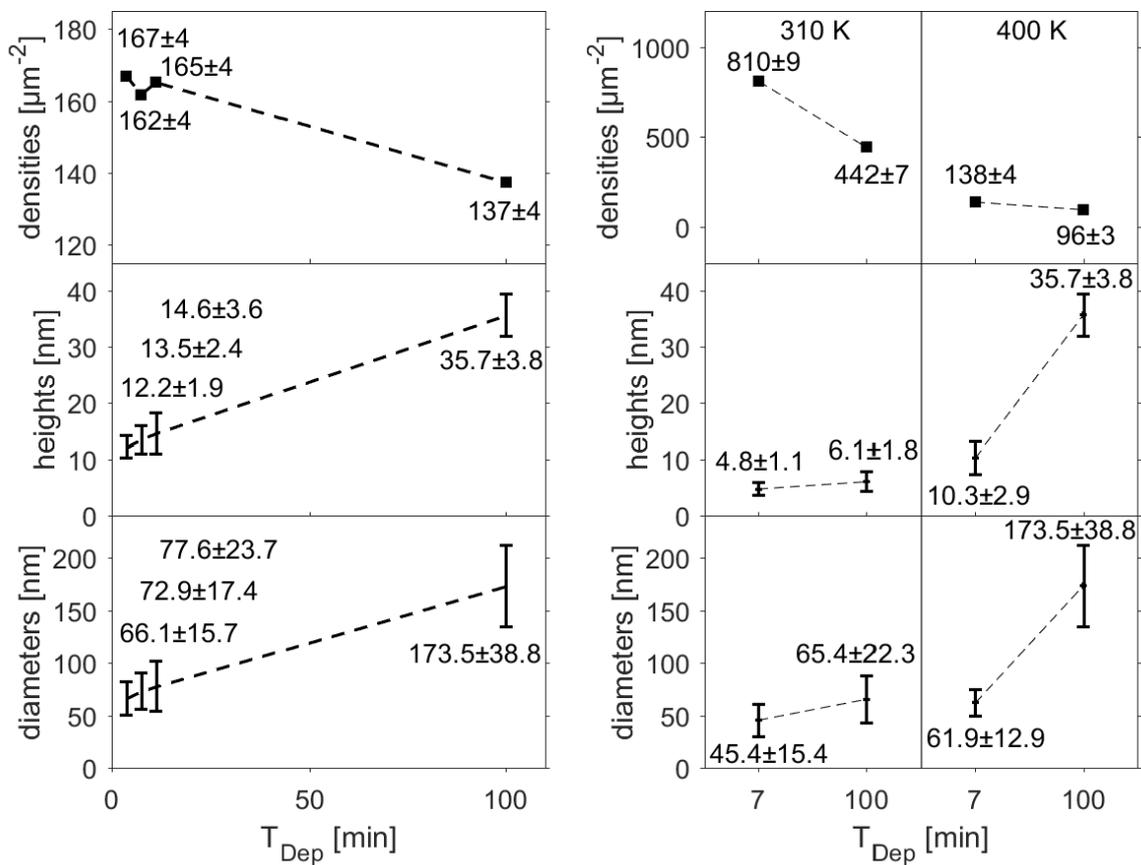
Figure 58:

Left: Different Amounts of Deposited Material at $T_{sub} = 400\,K$:

C_{60} thin films grown at 2 Å/min for 3:45 min, 7:30 min, 11:15 min. and 100 min.

Right:Different Amounts of Deposited Material at $T_{sub} = 310\,K$ and $T_{sub} = 400\,K$:

C_{60} thin films grown at 2 Å/min for 7:00 min and 100 min at 310 K and 400 K.

5.3.6. Summary of Results

A comprehensive picture of C60 growth on native silicon oxide was gained by means of X-ray diffraction experiments and extensive AFM image evaluations. The influence of substrate temperature T_{Sub}, deposition rate R_{Dep} and the amount of deposited material on the surface roughness σ_{RMS}, the domain sizes d_{coh} and the island density ρ was investigated in detail.

Similar to CuPc and many other small organic molecules, d_{coh} increases while ρ decreases upon heating of the substrate during growth. The faster diffusion at elevated T_{sub} is likely the reason for the formation of larger islands. A similar effect was obtained by reducing R_{Dep}, but in this case the islands became flatter. In both cases, the flux-to-diffusion ratio F/D is reduced either by increasing T_{Sub} or by reducing R_{Dep}, such that the molecules have more time for diffusion before the next particles impinge within their vicinity, which reduces the nucleation density and leads to less and larger islands. Variations of the amount of deposited material by varying the duration of deposition revealed that the island densities decrease during the growth, which is mediated by coalescence of neighboring islands. At higher substrate temperatures the island density is already low at the beginning of growth and coalescence plays a minor role. Instead the increase of island heights and diameters is more pronounced.

Despite the similarities concerning d_{coh} and ρ, the growth of C$_{60}$ on native silicon oxide behaves contrary to CuPc in many ways. C$_{60}$ molecules are almost isotropic and no special growth direction is preferred. C$_{60}$ crystallites are not aligned with the substrate and the island shape is rather compact than elongated. It is not surprising that this has an impact on the surface roughness. In contrast to CuPc, thin films of C$_{60}$ are getting rougher upon heating of the substrate. The spherical shape of C$_{60}$ and the fcc crystal structure make an upward diffusion more favorable than the highly anisotropic growth of CuPc along the substrate.

6. Results and Discussion of Blended Thin Films

6.1. Preparation and Measurements

Pure and blended $CuPc$-C_{60} thin films were grown in a portable vacuum chamber equipped for *in-situ* XRD experiments during OMBD [152]. All films were prepared at two different substrate temperatures (310 K and 400 K) and at a deposition rate of $2\,\text{Å/min}$ for 100 min leading to an average film thickness of 20 nm. The preparation of blended thin films was carried out by simultaneous evaporation of $CuPc$ and C_{60} from two different effusion cells. The evaporation temperatures of the single effusion cells were calibrated in advance and set such that the total deposition rate was $r_{\text{tot}} = r_{\text{CuPc}} + r_{\text{C60}} = 2\,\text{Å/min}$. $CuPc$ was evaporated at a rate of $0.9\,\text{Å/min}$ and C_{60} at a rate of $1.1\,\text{Å/min}$ in order to obtain a molar ratio of 1:1 according to the volume per molecule: $V(CuPc) = 582\,\text{Å}^3$ and $V(C_{60}) = 692\,\text{Å}^3$. [99, 122]

In-situ XRR measurements were carried out in real-time during the growth at the material science beamline MS-X04 SA of the Swiss Light Source (beam energy: 12.7 keV) followed by *in-situ* XRR and GIXD measurements directly after the growth. GIXD was carried out at a grazing angle of incidence close to the total reflection edge of the silicon substrate. Some of the *in-situ* real-time experiments were repeated during a second beamtime at the same beamline (beam energy: 13.7 keV). The results of both beamtimes agree, but the growth rates and the flux of photons were more stable during the second beamtime, which was more favorable for the data evaluation.

Another set of samples was prepared under the same conditions for *ex-situ* measurement. AFM and SEM images were acquired *ex situ* several days after the growth. $3\,\mu m \times 3\,\mu m$ AFM images were measured using a JPK Nanowizard II instrument operating in tapping mode under ambient conditions. The data was complemented by SEM images at different magnifications using an XL30-device from Philips at an acceleration voltage of 20 kV. Furthermore, post-growth Q-maps as well as post-growth GIXD profiles of this second set of samples were measured *ex situ* at the ID03 beamline of the ESRF (beam energy: 24.0 keV). The grazing angle of incidence for GIXD and reciprocal space mapping was this time at half of the total reflection edge of the silicon substrate, which leads to a more surface sensitive measurement. The experimental results of the pure films were already discussed within the last sections. The corresponding data sets are replotted in this section for comparison.

6.2. Post-Growth X-ray Diffraction Experiments

This section gives insight into the phase separation and the structure formation in CuPc:C_{60} blends. The presence of both CuPc and C_{60} peaks in the GIXD profiles indicates that the molecules prefer phase separation although the large peak widths portend to the formation of very small crystallites whose diameter amounts to only 4 nm. The missing Bragg peaks in the XRR-profiles indicate that neither CuPc nor C_{60} exhibit vertical ordering in blends, which was corroborated by the needle-like CuPc-crystals found in AFM and SEM images. Concerning the crystal structure, there is no indication that new crystal structures such as for instance a 1:1-complex are present. Finally, the roughness strongly depends on the substrate temperature and its formation was followed in real-time during the growth. The corresponding explanation turned out to be challenging. Nevertheless, possible explanations are given in this section. All results were quantified, compared and discussed in Sec. 6.5. Section 6.6 presents further experiments on CuPc:C60 blends serving as an outlook for future studies.

6.2.1. Post-Growth XRR and GIXD

Figure 59 shows the post-growth XRR and GIXD scans of pure and blended CuPc-C_{60} thin films after transformation into q_z- and q_{xy}-space, respectively. The profiles of the pure films are replotted from the last sections for comparison to the 1:1-blends. For a detailed discussion of the pure films see Sec. 5.1 and Sec. 5.3.

Roughness: The numerous pronounced Kiessig oscillations in the XRR profile of the blended film grown at 310 K indicates that this film is the smoothest of all. A completely different behavior is observed at 400 K. The blended film grown at 400 K is extraordinarily rough such that no Kiessig oscillations are visible.

Crystal orientations: None of the two blended thin films exhibits vertical ordering, which can be seen from the missing Bragg peaks in their XRR profiles. The absence of XRR peaks indicates that the CuPc crystallites are no longer aligned with the substrate, as it was the case in pure CuPc thin films on silicon oxide. AFM and SEM images corroborate this result. They show needle-like CuPc crystallites protruding from the blended thin films and pointing into all directions in 3D-space. The C_{60} crystallites remain randomly oriented in co-evaporated blends. Prior studies show that C60 exhibits vertical ordering when deposited on top of a pentacene single crystal [169], but no vertical ordering was found on native silicon oxide or in co-deposited blends.

Mixing behavior: The GIXD profiles indicate that CuPc and C_{60} prefer de-mixing since Bragg peaks of both CuPc and C_{60} appear in the GIXD profiles of the blends. C_{60} is known to de-mix during co-deposition with other small organic molecules [43] such as sexithiophene (6T) [170, 171], diindenoperylene (DIP) [172, 173], and pentacene (PEN) [174], but the enormous widths of the GIXD Bragg peaks portend to the formation of very small crystallites. The size of coherently scattering domains goes down to 4 nm in the blends, which was referred to as nano-crystalline [175].

Crystal Structure: A new crystal structure cannot be found in blended $CuPc:C60$ thin films. No new Bragg peaks appear and the existence of a 1:1-complex can be excluded. Many of the results such as the missing vertical ordering and the temperature dependent roughness behavior become clearer when regarding the real space images in Sec. 6.3.
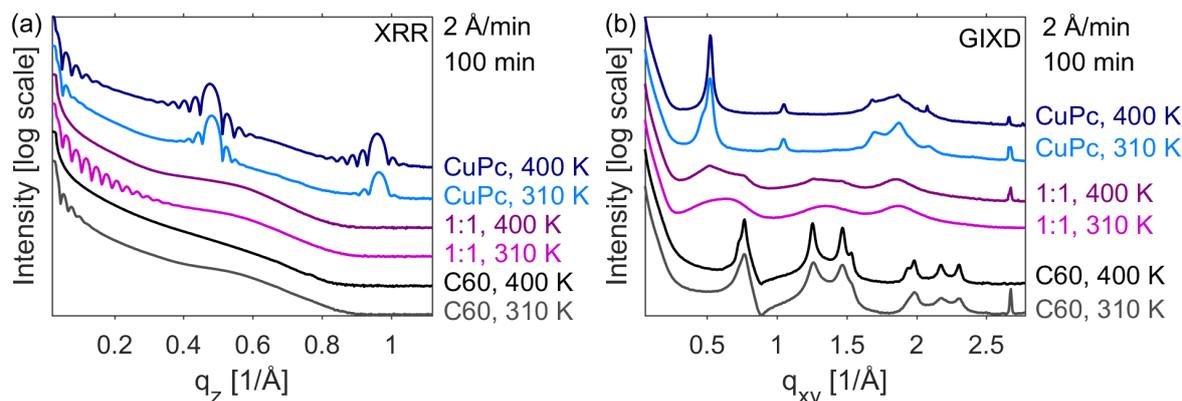

Figure 59: (a) Post-growth XRR and (b) post-growth GIXD of CuPc, C_{60} and 1:1-blends grown at a deposition rate of $2\,\text{Å/min}$ for $100\,\text{min}$ at two different substrate temperatures ($310\,\text{K}$ and $400\,\text{K}$). The measurements were carried out *in situ* directly after the growth at a beam energy of $12.7\,\text{keV}$. The grazing angle of incidence was close to the total reflection edge of silicon.

6.2.2. Post-Growth Q-Map

Figure 60 shows the Q-map of the $CuPc:C_{60}$ blend grown at $400\,\text{K}$ and below the corresponding GIXD measurements for comparison. Not much can be seen from the Q-map. Only a weak ring stemming from the CuPc (00 ± 1)-reflection appears. Two orientations predominate, which can be inferred from the inhomogeneous distribution of intensities around the ring. The intensities are strongest at $q_{xy} = 0\,\text{Å}^{-1}$ and at $q_z = 0\,\text{Å}^{-1}$, which means that the unit cell can rotate around the b-axis such that one of the unit cell faces, either the a-b-plane or the b-c-plane, is preferentially oriented parallel to the substrate surface. This behavior has already been observed in the pure CuPc film grown at $310\,\text{K}$ and was discussed in Sec. 5.1. Only in the pure CuPc-film grown at $400\,\text{K}$, the second orientation with the b-c-plane parallel to the substrate does not occur. In summary it may be said that lower substrate temperatures or the presence of another molecule such as C_{60} are responsible for the partial unit cell rotation. Kinetically limited diffusion induced by the growth process might be the reason for this behavior. At higher substrate temperatures such kinetic effects are less likely to appear since the diffusion length of the molecules is larger. Further conclusions about the crystal structures or the orientation of the C_{60} unit cell cannot be drawn due to the lack of diffraction features in the Q-map. Also a Q-map of the $CuPc:C_{60}$ blend grown at $310\,\text{K}$ was acquired but exhibits no diffraction features at all.

As a final remark, it should be mentioned that the strong GIXD signal between $0.0\,\text{Å}^{-1}$ and $0.3\,\text{Å}^{-1}$ is background noise from X-rays scattered in air. The Q-map does not show this background due to a background subtraction, which was done by measuring a bare silicon substrate without organic layer on top and subtracting its signal from the Q-map. Only the silicon {111} peak is still visible due to an unfavorable azimuthal orientation of the substrate. This peak was not recorded during the background measurement, which was acquired at a slightly different azimuthal angle. Hence, the silicon {111} peak could not be removed from the Q-map. The appearance of the silicon {111} peak is discussed in Sec. 5.1.
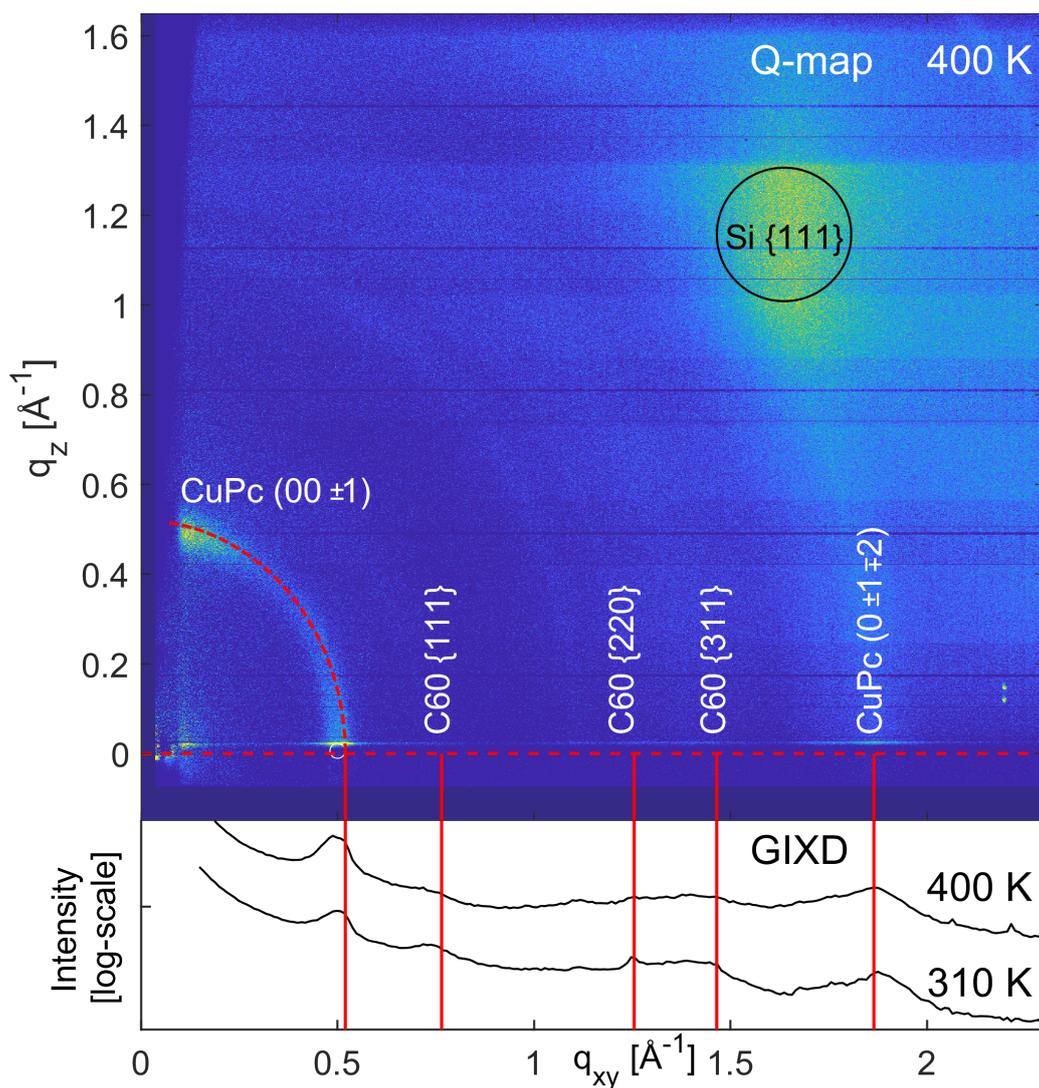
Figure 60: Q-Map of a CuPc:C_{60} blend (ratio 1:1) grown at a deposition rate of $2\,\text{Å/min}$ and a substrate temperature of $400\,\text{K}$ for $100\,\text{min}$. Below: Corresponding GIXD measurements at both substrate temperatures for comparison. The measurements were carried out *ex situ* at a beam energy of $24.0\,\text{keV}$ and a grazing angle of incidence at half of the total reflection edge of silicon.

6.3. Real-Space Imaging

6.3.1. Atomic Force Microscopy

Figure 61 shows $3\,\mu m \times 3\,\mu m$ AFM images ouf pure and blended CuPc-C$_{60}$ films. The images were evaluated with the help of various *Matlab* scripts, amongst those also the counting algorithm which was already employed in Sec. 5.3 for measuring island densities. Depending on the sample, a few hundred up to several thousand islands were detected on an area of $3\,\mu m \times 3\,\mu m$. Some differences between pure and blended thin films as well as between films grown at 310 K and at 400 K can be recognized directly from the AFM-images such as the interface width, which is the difference between the lowest and the highest measured data point. The interface width should not be mixed up with the root mean square roughness (σ_{RMS}), which requires a mathematical treatment and represents the roughness more precisely than the interface width.

Pure films: The first observable is the shape of islands. C$_{60}$ forms round islands due to its isotropic molecular shape and CuPc forms rather elongated worm-like islands, which reflects the anisotropic interactions between those planar molecules. The second observable is the size of islands, which increases visibly from 310 K to 400 K in both pure CuPc and pure C$_{60}$ thin films. Elevated substrate temperatures during growth accelerate the molecular diffusion while the flux of incoming particles remains constant. Consequently, the molecules can cover a larger distance before further impinging molecules obstruct their path on the substrate. Hence, larger islands form while the island density decreases at the same time. The shapes of CuPc and C$_{60}$ islands remain unaffected by the substrate temperature and the same features appear just at different length scales. Concerning the third observable, the roughness, CuPc and C$_{60}$ exhibit an opposite behavior. The interface width of the pure CuPc films decreases from 20 nm to 14 nm when raising the substrate temperature from 310 K to 400 K. The interface width of the pure C$_{60}$ films increases from 10 nm to 40 nm. Different intermolecular interactions are responsible for the different inter-layer diffusion processes leading to a molecular downward diffusion in the pure CuPc films and a preferential upward diffusion in the pure C$_{60}$ films, which is facilitated by elevating the substrate temperature. Note the distributions of heights plotted in addition to the color bar on the left side of each image. The heights of the pure films are symmetrically distributed around the average height such that interface width and σ_{RMS} are related to each other.

Blends: So far, the similarities and differences of pure films at different substrate temperatures were discussed. The blended thin films form the most peculiar morphological features. Only a few up to 50 nm tall islands rise from the extraordinarily smooth and thin blend grown at 310 K. The average height amounts to approximately 3 nm and the interface width of the smooth layer between the islands is about 4 nm, which agrees with the extremely low roughness found from the XRR profiles. The numerous tiny islands agree with the small lateral size of coherently scattering domains in Sec. 6.2. The tall islands are so rare that their influence on the average height and on the roughness is negligible. In order to see details of both tall islands and the smooth film underneath, a logarithmic color map was chosen. The number, the density and the maximum height of tall islands increase

significantly at 400 K. Some islands reach a height of 100 nm and the distribution of heights is no longer symmetric, which is due to the presence of two features. On the one hand, there are many tall islands, on the other hand, the layer between the islands is no longer smooth. Its interface width has increased to 40-50 nm, which is consistent with the complete damping of Kiessig oscillations in the corresponding XRR profile.


(a) CuPc at 400 K
335 islands

(b) 1:1-blend at 400 K
2053 islands

(c) C_{60} at 400 K
864 islands

(d) CuPc at 310 K
3609 islands

(e) 1:1-blend at 310 K
3649 islands

(f) C_{60} at 310 K,
3979 islands
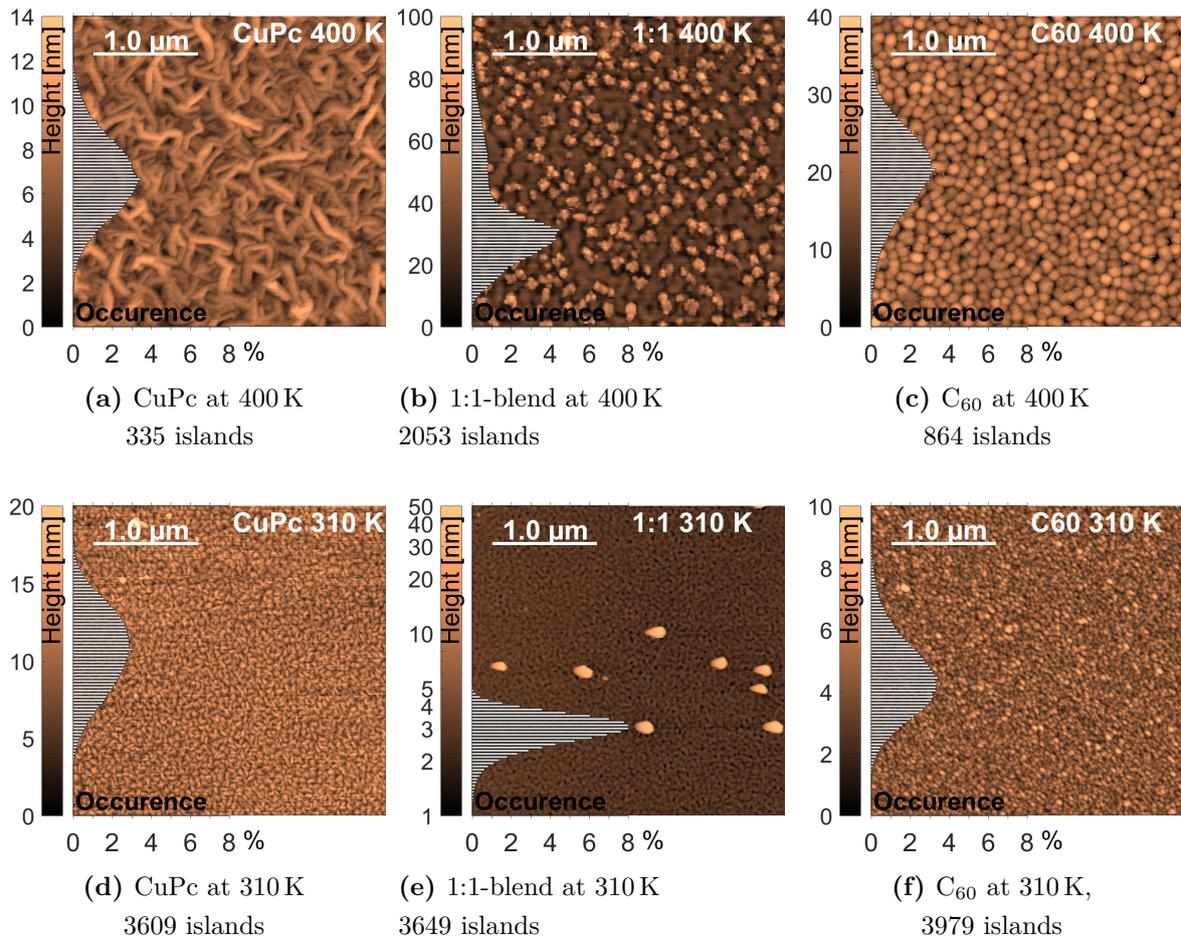
Figure 61: $3\,\mu m \times 3\,\mu m$ AFM images of pure and blended CuPc-C_{60} thin films grown at $2\,\text{Å/min}$ for 100 min at two different substrate temperatures (310 K and 400 K). The distribution of heights is shown on the left side of each image along with the color bar.

6.3.2. Scanning Electron Microscopy

Scanning electron microscopy (SEM) images were taken at an acceleration voltage of 20.0 kV and a working distance of 8.5-10.0 mm between objective lens and specimen. Representative SEM images are shown in Fig. 62. Island shapes, sizes and densities are in good agreement with the AFM images. Nevertheless, a few differences between AFM and SEM can be observed, which demonstrates the benefits and drawbacks of each technique.

Pure films: The resolution of structural features in organic thin films by SEM strongly relies on the surface roughness due to inclination and edge contrast effects, see Sec. 3.3.2. The roughness of the pure films is rather low and the contours of the islands are hardly visible. Only pure C_{60} grown at 400 K exhibits a sufficiently high roughness and the islands are clearly discernible. Although AFM imaging holds several advantages such as providing a height profile at a vertical resolution of less than 1 nm, there are also some drawbacks. The AFM runs into troubles when measuring very rough surfaces as already seen from the 1 μm long and randomly oriented coronene needles in Sec. 5.2. In this case, the contrast effects of SEM imaging are favorable albeit the exact height information is lost. All in all, one can say that AFM is well suited for smooth thin films whose interface width is below 100 nm, whereas SEM requires at least 40 nm of interface width for a good contrast and is more suited for rough surfaces.

Blends: Regarding the SEM images of the CuPc-C_{60} blends in Fig. 62, we see thin needles protruding from a smooth layer, which was not visible in the AFM images. It seems that the AFM tip cannot resolve such fine structures. It may also happen that the AFM tip pulls the needles down or even breaks them off. SEM instead is a contact-less and hence less invasive method. The SEM image of the sample grown at 400 K reveals that the needles are surrounded by molecular agglomerations forming larger islands of different heights, which is in good agreement with the height distribution from AFM. In contrast to this, there are only a few large islands at 310 K and some small needles appear in the surrounding matrix. It is known that CuPc forms needle-like crystals [176] such that the protruding needles can be assigned to pure CuPc domains. In agreement with the missing Bragg peaks in the XRR-profiles, the CuPc needles loose their alignment with the substrate and grow into random directions when C_{60} is present.

Comparison to previous studies: Not only the presence of another type of molecule can inhibit the alignment of CuPc with the substrate, but also a thick layer of CuPc screening the substrate potential leads to a loss of the alignment, as a previous SEM based study about vacuum deposited CuPc films on native silicon oxide demonstrated [95]. Studies on blended thin films without SEM imaging were barely able to assign structural features to pure and mixed domains. A very similar study on zinc phthalocyanine (ZnPc) co-deposited with C_{60} inferred the presence of a mixed underlying phase from spectroscopic observations, but the composition of the islands remained unclear [177]. Another study on co-deposited blends of diindenoperylene (DIP) with C_{60} assumes that the islands are most likely phase separated crystalline DIP domains. [178]. The high contrast in SEM images could resolve more details and could help to assign the structural features in DIP-C_{60} blends in future studies.

Solely one study on blends of pentacene (PEN) with C_{60} was able to assign tall islands seen from AFM images to pure PEN domains by the width of XRR Bragg peaks, which indicated a vertical crystallite size that exceeded the nominal film thickness [174]. Here, in CuPc-C_{60} blends there are no such XRR Bragg peaks and this kind of conclusion is not possible. Instead, SEM was applied and needles of pure CuPc were found. In contrast to CuPc-C_{60} blends, the alignment of PEN-crystallites with the substrate remained in the blend [174].

Another advantage of SEM is the fast data acquisition, which enables to scan large areas within less than one minute, a velocity that cannot be reached by AFM. In order to check the homogeneity of the blended thin films, SEM images were taken at different magnifications ranging from $2\,500\times$ to $35\,000\times$, see the enlarged SEM images in Appx. J. The images verify that the islands are homogeneously distributed over a large area at both substrate temperatures. Furthermore, the direct comparison of images acquired at the same magnification shows that the density of tall islands is significantly larger at 400 K than at 310 K, albeit the film grown at 310 K exhibits numerous tiny islands.

(a) CuPc at 400 K   (b) 1:1-blend at 400 K   (c) C_{60} at 400 K

(d) CuPc at 310 K   (e) 1:1-blend at 310 K   (f) C_{60} at 310 K
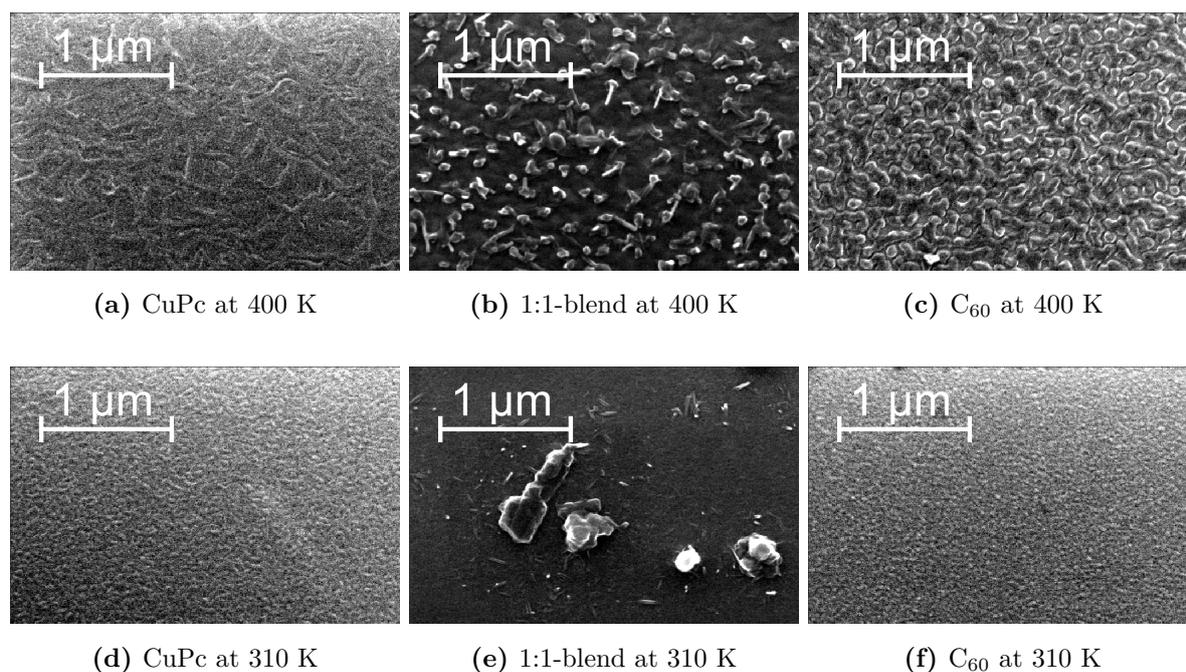
Figure 62: $2\,\mu m \times 3\,\mu m$ SEM images of 1:1-blends of CuPc-C_{60} grown at $2\,\text{Å/min}$ for $100\,\text{min}$ at two different substrate temperatures (310 K and 400 K). The images were acquired at a magnification of $35\,000\times$ and an acceleration voltage of $20\,\text{kV}$.

6.3.3. Energy Dispersive X-Ray Analysis

As explained in Sec. 3.3.3, the possibility of complementing SEM images by an energy dispersive X-ray analysis (EDX) is another benefit of SEM. However, the structural features seen in the SEM images are smaller than the volume from which the X-ray signal originates. A scattering bulb of $1.5\,\mu$m in diameter and penetration depth results when bombarding the sample with electrons in normal incidence at a beam energy of $10\,$keV. The electrons penetrate deeply into the silicon substrate and only a little fraction of the signal stems from the thin organic layer on top.

Nevertheless, the assignment of structural features by means of EDX was tested. An SEM image of the 1:1-blend grown at $310\,$K was acquired in advance and specific spots on the sample were selected for an EDX analysis, see Fig. 63. In order to keep the lateral size of the scattering bulb below $1.0\,\mu$m and the signal-to-noise ratio sufficiently high, the selected spots were bombarded for 300 seconds with electrons at a rather low acceleration voltage of $5.0\,$kV. The spot diameters were measured by SEM afterwards. An accumulation of electrons within the scattering bulb made the region around the probed spots brighter than their surrounding. The diameter of the scattering bulb turned out to be well below $1\,\mu$m, which is indicated by the radius of the red circles in Fig. 63.

The energy distribution of X-rays emitted from the different spots is shown in Fig. 64. Spectrum 1 was measured on top of an island. The signal of silicon is lowest in this spectrum due to the screening of the substrate by the huge amount of organic material on top. The second largest peak close to $0\,$keV stems from electrons which experienced only a little energy loss during scattering. The third largest peak is the one from carbon, which is obvious due to the abundance of carbon in C_{60} and CuPc. A small oxygen K_α-peak stemming from the solely 1-2 nm thin silicon oxide layer on the top of the substrate appears. The amount of oxygen was sufficient for being detected by EDX, but the signal is quite low compared to the noise. Finally, the most interesting chemical elements nitrogen and copper, indicating the presence of CuPc, are barely visible, neither on top of a mount, nor in the surrounding matrix. The amount of 8 nitrogen atoms and 1 copper atom per molecule is clearly too low for EDX. Thicker films or a higher fraction of CuPc molecules in the blend may solve this problem. Although the desired assignment of pure and mixed domains to structural features was not possible, this experiment has shown that low beam energies can reach a resolution which is suitable for an EDX analysis of organic films. An assignment of structural features may be possible in future studies on thicker films with a larger amount of CuPc.
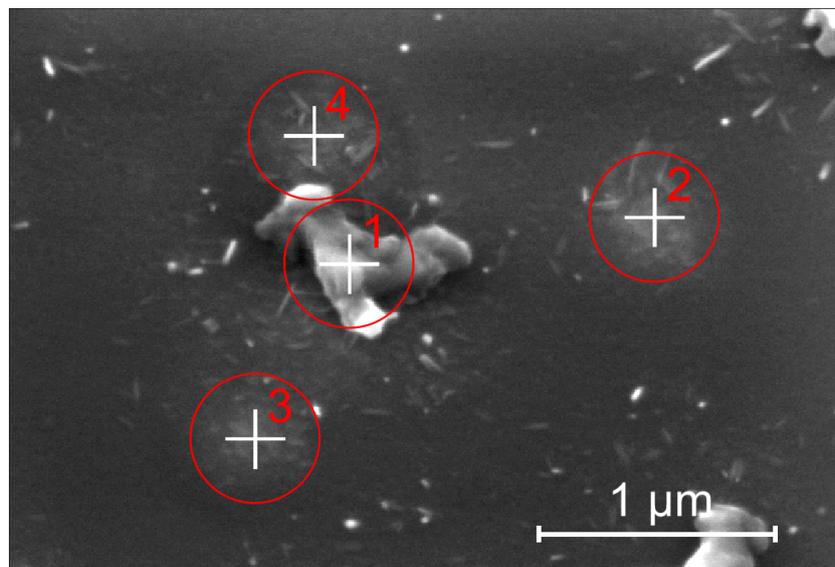
Figure 63: Corresponding SEM image indicating the places at which EDX spectra were taken.
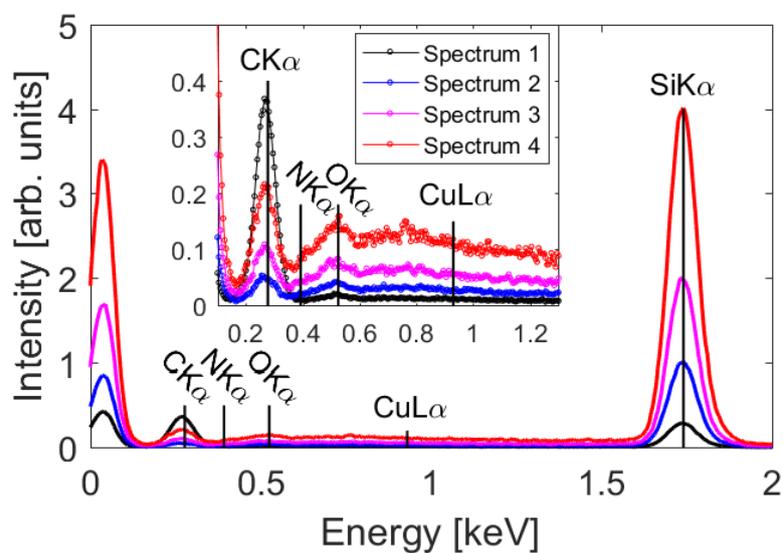
Figure 64: EDX spectra taken from a CuPc-C60 blend grown at 310 K at different points on the sample. The inset shows an enlarged plot of the region between 0.1 keV and 1.2 keV.

Acquisition time: 300 seconds

Beam energy: 5 keV

6.4. Evolution of Roughness

It would not be clear whether certain features evolved during or after the growth unless real-time measurements are employed. As already discussed in previous sections, the roughness of thin films can be measured by means of XRR, which works, in contrast to AFM, also *in-situ* and in real-time during the growth inside of a vacuum chamber. Frequency and damping of the Kiessig oscillations in XRR profiles provide information about the film thickness and its roughness. Unfortunately, XRR profiles which were acquired during the growth cannot be simply fitted with multilayer models without further considerations. The film is growing while the acquisition of XRR scans is running such that thickness and roughness at the beginning ($q_z = 0$) and at the end ($q_z > 0$) of an XRR scan differ. One solution is the measurement of intensity oscillations at specific q_z-values, which requires significantly less time and increases the time resolution. Those q_z-values are the Anti-Bragg point ($q_{Bragg}/2$) and further fractions of q_{Bragg}, usually $q_{Bragg} \cdot n/(n+1)$ and $n \in \{1, 2, 3, ...\}$. However, pure C_{60} films and CuPc-C_{60} blends grown on native silicon oxide exhibit no such Bragg peak such that acquisition of Anti-Bragg oscillations is not possible. Instead, full XRR scans up to $q_z = 0.6\,\text{Å}^{-1}$ were measured, which is time expensive but enables to measure the roughness *in-situ* and in real-time during the growth by means of XRR without having a Bragg peak. Simultaneously, the presence/absence of the first Bragg peak can be observed during the entire growth within this q_z-range. It turned out that there was no vertical ordering throughout the entire growth of the C_{60} and the blended films due to the permanent absence of the Bragg peak.

Figure 65 shows the *in-situ* XRR scans measured in real-time during the growth. The shutter of the effusion cell was opened at $t = 0\,\text{min}$ and closed at $t = 100\,\text{min}$. Each scan took on average 6:45 min such that the growth was finished after 15 scans. Due to varying scan durations, the number of scans had to be adjusted for each measurement. All real-time plots acquired at 310 K exhibit Kiessig oscillations, which will be discussed in more detail in the following. The real-time plots of C_{60} and the blend grown at 400 K exhibit neither Kiessig oscillations nor Bragg peaks throughout the entire film growth and appear at first glance not very instructive. Nevertheless, those data sets imply that both films were rough from the beginning of growth and stay rough until the growth was stopped. Furthermore, a vertical ordering never existed during the growth.

The evolution of roughness was analyzed for the samples grown at 310 K as follows: The Kiessig oscillations in the low q_z-range were fitted up to $q_z = 0.2\,\text{Å}^{-1}$ for pure CuPc and the blend and up to $q_z = 0.15\,\text{Å}^{-1}$ for pure C_{60} using the software *GenX*. The layer model was simplified by a single layer whose thickness and roughness increase during the growth. Modeling a multilayer system for real-time growth would be quite sophisticated and in this case less reasonable due to the missing vertical ordering in C_{60} and its blend with CuPc. The electron densities were determined in advance from post-growth measurements and assumed to be constant during the entire growth. Also thickness and roughness of the native silicon oxide substrate were determined in advance and assumed to be constant since changes inside the substrates are negligibly low at the chosen temperatures of 310 K–400 K.

(a) CuPc 310 K

(b) CuPc 400 K

(c) Blend 310 K

(d) Blend 400 K

(e) C60 310 K

(f) C60 400 K
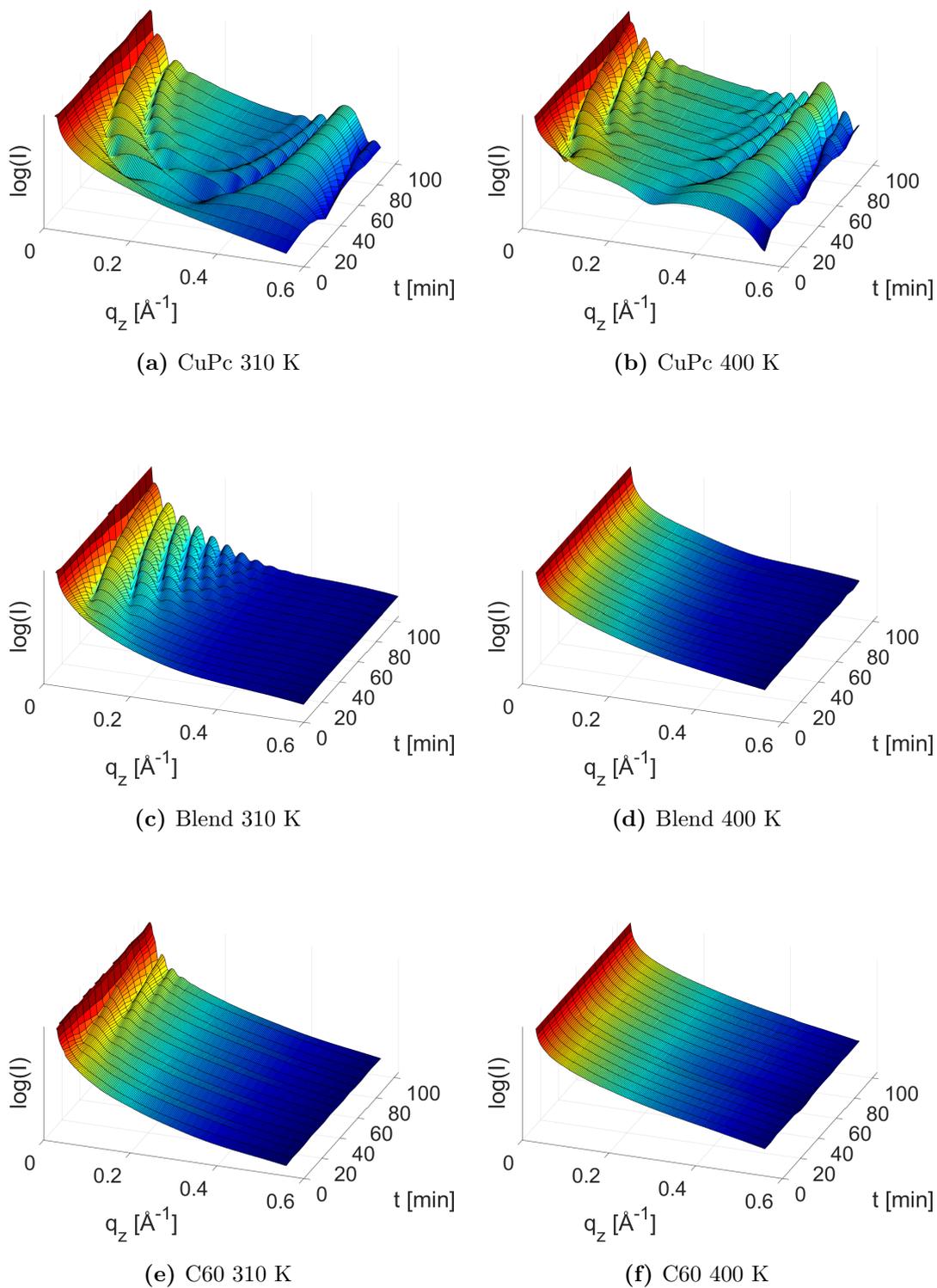
Figure 65: X-ray reflectivity (XRR) measured *in situ* and in real-time during the growth.

Fitted roughness values as a function of the fitted thickness are plotted in Fig. 66. The large gap in the pure CuPc data between 13 nm and 19 nm is due to a diminishing X-ray intensity during the measurements, which occurs in synchrotron rings when the ring current decreases by loosing electrons. The missing data points were linearly interpolated in Fig. 65 and Fig. 66. Roughness values for a thickness below 2 nm do not exist since the Kiessig oscillations of these first scans are not sufficiently pronounced for a good fit.

Due to the extremely damped Kiessig oscillations in the C_{60} scan, data points are only available starting from a thickness of 7 nm. The roughness of C_{60} varies around 3 nm and remains high during the entire growth, which is likely due to the formation of tall islands. CuPc exhibits an increasing roughness followed by a small decrease after the first few nanometers. Afterwards its roughness increases linearly, which could be interpreted as an initial layer-by-layer growth followed by a rapid roughening. Every time a layer is filled, the roughness decreases and rises again as soon as the growth of the next layer begins. Although an oscillating roughness could not be resolved in this experiment, the initial layer-by-layer growth followed by rapid roughening is likely. A similar behavior was observed during the growth of various other thin films consisting of small organic molecules, amongst those pentace (PEN) [179] , diindenoperylene (DIP) [173, 180–182] and perfluorinated copper-phthalocyanine (F16-CuPc) [183].

The data of CuPc grown at 400 K could not be evaluated due to erratic intensity changes between the single scans. Possible reasons could be an unstable deposition rate or an unstable flux of photons during the measurements. This also applied to the CuPc-C_{60} blend grown at 310 K. For this reason, the measurement was repeated one year after and delivered much better results than before. The roughness evolution of the 1:1-blend grown at 310 K was the most peculiar result. It increases during the growth of the first five nanometers and then, it falls considerably below the roughness of both the pure CuPc and the pure C_{60} thin film, which is in good agreement with the low roughness measured post-growth by AFM and XRR. Competing processes may be responsible for this peculiar behavior. In the beginning of growth, the evolution of roughness might be dominated by the formation of C_{60} islands, while CuPc fills the gaps in between due to its preferential wetting of the substrate. As the C_{60} islands grow, the roughness increases, but the presence of CuPc hinders the formation of large C_{60} clusters. Finally, the smoothing effect of CuPc prevails after a certain film thickness is reached.

Figure 66:

Evolution of roughness of a pure CuPc thin film, a pure C_{60} thin film and a molar 1:1-blend of CuPc and C_{60} grown at 310 K and a deposition rate of 2 Å/min for 100 min each.
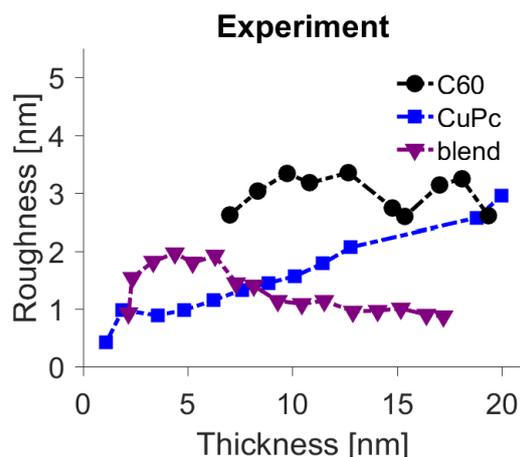
6.5. Quantitative Results

Figure 67 summarizes the quantitative results determined from XRR, GIXD and AFM. The corresponding numbers are shown in Tab. 6.

Influence of T_{sub} on domain sizes and island densities: The domain sizes increase in all films grown at 400 K while their island densities decrease at the same time, which was already explained in Sec. 6.3.1 by a faster molecular diffusion at a constant molecular flux. Diffusing molecules cover larger distances before further impinging molecules obstruct their path on the substrate. Furthermore, the formation of numerous small islands may be inhibited by a temperature driven dissociation of small islands. In other words, the critical size of stable islands increases with increasing substrate temperature.

Influence of mixing on domain sizes and island densities: Compared to the pure films, the domain sizes in blends are clearly reduced at both substrate temperatures and the density of islands increases at 400 K. The presence of another molecular species seems to inhibit the formation of larger pure domains. Concerning the island density at 310 K, there is no major difference between pure and blended CuPc-C_{60} films. The island density of the pure films is already comparatively high and stays around 400 μm^{-2} in the blend, which is due to the numerous tiny islands in the surrounding of a few tall mounts. Regarding solely the tall islands, see for instance the SEM images in Appx. J, the island density of one tall island per μm^2 is extremely low at 310 K. So, due to the presence of two types of islands, a distinction between the rare tall islands and the numerous tiny islands is meaningful.

Roughness: Finally, the roughness was quantified from both *in-situ* XRR and *ex-situ* AFM. The deviation between XRR and AFM amounts to less than 2 Å for pure CuPc grown at both substrate temperatures, which excludes the occurrence of post-growth effects. The pure C_{60} film grown at 310 K is about 1.0 nm smoother when measuring by (*ex-situ*) AFM compared to the *in-situ* XRR. A post-growth effect might be possible but also the limited lateral resolution of the AFM can underestimate the roughness. The island density of C_{60} grown at 310 K is the highest of all films grown during this study and the islands are barely resolved in the AFM images such that the tip cannot follow the surface profile and the corrugations are smoothed out by a convolution of the AFM

tip shape and the surface profile. Only a lower limit for the roughness of C_{60} and its blend with CuPc both grown at 400 K can be estimated from XRR due to the missing Kiessig oscillations. Fortunately, AFM delivers roughness values also for rough surfaces. While the roughness of pure and blended films grown at 310 K is similar, it increases significantly in the blend grown at 400 K compared to the pure films. Agglomerations of molecules around the protruding, needle-like CuPc-crystallites can seen from the SEM-images. A temperature driven upward diffusion along the CuPc crystals may account for the increased roughness in the CuPc-C_{60} blend.
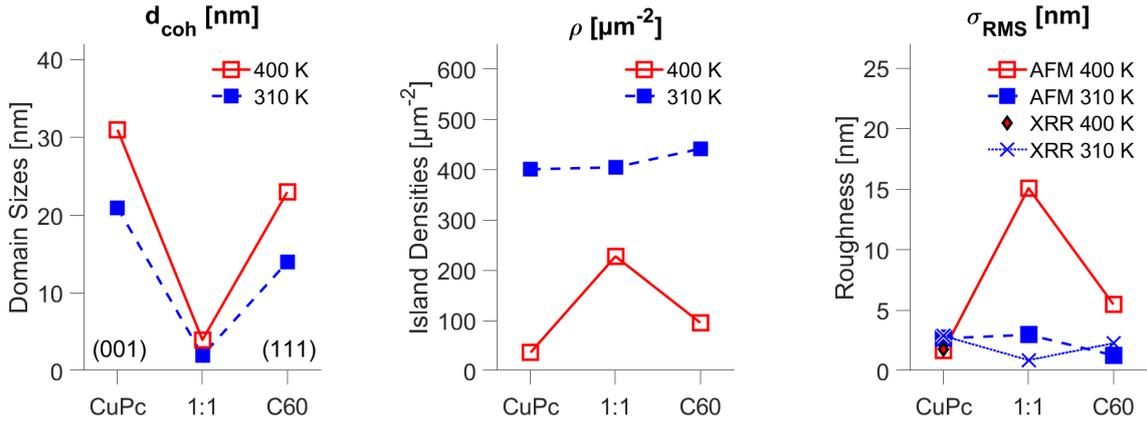
Figure 67: Summary of quantitative results in pure and blended CuPc-C_{60} thin films (ratio 1:1) grown at a total deposition rate of 2 Å/min for 100 min at two different substrate temperatures (310 K and 400 K). Left: Size of coherently scattering domains d_{coh} determined from the GIXD peak widths, middle: Island densities determined from the AFM images and right: Root mean square roughness σ_{RMS} determined from XRR and AFM

	Domain sizes d_{coh} [nm]	Island densities ρ [μm^{-2}]	Roughness (XRR) σ_{RMS} [nm]	Roughness (AFM) σ_{RMS} [nm]
CuPc 400 K	31	37	1.8	1.7
CuPc 310 K	21	401	2.9	2.7
Blend 400 K	4	228	> 3	15.1
Blend 310 K	< 4	405	0.9	3.0
C_{60} 400 K	23	96	> 3	5.5
C_{60} 310 K	14	442	2.3	1.3

Table 6: Summary of quantitative results in pure and blended CuPc-C_{60} thin films (ratio 1:1) grown at a total deposition rate of 2 Å/min for 100 min at two different substrate temperatures (310 K and 400 K).

6.6. Further Experiments

6.6.1. Interrupted Growth

For this experiment, blends of CuPc and C_{60} were grown at a mixing ratio of 1:1 at 400 K, both continuously and intermittent up to a nominal film thickness of 200 Å. The procedure of the intermittent growth is visualized in Fig. 68: The molecules were deposited for 2:30 min at a deposition rate of 4 Å/min. Then the growth was interrupted for further 2:30 min. This pattern was repeated 20 times by opening and closing the shutter of the effusion cell until 100 min later a nominal film thickness of 200 Å was reached. For comparison, two continuously grown CuPc-C_{60} blends were prepared at two different deposition rates, again at a molar mixing ratio of 1:1 and a substrate temperature of 400 K. The duration of growth was adjusted such that the nominal film thickness resulted as well in 200 Å. One blend was continuously grown at a deposition rate of 2 Å/min for 100 min, which corresponds to the overall deposition rate of the intermittent growth. The other blend was continuously grown at a deposition rate of 4,Å/min for 50 min, which corresponds to the actual deposition during the growth periods of the intermittent growth.

The resulting films were analyzed *in-situ* directly after the growth by means of GIXD at the material science beam line of the Swiss Light Source at a beam energy of 13.7 keV. The angle of incidence was chosen close to the total reflection edge of silicon and at half of this angle in order to probe both, the bulk and the surface, see Sec. 3.2. The presence of both CuPc and C_{60} peaks proves the phase separation into pure CuPc and pure C60 domains. The lateral size of coherently scattering CuPc and C_{60} domains was determined from the width of the first two GIXD peaks, i.e. from the CuPc (001) and the C_{60} (111) peak. Due to their partial overlapping, both peaks were fitted at once by a multiple Gauss fit. The results are shown in Fig. 69. It should be mentioned that the C_{60} (111) peak is representative for all crystallographic directions, while the strongly anisotropic CuPc molecule grows much faster in (010)-direction than into the other two directions resulting in rod-like crystallites. Hence, the width of the CuPc (001) peak represents the diameter of such a rod-like crystallite but not its length.

Regarding Fig. 69, a clear trend can be seen at all deposition rates, albeit the domains are nano-crystals, i.e. comprising only a few molecules. The domain sizes of CuPc are smaller at the surface compared to the bulk. In the case of C_{60} it is exactly the other way round. The domain sizes are larger at the surface than in the bulk. A previous study on diindenoperylene (DIP) co-evaporated with C_{60} reports increasing domain sizes at the film surface for both DIP and C_{60} and explains this effect by a kinetically limited phase separation [172]. Phase separated domains emerge slowly from a mixed phase and expand laterally due to molecular diffusion while the film is growing. As a result of this, the phase separated domains are smaller at the bottom of the film and grow laterally towards the surface [172]. Interestingly, this is not the case for CuPc. Instead, the phase separated C_{60} domains grow laterally while the pure CuPc domains shrink at the surface. The different wetting behavior of CuPc and C_{60} might account for this effect. CuPc tends to wet the substrate whereas

(a) Growth Rates   **(b)** GIXD profiles
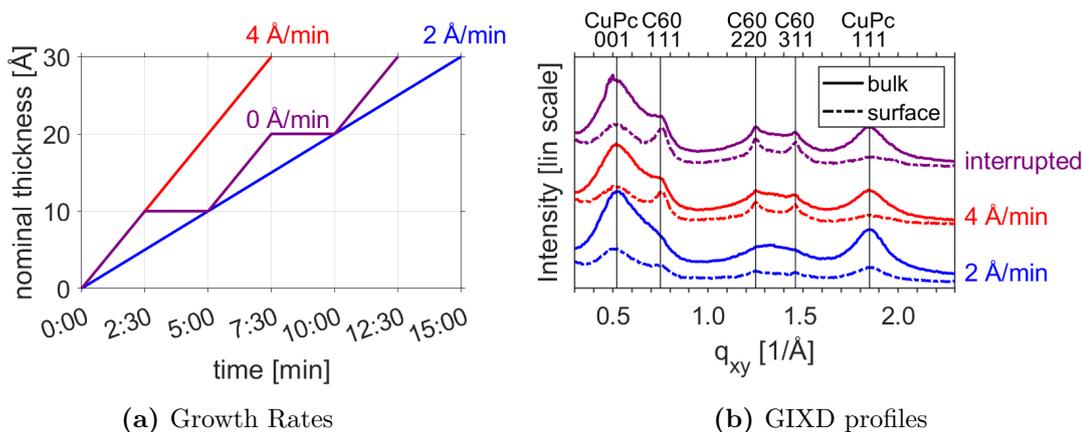
Figure 68: (a) Nominal film thickness as a function of time for continuous and interrupted growth. The plot shows only a magnified extract of the first few minutes, but actually the growth of each film was stopped after a nominal thickness of 100 Å was reached. (b) GIXD profiles of the corresponding CuPc-C_{60} 1:1-blends measured at two grazing angles of incidence.

C_{60} tends to de-wetting. This finding could explain, why CuPc molecules accumulate preferentially in lower layers and impinging C_{60} molecules mainly contribute to the surface.

Influence of the deposition rate: At 4 Å/min, the C_{60} domains are getting larger and the CuPc domains decrease, which is also valid for the interrupted growth. A deviation of the mixing ratio from the 1:1- ratio cannot be excluded. The deposition rate of CuPc should increase from 0.9 Å/min to 1.8 Å/min and the deposition rate of C_{60} should increase from 1.1 Å/min to 2.2 Å/min for a molar ratio of 1:1 at an overall deposition rate of 4 Å/min. Errors during the rate calibration might lead to a deviation from the desired mixing ration (see Sec.3.1). A comparison to the deposition at 2 Å/min is therefore difficult and it cannot be said whether the observed changes are due to the overall deposition rate or due to the mixing ratio.

Influence of interruptions: A comparison of the intermittent growth to the continuously grown film at 4 Å/min is still possible and it shows that significant changes occur mainly in the bulk but not at the surface. The domain sizes differ at the top are about 1 Å, but their difference amounts to more than 4 Å in the bulk. Although these differences are smaller than the size of a molecule, one has to bear in mind that they are average values. Furthermore a trend can be seen that the interruptions enhance the domain sizes of CuPc at the expense of the C_{60} domain sizes in the bulk. In principle, interruptions during growth provide additional time for molecular diffusion and hence promote the preferred growth mode of each molecular species. In this case, there is more time for the downward diffusion of CuPc leading to pronounced wetting of the substrate and there is more time for the upward diffusion of the preferentially de-wetting C_{60}, which makes space for CuPc in the bulk.

	$2\,\text{Å/min}$	$4\,\text{Å/min}$	interp.
C_{60} (111)			
surf.	$31.7\,\text{Å}$	$62.1\,\text{Å}$	$61.1\,\text{Å}$
bulk	$21.3\,\text{Å}$	$35.6\,\text{Å}$	$29.0\,\text{Å}$
CuPc (001)			
surf.	$25.0\,\text{Å}$	$17.4\,\text{Å}$	$18.5\,\text{Å}$
bulk	$30.7\,\text{Å}$	$23.0\,\text{Å}$	$27.1\,\text{Å}$
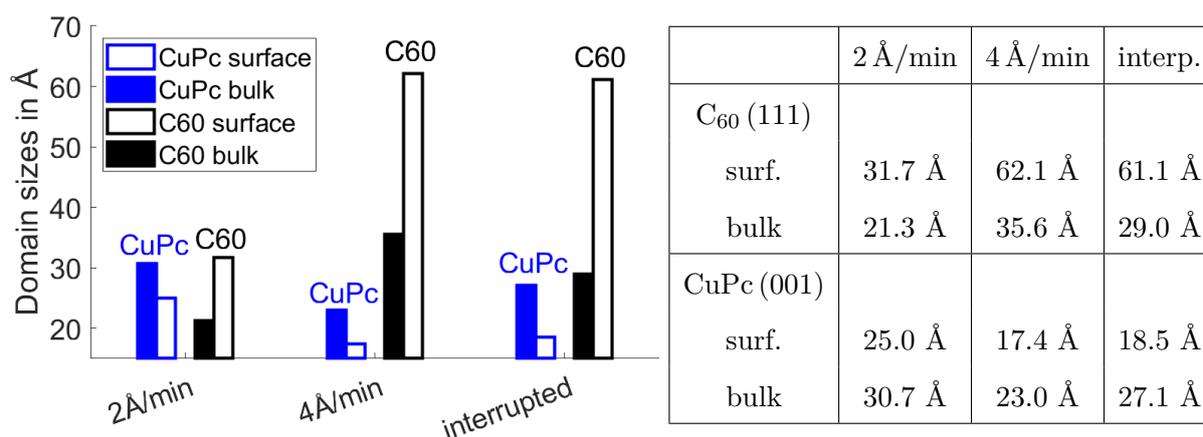
Figure 69: Lateral size of coherently scattering domains determined from the CuPc (001) and the C_{60} (111) Bragg peaks

Comparison to prior experiments: A prior study on intermittent growth of co-deposited DIP:C_{60} blends showed that interruptions do have an impact on the resulting morphology, especially at deposition rates below $10\,\text{Å/min}$ [178]. The present study corroborates this finding.

6.6.2. Template Growth

The following experiment is similar to the experiment of the previous section, but instead of several interruptions during growth, only one 24 hour break was taken and the substrate temperature was either kept or varied during the break. Due to the single break, one could regard this kind of experiment as template growth. A 1:1-blend of CuPc and C_{60} was grown at a deposition rate of $2\,\text{Å/min}$ for 6:30 min as template layer. Then the growth was stopped for 24 hours and resumed again at $2\,\text{Å/min}$ and a molar mixing ratio of 1:1 for further 93:30 min in order to obtain a nominal film thickness of 200 Å. A substrate temperature of 310 K was kept during the entire preparation process of the first sample (310 K/310 K). The template for the second sample (400 K/310 K) was grown at 400 K and then the substrate heating was set to keep 310 K during the 24-hour break and the second growth period.

Figure 70 shows XRR and GIXD scans measured *ex situ* at the material science beamline MS-X04 SA of the Swiss Light Source at a beam energy of 13.7 keV and a grazing angle of incidence close to the total reflection edge of silicon for GIXD. For comparison, the XRD data of continuously grown CuPc-C60 1:1-blends (deposition rate $2\,\text{Å/min}$, duration 100 min) are replotted from Fig. 59. Due to the broad GIXD peaks, a reliable determination of domain sizes is not possible. The 24-hour break was obviously not able to increase the size of coherently scattering domains and the pure domains remain nano-crystalline in the films grown on templates. Thickness and roughness were determined from XRR and turned out to be lower than expected, see Tab. 7. The nominal thickness of the

310 K/310 K sample amounts to 15.7 nm and the nominal thickness of the 400 K/310 K sample to 13.4 nm. Either the deposition rate was lower than 2 Å/min or some material evaporated from the sample during the 24-hour break. The fact that the film thickness of the 400 K/310 K-sample is lower than the film thickness of the 310 K/310 K-sample portends that evaporating molecules could be the reason for the lower thickness. Both samples were deposited under the exact same conditions apart from the substrate temperature during the template growth. It is reasonable that the higher substrate temperature led to more evaporation of molecules, while the second sample cooled down during the 24-hour break.

(a) XRR   **(b)** GIXD
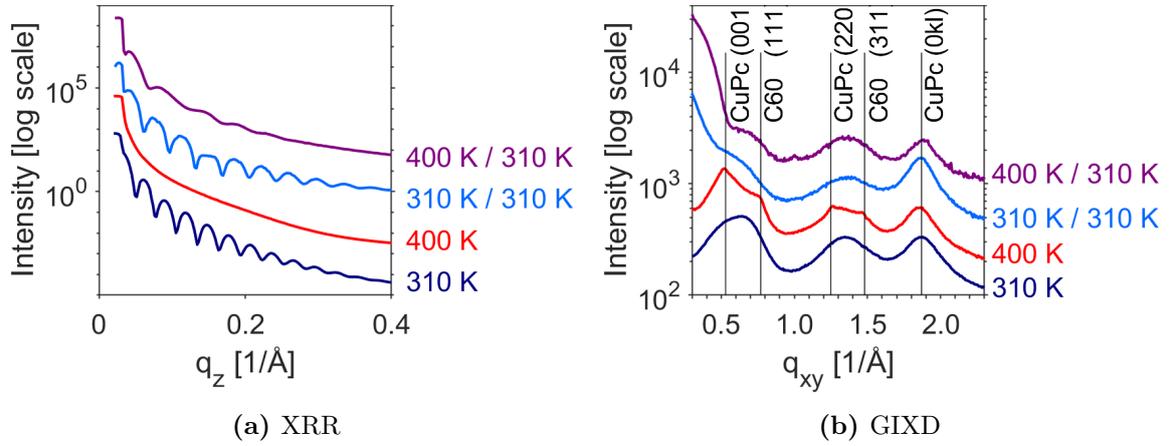
Figure 70: Growth of CuPc-C_{60} 1:1-blends with an interruption of 24 hours and without interruption.

Sample	d_{XRR} [nm]	σ_{XRR} [nm]	σ_{AFM} [nm]	ρ [μm^{-2}]
310 K (continuous)	20.5	0.9	3.0	405±7
310 K/310 K	15.7	0.8	0.5	414±7
400 K (continuous)	-	> 3.0	15.1	228±5
400 K/310 K	13.4	2.4	1.6	218±5

Table 7: Thickness d and roughness σ from XRR and AFM as well as island densities ρ from AFM for CuPc-C_{60} 1:1-blends grown with and without 24-hour interruption. d_{XRR} and σ_{XRR} of the continuously grown film at 400 K are not available due to the missing Kiessig oscillations.

The roughness of the samples grown on templates is in general smaller than for the continuously grown samples, which might be due to the lower film thickness, but also other effects such as a molecular downward diffusion during the 24-hour break are possible. Especially, the 400 K/310 K-sample became smoother than the continuously grown 400 K-sample due to the lower substrate temperature during the second growth period. The island density was not affected by the 24-hour break, see the AFM images in Fig. 71 and Tab. 7. The film grown at 310 K on the 400 K-template adopted the low island density of the 400 K-template which demonstrates that no new islands nucleation during the second growth period at 310 K and impinging molecules attached to the existing islands from the first growth period at 400 K. Either impinging molecules directly contribute to the the lateral and vertical growth of already existing islands, or they form small clusters, which diffuse as a whole and attach to a larger island. Agglomerations of CuPc- or C60-clusters can form large pure domains at low coherently scattering domain sizes.
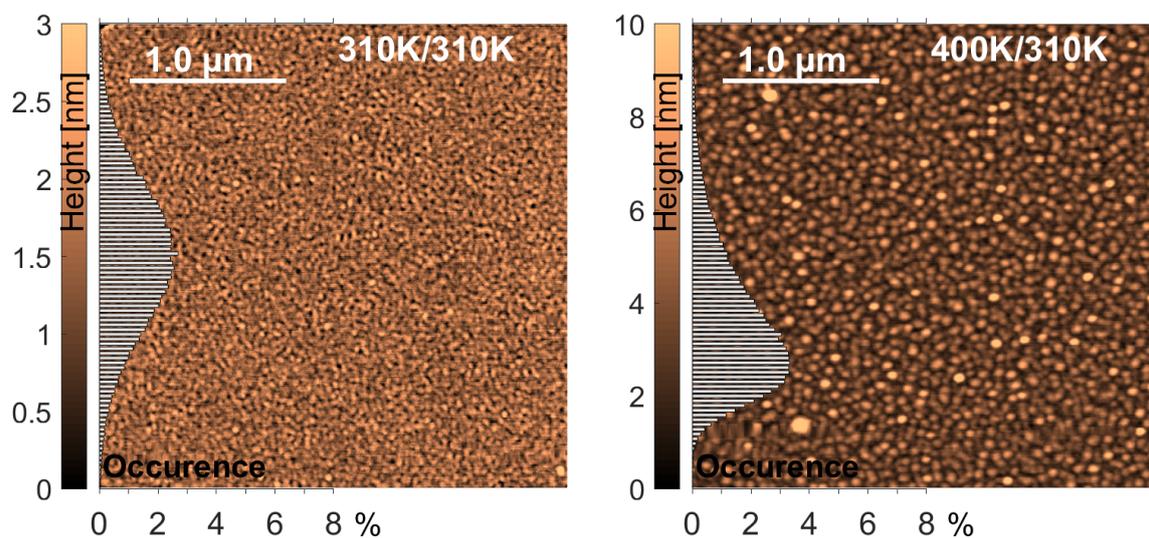
Figure 71: $3\,\mu m \times 3\,\mu m$ AFM images of CuPc-C$_{60}$ blends grown on CuPc-C$_{60}$ templates and distribution of heights at the side of each image along with the color bar.

7. Summary and Conclusion

The structure formation during organic molecular beam deposition (OMBD) of copper phthalocyanine (CuPc), coronene (Cor) and the Buckminster fullerene (C_{60}) was investigated by various imaging and X-ray diffraction (XRD) techniques. Polished silicon wafers covered by an amorphous native oxide layer were applied as substrates. Special attention was paid to the influence of substrate temperature (T_{Sub}) and deposition rate (R_{Dep}) on the structure formation during thin film growth. An algorithm for the automated evaluation of AFM images was developed in *Matlab* and provided quantitative results such as island densities, island sizes, statistics and histograms of the corresponding size distributions. In the following, the results of the distinct thin films are compared and summarized.

7.1. Comparison of pure films: CuPc versus C_{60}

In general, larger islands at lower island densities were found when increasing T_{Sub} from 310 K to 400 K for both CuPc and C_{60}, but also strong differences were found concerning their roughness behavior. The analysis of layer coverages determined from XRR and AFM revealed that the roughness of CuPc decreases by a temperature driven downward diffusion of molecules whereas C_{60} thin films become rougher upon heating of the substrate during growth. The impact of the molecular shape and ordering behavior on the roughness was discussed in detail. Several X-ray diffraction experiments proved that the CuPc crystallites are highly oriented with respect to the substrate surface. The preferred growth along the substrate surface, which is a result of the anisotropic shape of CuPc, might account for the temperature driven downward diffusion. While the crystallites are randomly oriented in horizontal direction, they form well ordered layers of 13 Å in vertical direction, which can be seen from the well pronounced Bragg peaks and oscillations in XRR. In contrast to the 2D powder-like structure of CuPc thin films, the orientation of C_{60} crystallites is completely random. The absence of XRR Bragg peaks indicates that no growth direction is preferred, which is not surprising considering that the shape of C_{60} is almost isotropic. Possibly, the barriers for step edge diffusion are lower due to the spherical shape of C_{60} and the most favorable formation of compact round islands minimizing the free energy becomes possible.

7.2. The impact of T_{Sub} on the formation of C_{60} islands

The automated evaluation of AFM images has shown that the density of C_{60} islands decreases continuously when raising T_{Sub} while the island heights and diameters increase at the same time. The faster diffusion and a larger critical island size i^*+1 for the nucleation of stable islands are most-likely the reason for the reduced island density at elevated substrate temperatures. Diffusing molecules can cover a larger distance until further molecules impinge on the substrate and the probability that two or more single molecules meet and form a new nucleation center decreases. Instead diffusing molecules attach to already existing islands and increase their size further. The diffusion of entire clusters and the coalescence and shape relaxation of neighboring molecular islands might additionally increase the island sizes.

7.3. The impact of R$_{Dep}$ on the formation of C$_{60}$ islands

The reduction of R$_{Dep}$ from 2 Å/min to 1 Å/min resulted in even lower island densities. The effect is similar to elevating the T$_{Sub}$. In both cases, the flux-to-diffusion ratio is reduced such that diffusing molecules cover larger distances until nucleation occurs. Interestingly, the islands become laterally larger but flatter instead of taller upon reducing R$_{Dep}$. Obviously, the nucleation of a second layer becomes less likely and more downward diffusion takes place. It should be mentioned that increasing R$_{Dep}$ from 2 Å/min to 4 Å/min did not lead to the opposite effect of larger island densities and lower diameters. Either, the behavior saturates beyond a certain deposition rate, or R$_{Dep}$ deviated from the desired value such that the duration of deposition was too short.

7.4. The duration of deposition during growth of C$_{60}$ thin films

It turned out that a longer duration of deposition leads to larger islands, both laterally and vertically, at lower island densities, which corroborates the assumption that many islands nucleate in the beginning and start to coalesce during growth. At lower T$_{Sub}$, the island density is more affected while the island sizes exhibit only minor changes and at higher T$_{Sub}$, it is the opposite case. The influence on the island sizes is much stronger than on the island density. The data sets show that the island density at 400 K is already low at the beginning of growth. The interpretation of these results is quite challenging and future growth simulations are required for a deeper understanding. Nevertheless, the systematic preparation and the quantitative evaluation of those experimental data sets has formed the basis for future research on growth processes.

7.5. Comparison of pure films: CuPc versus coronene

Both, CuPc and coronene, exhibit polymorphism and a co-existence of two polymorphs was found in coronene and CuPc thin films. The γ- and the β-polymorph of coronene are well known and agree with the X-ray diffraction patterns found in the present study. Also the β-polymorph of CuPc is well known, whereas the structure of the α-polymorph is disputed and arouse controversial discussion. A co-existence of the simply stacked $P\bar{1}$-structure published by Hoshino et al. in 2003 and a crystal structure similar to the more complex $C2/c$-structure suggested by Ashida et al. in 1966 was found. Excluded volume calculations showed that several molecular configurations are possible and that the molecules can glide past each other without penetrating the forbidden volume. The comparison of *ex-situ* and *in-situ* X-ray data acquired at different angles of incidence suggest that a transition from the $C2/c$- to the $P\bar{1}$-structure is possible and occurs most likely at the film-air interface after the growth. Regarding the crystallites, CuPc and coronene form elongated, needle-like crystallites, which are much larger in the case of coronene by at least two orders of magnitude. In contrast to CuPc, the coronene crystallites are not aligned with the substrate and point into all directions in 3D space. An increase of R$_{Dep}$ did not lead to a significant change of coronene island sizes or densities, which might be a saturation effect as it was described for C$_{60}$. Nevertheless, a peculiar finding in one of the coronene thin films revealed that the island sizes became larger and the island density was reduced in the vicinity of an impurity.

7.6. CuPc-C_{60} blends and comparison to the pure films

Blends of CuPc and C_{60} were prepared by simultaneous evaporation and co-deposition, at a molar mixing ratio of 1:1. Bragg peaks of both materials appear and indicate that the molecules tend to phase separate, though the domain sizes are markedly smaller compared to the pure films. A strong temperature dependent impact on the surface roughness was observed. Only a few tall islands reaching a height of 50 nm surrounded by numerous tiny islands grew at 310 K. Due to the rare occurrence of tall islands, the overall roughness was considerably low. At 400 K, the number of tall islands increased significantly as well as the surface roughness. There was no vertical ordering at both substrate temperatures. SEM images showed needle-like CuPc crystallites protruding from the thin film. The CuPc crystallites lost their alignment with the substrate due to the presence of C_{60}. Although this behavior was observed in prior studies on thicker CuPc films, it was not yet observed in that clarity for CuPc-C_{60} blends.

Real-time XRR measurements showed that CuPc-C_{60} blends grown at 400 K are rough from the beginning and stay rough throughout the entire growth. An initially increasing roughness followed by a smoothing was found in the CuPc-C_{60} blend grown at 310 K. Pure CuPc tends to wet the substrate by a layered growth with linearly increasing roughness, whereas C_{60} quickly forms a rough surface consisting of numerous islands, which is referred to as de-wetting. One might speculate that CuPc fills the gaps between the C_{60} islands and counteracts the roughening effect of C_{60}, but intermolecular interactions, molecular shapes and diffusion barriers may also play a role. Furthermore, it was shown that CuPc crystallites are larger in the bulk and C_{60} crystallites are larger at the surface, which corroborates the assumption that CuPc prefers to wet the substrate and fills the gaps in between the C_{60} islands.

7.7. Outlook

Although the interpretation of the data is quite challenging, the present studies have shown that a systematic and quantitative analysis is possible. The knowledge about the influence of growth parameters such as substrate temperature and deposition rate on the structure formation makes a calculated manipulation of thin film features possible, which is of paramount importance for the application in electronic devices. In particularly, the structural study of blended thin films is still at its beginning. The electronic and optical features of CuPc-C_{60} blends for instance have been investigated frequently for the application in organic solar cells, but their thin film structure has rarely been studied and no clear picture existed so far. More insight into the structure formation during growth processes can be expected in the near future owing to continuously improving synchrotron and neutron sources and the increasing power of modern computers.

Appendices

A. Triclinic Unit Cell Vectors in Cartesian Coordinates

The triclinic unit cell is the most general case. All other unit cells (monoclinic, orthorhombic, tetragonal, rhombohedral, hexagonal and cubic) represent special cases of the triclinic unit cell. The unit cell angles (α, β, γ) are conventionally defined such that α is between the b- and c-axis, β is between the a- and c-axis, and γ is between the a- and b-axis, see Fig. 72. The orientation of the unit cell was chosen such that the c-axis is parallel to the Cartesian y-axis and the b-axis is parallel to the x-y-plane (i.e. parallel to the substrate surface). The Cartesian coordinates of the b- and c-axis can be directly derived from Fig. 72. The derivation of the Cartesian coordinates of the unit cell vector $\vec{a}$ requires a few mathematical considerations. For simplicity we write a instead of $|\vec{a}|$, b instead of $|\vec{b}|$ and c instead of $|\vec{c}|$.

$$\vec{a} = \begin{pmatrix} a_x \\ a \cdot cos(\beta) \\ a_z \end{pmatrix}$$

$$\vec{b} = \begin{pmatrix} b \cdot sin(\alpha) \\ b \cdot cos(\alpha) \\ 0 \end{pmatrix}$$

$$\vec{c} = \begin{pmatrix} 0 \\ c \\ 0 \end{pmatrix}$$
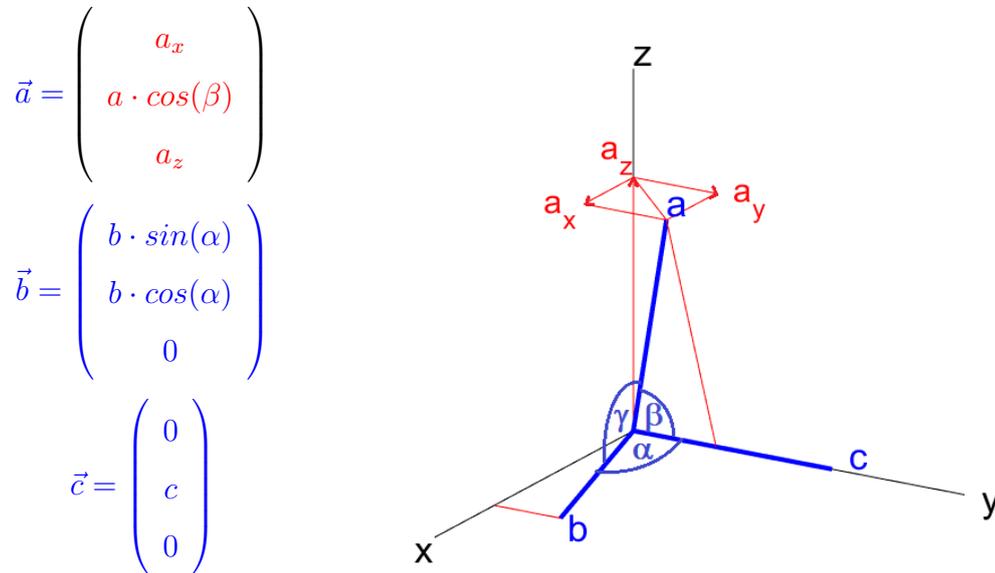
Figure 72: A triclinic unit cell in Cartesian coordiantes.

The a_y-component can be directly determined from Fig. 72:

$$a_y = a \cdot cos(\beta)$$

Using the definition of the scalar product $|\vec{a} \cdot \vec{b}| = |\vec{a}| \cdot |\vec{b}| \cdot cos(\gamma)$ we receive a_x:

$$cos(\gamma) = \frac{|\vec{a} \cdot \vec{b}|}{|\vec{a}| \cdot |\vec{b}|} = \frac{a_x \cdot b_x + a_y \cdot b_y + a_z \cdot b_z}{a \cdot b} = \frac{a_x \cdot b \cdot sin(\alpha) + a \cdot cos(\beta) \cdot b \cdot cos(\alpha) + a_z \cdot 0}{a \cdot b}$$

$$a_x = \frac{a}{sin(\alpha)} \cdot (cos(\gamma) - cos(\alpha) \cdot cos(\beta))$$

Now a_z can be derived from a_x and a_y using Pythagoras $a^2 = a_x^2 + a_y^2 + a_z^2$:

$$a_z = \sqrt{a^2 - a_x^2 - a_y^2} = \sqrt{a^2 - \frac{a^2}{sin^2(\alpha)} \cdot \left(cos(\gamma) - cos(\alpha) \cdot cos(\beta)\right)^2 - a^2 \cdot cos^2(\beta)}$$

$$a_z = \frac{a}{sin(\alpha)} \cdot \sqrt{sin^2(\alpha) - cos^2(\gamma) + 2 \cdot cos(\alpha) \cdot cos(\beta) \cdot cos(\gamma) - cos^2(\alpha) \cdot cos^2(\beta) - sin^2(\alpha) \cdot cos^2(\beta)}$$

Replace $sin^2(\alpha)$ by $1 - cos^2(\alpha)$ and cancel out $cos^2(\alpha) \cdot cos^2(\beta)$:

$$a_z = \frac{a}{sin(\alpha)} \cdot \sqrt{R}$$

$$R = 1 - cos^2(\alpha) - cos^2(\beta) - cos^2(\gamma) + 2 \cdot cos(\alpha) \cdot cos(\beta) \cdot cos(\gamma)$$

Finally, we obtain:

$$\vec{a} = \frac{a}{sin(\alpha)} \cdot \begin{pmatrix} cos(\gamma) - cos(\alpha) \cdot cos(\beta) \\ sin(\alpha) \cdot cos(\beta) \\ \sqrt{R} \end{pmatrix}$$

The volume of the triclinic unit cell is as follows:

$$V = \vec{a} \cdot (\vec{b} \times \vec{c}) = \vec{a} \cdot \begin{pmatrix} b \cdot sin(\alpha) \\ b \cdot cos(\alpha) \\ 0 \end{pmatrix} \times \begin{pmatrix} 0 \\ c \\ 0 \end{pmatrix} = \vec{a} \cdot \begin{pmatrix} 0 \\ 0 \\ b \cdot c \cdot sin(\alpha) \end{pmatrix}$$

A simple equation results:

$$V = a \cdot b \cdot c \cdot \sqrt{R}$$

B. Calculation of Reciprocal Unit Cell Vectors

$$\vec{a}^{\,*} \quad = \quad \frac{2\pi}{V} \cdot (\vec{b} \times \vec{c}) \quad = \quad \frac{2\pi}{a} \cdot \begin{pmatrix} 0 \\ 0 \\ sin(\alpha)/\sqrt{R} \end{pmatrix}$$

$$\vec{b}^{\,*} = \quad \frac{2\pi}{V} \cdot (\vec{c} \times \vec{a}) \quad = \quad \frac{2\pi}{b} \cdot \frac{1}{sin(\alpha)} \cdot \begin{pmatrix} 1 \\ 0 \\ \left[cos(\alpha) \cdot cos(\beta) - cos(\gamma) \right]/\sqrt{R} \end{pmatrix}$$

$$\vec{c}^{\,*} \quad = \quad \frac{2\pi}{V} \cdot (\vec{a} \times \vec{b}) \quad = \frac{2\pi}{c} \cdot \frac{1}{sin(\alpha)} \cdot \begin{pmatrix} -cos(\alpha) \\ sin(\alpha) \\ \left[cos(\alpha) \cdot cos(\gamma) - cos(\beta) \right]/\sqrt{R} \end{pmatrix}$$

A general reciprocal lattice vector with Miller indices (h, k, l) is:

$$\vec{G}_{hkl} \quad = \quad h \cdot \vec{a}^{\,*} + k \cdot \vec{b}^{\,*} + l \cdot \vec{c}^{\,*}$$

The Cartesian components of $\vec{G}_{hkl}$ for a triclinic unit cell are:

$$G_x = \quad \frac{2\pi}{sin(\alpha)} \cdot \left(\frac{k}{b} - \frac{l}{c} \cdot cos(\alpha) \right) \qquad\qquad G_y = \quad 2\pi \cdot \frac{l}{c}$$

$$G_{xy} = \quad \sqrt{G_x{}^2 + G_y{}^2} = \quad 2\pi \cdot \sqrt{ \frac{k^2}{b^2 \cdot sin^2(\alpha)} - \frac{k \cdot l}{b \cdot c} \cdot \frac{1}{tan(\alpha)} + \frac{l^2}{c^2} \cdot \frac{1}{sin^2(\alpha)} }$$

$$G_z = \quad \frac{2\pi}{\sqrt{R}} \cdot \left[\frac{h}{a} \cdot sin(\alpha) + \frac{k}{b} \cdot \left(\frac{cos(\alpha) \cdot cos(\beta) - cos(\gamma)}{sin(\alpha)} \right) + \frac{l}{c} \cdot \left(\frac{cos(\alpha) \cdot cos(\gamma) - cos(\beta)}{sin(\alpha)} \right) \right]$$

$$R = \quad 1 - cos^2(\alpha) - cos^2(\beta) - cos^2(\gamma) + 2 \cdot cos(\alpha) \cdot cos(\beta) \cdot cos(\gamma)$$

C. Space Group Symmetries and Extinction Rules (Example)

The kinematic scattering theory enables us to calculate the intensities of X-ray diffraction peaks:

$$I_{hkl} = |f(\vec{G}_{hkl})|^2 = \left| \sum_{j=1}^{N} f_j(\vec{G}_{hkl}) \cdot exp\left(2\pi i \cdot \vec{G}_{hkl} \cdot \vec{r}_j\right) \right|^2 \tag{5}$$

$f_j(\vec{G}_{hkl})$ is the atomic form factor and $\vec{r}_j$ contains the coordinates of atom number j. We recall the general reciprocal lattice vector as a linear combination of reciprocal unit cell vectors:

$$\vec{G}_{hkl} = h \cdot \vec{a}^* + k \cdot \vec{b}^* + l \cdot \vec{c}^* \tag{6}$$

Each triplet of Miller indices (h, k, l) can be assigned to one of the diffraction peaks. Some crystal structures exhibit special symmetries that lead to an extinction of specific diffraction peaks. The connection between space group symmetries and extinction rules will be explained by the example of the space group $C2/c$ on the following page.

The kinematic scattering factor $f(\vec{G}_{hkl})$ will be calculated for two identical atoms ($j = 1,2$). The atomic form factor $f_j(\vec{G}_{hkl})$ is the same for both atoms and can be ignored. The first atom is placed at the coordinates:

$$\vec{r}_1 = x \cdot \vec{a} + y \cdot \vec{b} + z \cdot \vec{c} \tag{7}$$

From now on, we simply note down the fractions of the unit cell vectors as $[x, y, z]$. The scalar product in Eq. 5 then simplifies to:

$$\vec{G}_{hkl} \cdot \vec{r}_j = h \cdot x + k \cdot y + l \cdot z \tag{8}$$

This is valid for all kinds of unit cells. They do not have to be rectangular since $\vec{a}^* \cdot \vec{a} = 1$ by definition, which of course also applies to $\vec{b}$ and to $\vec{c}$.

The positions $\vec{r}_2$ of all equivalent atoms can be calculated due to Wyckoff by applying the symmetry operations of the given space group to the coordinates of an arbitrarily chosen atom placed at the location $\vec{r}_1 = [x, y, z]$. The equivalent Wyckoff positions were compiled for all space groups on the Bilbao Crystallographic Server. [159]

The space group $C2/c$ describes a monoclinic unit cell which exhibits C-centering, a 2-fold screw axis and a gliding mirror plane. Due to the Hermann–Manguin convention, the capital C stands for the base centering in the a-b-plane, the 2 stands for the 2-fold screw axis along the unique b-axis and the lower case c for the gliding mirror plane, gliding along the c-direction and reflecting at a plane perpendicular to the 2-fold screw axis, which is indicated by the slash "/". We now calculate the impact of these symmetries on the peak intensities and derive the extinction conditions for this space group:

C-Centering and Integral Extinction

C-centering means that additionally to the lattice points at the corners of each unit cell $(\vec{r}_1)$, also lattice points at the center of the a-b-plane $(\vec{r}_2)$ appear:

$$\vec{r}_1 = [x, \ y, \ z] \qquad \vec{r}_2 = [x + {}^1\!/_2, \ y + {}^1\!/_2, \ z]$$

$$f(\vec{G}_{hkl}) = f_j(\vec{G}_{hkl}) \cdot exp\Big(2\pi i \cdot (x + y + z)\Big) \cdot \left(1 + exp\Big(2\pi i \cdot (h \cdot {}^1\!/_2 \ + \ k \cdot {}^1\!/_2)\Big)\right)$$

The extinction condition $f(\vec{G}_{hkl}) = 0$ is satisfied if $h + k$ is an odd number. Specific peaks in the entire reciprocal space are affected, which is called integral extinction.

2-Fold Screw Axis and Serial Extinction

An n-fold screw axis means that the crystal structure is invariant to a shift along a unit cell vector $\vec{v}$ by $|\vec{v}|/n$ followed by a rotation around this vector by $(360/n)°$. The unique b-axis represents the 2-fold screw axis for this space group $C2/c$.

$$\vec{r}_1 = [x, \ y, \ z] \qquad \vec{r}_2 = [-x, \ y + {}^1\!/_2, \ -z]$$

$$f(\vec{G}_{hkl}) = f_j(\vec{G}_{hkl}) \cdot exp\Big(2\pi i \cdot (x + y + z)\Big) \cdot \left(1 + exp\Big(2\pi i \cdot (-2 \cdot h \cdot x \ + \ k \cdot {}^1\!/_2 \ - \ 2 \cdot l \cdot z)\Big)\right)$$

The extinction condition $f(\vec{G}_{hkl}) = 0$ is satisfied if $h = 0$ and $l = 0$ and if k is an odd number. Peaks along an axis specified by $h = 0$ and $l = 0$ in the reciprocal space are affected, which is called serial extinction.

Gliding Mirror Plane and Zonal Extinction

Gliding mirror plane means that the unit cell is invariant to shifting along a real space vector $\vec{v}$ by $|\vec{v}|/2$ or $|\vec{v}|/4$ followed by a reflection at a plane parallel to $\vec{v}$. The vector can be a unit cell vector or a body/face diagonal of the unit cell. The space group $C2/c$ allows a shift along the c-axis by $|\vec{c}|/2$ followed by a reflection at the a-c-plane.

$$\vec{r}_1 = [x, \ y, \ z] \qquad \vec{r}_2 = [x, \ -y, \ z + {}^1\!/\!{}_2]$$

$$f(\vec{G}_{hkl}) = f_j(\vec{G}_{hkl}) \cdot exp\Big(2\pi i \cdot (x + y + z)\Big) \cdot \Big(1 + exp\Big(2\pi i \cdot \big(-2 \cdot k \cdot y + l \cdot {}^1\!/\!{}_2\big)\Big)\Big)$$

The extinction condition $f(\vec{G}_{hkl}) = 0$ is satisfied if $k = 0$ and l is an odd number. Peaks along a plane specified by $k = 0$ in the reciprocal space are affected, which is called zonal extinction.

Table 8 summarizes the extinction conditions for the space group $C2/c$. Tables of extinction/reflection conditions for all kind of space groups can be found in the International Tables for Crystallography A. [158]

Symmetry Operation	Extinct (hkl)-Reflections	Type
C-Centering (in the a-b-plane)	(hkl)-reflections with $h + l$ being odd	integral
2-fold screw axis parallel to the unique b-axis	($0k0$)-reflections with k being odd	serial
Gliding mirror plane along the c-axis	($h0l$)-reflections with l being odd	zonal

Table 8: Extinction conditions for the space group $C2/c$.

D. Rotations in 3D-Space by Quaternions

We want to rotate an atom located at $\vec{r} = (X, Y, Z)$ around an arbitrary axis by an angle φ. The rotation axis goes through the origin of the coordinate system and through the point $\vec{s} = (u, v, w)$. The rotated vector $\vec{r}\,' = (X', Y', Z')$ is calculated by: $\vec{r}\,' = \vec{s} \cdot \vec{r} \cdot \vec{s}\,^*$

$$\vec{r}\,' = \Big(cos(\varphi/2) + sin(\varphi/2) \cdot (\bar{u}i + \bar{v}j + \bar{w}k)\Big) \cdot (xi + yj + zk) \cdot \Big(cos(\varphi/2) - sin(\varphi/2) \cdot (\bar{u}i + \bar{v}j + \bar{w}k)\Big) \quad (9)$$

$\vec{s}$ has to be normalized such that $\vec{s} \cdot \vec{s}\,^* = 1$ in order to maintain the length of the rotated vector $\vec{r}\,'$. By dividing the coordinates (u, v, w) by $\sqrt{u^2 + v^2 + w^2}$ we obtain the normalized coordinates $(\bar{u}, \bar{v}, \bar{w})$. The complex conjugated vector $\vec{s}\,^*$ makes sure that the rotated vector $\vec{r}\,'$ goes back to the 3D-space. Equation 9 is solved by applying the distributive law and the quaternion algebra:

$$i^2 = j^2 = k^2 = i \cdot j \cdot k = -1$$
$$i \cdot j = +k, \quad j \cdot k = +i, \quad k \cdot i = +j$$
$$j \cdot i = -k, \quad k \cdot j = -i, \quad i \cdot k = -j$$

The imaginary axis (i, j, k) represent the Cartesian coordinates (x, y, z) in 3D-space. We skip the at least two pages filling derivation and directly present the results here. The final coordinates of the rotated vector after solving Eq. 9 are:

$$X' = cos(\varphi/2) \cdot A + sin(\varphi/2) \cdot (+D \cdot \bar{u} + C \cdot \bar{v} - B \cdot \bar{w})$$
$$Y' = cos(\varphi/2) \cdot B + sin(\varphi/2) \cdot (-C \cdot \bar{u} + D \cdot \bar{v} + A \cdot \bar{w})$$
$$Z' = cos(\varphi/2) \cdot C + sin(\varphi/2) \cdot (+B \cdot \bar{u} - A \cdot \bar{v} + D \cdot \bar{w})$$

The factors A, B, C and D are:

$$A = cos(\varphi/2) \cdot X + sin(\varphi/2) \cdot (\bar{v} \cdot \bar{w} - \bar{w} \cdot \bar{v})$$
$$B = cos(\varphi/2) \cdot Y + sin(\varphi/2) \cdot (\bar{w} \cdot \bar{u} - \bar{u} \cdot \bar{w})$$
$$C = cos(\varphi/2) \cdot Z + sin(\varphi/2) \cdot (\bar{u} \cdot \bar{v} - \bar{v} \cdot \bar{u})$$
$$D = sin(\varphi/2) \cdot (X \cdot \bar{u} + Y \cdot \bar{v} + Z \cdot \bar{w})$$

E. Calculation of Electron Densities for GenX

Pure silicon crystals have a mass density of $\rho_{mass} = 2.336 g/cm^3$ Each silicon atom has 14 electrons. The average mass of a single silicon atom is $m_{Si} = 28.085u$, averaged over all silicon isotopes and expressed in terms of the Dalton unit $u = 1.660539 \cdot 10^{-24} g$. The electron density ρ_{el} of such a silicon crystal is calculated by:

$$\rho_{el} = \frac{\rho_{mass}}{m_{Si}} \cdot N_{el} = \frac{2.336 \, g/cm^3}{28.085 \, u} \cdot 14 \approx 0.70 \, el./\text{Å}^3$$

Alternatively, the electron density of silicon can be calculated from the unit cell volume. Pure silicon crystals form cubic unit cells of length $a = 5.43$ Å and their diamond structure comprises $8 \, \text{atoms} \times 14 \, \text{electrons}$ per unit cell.

$$\rho_{el} = \frac{N_{el}}{V} = \frac{8 \cdot 14}{(5.43 \, \text{Å})^3} \approx 0.70 \, el./\text{Å}^3$$

The variable `Si.Dens` in the software GenX solely refers to the inverse unit cell volume and the command "`f = fp.Si*8`" calculates the electron density automatically. The unit "at./AA" indicated in GenX may be misleading and does not mean atoms per Å^3. Instead, it means one compound unit (a set of atoms or molecules) per Å^3:

$$Si.Dens = \frac{1}{V} = \frac{1}{(5.43 \, \text{Å})^3} \approx 0.00625 \, \text{at./AA}$$

The electron density of amorphous silicon oxide, whose mass density is $\rho_{mass} = 2.2 \, g/cm^3$ [150], is calculated in the same way:

$$\rho_{el} = \frac{\rho_{mass}}{m_{SiO_2}} \cdot N_{el} = \frac{2.2 \, g/cm^3}{28.085 \, u + 2 \cdot 15.999 \, u} \cdot (14 + 2 \cdot 8) \approx 0.66 \, el./\text{Å}^3$$

Since this amorphous material has no specific unit cell, the density of compound units per Å^3 is calculated from ρ_{el} and N_{el} and GenX calculates ρ_{el} from this value by "`f = fp.Si + fp.O*2`".

$$SiO2.Dens = \frac{\rho_{el}}{N_{el}} = \frac{0.66 \, el./\text{Å}^3}{14 + 2 \cdot 8} \approx 0.022 \, \text{at./AA}$$

The pseudo unit cell volume of amorphous silicon oxide was calculated from $V = m_{CuPc}/\rho_{mass}$ and is written here in parenthesis. Accordingly, the electron density of organic thin films can be calculated when the volume of the unit cell, the chemical structure of the molecule and the number of molecules per unit cell is known. Table 9 summarizes the required data for pure silicon, amorphous silicon oxide, CuPc and C60. The unit cell volume of CuPc was taken from Ref. [99] and the unit cell volume of C60 from Ref. [122]. The compound densities were calculated by $1/V$, the electron

116

densities were calculated by N_{el}/V and the mass densities by m_{CuPc}/V and m_{C60}/V, respectively. The atomic masses of the most frequent elements in organic compounds and in the substrates are compiled in Tab. 10.

name .	Silicon	Amorphous SiO_2	CuPc	C60
compound unit	$8 \times Si$	$1 \times SiO_2$	$1 \times Cu\,N_8\,C_{32}\,H_{16}$	$4 \times C_{60}$
V [Å^3]	$(5.43)^3 = 160$	(45)	582	$(14.0)^3 = 2744$
N_{el} [el.]	$8 \cdot 14$	$1 \cdot (1 \cdot 14 + 2 \cdot 8)$	$1 \cdot (1 \cdot 29 + 8 \cdot 7 + 32 \cdot 6 + 16 \cdot 1)$	$4 \cdot (60 \cdot 6)$
Dens [at./AA]	0.00625	0.022	0.0017	0.00036
ρ_{el} [el./Å^3]	0.70	0.66	0.50	0.52
ρ_{mass} [g/cm^3]	2.336	2.2	1.64	1.74

Table 9: Electron density of pure silicon, amorphous silicon oxide, CuPc and C60

H	1.0079 u
C	12.0107 u
N	14.0067 u
O	15.9994 u
Si	28.0855 u
P	30.9738 u
S	32.065 u
Cu	63.546 u

Table 10: Atomic masses of the most frequently used elements for organic thin films in inert substrates such as silicon oxide, sorted by their mass. One unit is $u = 1.660539 \cdot 10^{-24} g$.

F. Layer Model for GenX

The XRR profiles of CuPc grown at 310 K and at 400 K were fitted by a multilayer model using the software *GenX*. The customized multilayer model consists of three main parts, the **substrate stack**, the **organic stack** representing the completely filled layers and N stacks of partially filled **bilayers**, see Fig. 73 and Ref. [184]. Each bilayer consists of a void and a CuPc layer modeling the oscillating electron density. The substrate stack consists of a thick silicon layer, a thin silicon oxide layer and a void layer simulating the electron density at the film-substrate interface. The electron density of the substrate was calculated as described in the previous section (Appx. E). Thickness and roughness of the oxide layer were fitted in advance from an XRR profile of a pure substrate without the organic thin film on top. Thickness, roughness and electron densities of all other layers as well as the number of completely filled layers was fitted in *GenX*. The partially filled bilayers were added manually one after another until the function of merit (**FOM**), which is a measure for the deviation between measured and simulated XRR curve, was less than 0.1 and did not drop further when adding more layers, see Fig. 74. The partial filling was simulated by reducing the electron density according to the coverage of the respective layer in percent.

Figure 73: Layer model for CuPc consisting of a substrate stack, an organic stack of M completely filled layers and a stack of N partially filled layers. The coverage of each layer is indicated in percent.

118
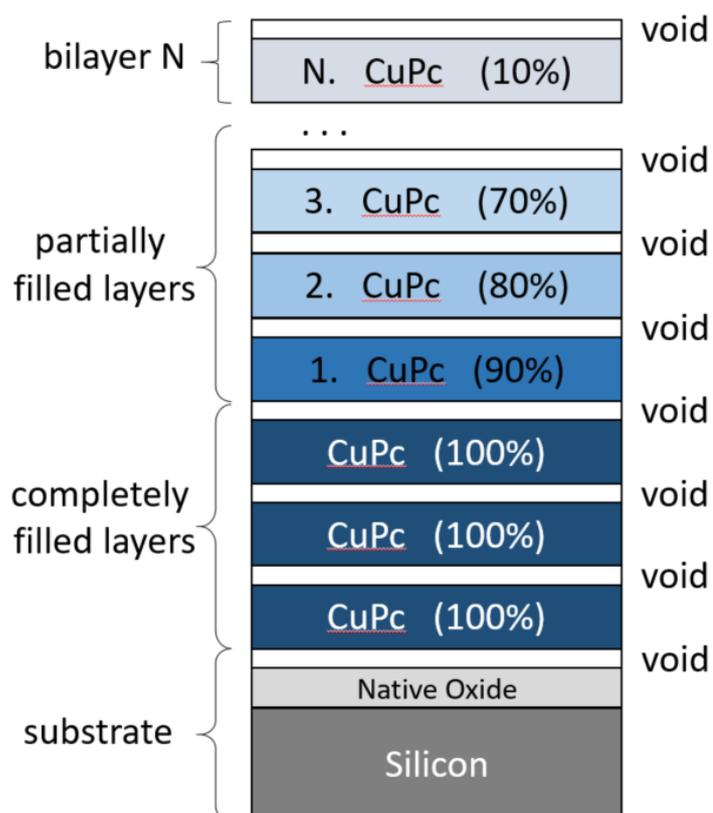
The following lines show how the layer model is built up in the **Sample-Tab** of *GenX*. Starting values from an educated guess for the thickness `D`, the roughness `Sigma` and the electron densities `Dens` are given in parentheses. Ten repetitions of completely filled layers were chosen as starting value.

```
Bilayer[N] = Stack:  Repetitions = 1
  Void[N] (D = D(Void), Sigma = Sigma(Void) , Dens = 0.00000 at./AA)
  CuPc[N] (D = D(CuPc), Sigma = Sigma(CuPc) , Dens = Dens(CuPc) × Coverage[N])

        ⋮

        ⋮

Bilayer02 = Stack:  Repetitions = 1
  Void02 (D = D(CuPc) , Sigma = Sigma(Void) , Dens = 0.00000 at./AA)
  CuPc02 (D = D(CuPc) , Sigma = Simag(CuPc) , Dens = Dens(CuPc) × Coverage02)

Bilayer01 = Stack:  Repetitions = 1
  Void01 (D = D(CuPc) , Sigma = Sigma(Void) , Dens = 0.00000 at./AA)
  CuPc01 (D = D(CuPc) , Sigma = Simag(CuPc) , Dens = Dens(CuPc) × Coverage01)

Organic = Stack:  Repetitions = 10 (fitted)
  Void (D = D(Bilayer)-D(CuPc) , Sigma = 3.1 Å , Dens = 0.00000 at./AA)
  CuPc (D = 9.3 Å ,                Sigma = 2.9 Å , Dens = 0.00134 at./AA)

Substrate = Stack:  Repetitions = 1
  void00 (D = 5.7 Å , Sigma = 2.5 Å , Dens = 0.0000 at./AA)
  SiO2   (D = 10.6 Å , Sigma = 4.4 Å , Dens = 0.02200 at./AA)
  Sub    (D = 575 μm , Sigma = 2.0 Å , Dens = 0.00625 at./AA)
```

Two custom parameters, the bilayer thickness and the layer coverages, were defined in the **Simulation-Tab** of *GenX* by clicking on the **Nut-Symbol** (*edit user variables*). Those parameters received a starting value which was automatically fitted.

Custom Parameters (New Variables):

Assume that all bilayers have the same tickness of 13.1 Å

```
cp.new_var('BilayerD',13.1)
```

Set the coverage of layer N to 50% as a starting value

```
cp.new_var('Coverage[N]',0.5)
```

119

In the next step, the boundary conditions for the fit were set by couple parameters, i.e. clicking on the **Plus-Symbol** (*insert a command*) in the **Simulation**-**Tab**.

Simulation Commands:

Set the thickness D of the void layer such that D(void) + D(CuPc) = D(Bilayer):

```
void.setD(cp.getBilayerD()-CuPc.getD())
```

Set the density of layer N proportional to its coverage:

```
CuPc[N].setDens( cp.getCoverage[N]() * CuPc.getDens() )
```

Couple all other values to the values of the first layer:

```
CuPc[N].setD(CuPc.getD())

CuPc[N].setSigma(CuPc.getSigma())

void[N].setD(cp.getBilayerD()-CuPc.getD())

void[N].setSigma(void.getSigma())
```

The number of completely filled layers was automatically fitted by GenX. The number of incomplete (partially filled) layers was increased manually until the final value in the Figure-of-Merit (FOM), which is a measure for the goodness of the fit, was less than 0.1. Figure 74 shows the FOM-value and the fitted number of completely filled layers as a function of the manually chosen number of partially filled layers. Beyond 7 incomplete layers, the FOM-value did not drop further and the number of completely filled layers approached an integer value of 11 at 310 K and 12 at 400 K.
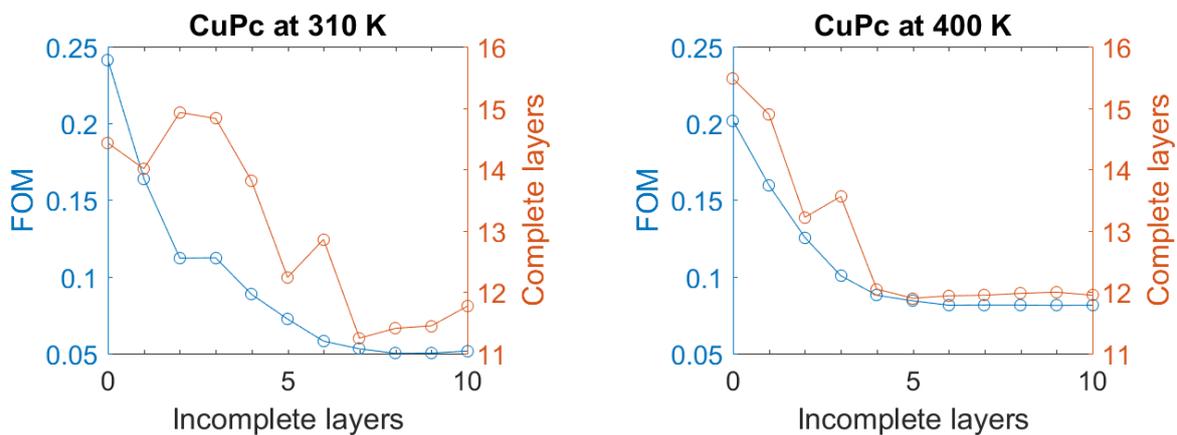
Figure 74: Final values resulting from the Figure-of-Merit (FOM) and fitted number of completely filled layers for various numbers of incomplete (partially filled) layers.

G. Counting Islands in AFM Images

In the beginning, the number of islands in an AFM image was counted in the conventional way by applying a threshold. Pixels whose height exceeds the threshold value were marked in black and assigned to the value -1. The remaining pixels were marked in white color and assigned to the value 0. Background noise was reduced by filling gaps inside the islands, i.e. changing the value of single white pixels inside the islands from 0 to -1, and by removing detached pixels, which means changing the value of single black pixels far apart from the islands from -1 to 0. The rim of each AFM image was set to zero in order to avoid boundary errors. In a second step, the computer went through the image line by line and started counting as soon as the cursor hit the first island. All pixels belonging to this island receive the number 1 and a randomly chosen color. The algorithm painting the island is shown below. It makes sure that the entire islands is painted and no pixel is left out. Then the cursor continues going through the image line by line until it hits the next island. All pixels of this islands receive the number 2 and another randomly chosen color and so on. Islands which were already counted (i.e. whose pixels are no longer assigned to the value -1) were ignored in order to ensure that they are not counted twice. This is why it is important to detect all pixels of an island before proceeding to the next island.

The following code was programmed in *Matlab*. It goes through the AFM image line by line:

```
for row = 1:1:rows
  for column = 1:1:columns
    if data(row,column) == -1
      counter = counter + 1;
      paint_pixels(row,column)
    end
  end % of columns
end % of rows
```

As soon as the cursor hits a pixel of an uncounted island (i.e. whose value is -1), the function "paint_pixels" is called. This function paints all pixels to the right and to the left until it hits the left and the right rim of the island, respectively. At the same time this function checks whether there are pixels above and below the current line belonging to the same island. If yes, then the function calls itself and repeats its procedure in the upper/lower line over and over until the entire island is painted. Of course, painting also means that the values of all pixels belonging to the present island are changed from -1 to the current island number, which is called by the value of the variable counter. This procedure is vital when counting extremely elongated, curved or ramified islands, for instance see the extremely ramified network of percolating islands in Fig. 35 or the elongated and curved islands of CuPc in Fig. 44.

H. Vertical Scan Through AFM Images

$3 \times 3\,\mu m^2$ AFM images of different C60 thin films were scanned vertically from bottom to top in steps of 0.05 nm. The number of islands was counted at each height and plotted in Fig. 75. The true number of islands was plotted as horizontal line for comparison. It results from a linear extrapolation of the relationship between island densities and step sizes and represents the expected value for infinitely small step sizes, see Fig. 37. As we can see, there is no threshold at which the number of islands is counted correctly making the extrapolation indispensable.
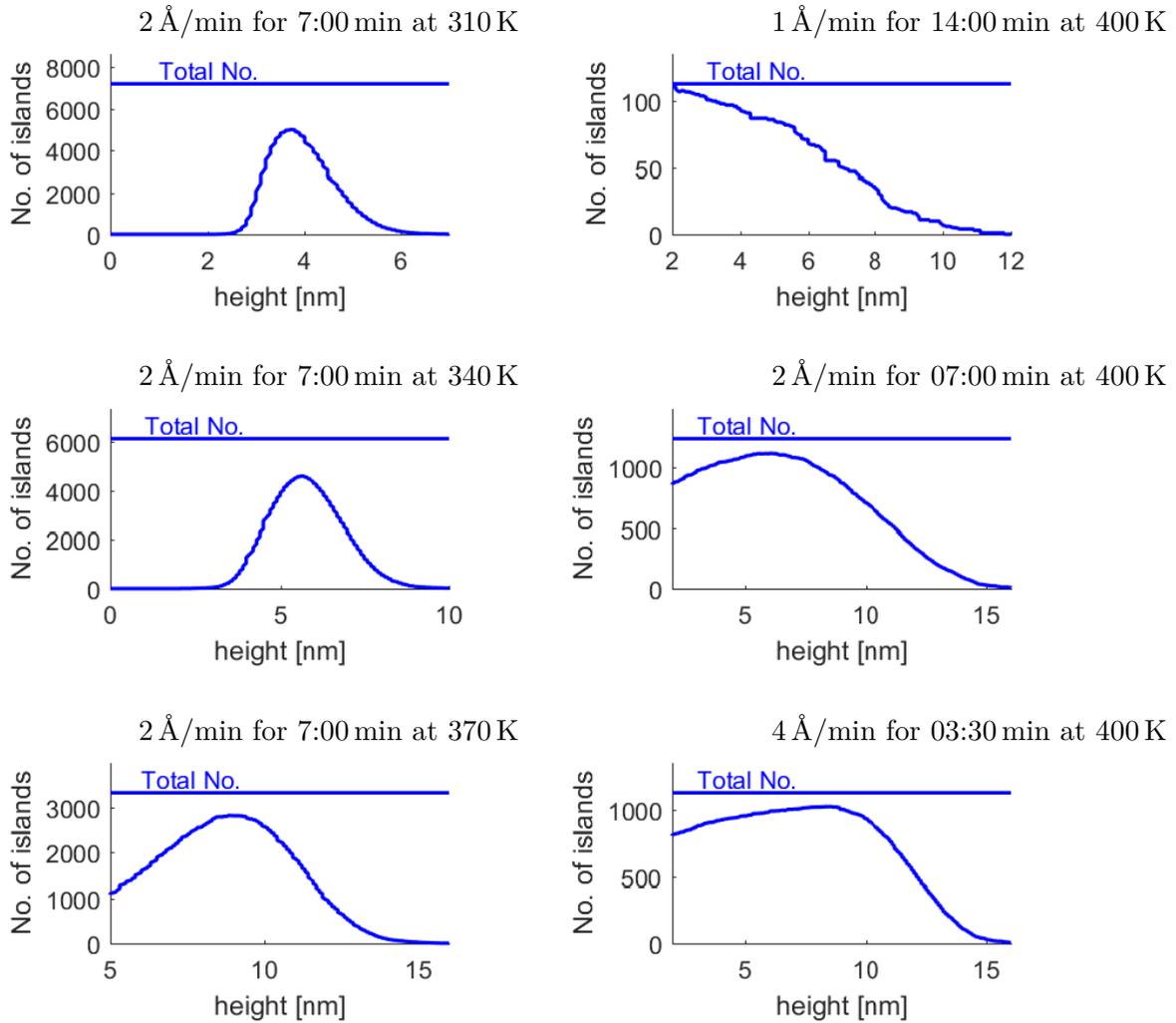
Figure 75: Number of detected islands at different threshold heights in $3 \times 3\,\mu m^2$ AFM images of C60 grown at different substrate temperatures and deposition rates. For comparison the total (true) number of islands.

I. AFM Images of C60 Thin Films

Different Substrate Temperatures (at 2 Å/min for 7:00 min)

The following four samples shown on this page were grown at a deposition rate of 2 Å/min for 7:00 min each at four different substrate temperatures (310 K, 340 K, 370 K and 400 K). The distribution of heights is shown on the left side of each $3\,\mu m \times 3\,\mu m$ AFM image together with the colorbar. The heights from 0 nm to 16 nm were divided into 100 height classes and the occurrence of each height is shown in percent. The total number N of counted islands is given in the upper right corner. Heights and diameters of all islands are plotted in the lower right inset of each AFM image. Each data point represents the height and the diameter of one of the islands.
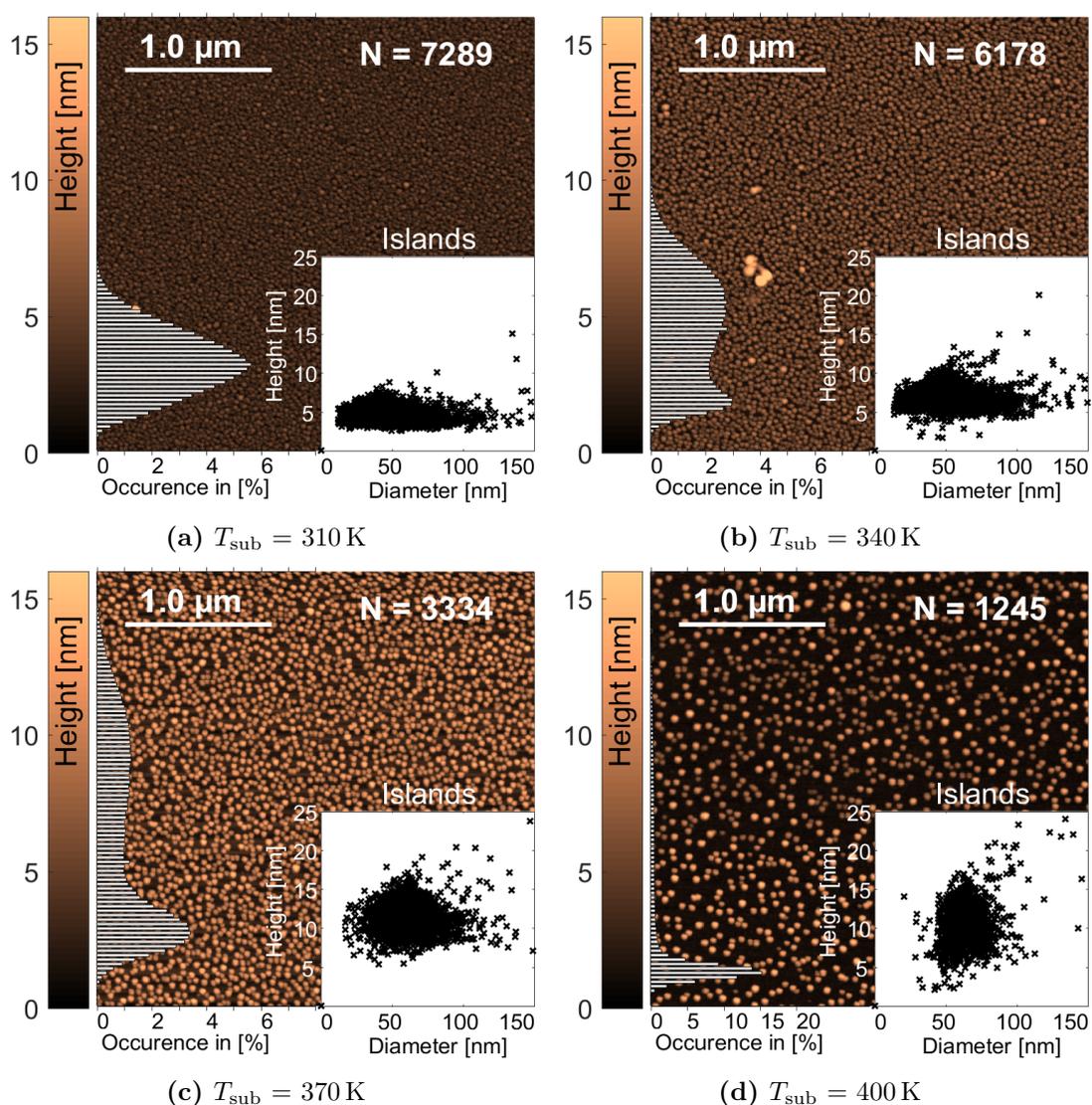
Figure 76: $3\,\mu m \times 3\,\mu m$ AFM images of 1.4 nm thin C60 films grown at 2 Å/min for 7:00 min at four different substrate temperatures T_{sub}.

Different Deposition Rates (at 400 K and an average thickness of 1.4 nm)

The following three samples shown on this page were grown at a substrate temperature of 400 K and three different deposition rates: 1 Å/min for 14:00 min (upper left), 4 Å/min for 3:30 min (upper right) and 2 Å/min for 7:00 min (lower image). The duration of deposition was chosen such that the effective amount of deposited material corresponds to an average height of 1.4 nm. The lower image was replotted here for comparison from Fig. 76 (last image on the lower right).

(a) $R_{\text{dep}} = 1\,\text{Å/min}$, $\Delta t = 14{:}00\,\text{min}$

(b) $R_{\text{dep}} = 4\,\text{Å/min}$, $\Delta t = 3{:}30\,\text{min}$

(c) $R_{\text{dep}} = 2\,\text{Å/min}$, $\Delta t = 7{:}00\,\text{min}$
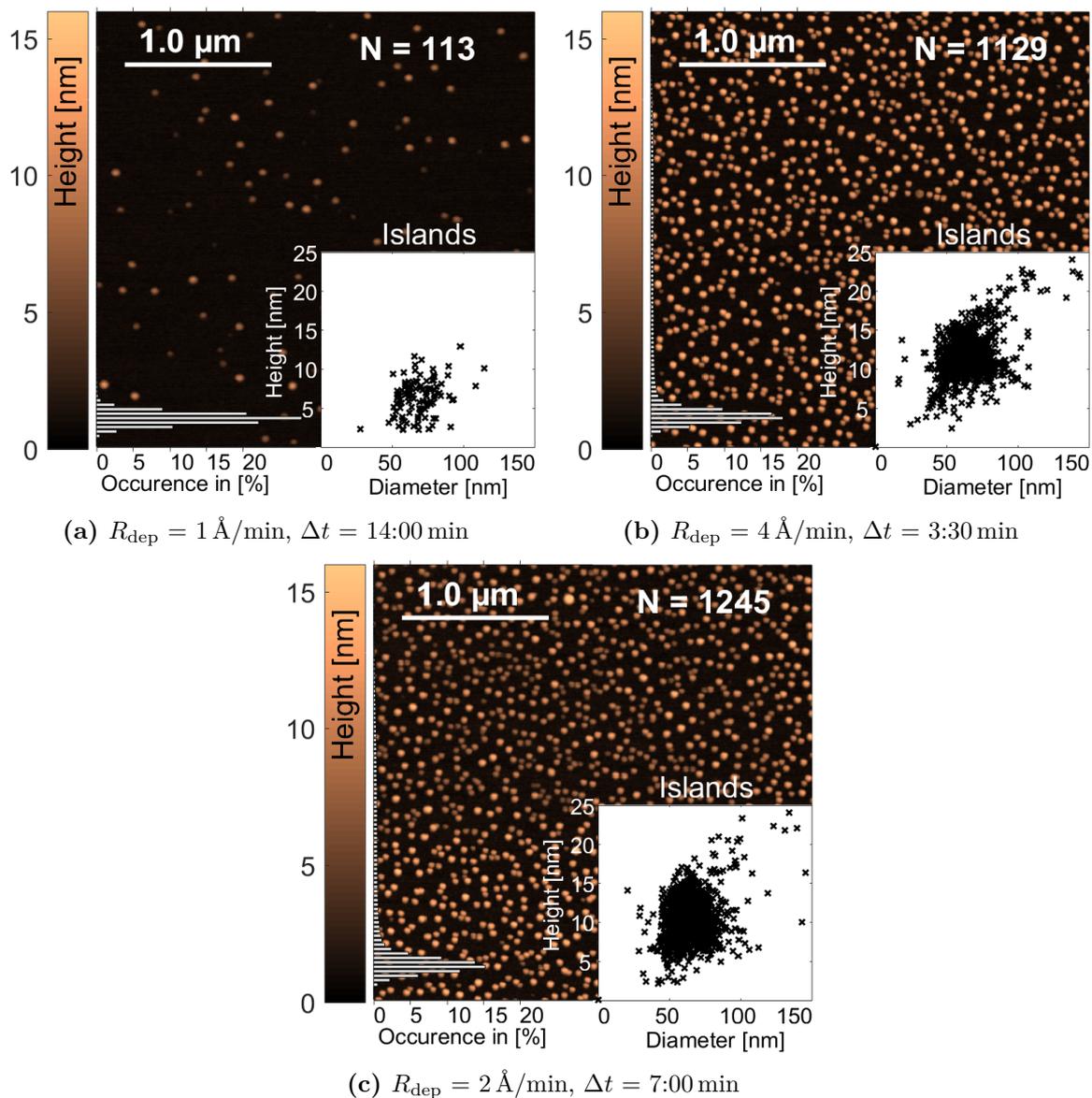
Figure 77: $3\,\mu m \times 3\,\mu m$ AFM images of 1.4 nm thin C60 films grown at a substrate temperature of 400 K at 1 Å/min for 14:00 min (upper left), at 4 Å/min for 3:30 min (upper right) and at at 2 Å/min for 7:00 min (lower)

Different Amount of Deposited Material (at 400 K and 2 Å/min)

The influence of the amount of deposited material was investigated by changing the duration of deposition at a constant deposition rate of 2 Å/min and a constant substrate temperature of 400 K.

(a) $\Delta t = 3{:}45\,\text{min}$

(b) $\Delta t = 11{:}15\,\text{min}$
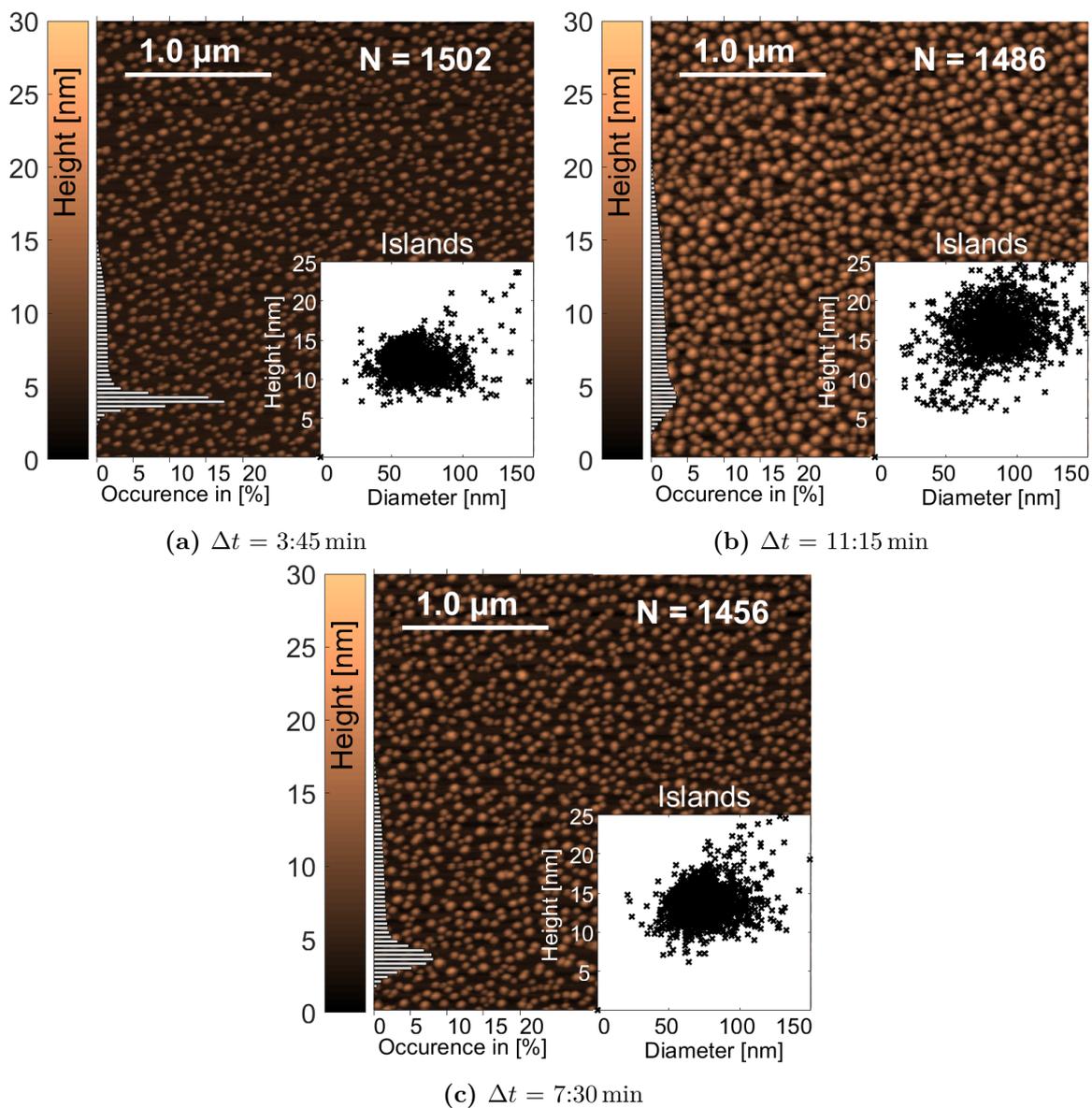
(c) $\Delta t = 7{:}30\,\text{min}$

Figure 78: $3\,\mu m \times 3\,\mu m$ AFM images of C60 thin films grown at $2\,\text{Å/min}$ and a substrate temperature of $400\,\text{K}$ for 3:45 min (upper left) 11:15 min (upper right) and 7:30 min (lower image).

J. Further SEM and HIM Images of CuPc-C60 Blends
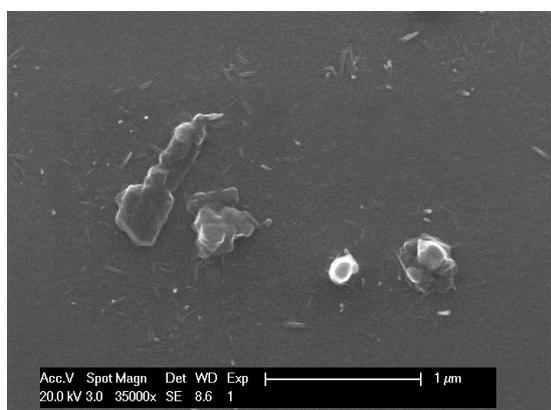
(a) 1:1-blend at 310 K, magn. $35\,000\times$
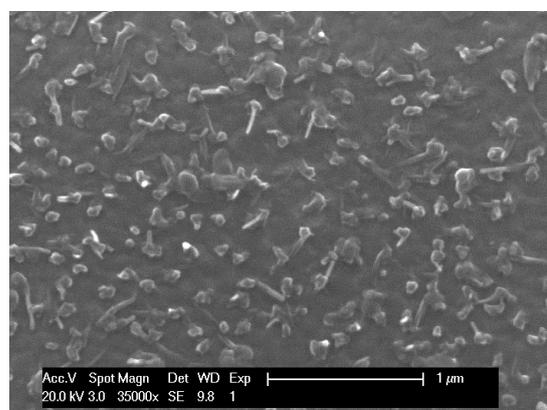
(b) 1:1-blend at 400 K, magn. $35\,000\times$
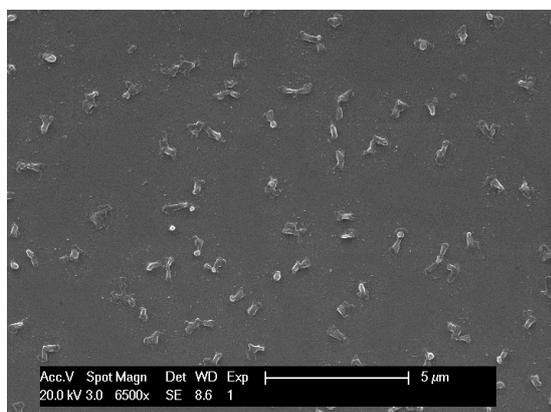
(c) 1:1-blend at 310 K, magn. $6\,500\times$
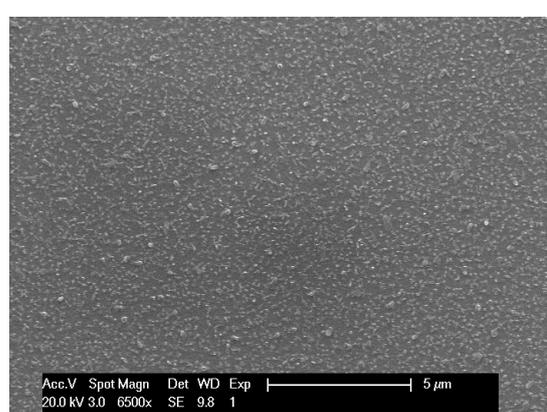
(d) 1:1-blend at 400 K, magn. $6\,500\times$
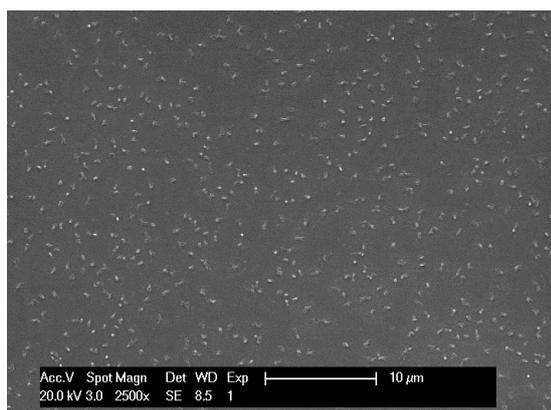
(e) 1:1-blend at 310 K, magn. $2\,500\times$

Figure 79: SEM images at different magnifications of blended CuPc-C60 thin films (molar ratio 1:1) grown at $310\,\mathrm{K}$ and at $400\,\mathrm{K}$. The islands are homogeneously distributed over the surface area. The island density is clearly lower at $310\,\mathrm{K}$ compared to $400\,\mathrm{K}$.
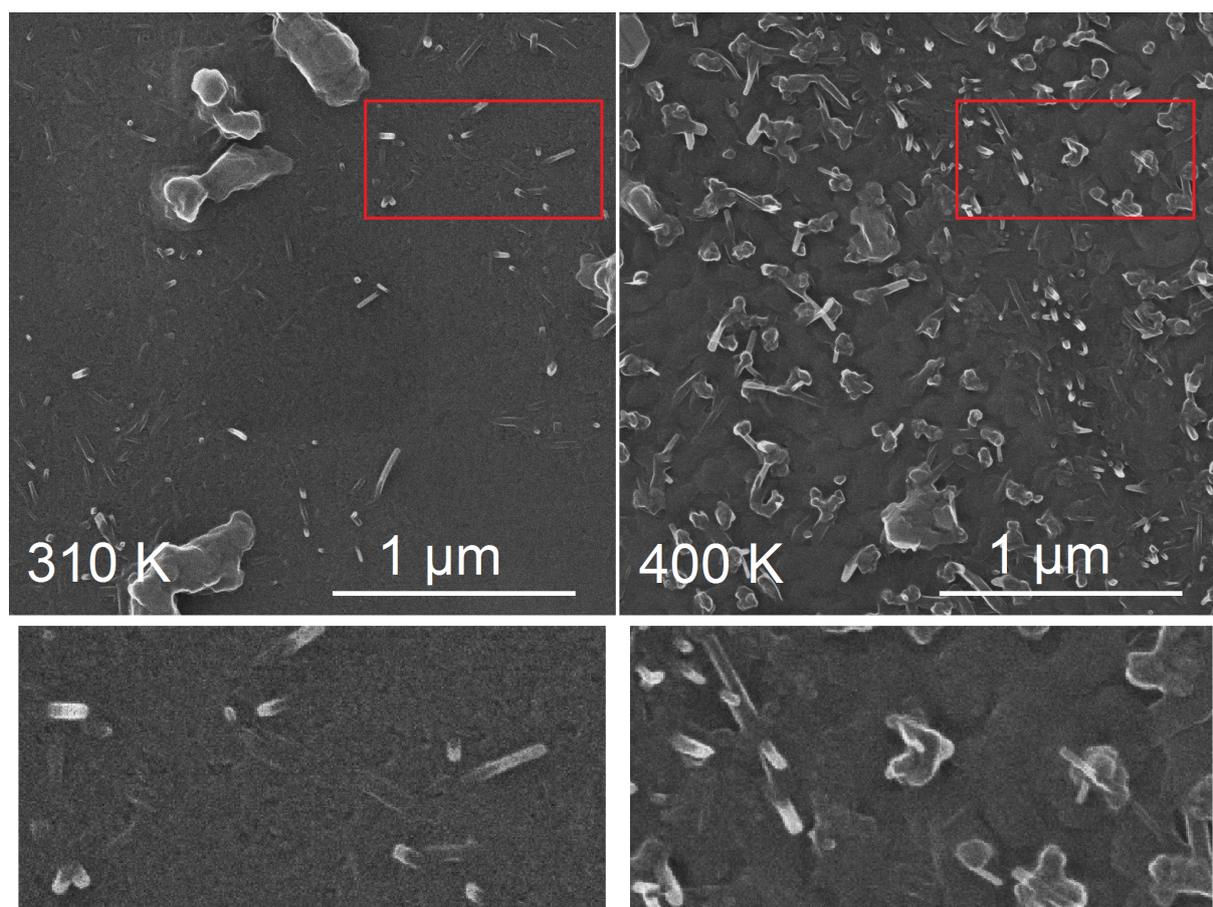
Figure 80: HIM images of blended CuPc-C60 thin films grown at 310 K and at 400 K. The areas within the red frames are enlarged below and show the needle-like CuPc crystals
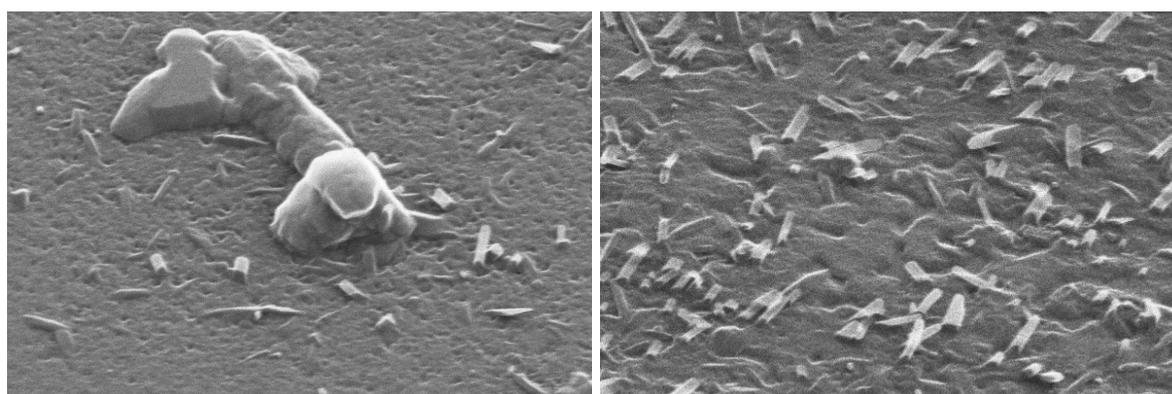
(a) 1:1-blend at 310 K

(b) 1:1-blend at 400 K

Figure 81: HIM images of blended CuPc-C60 thin films grown at 310 K and at 400 K and measured at an angle of 45°.

References

[1] S. R. Forrest, The path to ubiquitous and low-cost organic electronic appliances on plastic, *Nature* **428**, 911, doi:10.1038/nature02498 (2004).

[2] B. Ecker, Flexibel, leicht und durchsichtig, *Physik in unserer Zeit* **44**(2), 84, doi:10.1002/piuz.201301322 (2013).

[3] C. Deibel and V. Dyakonov, Polymer-fullerene bulk heterojunction solar cells, *Rep. Prog. Phys.* **73**(9), 096401, doi:10.1088/0034-4885/73/9/096401 (2010).

[4] J. Yoon, H. Kwon, M. Lee, Y.-y. Yu, N. Cheong, S. Min, J. Choi, H. Im, K. Lee, J. Jo, H. Kim, H. Choi, Y. Lee, C. Yoo, S. Kuk, M. Cho, S. Kwon, W. Park, S. Yoon, I. Kang, and S. Yeo, World 1st Large Size 18-inch Flexible OLED Display and the Key Technologies, *Information Dislpay* **46**, doi:10.1002/sdtp.10275 (2015).

[5] J.-Y. Yan, J.-C. Ho, and J. Chen, Foldable AMOLED Display Development: Progress and Challenges, *Information Display* **31**(1), 12, doi:10.1002/j.2637-496X.2015.tb00780.x (2015).

[6] C. I. Park, M. Seong, M. A. Kim, D. Kim, H. Jung, M. Cho, S. H. Lee, H. Lee, S. Min, J. Kim, M. Kim, J.-H. Park, S. Kwon, B. Kim, S. J. Kim, W. Park, J.-Y. Yang, S. Yoon, and I. Kang, World's first large size 77-inch transparent flexible OLED display, *Jnl Soc Info Display* **26**(5), 287, doi:10.1002/jsid.663 (2018).

[7] G. Witte and C. Wöll, Growth of aromatic molecules on solid substrates for applications in organic electronics, *J. Mater. Res.* **19**(7), 1889, doi:10.1557/JMR.2004.0251 (2004).

[8] S. R. Forrest, Ultrathin organic films grown by organic molecular beam deposition and related techniques, *Chem. Rev.* **97**(6), 1793, doi:10.1021/cr941014o (1997).

[9] D. Hertel and H. Bässler, Photoconduction in Amorphous Organic Solids, *ChemPhysChem* **9**(5), 666, doi:10.1002/cphc.200700575 (2008).

[10] C. W. Tang, Two-layer organic photovoltaic cell, *Appl. Phys. Lett.* **48**(2), 183, doi:10.1063/1.96937 (1986).

[11] P. Peumans, A. Yakimov, and S. R. Forrest, Small molecular weight organic thin-film photode-tectors and solar cells, *J. Appl. Phys.* **93**(7), 3693, doi:10.1063/1.1534621 (2003).

[12] D. Kurrle and J. Pflaum, Exciton diffusion length in the organic semiconductor diindenopery-lene, *Appl. Phys. Lett.* **92**(13), 133306, doi:10.1063/1.2896654 (2008).

[13] A. Opitz, J. Wagner, W. Brütting, I. Salzmann, N. Koch, J. Manara, J. Pflaum, A. Hin-derhofer, and F. Schreiber, Charge separation at molecular donor-acceptor interfaces: corre-lation between morphology and solar cell performance, *IEEE J. Sel. Top. Quant.* **16**, 1707, doi:10.1109/JSTQE.2010.2048096 (2010).

[14] B. P. Rand, J. Xue, S. Uchida, and S. R. Forrest, Mixed donor-acceptor molecular hetero-junctions for photovoltaic applications. I. Material properties, *J. Appl. Phys.* **98**, 124902, doi:10.1063/1.2142072 (2005).

[15] H. Kim, A. Piqué, J. S. Horwitz, H. Mattoussi, H. Murata, Z. H. Kafafi, and D. B. Chrisey, Indium tin oxide thin films for organic light-emitting devices, *Appl. Phys. Lett.* **74**(23), 3444, doi:10.1063/1.124122 (1999).

[16] K.-M. Lee, W.-H. Chiu, H.-Y. Wei, C.-W. Hu, V. Suryanarayanan, W.-F. Hsieh, and K.-C. Ho, Effects of mesoscopic poly(3,4-ethylenedioxythiophene) films as counter electrodes for dye-sensitized solar cells, *Thin Solid Films* **518**(6), 1716, doi:10.1016/j.tsf.2009.11.058 (2010).

[17] B. Lee, S. Jeong, Y. Cho, M. Jeong, S. M. Lee, J. Oh, and C. Yang, Highly Efficient Organic Photovoltaics Enhanced Using Organic Passivation Layer Vacuum Deposition, *Adv. Funct. Mater.* **30**(51), 2005037, doi:10.1002/adfm.202005037 (2020).

[18] J. You, L. Dou, K. Yoshimura, T. Kato, K. Ohya, T. Moriarty, K. Emery, C.-C. Chen, J. Gao, G. Li, and Y. Yang, A polymer tandem solar cell with 10.6% power conversion efficiency, *Nat Commun* **4**(1), doi:10.1038/ncomms2411 (2013).

[19] L. Meng, Y. Zhang, X. Wan, C. Li, X. Zhang, Y. Wang, X. Ke, Z. Xiao, L. Ding, R. Xia, H.-L. Yip, Y. Cao, and Y. Chen, Organic and solution-processed tandem solar cells with 17.3% efficiency, *Science* **361**(6407), 1094, doi:10.1126/science.aat2612 (2018).

[20] M. I. Alonso, M. Garriga, N. Karl, J. O. Ossó, and F. Schreiber, Anisotropic optical properties of single crystalline PTCDA studied by spectroscopic ellipsometry, *Org. Electron.* **3**, 23, doi:10.1016/S1566-1199(01)00027-1 (2002).

[21] T. Storzer, A. Hinderhofer, C. Zeiser, J. Novák, Z. Fišer, V. Belova, B. Reisz, S. Maiti, G. Duva, R. K. Hallani, A. Gerlach, J. E. Anthony, and F. Schreiber, Growth, Structure, and Anisotropic Optical Properties of Difluoro-anthradithiophene Thin Films, *J. Phys. Chem. C* **121**(38), 21011, doi:10.1021/acs.jpcc.7b06558 (2017).

[22] F. Gao, Z. Li, J. Wang, A. Rao, I. A. Howard, A. Abrusci, S. Massip, C. R. McNeill, and N. C. Greenham, Trap-Induced Losses in Hybrid Photovoltaics, *ACS Nano* **8**(4), 3213, doi:10.1021/nn501185h (2014).

[23] C. W. Tang and S. A. VanSlyke, Organic electroluminescent diodes, *Appl. Phys. Lett.* **51**(12), 913, doi:10.1063/1.98799 (1987).

[24] H. Yersin, Triplet Emitters for OLED Applications. Mechanisms of Exciton Trapping and Control of Emission Properties, pages 1–26 (Springer Berlin Heidelberg, Berlin, Heidelberg, 2004), doi:10.1007/b96858.

[25] O.-K. Kwon, Driving and System Consideratons of PM- and AM-OELDs, *Korean Science* pages 963–968 (2002).

[26] M. Han, AM backplane for AMOLED, *Proc. of ASID* pages 53–58 (2006).

[27] J.-S. Park, T.-W. Kim, D. Stryakhilev, J.-S. Lee, S.-G. An, Y.-S. Pyo, D.-B. Lee, Y. G. Mo, D.-U. Jin, and H. K. Chung, Flexible full color organic light-emitting diode display on polyimide plastic substrate driven by amorphous indium gallium zinc oxide thin-film transistors, *Appl. Phys. Lett.* **95**(1), 013503, doi:10.1063/1.3159832 (2009).

[28] G. Horowitz, Organic field-effect transistors, *Adv. Mater.* **10**(5), 365, doi:10.1002/(SICI)1521-4095(199803)10:5<365::AID-ADMA365>3.0.CO;2-U (1998).

[29] C. D. Dimitrakopoulos and P. R. L. Malenfant, Organic Thin Film Transistors for Large Area Electronics, *Adv. Mater.* **14**, 99, doi:10.1002/1521-4095(20020116)14:2<99::AID-ADMA99>3.0.CO;2-9 (2002).

[30] F. Garnier, A. Yassar, R. Hajlaoui, G. Horowitz, F. Deloffre, B. Servet, S. Ries, and P. Alnot, Molecular engineering of organic semiconductors: design of self-assembly properties in conjugated thiophene oligomers, *J. Am. Chem. Soc.* **115**(19), 8716, doi:10.1021/ja00072a026 (1993).

[31] J. G. Laquindanum, H. E. Katz, A. J. Lovinger, and A. Dodabalapur, Morphological Origin of High Mobility in Pentacene Thin-Film Transistors, *Chem. Mater.* **8**(11), 2542, doi:10.1021/cm9603664 (1996).

[32] S. F. Nelson, Y.-Y. Lin, D. J. Gundlach, and T. N. Jackson, Temperature-independent transport in high-mobility pentacene transistors, *Appl. Phys. Lett.* **72**(15), 1854, doi:10.1063/1.121205 (1998).

[33] O. D. Jurchescu, J. Baas, and T. T. M. Palstra, Effect of impurities on the mobility of single crystal pentacene, *Appl. Phys. Lett.* **84**(16), 3061, doi:10.1063/1.1704874 (2004).

[34] J. Schön, C. Kloc, and B. Batlogg, On the intrinsic limits of pentacene field-effect transistors, *Organic Electronics* **1**(1), 57, doi:10.1016/S1566-1199(00)00010-0 (2000).

[35] L. Zhou, A. Wanga, S.-C. Wu, J. Sun, S. Park, and T. N. Jackson, All-organic active matrix flexible display, *Appl. Phys. Lett.* **88**(8), 083502, doi:10.1063/1.2178213 (2006).

[36] M. Schwoerer and H. C. Wolf, Organische molekulare Festkörper (2005).

[37] J. H. Williams, The molecular electric quadrupole moment and solid-state architecture, *Acc. Chem. Res.* **26**(11), 593, doi:10.1021/ar00035a005v (1993).

[38] E. A. Meyer, R. K. Castellano, and F. Diederich, Interactions with Aromatic Rings in Chemical and Biological Recognition, *Angew. Chem. Int. Ed.* **42**(11), 1210, doi:10.1002/anie.200390319 (2003).

[39] K. Müller-Dethlefs and P. Hobza, Noncovalent Interactions: A Challenge for Experiment and Theory, *Chem. Rev.* **100**(1), 143, doi:10.1021/cr9900331 (2000).

[40] C. A. Hunter and J. K. M. Sanders, The nature of .pi.-.pi. interactions, *J. Am. Chem. Soc.* **112**(14), 5525, doi:10.1021/ja00170a016 (1990).

[41] A. I. Kitaigorodsky, In mixed crystals, chapter 4.2.1 Free energy of mixing, page 92 ff. (Springer series in solid state sciences, 1984).

[42] B. Reisz, Preparation and Characterization of Mixed Organic Thin Films Containing Sexithiophene and Perfluorinated Sexithiophene, Master's thesis, University of Tübingen (2015).

[43] A. Hinderhofer and F. Schreiber, Organic-organic heterostructures: Concepts and applications, *ChemPhysChem* **13**(3), 628, doi:10.1002/cphc.201100737 (2012).

[44] F. Family, Dynamic scaling and phase transitions in interface growth, *Physica A* **168**(1), 561, doi:10.1016/0378-4371(90)90409-L (1990).

[45] J. A. Venables, G. D. T. Spiller, and M. Hanbücken, Nucleation and growth of thin films, *Rep. Prog. Phys.* **47**(4), 399, doi:10.1088/0034-4885/47/4/002 (1984).

[46] J.-F. Gouyet, Physics and fractal structures, chapter 4. Growth Models, pages 157–181 (Springer Verlag, 1996).

[47] J. G. Amar and F. Family, Kinetics of submonolayer and multilayer epitaxial growth, *Thin Solid Films* **272**, 208, doi:10.1016/0040-6090(95)06947-X (1996).

[48] J. Krug, Origins of scale invariance in growth processes, *Adv. Phys.* **46**(2), 139, doi:10.1080/00018739700101498 (1997).

[49] J. Evans, P. Thiel, and M. Bartelt, Morphological evolution during epitaxial thin film growth: Formation of 2D islands and 3D mounds, *Surf. Sci. Rep.* **61**, 1, doi:10.1016/j.surfrep.2005.08.004 (2006).

[50] K. Pearson, The Problem of the Random Walk, *Nature* **72**(1867), 342, doi:10.1038/072342a0 (1905).

[51] S. Havlin and D. Ben-Avraham, Diffusion in disordered media, *Advances in Physics* **36**(6), 695, doi:10.1080/00018738700101072 (1987).

[52] M. Einax, W. Dieterich, and P. Maass, Colloquium: Cluster growth on surfaces: Densities, size distributions, and morphologies, *Rev. Mod. Phys.* **85**(3), 921, doi:10.1103/RevModPhys.85.921 (2013).

[53] M. Eden, Proceedings of the 4th Berkeley symposium on mathematical statistics and probability, chapter A Two Dimensional Growth Process, pages 223–240 (University of California Press, 1961).

[54] H. Herrmann, Geometrical cluster growth models and kinetic gelation, *Physics Reports* **136**(3), 153, doi:10.1016/0370-1573(86)90047-5 (1986).

[55] T. Williams and R. Bjerknes, Stochastic Model for Abnormal Clone Spread through Epithelial Basal Layer, *Nature* **236**(5340), 19, doi:10.1038/236019a0 (1972).

[56] T. A. Witten and L. M. Sander, Diffusion-Limited Aggregation, a Kinetic Critical Phenomenon, *Phys. Rev. Lett.* **47**(19), 1400, doi:10.1103/PhysRevLett.47.1400 (1981).

[57] L. M. Sander, Diffusion-limited aggregation: A kinetic critical phenomenon?, *Contemporary Physics* **41**(4), 203, doi:10.1080/001075100409698 (2000).

[58] M. Bartelt and J. Evans, Dendritic islands in metal-on-metal epitaxy I. Shape transitions and diffusion at island edges, *Surf. Sci.* **314**(1), L829, doi:10.1016/0039-6028(94)90203-8 (1994).

[59] M. Bartelt and J. Evans, Dendritic islands in metal-on-metal epitaxy II. Coalescence and multilayer growth, *Surface Science* **314**(1), L835, doi:10.1016/0039-6028(94)90204-6 (1994).

[60] S. Ogura, K. Fukutani, M. Matsumoto, T. Okano, M. Okada, and T. Kawamura, Dendritic to non-dendritic transitions in Au islands investigated by scanning tunneling microscopy and Monte Carlo simulations, *Phys. Rev. B* **73**(12), doi:10.1103/PhysRevB.73.125442 (2006).

[61] P. Meakin, Formation of Fractal Clusters and Networks by Irreversible Diffusion-Limited Aggregation, *Phys. Rev. Lett.* **51**(13), 1119, doi:10.1103/PhysRevLett.51.1119 (1983).

[62] M. Kolb, R. Botet, and R. Jullien, Scaling of Kinetically Growing Clusters, *Phys. Rev. Lett.* **51**(13), 1123, doi:10.1103/PhysRevLett.51.1123 (1983).

[63] P. A. Mulheran and J. A. Blackman, The origins of island size scaling in heterogeneous film growth, *Phil. Mag. Lett.* **72**, 55, doi:10.1080/09500839508241614 (1995).

[64] P. A. Mulheran and J. A. Blackman, Capture zones and scaling in homogeneous thin-film growth, *Phys. Rev. B* **53**, 10261, doi:10.1103/PhysRevB.53.10261 (1996).

[65] C. D. Pownall and P. A. Mulheran, Simulation and theory of island nucleation, growth, and coalescence on stepped substrates, *Phys. Rev. B* **60**, 9037, doi:10.1103/PhysRevB.60.9037 (1999).

[66] F. Family and P. Meakin, Kinetics of droplet growth process: simulations, theory, and experiment, *Phys. Rev. A* **40**, 3836, doi:10.1103/PhysRevA.40.3836 (1989).

[67] F. Haußer and A. Voigt, Ostwald ripening of two-dimensional homoepitaxial islands, *Phys. Rev. B* **72**(3), doi:10.1103/PhysRevB.72.035437 (2005).

[68] P. G. de Gennes, Wetting: statics and dynamics, *Rev. Mod. Phys.* **57**, 827, doi:10.1103/RevModPhys.57.827 (1985).

[69] J. G. Amar and F. Family, Critical Cluster Size: Island Morphology and Size Distribution in Sub-monolayer Epitaxial Growth, *Phys. Rev. Lett.* **74**(11), 2066, doi:10.1103/PhysRevLett.74.2066 (1995).

[70] V. Dubrovskii, Y. Berdnikov, D. Olyanich, V. Mararov, T. Utas, A. Zotov, and A. Saranin, Scaling of size distributions of C 60 and C 70 fullerene surface islands, *Appl. Surf. Sci.* **407**, 117, doi:10.1016/j.apsusc.2017.02.161 (2017).

[71] M. Groce, B. Conrad, W. Cullen, A. Pimpinelli, E. Williams, and T. Einstein, Temperature-dependent nucleation and capture-zone scaling of C60 on silicon oxide, *Surf. Sci.* **606**(1-2), 53, doi:10.1016/j.susc.2011.08.020 (2012).

[72] T. Vicsek and F. Family, Dynamic Scaling for Aggregation of Clusters, *Phys. Rev. Lett.* **52**(19), 1669, doi:10.1103/PhysRevLett.52.1669 (1984).

[73] G. Ehrlich and F. G. Hudda, Atomic View of Surface Self-Diffusion: Tungsten on Tungsten, *J. Chem. Phys.* **44**(3), 1039, doi:10.1063/1.1726787 (1966).

[74] J. E. Goose, E. L. First, and P. Clancy, Nature of step-edge barriers for small organic molecules, *Phys. Rev. B* **81**(20), 205310, doi:10.1103/PhysRevB.81.205310 (2010).

[75] A. Pimpinelli and J. Villain, Physics of Crystal Growth (Cambridge University Press, Cambridge, 1998).

[76] J. Tersoff, A. W. D. Vandergon, and R. M. Tromp, Critical Island Size for Layer-by-Layer Growth, *Phys. Rev. Lett.* **72**(2), 266, doi:10.1103/PhysRevLett.72.266 (1994).

[77] J. Krug, P. Politi, and T. Michely, Island nucleation in the presence of step-edge barriers: Theory and applications, *Phys. Rev. B* **61**, 14037, doi:10.1103/PhysRevB.61.14037 (2000).

[78] J. Villain, A. Pimpinelli, L. Tang, and D. Wolf, Terrace sizes in molecular beam epitaxy, *J. Phys. I France* **2**(11), 2107, doi:10.1051/jp1:1992271 (1992).

[79] E. Bauer and H. Poppa, Recent advances in epitaxy, *Thin Solid Films* **12**(1), 167, doi:10.1016/0040-6090(72)90412-9 (1972).

[80] K. Broch, Interplay of Ordering Behavior and Optical Properties in Organic Semiconductor Blends, Ph.D. thesis, University of Tübingen (2013).

[81] S. M. Hu, Misfit dislocations and critical thickness of heteroepitaxy, *J. Appl. Phys.* **69**(11), 7901, doi:10.1063/1.347476 (1991).

[82] J. Kertesz and D. E. Wolf, Noise reduction in Eden models: II. Surface structure and intrinsic width, *J. Phys. A: Math. Gen.* **21**(3), 747, doi:10.1088/0305-4470/21/3/030 (1988).

[83] M. J. Vold, Sediment Volume and Structure in Dispersions of Anisometric Particles, *J. Phys. Chem.* **63**(10), 1608, doi:10.1021/j150580a011 (1959).

[84] K. L. Chopra, Thin Film Phenomena (McGraw-Hill, New York, 1969).

[85] J. Krug, Four lectures on the physics of crystal growth, *Physica A* **313**(1-2), 47, doi:10.1016/S0378-4371(02)01034-8 (2002).

[86] J. Krug, On the shape of wedding cakes, *J. Stat. Phys.* **87**(3), 505, doi:10.1007/BF02181234 (1997).

[87] M. Kalff, G. Comsa, and T. Michely, How Sensitive is Epitaxial Growth to Adsorbates?, *Phys. Rev. Lett.* **81**(6), 1255, doi:10.1103/PhysRevLett.81.1255 (1998).

[88] F. Family, Scaling of rough surfaces: effects of surface diffusion, *J. Phys. A: Math. Gen.* **19**(8), L441, doi:10.1088/0305-4470/19/8/006 (1986).

[89] M. Kardar, G. Parisi, and Y. Zhang, Dynamic scaling of growing interfaces, *Phys. Rev. Lett.* **56**(9), 889, doi:10.1103/PhysRevLett.56.889 (1986).

[90] S. F. Edwards and W. D. R, The surface statistics of a granular aggregate, *Proceedings of the Royal Society London A* **381**, 17, doi:10.1098/rspa.1982.0056 (1982).

[91] N. B. McKeown, Phthalocyanine Materials - Synthesis, Structure and Function, chapter 1 An Introduction to Phthalocyanines, page 3 (Cambridge University Press, 1998).

[92] I. G. Hill and A. Kahn, Combined photoemission/*in vacuo* transport study of the indium tin oxide/copper phthalocyanine/N,N'-diphenyl-N,N'-bis(l-naphthyl)-1,1'biphenyl-4,4''diamine molecular organic semiconductor system, *J. Appl. Phys.* **86**(4), 2116, doi:10.1063/1.371018 (1999).

[93] H. Riel, S. Barth, T. A. Beierlein, W. Brütting, S. Karg, P. Müller, and W. Riess, Grading interfaces: a new concept to improve device performance in organic multilayer light-emitting diodes, *Proc. SPIE* **4105**(1), 167, doi:10.1117/12.416891 (2001).

[94] Z. Bao, A. Lovinger, and A. Dodabalapur, Organic Field-Effect Transistors with High Mobility Based on Copper Phthalocyanine, *Appl. Phys. Lett.* **69**, 3066, doi:10.1063/1.116841 (1996).

[95] O. Berger, W.-J. Fischer, B. Adolphi, S. Tierbach, V. Melev, and J. Schreiber, Studies on phase transformations of Cu-phthalocyanine thin films, *J. Mater. Sci. Mater. Electron.* **11**(4), 331, doi:10.1023/A:1008933516940 (2000).

[96] T. Nonaka, Y. Nakagawa, Y. Mori, M. Hirai, T. Matsunobe, M. Nakamura, T. Takahagi, A. Ishitani, H. Lin, and K. Koumoto, Epitaxial growth of α-copper phthalocyanine crystal on Si(001) substrate by organic molecular beam deposition, *Thin Solid Films* **256**(1-2), 262, doi:10.1016/0040-6090(94)06304-4 (1995).

[97] R. Hiesgen, M. Räbisch, H. Böttcher, and D. Meissner, STM investigation of the growth structure of Cu-phthalocyanine films with submolecular resolution, *Sol. Energ. Mat. Sol. Cells* **61**, 73, doi:10.1016/S0927-0248(99)00098-7 (2000).

[98] M. Ashida, N. Uyeda, and E. Suito, Unit Cell Metastable-form Constants of Various Phthalocyanines, *Bull. Chem. Soc. Jpn.* **39**, 2616, doi:10.1246/bcsj.39.2616 (1966).

[99] A. Hoshino, Y. Takenaka, and H. Miyaji, Redetermination of the crystal structure of α-copper phthalocyanine grown on KCl, *Acta Cryst.* **B59**(3), 393, doi:10.1107/S010876810300942X (2003).

[100] J. M. Robertson, An X-Ray Study of the Structure of the Phthalocyanines. Part I. The Metal Free, Nickel, Copper, and Platinum Compounds, *J. Chem. Soc.* **136**, 615, doi:10.1039/jr9350000615 (1935).

[101] C. Brown, Crystal structure of β-copper phthalocyanine, *J. Chem. Soc., A.* **A**, 2488 , doi:10.1039/J19680002488 (1968).

[102] F. A. Hamm and E. Van Norman, Transformations in Organic Pigments, *J. Appl. Phys.* **19**(12), 1097, doi:10.1063/1.1715026 (1948).

[103] G. Susich, Identification of Organic Dyestuffs by X-Ray Powder Diffraction, *Anal. Chem.* **22**(3), 425, doi:10.1021/ac60039a012 (1950).

[104] A. A. Ebert and H. B. Gottlieb, Infrared Spectra of Organic Compounds Exhibiting Polymorphism, *J. Am. Chem. Soc.* **74**(11), 2806, doi:10.1021/ja01131a031 (1952).

[105] J. W. Eastes, Preparation of Phthalocyanine Pigments (1956), uS Patent 2.

[106] J. M. Assour, On the Polymorphic Modifications of Phthalocyanines, *J. Phys. Chem.* **69**(7), 2295, doi:10.1021/j100891a026 (1965).

[107] M. T. Robinson and G. E. Klein, Unit Cell Constants of α-Copper Phthalocyanine, *J. Am. Chem. Soc.* **74**(24), 6294, doi:10.1021/ja01144a520 (1952).

[108] F. W. Karasek and J. C. Decius, Observations Concerning Polymorphic Crystalline Modifications of the Phthalocyanines, *J. Am. Chem. Soc.* **74**(18), 4716, doi:10.1021/ja01138a518 (1952).

[109] E. Suito, N. Uyeda, and M. Ashida, Epitaxial Growth of Condensed Aromatic Polycyclic Compounds, *Nature* **194**(4825), 273, doi:10.1038/194273a0 (1962).

[110] B. Honigmann, H.-U. Lenné, and R. Schrodel, Beziehungen zwischen den Strukturen der Modifikationen des Platin- und Kupferphthalocyanins und einiger Chlorderivate, *Zeitschrift für Kristallographie* **122**, 158, doi:10.1515/zkri-1965-1-618 (1965).

[111] C. R. Groom, I. J. Bruno, M. P. Lightfoot, and S. C. Ward, The Cambridge Structural Database, *Acta Crystallogr. B* **72**(2), 171, doi:10.1107/s2052520616003954 (2016).

[112] M. K. Debe, R. J. Poirier, D. D. Erickson, T. N. Tommet, D. R. Field, and K. M. White, Effect of Gravity on Copper Phthalocyanine Thin Films I: Enhanced Smoothness and Local Homogeneity of Copper Phthalocyanine Thin Films Grown in a Microgravity Environment, *Thin Solid Films* **186**, 257, doi:10.1016/0040-6090(90)90147-6 (1990).

[113] M. K. Debe and R. J. Poirier, Effect of Gravity on Copper Phthalocyanine Thin Films I: Microstructure Comparisons of Copper Phthalocyanine Thin Films Grown in Microgravity and Unit Gravity, *Thin Solid Films* **186**, 327, doi:10.1016/0040-6090(90)90149-8 (1990).

[114] M. Debe and K. Kam, Effect of gravity on copper phthalocyanine thin films II: Spectroscopic evidence for a new oriented thin film polymorph of copper phthalocyanine grown in a microgravity enviroment, *Thin Solid Films* **186**(2), 289, doi:10.1016/0040-6090(90)90148-7 (1990).

[115] M. K. Debe, R. J. Poirier, and K. K. Kam, Organic-Thin-Film-Induced Molecular Epitaxy from the Vapor Phase, *Thin Solid Films* **197**, 335, doi:10.1016/0040-6090(91)90244-R (1991).

[116] M. K. Debe and D. R. Field, Variable angle spectroscopic ellipsometry studies of oriented phthalocyanine films, *J. Vac. Sci. Technol. A* **9**(3), 1265, doi:10.1116/1.577610 (1991).

[117] M. K. Debe, Variable angle spectroscopic ellipsometry studies of oriented phthalocyanine films. II. Copper phthalocyanine, *J. Vac. Sci. Technol. A* **10**(4), 2816, doi:10.1116/1.577916 (1992).

[118] S. Heutz, S. M. Bayliss, R. L. Middleton, G. Rumbles, and T. S. Jones, Polymorphism in Phthalocyanine Thin Films: Mechanism of the $\alpha \to \beta$ Transition, *J. Phys. Chem. B* **104**(30), 7124, doi:10.1021/jp0000836 (2000).

[119] E. A. Rohlfing, D. M. Cox, and A. Kaldor, Production and characterization of supersonic carbon cluster beams, *The Journal of Chemical Physics* **81**(7), 3322, doi:10.1063/1.447994 (1984).

[120] H. W. Kroto, J. R. Heath, S. C. OB́rien, R. F. Curl, and R. E. Smalley, C_{60}: Buckminsterfullerene, *Nature* **318**(6042), 162, doi:10.1038/318162a0 (1985).

[121] H. Kroto, Space, Stars, C60, and Soot, *Science* **242**(4882), 1139, doi:10.1126/science.242.4882.1139 (1988).

[122] W. I. F. David, R. M. Ibberson, J. C. Matthewman, K. Prassides, T. J. S. Dennis, J. P. Hare, H. W. Kroto, R. Taylor, and D. R. M. Walton, Crystal structure and bonding of ordered C_{60}, *Nature* **353**(6340), 147, doi:10.1038/353147a0 (1991).

[123] H.-B. Bürgi, E. Blanc, D. Schwarzenbach, S. Liu, Y.-j. Lu, M. M. Kappes, and J. A. Ibers, The Structure of C60: Orientational Disorder in the Low-Temperature Modification of C60, *Angew. Chem. Int. Ed. Engl.* **31**(5), 640, doi:10.1002/anie.199206401 (1992).

[124] J. L. de Boer, S. van Smaalen, V. Petricek, M. Dusek, M. A. Verheijen, and G. Meijer, Hexagonal close-packed C_{60}, *Chem. Phys. Lett.* **219**(5–6), 469, doi:10.1016/0009-2614(94)00110-3 (1994).

[125] A. Bondi, Van der Waals Volumes and Radii, *J. Phys. Chem. C* **68**(3), 441, doi:10.1021/j100785a001 (1964).

[126] L. A. Girifalco, Molecular properties of fullerene in the gas and solid phases, *J. Phys. Chem.* **96**(2), 858, doi:10.1021/j100181a061 (1992).

[127] P. A. Gravil, M. Devel, P. Lambin, X. Bouju, C. Girard, and A. A. Lucas, Adsorption of C_{60} molecules, *Phys. Rev. B* **53**(3), 1622, doi:10.1103/PhysRevB.53.1622 (1996).

[128] L. A. A. Pettersson, L. S. Roman, and O. Inganas, Modeling photocurrent action spectra of photovoltaic devices based on organic thin films, *J. Appl. Phys.* **86**(1), 487, doi:10.1063/1.370757 (1999).

[129] P. Peumans and S. R. Forrest, Very-high-efficiency double-heterostructure copper phthalocyanine/C60 photovoltaic cells, *Appl. Phys. Lett.* **79**(1), 126, doi:10.1063/1.1384001 (2001).

[130] C. Joachim, J. K. Gimzewski, and A. Aviram, Electronics using hybrid-molecular and mono-molecular devices, *Nature* **408**(6812), 541, doi:10.1038/35046000 (2000).

[131] H. Park, J. Park, A. K. L. Lim, E. H. Anderson, A. P. Alivisatos, and P. L. McEuen, Nanomechanical oscillations in a single-C60 transistor, *Nature* **407**(6800), 57, doi:10.1038/35024031 (2000).

[132] J. Weckesser, J. V. Barth, and K. Kern, Mobility and bonding transition of C_{60} on Pd(110), *Phys. Rev. B* **64**(16), doi:10.1103/PhysRevB.64.161403 (2001).

[133] F. Loske, J. Lübbe, J. Schütte, M. Reichling, and A. Kühnle, Quantitative description of C_{60} diffusion on an insulating surface, *Phys. Rev. B* **82**(15), doi:10.1103/PhysRevB.82.155428 (2010).

[134] A. Matetskiy, L. Bondarenko, D. Gruznev, A. Zotov, A. Saranin, J. Chou, C. Hsing, C. Wei, and Y. Wang, Peculiar diffusion of C60 on In-adsorbed Si(111)$\sqrt{(3)} \times \sqrt{(3)}$-Au surface, *Surf. Sci.* **616**, 44, doi:10.1016/j.susc.2013.05.011 (2013).

[135] N. Sibirev, V. Dubrovskii, A. Matetskiy, L. Bondarenko, D. Gruznev, A. Zotov, and A. Saranin, Size distributions of fullerene surface clusters, *Appl. Surf. Sci.* **307**, 46, doi:10.1016/j.apsusc.2014.03.132 (2014).

[136] D. Olyanich, V. Mararov, T. Utas, A. Zotov, and A. Saranin, C 70 self-assembly on In- and Tl-adsorbed Si(111)$\sqrt{(3)} \times \sqrt{(3)}$-Au surfaces, *Surf. Sci.* **656**, 1, doi:10.1016/j.susc.2016.09.005 (2017).

[137] Y. Z. LI, M. Chander, J. C. Patrin, J. H. Weaver, L. P. F. Chibante, and R. E. Smalley, Order and Disorder in C60 and KxC60 Multilayers: Direct Imaging with Scanning Tunneling Microscopy, *Science* **253**(5018), 429, doi:10.1126/science.253.5018.429 (1991).

[138] T. Thundat, R. J. Warmack, D. Ding, and R. N. Compton, Atomic force microscope investigation of C_{60} adsorbed on silicon and mica, *Appl. Phys. Lett.* **63**(7), 891, doi:10.1063/1.109892 (1993).

[139] T. Sato, T. Sueyoshi, and M. Iwatsuki, Multilayer growth process of C60 on a Si(111) 7 × 7 surface, *Surf. Sci.* **321**(1-2), L137, doi:10.1016/0039-6028(94)90017-5 (1994).

[140] S. A. Burke, J. M. Mativetsky, S. Fostner, and P. Grütter, C60 on alkali halides: Epitaxy and morphology studied by noncontact AFM, *Phys. Rev. B* **76**(3), doi:10.1103/PhysRevB.76.035419 (2007).

[141] M. Körner, F. Loske, M. Einax, A. Kühnle, M. Reichling, and P. Maass, Second-Layer Induced Island Morphologies in Thin-Film Growth of Fullerenes, *Phys. Rev. Lett.* **107**(1), doi:10.1103/PhysRevLett.107.016101 (2011).

[142] S. Bommel, H. Spranger, C. Weber, N. Kleppmann, S. V. Roth, S. H. L. Klapp, and S. Kowarik, Thermally-activated post-growth dewetting of fullerene C60 on mica, *Phys. Status Solidi RRL* **9**(11), 646, doi:10.1002/pssr.201510258 (2015).

[143] S. Bommel, N. Kleppmann, C. Weber, H. Spranger, P. Schäfer, J. Novák, S. Roth, F. Schreiber, S. Klapp, and S. Kowarik, Unravelling the multilayer growth of the fullerene C_{60} in real time, *Nat. Comm.* **5**, 5388, doi:10.1038/ncomms6388 (2014).

[144] Y. M. Acevedo, R. A. Cantrell, P. G. Berard, D. L. Koch, and P. Clancy, Multiscale Simulation and Modeling of Multilayer Heteroepitactic Growth of C60 on Pentacene, *Langmuir* **32**(12), 3045, doi:10.1021/acs.langmuir.5b04500 (2016).

[145] J. M. Robertson and J. G. White, The crystal structure of coronene: a quantitative X-ray investigation, *J. Chem. Soc.* doi:10.1039/jr9450000607 (1945).

[146] T. M. Krygowski, M. Cyrański, A. Ciesielski, B. Świrska, and P. Leszczyński, Separation of the Energetic and Geometric Contributions to Aromaticity. 2. Analysis of the Aromatic Character of Benzene Rings in Their Various Topological Environments in the Benzenoid Hydrocarbons. Crystal and Molecular Structure of Coronene, *J. Chem. Inf. Comput. Sci.* **36**(6), 1135, doi:10.1021/ci960367g (1996).

[147] J. M. Robertson and J. G. White, Crystal Structure of Coronene, *Nature* **154**(3915), 605, doi:10.1038/154605a0 (1944).

[148] J. Potticary, L. R. Terry, C. Bell, A. N. Papanikolopoulos, P. C. M. Christianen, H. Engelkamp, A. M. Collins, C. Fontanesi, G. Kociok-Köhn, S. Crampin, E. Da Como, and S. R. Hall, An unforeseen polymorph of coronene by the application of magnetic fields during crystal growth, *Nat Comms* **7**, 11555, doi:10.1038/ncomms11555 (2016).

[149] B. N. Dutta, Lattice constants and thermal expansion of silicon up to 900°C by X-ray method, *phys. stat. sol. (b)* **2**(8), 984, doi:10.1002/pssb.19620020803 (1962).

[150] K. A. Hofmann, U. Hofmann, and W. Rüdorff (Editors), Anorganische Chemie, volume 1, page 365 (Springer-Verlag Wiesbaden, 1973), 21 edition.

[151] J. A. Venables, Introduction to Surface and Thin Film Processes, chapter 2. Surfaces in vacuum: Ultra-high vacuum techniques and processes, pages 36 – 62 (Cambridge University Press, 2000).

[152] K. A. Ritley, B. Krause, F. Schreiber, and H. Dosch, A portable ultrahigh vacuum organic molecular beam deposition system for *in situ* x-ray diffraction measurements, *Rev. Sci. Instrum.* **72**, 1453, doi:10.1063/1.1336822 (2001).

[153] A. Patterson, The Scherrer Formula of X-Ray particle size determination, *Phys. Rev.* **56**, 978, doi:10.1103/PhysRev.56.978 (1939).

[154] J. Instruments, The JPK NanoWizard II AFM User Manual (2007), sPM Software Release 3.1.

[155] J. Instruments, The NanoWizard AFM Handbook (2005), version 1.3.

[156] L. Reimer, Scanning Electron Microscopy, Physics of Image Formation and Microanalysis (1998).

[157] E. N. Maslen, A. Fox, and M. A. O'Keefe, International Tables for Crystallography, volume C: Mathematical, physical and chemical tables, chapter 6.1.1. X-ray Scattering, pages 554–590 (International Union of Crystallography, 2006), table 6.1.1.4. on p. 578.

[158] T. Hahn and A. Looijenga-Voss, International Tables for Crystallography, volume A: Space-group symmetry, chapter 2.2.13. Reflection Conditions, pages 29–32 (International Union of Crystallography, 2006), table 2.2.13.2. and 2.2.13.3.

[159] M. I. Aroyo, J. M. Perez-Mato, C. Capillas, E. Kroumova, S. Ivantchev, G. Madariaga, A. Kirov, and H. Wondratschek, Bilbao Crystallographic Server: I. Databases and crystallographic computing programs, *Zeitschrift für Kristallographie* **221**(1), 15, doi:10.1524/zkri.2006.221.1.15 (2006).

[160] S. R. Hall, J. D. Westbrook, N. Spadaccini, I. D. Brown, H. J. Bernstein, and B. McMahon, International Tables for Crystallography, volume G: Definition and exchange of crystallographic data, chapter 2.2. Specification of Crystallographic Information File (CIF), pages 20–36 (International Union of Crystallography, 2006), 2.2.3. The Syntax of a CIF.

[161] S. S. Batsanov, Van der Waals Radii of Elements, *Inorg. Mater.* **37**(9), 871, doi:10.1023/A:1011625728803 (2001).

[162] S. Alvarez, A cartography of the van der Waals territories, *Dalton Trans.* **42**(24), 8617, doi:10.1039/c3dt50599e (2013).

[163] M. Björck and G. Andersson, GenX: An extensible X-ray reflectivity refinement program utilizing differential evolution, *J. Appl. Cryst.* **40**, 1174, doi:10.1107/S0021889807045086 (2007).

[164] G. Cerofolini, Roughness and crystal size of evaporated metal films, *Thin Solid Films* **27**(2), 297, doi:10.1016/0040-6090(75)90036-X (1975).

[165] F. Family and T. Vicsek, Scaling of the active zone in the Eden process on percolation networks and the ballistic deposition model, *J. Phys. A: Math. Gen.* **18**(2), L75, doi:10.1088/0305-4470/18/2/005 (1985).

[166] D. E. Wolf and J. Villain, Growth with Surface Diffusion, *Europhys. Lett.* **13**, 389, doi:10.1209/0295-5075/13/5/002 (1990).

[167] M. Nakamura, Morita, Y. Mori, A. Ishitani, and H. Tokumoto, Molecular Arrangement of Copper Phthalocyanine on Hydrogen-Terminated Si(111): Influence of Surface Roughness, *J. Vac. Sci. Technol. B* **14**, 1109, doi:10.1116/1.588409 (1996).

[168] A. Hinderhofer, A. Gerlach, K. Broch, T. Hosokai, K. Yonezawa, K. Kato, S. Kera, N. Ueno, and F. Schreiber, Geometric and electronic structure of templated C_{60} on diindenoperylene thin films, *J. Phys. Chem. C* **117**(2), 1053, doi:10.1021/jp3106056 (2013).

[169] Y. Nakayama, Y. Mizuno, T. Hosokai, T. Koganezawa, R. Tsuruta, A. Hinderhofer, A. Gerlach, K. Broch, V. Belova, H. Frank, M. Yamamoto, J. Niederhausen, H. Glowatzki, J. P. Rabe, N. Koch, H. Ishii, F. Schreiber, and N. Ueno, Epitaxial Growth of an Organic p–n Heterojunction: C_{60} on Single-Crystal Pentacene, *ACS Appl. Mater. Interfaces* **8**(21), 13499, doi:10.1021/acsami.6b02744 (2016).

[170] S. Veenstra, G. Malliaras, H. Brouwer, F. Esselink, V. Krasnikov, P. van Hutten, J. Wildeman, H. Jonkman, G. Sawatzky, and G. Hadziioannou, Sexithiophene-C_{60} blends as model systems for photovoltaic devices, *Synth. Met.* **84**(1-3), 971, doi:10.1016/S0379-6779(96)04235-X (1997).

[171] C. Lorch, K. Broch, V. Belova, G. Duva, A. Hinderhofer, A. Gerlach, M. Jankowski, and F. Schreiber, Growth and annealing kinetics of α-sexithiophene and fullerene C60 mixed films, *J Appl Crystallogr* **49**(4), 1266, doi:10.1107/S1600576716009936 (2016).

[172] R. Banerjee, J. Novák, C. Frank, C. Lorch, A. Hinderhofer, A. Gerlach, and F. Schreiber, Evidence for Kinetically Limited Thickness Dependent Phase Separation in Organic Thin Film Blends, *Phys. Rev. Lett.* **110**(18), 185506 (1, doi:10.1103/PhysRevLett.110.185506 (2013).

[173] C. Lorch, J. Novák, R. Banerjee, S. Weimer, J. Dieterle, C. Frank, A. Hinderhofer, A. Gerlach, F. Carla, and F. Schreiber, Influence of C60 co-deposition on the growth kinetics of diindenoperylene - From rapid roughening to layer-by-layer growth in blended organic films, *J. Chem. Phys.* **146**(5), 052807, doi:10.1063/1.4966583 (2017).

[174] I. Salzmann, S. Duhm, R. Opitz, R. L. Johnson, J. P. Rabe, and N. Koch, Structural and electronic properties of pentacene-fullerene heterojunctions, *J. Appl. Phys.* **104**(11), 114518, doi:10.1063/1.3040003 (2008).

[175] C. Schünemann, D. Wynands, L. Wilde, M. Hein, S. Pfützner, C. Elschner, K.-J. Eichhorn, K. Leo, and M. Riede, Phase separation analysis of bulk heterojunctions in small-

molecule organic solar cells using zinc-phthalocyanine and C_{60}, *Phys. Rev. B* **85**(24), 245314, doi:10.1103/PhysRevB.85.245314 (2012).

[176] H. Jiang, P. Hu, J. Ye, Y. Li, H. Li, X. Zhang, R. Li, H. Dong, W. Hu, and C. Kloc, Molecular Crystal Engineering: Tuning Organic Semiconductor from p-type to n-type by Adjusting Their Substitutional Symmetry, *Adv. Mater.* **29**(10), 1605053, doi:10.1002/adma.201605053 (2017).

[177] S. Heutz, P. Sullivan, B. Sanderson, S. Schultes, and T. Jones, Influence of molecular architecture and intermixing on the photovoltaic, morphological and spectroscopic properties of CuPc-C_{60} heterojunctions, *Sol. Energ. Mat. Sol. Cells* **83**, 229, doi:10.1016/j.solmat.2004.02.027 (2004).

[178] R. Banerjee, A. Hinderhofer, M. Weinmann, B. Reisz, C. Lorch, A. Gerlach, M. Oettel, and F. Schreiber, Interrupted Growth to Manipulate Phase Separation in DIP:C60 Organic Semiconductor Blends, *J. Phys. Chem. C* **122**(3), 1839, doi:10.1021/acs.jpcc.7b09637 (2018).

[179] S. Kowarik, A. Gerlach, W. Leitenberger, J. Hu, G. Witte, C. Wöll, U. Pietsch, and F. Schreiber, Energy-dispersive X-ray reflectivity and GID for real-time growth studies of pentacene thin films, *Thin Solid Films* **515**(14), 5606, doi:10.1016/j.tsf.2006.12.020 (2007).

[180] S. Kowarik, A. Gerlach, M. W. A. Skoda, S. Sellner, and F. Schreiber, Real-time studies of thin film growth: Measurement and analysis of X-ray growth oscillations beyond the anti-Bragg point, *Eur. Phys. J. Special Topics* **167**, 11, doi:10.1140/epjst/e2009-00930-y (2009).

[181] X. Zhang, E. Barrena, D. de Oteyza, and H. Dosch, Transition from layer-by-layer to rapid roughening in the growth of DIP on SiO_2, *Surf. Sci.* **601**(12), 2420, doi:10.1016/j.susc.2007.04.051 (2007).

[182] A. C. Dürr, F. Schreiber, K. A. Ritley, V. Kruppa, J. Krug, H. Dosch, and B. Struth, Rapid Roughening in Thin Film Growth of an Organic Semiconductor (Diindenoperylene), *Phys. Rev. Lett.* **90**(1), 016104, doi:10.1103/PhysRevLett.90.016104 (2003).

[183] J. Yang, S. Yim, and T. S. Jones, Molecular-Orientation-Induced Rapid Roughening and Morphology Transition in Organic Semiconductor Thin-Film Growth, *Sci. Rep.* **5**, 9441, doi:10.1038/srep09441 (2015).

[184] A. Aufderheide, Optical and Structural Properties of Molecular Mixtures of Pentacene and Diindenoperylene in Thin Films, Diploma thesis, University of Tübingen (2012).

List of Publications

B. Reisz, E. Empting, M. Zwadlo, M. Hodas, G. Duva, V. Belova, C. Zeiser, J. Hagenlocher, S. Maiti, A. Hinderhofer, A. Gerlach, M. Oettel and F. Schreiber, Thin Film Growth of Phase Separating Phthalocyanine-Fullerene Blends: A Combined Experimental and Computational Study, *Phys. Rev. Materials* **5**, 045601, doi:10.1103/PhysRevMaterials.5.045601 (2021).

B. Reisz, V. Belova, G. Duva, C. Zeiser, M. Hodas, J. Hagara, P. Siffalovič, L. Pithan, T. Hosokai, A. Hinderhofer, A. Gerlach and F. Schreiber, Polymorphism and Structure Formation in Copper Phthalocyanine Thin Films, *J Appl Crystallogr* **54**(1), 203, doi:10.1107/S1600576720015472 (2021).

G. Duva, L. Pithan, C. Zeiser, B. Reisz, J. Dieterle, B. Hofferberth, P. Beyer, L. Bogula, A. Opitz, S. Kowarik, A. Hinderhofer, A. Gerlach and F. Schreiber, Thin-Film Texture and Optical Properties of Donor/Acceptor Complexes. Diindenoperylene/F6TCNNQ vs Alpha-Sexithiophene/F6TCNNQ, *J. Phys. Chem. C* **122**, 18705, doi:10.1021/acs.jpcc.8b03744 (2018).

M. Hodas, P. Siffalovic, P. Nádaždy, N. Mrkyvková, M. Bodík, Y. Halahovets, G. Duva, B. Reisz, O. Konovalov, W. Ohm, M. Jergel, E. Majková, A. Gerlach, A. Hinderhofer and F. Schreiber, Real-Time Monitoring of Growth and Orientational Alignment of Pentacene on Epitaxial Graphene for Organic Electronics, *ACS Appl. Nano Mater.* **1**, 2819, doi:10.1021/acsanm.8b00473 (2018).

R. Banerjee, A. Hinderhofer, M. Weinmann, B. Reisz, C. Lorch, A. Gerlach, M. Oettel, and F. Schreiber, Interrupted Growth to Manipulate Phase Separation in DIP:C60 Organic Semiconductor Blends, *J. Phys. Chem. C* **122**, 1839, doi:10.1021/acs.jpcc.7b09637 (2018).

V. Belova, B. Wagner, B. Reisz, C. Zeiser, G. Duva, J. Rozbořil, J. Novák, A. Gerlach, A. Hinderhofer and F. Schreiber, Real-Time Structural and Optical Study of Growth and Packing Behavior of Perylene Diimide Derivative Thin Films: Influence of Side-Chain Modification, *J. Phys. Chem. C* **122**, 8589, doi:10.1021/acs.jpcc.8b00787 (2018).

T. Storzer, A. Hinderhofer, C. Zeiser, J. Novák, Z. Fišer, V. Belova, B. Reisz, S. Maiti, G. Duva, R. K. Hallani, A. Gerlach, J. E. Anthony and F. Schreiber, Growth, Structure, and Anisotropic Optical Properties of Difluoro-anthradithiophene Thin Films, *J. Phys. Chem. C* **121**, 21011, doi:10.1021/acs.jpcc.7b06558 (2017).

B. Reisz, S. Weimer, R. Banerjee, C. Zeiser, C. Lorch, G. Duva, J. Dieterle, K. Yonezawa, J.P. Yang, N. Ueno, S. Kera, A. Hinderhofer, A. Gerlach and F. Schreiber, Structural, Optical, and Electronic Characterization of Perfluorinated Sexithiophene Films and Mixed Films with Sexithiophene, *J. Mater. Res.* **32**, 1908, doi:10.1557/jmr.2017.99 (2017).

List of Abbreviations

Experimental techniques:

AFM   Atomic force microscopy

EDX   Energy dispersive X-ray analysis

GISAXS   Grazing incidence small angle X-ray diffraction

GIWAXS   Grazing incidence wide angle X-ray diffraction

GIXD   Grazing incidence X-ray diffraction

OMBD   Organic molecular beam deposition

Q-Map   Reciprocal space map

SAXS   Small angle X-ray scattering

SEM   Scanning electron Microscopy

WAXS   Wide angle X-ray scattering

XRD   X-ray diffraction

XRR   X-ray reflectivity

Devices:

IGP   Ion getter pump

OFET   Organic field effect transistor

OLED   Organic light emitting diode

OPV   Organic photovoltaic

TFT   Thin film transistors

TMP   Turbo molecular pump

TSP   Titanium sublimation pump

Further abbreviations:

C_{60}	The Buckminster fullerene
CIF	Crystallographic information file
CuPc	Copper phthalocyanine
fcc	face centered cubic
FOM	Figure of merit (in *GenX*)
hcc	hexagonal closed packed
HOMO	Highest occupied molecular orbital
LUMO	Lowest unoccupied molecular orbital
R_{Dep}	Deposition rate
SLD	Scattering length density (electron density)
σ_{RMS}	Root mean square roughness
T_{Sub}	substrate temperature
θ_n	layer coverage
UHV	Ultra high vacuum
VdW	Van der Waals

Software:

GenX	A software for fitting XRR profiles.
Gwyddion	A software for the evaluation of AFM images.
Matlab	Matrix calculation software for scientific and engineering purposes.

Synchrotron rings and beam lines:

Abbrev.	Synchrotron	Country	Beamline
SLS	Swiss Light Source	Switzerland	MS-X04 SA
ESRF	European Synchrotron Radiation Facility	France	ID03
DESY	Deutsches Elektronen Synchrotron	Germany	P03 at Petra III
DLS	Diamond Light Source	United Kingdom	I07

Deutsche Zusammenfassung

Organische Dünnfilme weisen oft halbleitende Eigenschaften auf und werden in organischen Leuchtdioden (OLEDs), organischen Feldeffekttransistoren (OFETs) und organischen Photovoltaikzellen (OPVs) verwendet. Die Leistungsfähigkeit dieser Bauteile hängt entscheidend von der Dünnfilmstruktur ab. Geeignete Materialien sind kleine organische Moleküle und Polymere. Kleine organische Moleküle können mittels organischer Molekularstrahldeposition (OMBD) auf ein Substrat im Vakuum aufgedampft werden, was sowohl eine reine Umgebung, als auch eine präzise Schichtdickenkontrolle gewährleistet. Die dabei entstehenden Dünnfilme weisen typischerweise kristalline Inseln auf. Die Oberflächenmorphologien reichen von glatten Filmen, welche das Substrate vollständig benetzen, bis hin zu rauen Oberflächen mit ausgeprägter Clusterbildung. Im Allgmeinen sind organische Dünnfilme durch die Größe und Orientierung ihrer Kristallite, durch ihre Kristallstrukturen und durch ihre Morphologien, d.h. die Oberflächenrauheit, die Größe, die Form und die Dichte der Inseln charakterisiert. Binäre Mischungen bestehend aus zwei Arten von Molekülen werden zusätzlich durch ihr Mischungsverhalten charakterisiert. Binäre Mischungen aus einem Donor- und einem Akzeptormaterial werden zum Beispiel in organischen Solarzellen eingesetzt, um optisch angeregte Ladungsträger voneinander zu trennen. Phasenseparation, große Kontaktflächen zwischen Donor und Akzeptorbereichen, sowie durchgehende Verbindungen zu den jeweiligen Elektroden sind günstig für eine effiziente Trennung der Ladungsträger. Die gewünschten Strukturen können entweder durch sequenzielle Deposition erreicht werden, d.h. Donor- und Akzeptormaterial werden nacheinander aufgedampft, oder durch co-Deposition, d.h. beide Materialien werden gleichzeitig aus zwei getrennten Verdampferzellen aufgedampft. Je nach Wahl der Wachstumsbedingungen, wie zum Beispiel die Aufdampfrate, die Substrattemperatur und das Mischungsverhältnis, können unterschiedliche Dünnfilmstrukturen realisiert werden.

Die vorliegende Arbeit untersucht den Einfluss der Aufdampfrate und der Substrattempertur während der Molekularstrahldeposition auf die Bildung von Kristallstrukturen und Inseln und diskutiert dabei auch die Rolle der Moleküldiffusion während des Wachstumsprozesses. Drei sehr kleine und einfache organische Moleküle wurden ausgewählt: Kupfer Phthalocyanin (CuPc), Coronen und das Buckminster Fulleren (C_{60}). Von einer natürlichen, amorphen Oxidschicht bedeckte Siliziumwafer wurden als schwach wechselwirkende Substrate verwendet. Zunächst werden die Kristallstrukturen und Morphologien der reinen Filme diskutiert und miteinander verglichen. Anschließend werden die Morphologien und das Mischungsverhalten von simultan aufgedampften 1:1 Mischungen aus CuPc und C_{60}, welche für ihren hohen Wirkungsgrad in der Photovoltaik bekannt sind, analysiert. Eine Kombination aus bildgebenden Verfahren bestehend aus Rastkraft-, Rasterelektronen- und Lichtmikroskopie, sowie verschiedenen Röntgenbeugungsexperimenten diente den vorliegenden Studien. Zusäzlich lieferten fortgeschrittene Datenanalyseverfahren quantitative Ergebnisse. Die Daten zeigen, dass erhöhte Substrattemperaturen sowie reduzierte Aufdampfraten zur Bildung von größeren Inseln und geringeren Inseldichten führen. Darüberhinaus zeigen die Daten auch, dass die temperaturgetriebene Abwärtsdiffusion von CuPc dem rau machenden Effekt von C_{60} entgegenwirkt, sodass die gesamte Rauigkeitsentwicklung stark von der Substrattemperatur während des Wachstums gemischter CuPc-C_{60} Dünnfilme abhängt.

Acknowledgments